ENERGY STORAGE SYSTEMS BEYOND LI-ION INTERCALATION CHEMISTRY

EDITED BY: Kai Zhu, Zhumabay Bakenov, Jian Liu and Hossein Yadegari
PUBLISHED IN: Frontiers in Energy Research

frontiers Research Topics

frontiers

ISSN 1664-8714
ISBN 978-2-88966-819-9
DOI 10.3389/978-2-88966-819-9

About Frontiers

Frontiers is more than just an open-access publisher of scholarly articles: it is a pioneering approach to the world of academia, radically improving the way scholarly research is managed. The grand vision of Frontiers is a world where all people have an equal opportunity to seek, share and generate knowledge. Frontiers provides immediate and permanent online open access to all its publications, but this alone is not enough to realize our grand goals.

Frontiers Journal Series

The Frontiers Journal Series is a multi-tier and interdisciplinary set of open-access, online journals, promising a paradigm shift from the current review, selection and dissemination processes in academic publishing. All Frontiers journals are driven by researchers for researchers; therefore, they constitute a service to the scholarly community. At the same time, the Frontiers Journal Series operates on a revolutionary invention, the tiered publishing system, initially addressing specific communities of scholars, and gradually climbing up to broader public understanding, thus serving the interests of the lay society, too.

Dedication to Quality

Each Frontiers article is a landmark of the highest quality, thanks to genuinely collaborative interactions between authors and review editors, who include some of the world's best academicians. Research must be certified by peers before entering a stream of knowledge that may eventually reach the public - and shape society; therefore, Frontiers only applies the most rigorous and unbiased reviews.
Frontiers revolutionizes research publishing by freely delivering the most outstanding research, evaluated with no bias from both the academic and social point of view. By applying the most advanced information technologies, Frontiers is catapulting scholarly publishing into a new generation.

What are Frontiers Research Topics?

Frontiers Research Topics are very popular trademarks of the Frontiers Journals Series: they are collections of at least ten articles, all centered on a particular subject. With their unique mix of varied contributions from Original Research to Review Articles, Frontiers Research Topics unify the most influential researchers, the latest key findings and historical advances in a hot research area! Find out more on how to host your own Frontiers Research Topic or contribute to one as an author by contacting the Frontiers Editorial Office: frontiersin.org/about/contact

ENERGY STORAGE SYSTEMS BEYOND LI-ION INTERCALATION CHEMISTRY

Topic Editors:
Kai Zhu, Harbin Engineering University, China
Zhumabay Bakenov, Nazarbayev University, Kazakhstan
Jian Liu, University of British Columbia Okanagan, Canada
Hossein Yadegari, University of Toronto, Canada

Citation: Zhu, K., Bakenov, Z., Liu, J., Yadegari, H., eds. (2021). Energy Storage Systems Beyond Li-Ion Intercalation Chemistry. Lausanne: Frontiers Media SA. doi: 10.3389/978-2-88966-819-9

Table of Contents

frontiers in Energy Research

EDITORIAL
published: 29 March 2021
doi: 10.3389/fenrg.2021.658875

Editorial: Energy Storage Systems Beyond Li-Ion Intercalation Chemistry

Zhumabay Bakenov[1,2]*, *Kai Zhu*[3], *Jian Liu*[4] and *Hossein Yadegari*[5]

[1]Department of Chemical and Materials Engineering, School of Engineering and Digital Sciences, Nazarbayev University, Kazakhstan, [2]National Laboratory Astana, Nazarbayev University, Kazakhstan, [3]Harbin Engineering University, China, [4]University of British Columbia Okanagan, Canada, [5]University of Toronto, Canada

Keywords: beyond Li-ion, rechargeable batteries, energy storage (batteries), next generation batteries, alternative battery technologies

Editorial on the Research Topic

Energy Storage Systems Beyond Li-Ion Intercalation Chemistry

Ecological and energy issues brought green energy production and low/zero-emission transportation to the front of emerging and rapidly developing areas of industry. Booming development and miniaturization of consumer electronics and communication devices are the critical paths of the recent technological progress supporting our social sustainability. The technologies in these crucial areas of sustainable development rely on the availability of high-performance energy storage/power source devices, and rechargeable batteries are the best options available now. Although the current leader of the market, lithium-ion batteries, provide the most advanced operation among other batteries, they cannot satisfy the ever-growing performance requirements of the emerging technologies in terms of safety, cost, and stable performance. Therefore, alternative battery technologies—"beyond lithium-ion" batteries were proposed and are rapidly developed. This Research Topic covers some areas of such emerging systems. The works published in the Research Topic includes technical and review papers in the areas of advanced electrode and electrolytes and the development of special interlayers to enhance the performance of the batteries, operating with both organic and aqueous electrolytes. Along with this, the Topic includes a paper that discusses the compromise between technology sustainability and maximization of electric performance, which the Editors considered as an essential topic to discuss when choosing the best option to power advanced and growing applications.

AUTHOR CONTRIBUTIONS

All authors listed have made a substantial, direct, and intellectual contribution to the work and approved it for publication.

Conflict of Interest: The authors declare that the research was conducted in the absence of any commercial or financial relationships that could be construed as a potential conflict of interest.

OPEN ACCESS

Edited and reviewed by:
Jonghyun Park,
Missouri University of Science and Technology, United States

***Correspondence:**
Zhumabay Bakenov
zbakenov@nu.edu.kz

†*These authors have contributed equally to this work*

Specialty section:
This article was submitted to Electrochemical Energy Conversion and Storage, a section of the journal Frontiers in Energy Research

Received: *26 January 2021*
Accepted: *09 February 2021*
Published: *29 March 2021*

Citation:
Bakenov Z, Zhu K, Liu J and Yadegari H (2021) Editorial: Energy Storage Systems Beyond Li-Ion Intercalation Chemistry. Front. Energy Res. 9:658875. doi: 10.3389/fenrg.2021.658875

frontiers in Energy Research

ORIGINAL RESEARCH
published: 16 July 2020
doi: 10.3389/fenrg.2020.00154

Facile Synthesis of Binder-Free Three-Dimensional Cu_xS Nanoflowers for Lithium Batteries

*Assyl Adylkhanova[1], Arailym Nurpeissova[2], Desmond Adair[2], Zhumabay Bakenov[2], Izumi Taniguchi[3] and Gulnur Kalimuldina[2]**

[1] Department of Chemistry, L. N. Gumilyov Eurasian National University, Nur-Sultan, Kazakhstan, [2] National Laboratory Astana, Institute of Batteries, Nazarbayev University, Nur-Sultan, Kazakhstan, [3] Department of Chemical Science and Engineering, Tokyo Institute of Technology, Tokyo, Japan

Copper sulfides (Cu_xS) with different stoichiometry are considered as prospective cathode materials for lithium batteries owing to their large energy storage capability. In this work, three-dimensional Cu_xS cathodes were synthesized via introducing commercially available copper foam into the solution of dimethyl sulfoxide (DMSO) and sulfur powder. The synthesis procedures were straightforward and ultrafast and did not require additional reagents, high temperature, or long processing time and can be considered as a facile one-step method. Copper sulfide materials with different stoichiometry (x = 1.8, 1.96) were obtained by changing the temperature and the residence time of the copper foam in the DMSO solution. The effects of the temperature and time on phase and morphology of Cu_xS were characterized by X-ray diffraction and scanning electron microscopy coupled with energy dispersive X-ray spectroscopy. Electrochemical tests resulted in a stable cyclability of $Cu_{1.8}S$ cathode with 100% Coulombic efficiency and capacity of approximately 250 mAh g^{-1}.

Keywords: lithium-ion batteries, copper foam, sulfur, one-step method, copper sulfide

OPEN ACCESS

Edited by:
Jun Yan,
Harbin Engineering University, China

Reviewed by:
Yurong Ren,
Changzhou University, China
Yijing Wang,
Nankai University, China
Yourong Wang,
Wuhan Polytechnic University, China

****Correspondence:***
Gulnur Kalimuldina
gkalimuldina@nu.edu.kz

Specialty section:
This article was submitted to Electrochemical Energy Conversion and Storage, a section of the journal Frontiers in Energy Research

Received: *14 April 2020*
Accepted: *17 June 2020*
Published: *16 July 2020*

Citation:
Adylkhanova A, Nurpeissova A, Adair D, Bakenov Z, Taniguchi I and Kalimuldina G (2020) Facile Synthesis of Binder-Free Three-Dimensional Cu_xS Nanoflowers for Lithium Batteries. Front. Energy Res. 8:154. doi: 10.3389/fenrg.2020.00154

INTRODUCTION

Currently, primary energy sources (i.e., fossil fuels such as oil, coal, and natural gas) are depleting at an increasing rate; thus, energy storage devices that suggest offering both rate performance and greater capacity are always of high interest. In addition to this, non-renewable energy sources are responsible for environmental hazards such as "greenhouse gas" emissions and contamination (Armaroli and Balzani, 2007). For the last three decades, lithium-ion batteries (LIBs) have been known as one of the superior technologies to store energy and are already used in portable electronics. Recently, LIBs made its progressive way into the field of electric vehicles, grid energy storage, and plug-in hybrid vehicles (Chung and Sohn, 2002). However, traditional LIBs are still not satisfying the needs for the high capacity, energy density, and, most importantly, safety aspects. For instance, a traditional LIB cell consists of a transition metal oxide (e.g., $LiCoO_2$) as the cathode material and graphite as the anode material. Today, their energy density has reached its limits of <260 Wh kg^{-1} and is not able to cope with the required energy demands of modern society

(Meng et al., 2012; Manthiram et al., 2017). Furthermore, inherent defects of LIBs such as safety concerns limit their development, with incidents ranging from Hewlett Packard's recall of hundreds of thousands of laptop batteries in 2009 due to overheating and fire, to the Samsung Galaxy Note 7 explosion in 2017 (Liu et al., 2018). Additionally, $LiCoO_2$ is expensive as well as toxic (Blomgren, 2017).

Alternatively, scholars have been investigating new electrode materials to solve these issues. Compared to conventional candidate materials, conversion-based materials [e.g., metal fluorides (Cabana et al., 2010; Wang et al., 2011), sulfides (Meng et al., 2014; Lu et al., 2017), phosphides, and nitrides (Cabana et al., 2010)] present an essential class that has not been well researched. Conversion-based materials have been suggested for LIBs because of their higher specific capacities and preferably cost-effectiveness. Over the past decades, copper sulfides (Cu_xS) have attracted considerable attention in the field of LIBs because of their different valence states and stoichiometric compositions (Chung and Sohn, 2002). The latest studies have shown that Cu_xS ($1 \leq x \leq 2$) are an upcoming cathode candidate for interaction with lithium metal (i.e., Li-Cu_xS, $1 \leq x \leq 2$) with long cyclic performance and high rate capability.

Copper sulfide is known to have five stable phases starting from chalcocite "copper-rich" Cu_2S to the covellite "copper-deficient" CuS. The excellent properties such as high electronic conductivity of 10^{-3} S cm^{-1} and theoretical capacities of 337–560 mAh g^{-1} make them attractive electrode material for large-scale applications in secondary lithium, magnesium, and sodium batteries because of their abundance and inexpensiveness (Lu et al., 2017; Xiao et al., 2018; Wang et al., 2019). It has been reported that the electrochemical and electronic properties of the Cu_xS system depend greatly on both the Cu/S ratios and crystalline structures. An increase in the bandgap occurs with an increase in the x value in bulk Cu_xS (i.e., 1.2 eV for Cu_2S, 1.5 eV for $Cu_{1.8}S$, and 2.0 eV for CuS). This implied that Cu_xS with the composition closer to Cu_2S will demonstrate higher electronic conductivity than that of CuS electrodes (Grozdanov and Najdoski, 1995; Zhao et al., 2009).

Thus far, many studies have been devoted to the synthesis of 1–3D structured CuS and Cu_2S electrodes by hydrothermal (Tao et al., 2014), solvothermal (Han et al., 2011; Liu and Xue, 2011), microwave (Xiao et al., 2016; Yuan et al., 2016; Wang et al., 2019), spray pyrolysis (Madarasz et al., 2001; Kalimuldina and Taniguchi, 2016a,b), and other methods. However, only a few have focused on the preparation of freestanding 3D structured Cu_xS electrodes (Ni et al., 2013; Tang et al., 2017). In this research, we investigate a facile way to prepare a 3D structured freestanding cathode material at a low temperature via a straightforward one-step method that does not require expensive apparatus and additional chemical agents compared to the conventional and complex ways of cathode preparation.

To develop a better battery with sufficient volumetric and power densities, the fabrication of freestanding cathodes is being considered as a reasonable approach. Therefore, the preparation of freestanding Cu_xS with high active mass loading by an ultrafast and low-cost method could benefit the simplification of cell packaging configurations as binders, and current collectors can be omitted (Zeng et al., 2015).

MATERIALS AND METHODS

Synthesis Procedure

The materials utilized in this work were commercialized copper foam (Cu foam; MTI Corp., United States), sulfur powder (S, LenReaktiv), and dimethyl sulfoxide (C_2H_6OS, DMSO; Sigma–Aldrich, Germany). Materials were analytical grade and were used as received without further purification. First, to assess the solubility of S powder in DMSO, different amounts of S powder were dissolved in 20 mL DMSO at a heating temperature of 80°C. It was found that more than 0.1 g of powder cannot be fully dissolved in the solution. Afterward, an optimized amount of 0.1 g was used in further experiments. The effect of temperature on the formation of Cu_xS phases was investigated by varying the reaction temperature from 80°C to 110°C with the help of a heater while keeping the time constant at 30 s. After finding the desired favorable temperature for the synthesis, time was varied from 10 s to 1 min to optimize the reaction time.

In a typical synthesis procedure, 0.1 g of S powder was weighed and added into 20 mL of DMSO solution under vigorous stirring with a magnetic stirrer at the above-stated temperatures. For the preparation of the copper foam, it was cut into small rectangular pieces, washed with acetone, and dried in a vacuum oven at 60°C for 1 h. After the total dissolution of S powder, the prepared copper foam pieces were soaked into the solution as seen in **Figure 1**. Subsequently, blackened copper foam pieces were then dried in a vacuum oven at 60°C for 24 h. The masses of the obtained Cu_xS active materials were calculated based on the fact that the Cu element from the Cu foam directly reacts with the S in the solution. First, the mass of the deposited S was calculated by subtracting the pristine Cu foam mass from the obtained Cu/Cu_xS material mass. After, the electrode's mass was calculated considering the molar masses of Cu_xS by the cross-multiplying method.

Physical and Electrochemical Characterizations of Cu_xS

Obtained Cu_xS materials were characterized by X-ray powder diffraction (XRD; Rigaku SmartLab® X-ray diffraction system, Japan) to investigate the phases of Cu_xS. The scanning electron microscope Crossbeam 540 coupled with energy-dispersive X-ray spectroscopy (SEM-EDS; Zeiss, Germany) was employed to observe the morphologies and distribution of separate

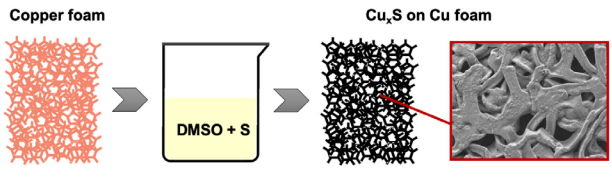

FIGURE 1 | Copper sulfide on Cu foam synthesis route scheme.

components of obtained materials. CR2032 type coin cells were assembled and tested to assess the electrochemical performances of the synthesized electrodes. Copper foam pieces were cut into 16 mm in diameter disks and were used as cathodes without any binders and additives in half-cells with Li metal. The mass loading of Cu_xS active material varied between 8.7 and 10.4 mg cm^{-2}, depending on the synthesis time. Glovebox (MBraun, Germany) was used to assemble the half-cells, where the role of the separator was served by the Celgard 2400, and 1 M LiTFSI in DOL/DME was utilized as an electrolyte. The cells were then tested in the multichannel battery test system Arbin in the voltage range between 1.0 and 3.0 V with a constant current in the form of a C/5 rate (1C = 7–7.3 mAh).

RESULTS AND DISCUSSION

X-ray powder diffraction patterns and SEM pictures of Cu_xS samples obtained at different temperatures with a constant time of 30 s are shown in **Figure 2**. The main diffraction peaks located at 43.5° and 50.7° for all samples can be assigned to the (1 1 1) and (2 0 0) crystal faces of the Cu foam, respectively. All other peaks could be indexed to $Cu_{1.8}S$ and $Cu_{1.96}S$ phases with the trace of very weak peaks (35°–38°) that could correspond to monoclinic Cu_2S (Potter and Evans, 1976). At lower temperatures of 80 and 90°C, phases of $Cu_{1.96}S$ prevail, whereas at slightly higher temperatures of 100 and 110°C, formation of more $Cu_{1.8}S$ can be noticed. Also, one can observe from the SEM results (**Figures 2b–e**) that the temperature had a considerable effect on the morphologies and structures of the Cu_xS phases. In essence, at 80°C, the only formation of two-dimensional irregular Cu_xS plates can be observed, whereas increasing the temperature only by 10°C results in a surface with rough structures that resemble flowers-like humps. Going up to 100°C leads to the formation of homogenous hierarchical petals. Eventually, at 110°C, petals assemble themselves in flower-like spherical structures.

Figure 3 represents the XRD results and SEM images of Cu_xS on Cu foam obtained at 90°C at different times. The time had a significant influence on the phases and morphologies of the formed material as well. The samples prepared at the time of 10, 20, and 30 s showed a similar tendency of $Cu_{1.96}S$ formation. However, material obtained at 10 s showed the purest phase of $Cu_{1.96}S$ among them.

On the other hand, 1-min synthesis triggered the formation of a flower-like $Cu_{1.8}S$ phase. As shown in **Figures 3b–e**, the morphology evolution of CuS from irregular form to the flower-like structure can be seen, involving several growth stages. The introduction of copper foam into a sulfur solution for 10 s resulted in the formation of irregular pieces (**Figure 3b**), whereas changing the time for 20 s enhanced the size of that particle (**Figure 3c**). After 30 s, pieces transformed into the sheets, and they became geometrically regular (**Figure 3d**). The time increase to 1 min affected significantly the structure of composites, forming a flower-like structure of Cu_xS (mainly $Cu_{1.8}S$) (**Figure 3e**).

The phase evolution of Cu_xS is depicted in **Figure 4**, and several steps are suggested: first, after the Cu foam is soaked in the solution, instant adsorption of sulfur molecules takes place on the surface of the foam. Then, after several seconds, the adsorbed sulfur molecules react with the copper molecules in the surface of the Cu foam, resulting in a copper-rich $Cu_{1.96}S$ phase. Subsequently, increasing the reaction time leads to the reaction of the $Cu_{1.96}S$ phase with the sulfur again causing the formation of sulfur-rich $Cu_{1.8}S$ phase. Also, it is worth to mention that the main transformation of $Cu_{1.96}S$ to the $Cu_{1.8}S$ phase is due to the large surface area of the nanocrystals (**Figures 3b–d**), which

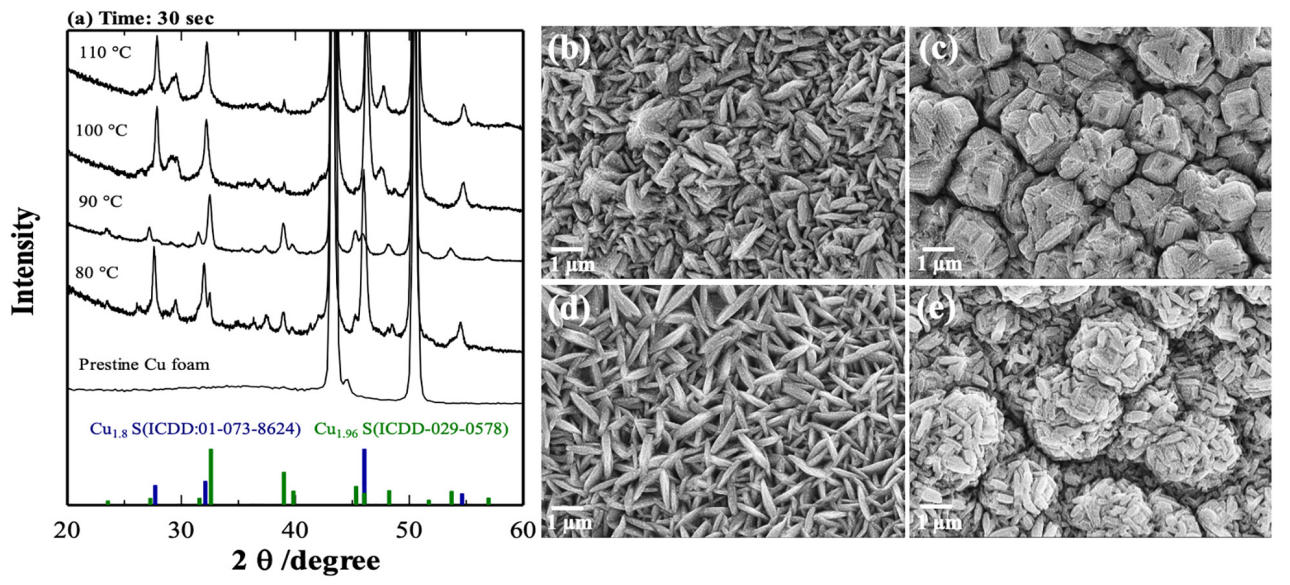

FIGURE 2 | X-ray powder diffraction patterns **(a)** and SEM pictures of Cu_xS samples obtained at different temperatures with the constant time of 30 s: **(b)** 80°C, **(c)** 90°C, **(d)** 100°C, and **(e)** 110°C.

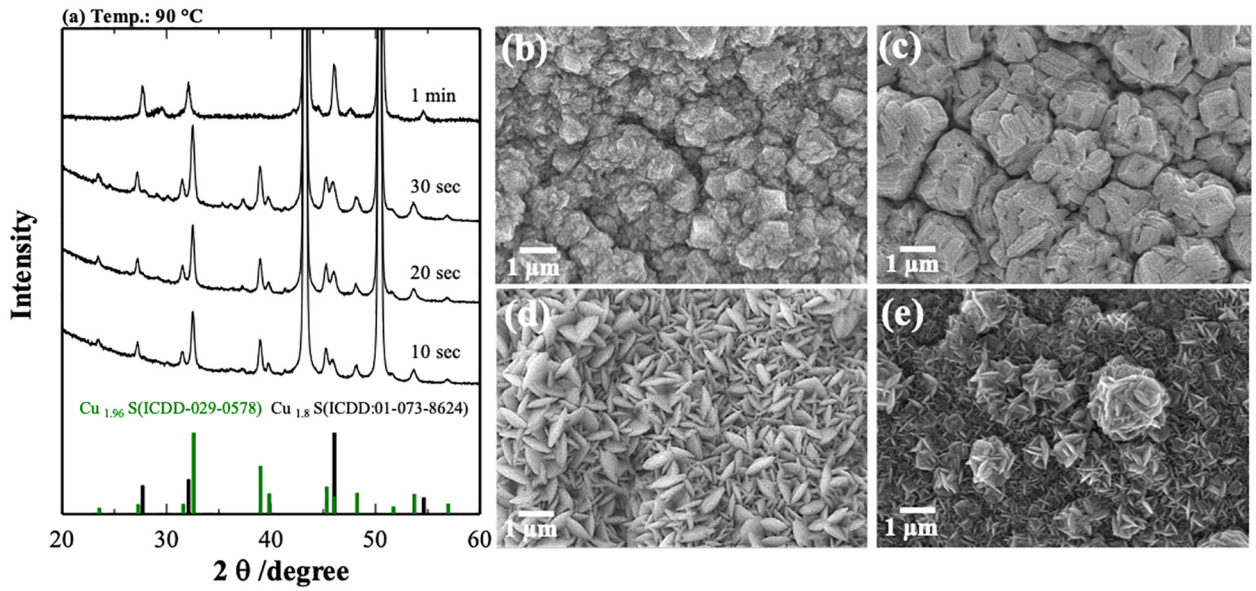

FIGURE 3 | X-ray powder diffraction patterns **(a)** and SEM pictures of Cu_xS samples obtained at different times with the constant temperature of 90°C: **(b)** 10 s, **(c)** 20 s, **(d)** 30 s, and **(e)** 1 min.

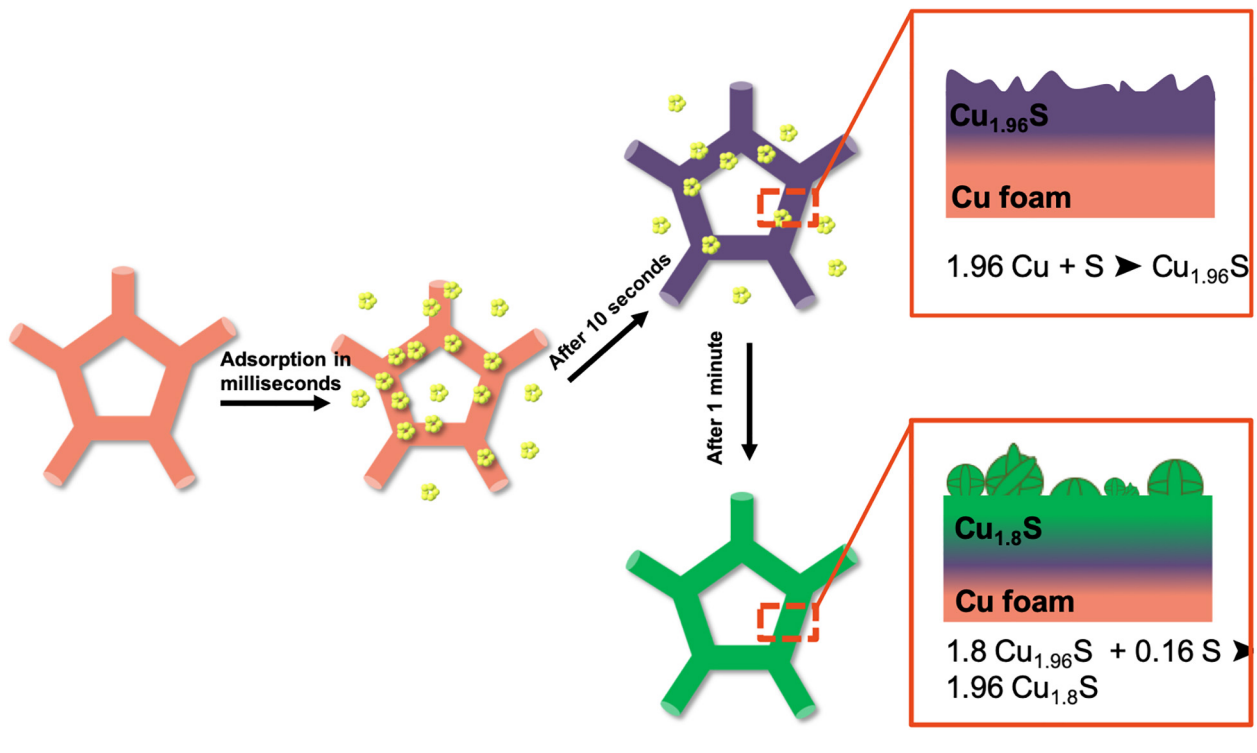

FIGURE 4 | Schematic representation of $Cu_{1.96}S$ and $Cu_{1.8}S$ formation on Cu foam.

allowed the rapid diffusion of Cu ions out of the crystal, thereby increasing the surface oxidation which possibly accelerated the djurleite formation (Green et al., 2012).

The scanning electron microscope–EDS images of $Cu_{1.8}S$ (**Figure 5**) indicated that the distribution of Cu and S elements on the copper foam's surface was uniform, and the coverage was even. Although the reaction between $Cu_{1.96}S$ and S continues on the surface of the Cu foam in a gradient pattern, the composition distribution of the main elements is homogenous throughout the 3D material.

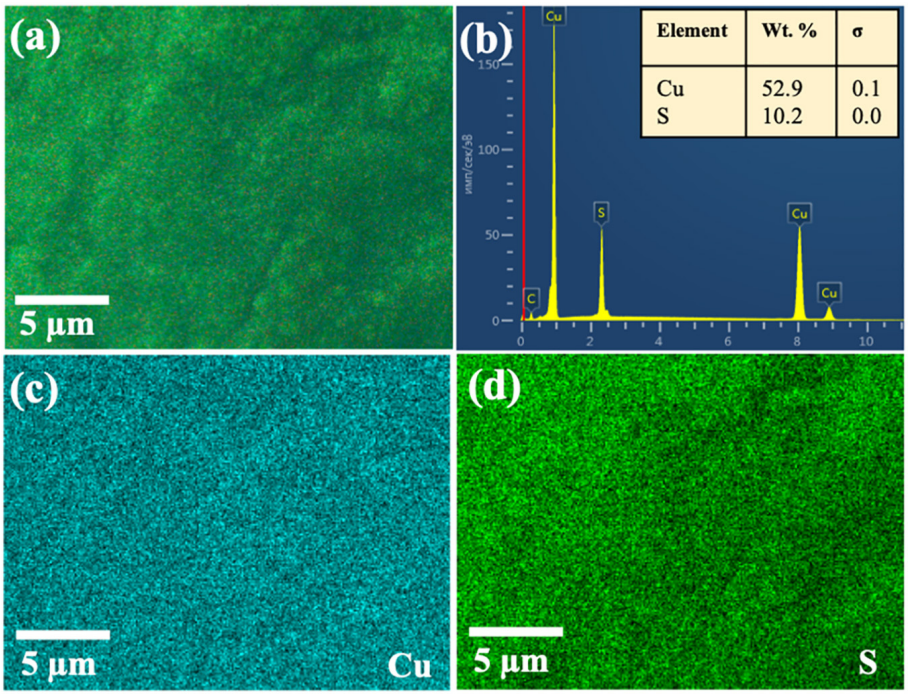

FIGURE 5 | Scanning electron microscope–EDS mappings of obtained $Cu_{1.8}S$ on Cu foam: **(a)** pristine sample, **(b)** EDS spectra, **(c)** Cu and **(d)** S element mapping images.

The electrochemical characterization of $Cu_{1.96}S$ and $Cu_{1.8}S$ as cathode materials in lithium half-cells is presented in **Figure 6**. Galvanostatic tests were carried out at a rate of C/5 based on the mass of Cu_xS. **Figure 6A** shows charge–discharge profiles of $Cu_{1.96}S$ freestanding electrodes. It can be observed that the first discharge profile exhibits short and prolonged plateaus at 2.0 and 1.73 V, respectively. The reaction mechanism for Cu_2S was reported as the initial discharge plateau should be at 1.73 V and corresponded to $Cu_2S + 2Li^+ + 2e^- \rightarrow Li_2S + 2Cu$ during the first cycle (Kalimuldina and Taniguchi, 2016b). However, for $Cu_{1.96}S$, additional small peaks at 2.0 V can be seen, which is a more typical discharge plateau to CuS electrode (Kalimuldina and Taniguchi, 2017). That difference might come from some impurities residing in the obtained $Cu_{1.96}S$ electrode. After the fifth cycle, the discharge profile showed almost disappeared plateau at 2.2 V and much prolonged at 1.75 V with a capacity of 100 mAh g^{-1}. Those changes might indicate the phase transformation of $Cu_{1.96}S$ with some impurities into pure $Cu_{1.96}S$ with the increase in the cycle number. The impurities could be the insignificant trace of copper-rich phases (Fu and Manthiram, 2013; Jache et al., 2014; Foley et al., 2018).

The first charge voltage profiles are depicted at 1.85 and 2.25 V, respectively. Furthermore, after five cycles, we can observe previously reported flattening of the charge plateau to 1.85 V (Jache et al., 2014). Consequently, we can write the reversible electrochemical reaction accordingly from the obtained charge–discharge profiles as $Li_2S + 2Cu$ Û $Cu_{1.96}S + 0.04Cu + 2Li^+ + 2e^-$ (Debart et al., 2006; Kalimuldina and Taniguchi, 2016b, 2017). The similar charge–discharge profile of $Cu_{1.8}S$ electrode is demonstrated in **Figure 6B**. However, the change in the discharge plateaus at 2.1 and 1.65 V can be seen as there longer 2.1 V discharge plateau than that of in **Figure 6A** for $Cu_{1.96}S$. However, after the fifth cycle, both charge and discharge show single plateaus at 1.75 and 1.85 V with about 250 mAh g^{-1}, respectively. This implies that the richer the sulfur content in the composition of Cu_xS, the more its electrochemical properties get closer to the behavior of the covellite CuS electrode (Jianga et al., 2019).

Cycling performance of both $Cu_{1.96}S$ and $Cu_{1.8}S$ is demonstrated in **Figure 7**. The residue time of 10 s to obtain $Cu_{1.96}S$ at 90°C released a low but stable capacity of 100 mAh g^{-1} for 20 cycles with 100% Coulombic efficiency. On the contrary, when the reaction residue time was increased up to 1 min to achieve $Cu_{1.8}S$, the significant capacity increase was observed. The capacity of $Cu_{1.8}S$ electrode with a mass loading of 10.4 mg cm^{-2} without any binders and additives achieved 250 mAh g^{-1} for 20 cycles with 100% Coulombic efficiency. It is well known that CuS is more attractive in the term of theoretical capacity (560 mAh g^{-1}); however, the electrode with higher copper content is more electrically conductive (Grozdanov and Najdoski, 1995). Based on the theoretical capacities of $Cu_{1.96}S$ and $Cu_{1.8}S$, the latter will deliver higher value. That can be considered as one of the reasons for such differences in the capacity between those electrodes.

The ultrafast and straightforward method of preparation of 3D Cu_xS electrodes on Cu foam showed very prospective

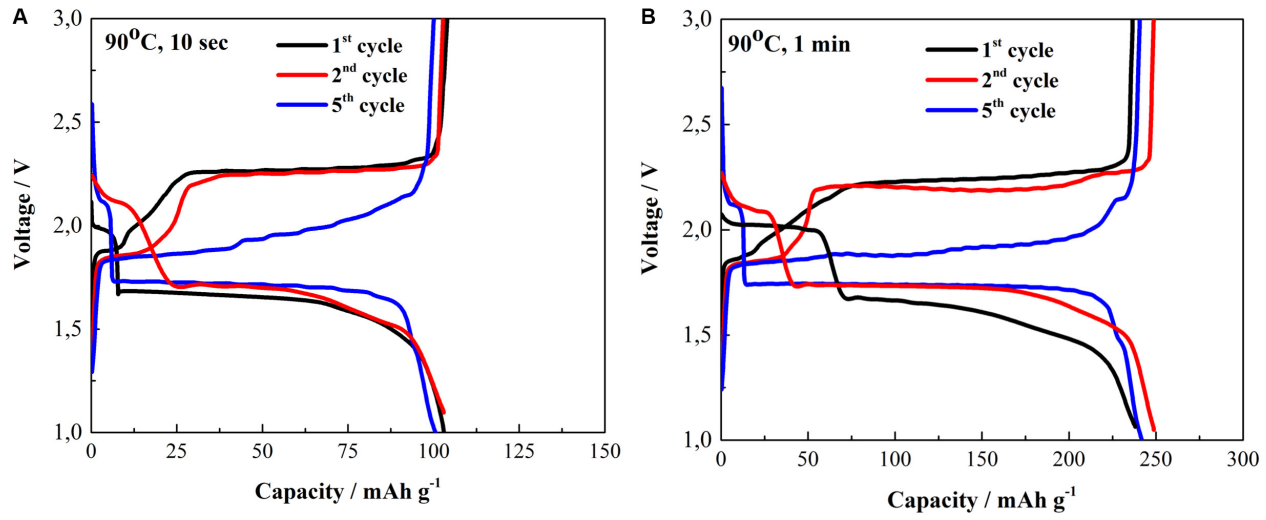

FIGURE 6 | Charge–discharge profiles of **(A)** $Cu_{1.96}S$ (90°C, 10 s) and **(B)** $Cu_{1.8}S$ (90°C, 1 min) cathodes between 1.0 and 3.0 V at C/5.

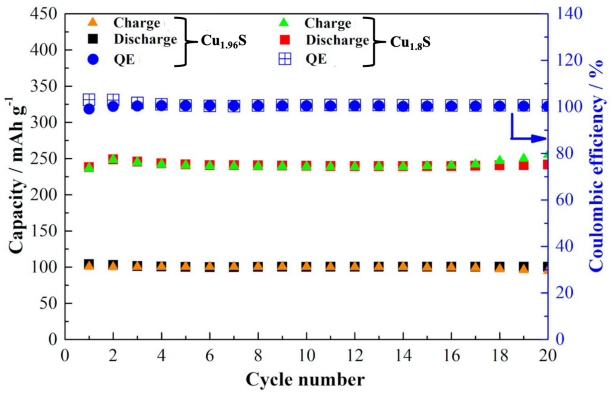

FIGURE 7 | Cycle performance of $Cu_{1.96}S$ (90°C, 10 s) and $Cu_{1.8}S$ (90°C, 1 min) cathodes between 1.0 and 3.0 V at C/5 over 20 cycles.

electrochemical properties as an applicable compartment in the future LIBs. The work confirms that other phases of Cu_xS are also electrochemically stable and have reversible charge–discharge processes even at high active mass loading conditions.

CONCLUSION

Different phases of Cu_xS as $Cu_{1.96}S$ and $Cu_{1.8}S$ were successfully prepared by a simple method of soaking Cu foam in an S/DMSO solution for a short period of time. The effect of temperature and synthesis time on the tendency for the reaction between Cu foam and S were studied. The morphology of Cu_xS samples was cubic-type irregular shapes at 80°C and grew further to the nanoflower-like structures at 110°C. The reaction activity of formed Cu_xS on the surface of Cu foam with remaining S in the DMSO solution was enhanced with the increase in the soaking time.

Electrochemical properties of $Cu_{1.96}S$ formed at 90°C and 10-s synthesis time showed only 100 mAh g^{-1} at 5/C rate, whereas the sample of $Cu_{1.8}S$ that was obtained by holding Cu foam up to 1 min at 90°C in S/DMSO solution reached stable cycling performance at 250 mAh g^{-1} with extremely high mass loading. This allows us to study the phase change of Cu_xS materials, depending on the time and temperature and its influence on the electrochemical properties of the cathode material.

DATA AVAILABILITY STATEMENT

The original contributions presented in the study are included in the article, further inquiries can be directed to the corresponding author.

AUTHOR CONTRIBUTIONS

AA, AN, and GK contributed to the synthesis, characterization, and manuscript writing. GK, DA, ZB, and IT contributed to the characterization, interpretation, and discussion of obtained results. All authors contributed to the article and approved the submitted version.

FUNDING

This work was supported by the research grant 091019CRP2114 "Three-Dimensional All Solid State Rechargeable Batteries," 240919FD3914 "Self-Charging Rechargeable Lithium-ion Battery" from Nazarbayev University and AP05133706 "Innovative high-capacity anodes based on lithium titanate for a next generation of batteries", AP08052143 "Development of wearable self-charging power unit" from the Ministry of Education and Science of the Republic of Kazakhstan.

REFERENCES

Armaroli, N., and Balzani, V. (2007). The future of energy supply: challenges and opportunities. *Angew. Chem. Int. Ed.* 46, 52–66.

Blomgren, G. E. (2017). The development and future of lithium ion batteries. *J. Electrochem. Soc.* 164, A5019–A5025.

Cabana, J., Monconduit, L., Larcher, D., and Palacín, M. R. (2010). Beyond intercalation-based Li-ion batteries: the state of the art and challenges of electrode materials reacting through conversion reactions. *Adv. Mater.* 22, E170–E192.

Chung, J.-S., and Sohn, H.-J. (2002). Electrochemical behaviors of CuS as a cathode material for lithium secondary batteries. *J. Power Sources.* 108, 226–231. doi: 10.1016/s0378-7753(02)00024-1

Debart, A., Dupont, L., Patrice, R., and Tarascon, J.-M. (2006). Reactivity of transition metal (Co, Ni, Cu) sulphides versus lithium: the intriguing case of copper sulphide. *Solid State Sci.* 8, 640–651. doi: 10.1016/j.solidstatesciences.2006.01.013

Foley, S., Geaney, H., Bree, G., Stokes, K., Connolly, S., Zaworotko, M. J., et al. (2018). Copper Sulfide (CuxS) Nanowire-in-Carbon Composites Formed from Direct Sulfurization of the Metal-Organic Framework HKUST-1 and Their Use as Li-Ion Battery Cathodes. *Adv. Funct. Mater.* 28, 1–8.

Fu, A., and Manthiram, A. (2013). Electrochemical properties of Cu2S with ether-based electrolyte in Li-ion batteries. *Electrochim. Acta* 109, 716–719. doi: 10.1016/j.electacta.2013.07.160

Green, M., Pattrick, R., Corr, S., Imai, H., Haigh, S., Young, R., et al. (2012). *Nanoscience: Volume 1: Nanostructures Through Chemistry*. London: Royal Society of Chemistry.

Grozdanov, I., and Najdoski, M. (1995). Optical and electrical properties of copper sulfide films of variable composition. *J. Solid State Chem.* 114, 469–475. doi: 10.1006/jssc.1995.1070

Han, Y., Wang, Y., Gao, W., Wang, Y., Jiao, L., Yuan, H., et al. (2011). Synthesis of novel CuS with hierarchical structures and its application in lithium-ion batteries. *Powder Techn.* 212, 64–68. doi: 10.1016/j.powtec.2011.04.028

Jache, B., Mogwitz, B., Klein, F., and Adelhelm, P. (2014). Copper sulfides for rechargeable lithium batteries: linking cycling stability to electrolyte composition. *J. Power Sources* 247, 703–711. doi: 10.1016/j.jpowsour.2013.08.136

Jianga, K., Chen, Z., and Menga, X. (2019). A Review on CuS and Cu2S as Cathode Materials for Lithium Batteries. *ChemElectroChem* 19, 2825–2840. doi: 10.1002/celc.201900066

Kalimuldina, G., and Taniguchi, I. (2016a). High performance stoichiometric Cu2S cathode on carbon fiber current collector for lithium batteries. *Electrochim. Acta* 224, 329–336. doi: 10.1016/j.electacta.2016.12.058

Kalimuldina, G., and Taniguchi, I. (2016b). Synthesis and electrochemical characterization of stoichiometric Cu2S as cathode material with high rate capability for rechargeable lithium batteries. *J. Power Sources* 331, 258–266. doi: 10.1016/j.jpowsour.2016.09.047

Kalimuldina, G., and Taniguchi, I. (2017). Electrochemical properties of stoichiometric CuS coated on carbon fiber paper and Cu foil current collectors as cathode material for lithium batteries. *J. Mater. Chem. A* 5, 6937–6946. doi: 10.1039/c7ta00614d

Liu, F., and Xue, D. (2011). CuS hierarchical Architectures by a combination of bottom-up and top-down method. *Nanosci. Nanotechnol. Lett.* 3:440. doi: 10.1166/nnl.2011.1172

Liu, K., Liu, Y., Lin, D., Pei, A., and Cui, Y. (2018). Materials for lithium-ion battery safety. *Adv. Sci.* 4:9820.

Lu, Y., Li, B., Zheng, S., Xu, Y., Xue, H., and Pang, H. (2017). Syntheses and energy storage applications of MxSy (M = Cu, Ag, Au) and their composites: rechargeable batteries and supercapacitors. *Adv. Funct. Mater.* 27:1703949. doi: 10.1002/adfm.201703949

Madarasz, J., Okuya, M., and Kaneko, S. (2001). Preparation of covellite and digenite thin films by an intermittent spray pyrolysis deposition method. *J. Eur. Ceram. Soc.* 2, 2113–2116. doi: 10.1016/s0955-2219(01)00183-2

Manthiram, A., Song, B., and Li, W. (2017). A perspective on nickel-rich layered oxide cathodes for lithium-ion batteries. *Energy Storage Mater.* 6, 125–139. doi: 10.1016/j.ensm.2016.10.007

Meng, X., He, K., Su, D., Zhang, X., Sun, C. J., Ren, Y., et al. (2014). Gallium sulfide–single-walled carbon nanotube composites: high-performance anodes for lithium-ion batteries. *Adv. Funct. Mater.* 24, 5435–5442. doi: 10.1002/adfm.201401002

Meng, X., Yang, X.-Q., and Sun, X. (2012). Emerging applications of atomic layer deposition for lithium-ion battery studies. *Adv. Mater.* 24, 3589–3615. doi: 10.1002/adma.201200397

Ni, S., Lv, X., Li, T., and Yang, X. (2013). Fabrication of Cu2S cathode for Li-ion battery via a low temperature dry thermal sulfuration method. *Mater. Chem. Phys.* 143, 349–354. doi: 10.1016/j.matchemphys.2013.09.008

Potter, R. W. II, and Evans, H. T. Jr. (1976). Definitive X-ray powder data for covellite, anilite, djurleite and chalcocite. *J. Res. U. S. Geol. Surv.* 4, 205–212.

Tang, J., Ni, S., Chen, Q., Zhang, J., and Yang, X. (2017). CuS@Cu freestanding electrode via electrochemical corrosion for high performance Li-ion batteries. *Mater. Lett.* 201, 13–17. doi: 10.1016/j.matlet.2017.04.120

Tao, H. C., Yang, X. L., Zhang, L. L., and Ni, S. B. (2014). One-pot facile synthesis of CuS/graphene composite as anode materials for lithium ion batteries. *J. Phys. Chem. Solids* 75, 1205–1209. doi: 10.1016/j.jpcs.2014.06.010

Wang, F., Robert, R., Chernova, N. A., Pereira, N., Omenya, F., Badway, F., et al. (2011). Conversion reaction mechanisms in lithium ion batteries: study of the binary metal fluoride electrodes. *J. Am. Chem. Soc.* 133, 18828–18836. doi: 10.1021/ja206268a

Wang, Z., Rafai, S., Qiao, C., Jia, J., Zhu, Y., Ma, X., et al. (2019). Microwave-assisted synthesis of CuS hierarchical nanosheets as the cathode material for high-capacity rechargeable magnesium batteries. *ACS Appl. Mater. Interfaces* 11, 7046–7054. doi: 10.1021/acsami.8b20533

Xiao, S., Li, X., Sun, W., Guan, B., and Wang, Y. (2016). General and facile synthesis of metal sulfide nanostructures: in situ microwave synthesis and application as binder-free cathode for Li-ion batteries. *Chem. Eng. J.* 306, 251–259. doi: 10.1016/j.cej.2016.05.068

Xiao, Y., Su, D., Wang, X., Wu, S., Zhou, L., Shi, L., et al. (2018). CuS microspheres with tunable interlayer space and micropore as a high-rate and long-life anode for sodium-ion batteries. *Adv. Energy Mater.* 8:1800930. doi: 10.1002/aenm.201800930

Yuan, D., Huang, G., Zhang, F., Yin, D., and Wang, L. (2016). Facile synthesis of CuS/rGO composite with enhanced electrochemical lithium-storage properties through microwave-assisted hydrothermal method. *Electrochim. Acta* 203, 238–245. doi: 10.1016/j.electacta.2016.04.042

Zeng, L., Jiang, Y., Xu, J., Wang, M., Li, W., and Yu, Y. (2015). Flexible copper-stabilized sulfur–carbon nanofibers with excellent electrochemical performance for Li-S batteries. *Nanoscale* 7, 10940–10949. doi: 10.1039/c5nr01861g

Zhao, Y., Pan, H., Lou, Y., Qiu, X., Zhu, J., and Burda, C. (2009). Plasmonic Cu2-xS Nanocrystals: Optical and Structural Properties of Copper-Deficient Copper(I) Sulfides. *J. Am. Chem. Soc.* 131, 4253–4261. doi: 10.1021/ja805655b

Conflict of Interest: The authors declare that the research was conducted in the absence of any commercial or financial relationships that could be construed as a potential conflict of interest.

frontiers in Energy Research

REVIEW
published: 02 September 2020
doi: 10.3389/fenrg.2020.00202

Recent Developments and Challenges in Hybrid Solid Electrolytes for Lithium-Ion Batteries

Lu Han[1], Michelle L. Lehmann[1,2], Jiadeng Zhu[1], Tianyi Liu[3], Zhengping Zhou[1], Xiaomin Tang[1], Chien-Te Heish[4,5], Alexei P. Sokolov[1,6], Pengfei Cao[1], Xi Chelsea Chen[1] and Tomonori Saito[1,2]**

[1] Chemical Sciences Division, Physical Sciences Directorate, Oak Ridge National Laboratory, Oak Ridge, TN, United States, [2] Bredesen Center for Interdisciplinary Research and Graduate Education, University of Tennessee, Knoxville, Knoxville, TN, United States, [3] Department of Chemistry, Virginia Tech, Blacksburg, VA, United States, [4] Department of Chemical Engineering and Materials Science, Yuan Ze University, Taoyuan, Taiwan, [5] Department of Mechanical, Aerospace, and Biomedical Engineering, University of Tennessee, Knoxville, Knoxville, TN, United States, [6] Department of Chemistry, University of Tennessee, Knoxville, Knoxville, TN, United States

OPEN ACCESS

Edited by:
Jian Liu,
The University of British Columbia, Canada

Reviewed by:
Wei Luo,
Tongji University, China
Yang Zhao,
University of Western Ontario, Canada
Yuan Yang,
Columbia University, United States

***Correspondence:**
Lu Han
lxh306@case.edu
Tomonori Saito
saitot@ornl.gov

Specialty section:
This article was submitted to Electrochemical Energy Conversion and Storage, a section of the journal Frontiers in Energy Research

Received: 18 June 2020
Accepted: 31 July 2020
Published: 02 September 2020

Citation:
Han L, Lehmann ML, Zhu J, Liu T, Zhou Z, Tang X, Heish C-T, Sokolov AP, Cao P, Chen XC and Saito T (2020) Recent Developments and Challenges in Hybrid Solid Electrolytes for Lithium-Ion Batteries. Front. Energy Res. 8:202. doi: 10.3389/fenrg.2020.00202

Lithium-ion batteries (LIBs) have attracted worldwide research interest due to their high energy density and long cycle life. Solid-state LIBs improve the safety of conventional liquid-based LIBs by replacing the flammable organic electrolytes with a solid electrolyte. Among the various types of solid electrolytes, hybrid solid electrolytes (HSEs) demonstrate great promise to achieve high ionic conductivity, reduced interfacial resistance between the electrolyte and electrodes, mechanical robustness, and excellent processability due to the combined advantages of both polymer and inorganic electrolyte. This article summarizes recent developments in HSEs for LIBs. Approaches for the preparation of hybrid electrolytes and current understanding of ion-transport mechanisms are discussed. The main challenges including unsatisfactory ionic conductivity and perspectives of HSEs for LIBs are highlighted for future development. The present review provides insights into HSE development to allow a more efficient and target-oriented future endeavor on achieving high-performance solid-state LIBs.

Keywords: lithium-ion batteries (LIBs), hybrid solid electrolytes (HSEs), solid electrolytes, polymer electrolytes, inorganic electrolytes, ionic conductivity, ion-transport mechanisms

INTRODUCTION

Lithium-ion batteries (LIBs) have revolutionized battery technologies, serving as the key component in personal portable electronics, electric vehicles, and stationary energy storage (Ge et al., 2014; Yanilmaz et al., 2016; Zhu et al., 2016b,d; Luo et al., 2017; Famprikis et al., 2019; Lagadec et al., 2019; Lee et al., 2019; Liu et al., 2019; Zhao et al., 2020). Driven by the growing number of applications and ever increasing use of consumer electronics, significant research effort has been focused on developing improved battery systems and reducing production costs (Fu et al., 2014; Luo et al., 2016; Zhu et al., 2018b,c). Conventional LIBs suffer from potential fire hazards caused by short-circuiting of the battery that may cause thermal runaway (Varzi et al., 2016; Manthiram et al., 2017; Wang X. et al., 2020; Zhang C. et al., 2019). In addition, the high reactivity of liquid electrolytes with the electrodes leads to side reactions and capacity fade over time (Xiao et al., 2020). Solid-state electrolytes, on the other hand, are non-flammable, offering

higher thermal stability, providing improved safety compared to liquid electrolytes batteries. Furthermore, their potential for enabling the use of a high capacity Li metal anode may greatly enhance the energy and power density and cycle life of current batteries (Pomerantseva et al., 2019). Therefore, the replacement of liquid electrolytes with high-performance solid electrolytes is imperative to overcome the related safety issues of conventional batteries, as well as to improve their energy density by enabling the use of high energy density electrodes (Janek and Zeier, 2016).

An ideal solid electrolyte should possess the characteristics of (1) high ionic conductivity, (2) high electronic resistance, (3) high cation-transference number, (4) wide electrochemical stability window, (5) outstanding thermal stability, (6) excellent mechanical strength, (7) reduced interfacial resistance, and (8) low cost and ease of synthesis (Manthiram et al., 2017). Since an alumina-based solid electrolyte was used in a high-temperature sodium-sulfur battery in the 1960s (Kummer and Neill, 1968; Hsueh and Bennion, 1971), tremendous effort has been made to develop advanced solid electrolytes with the above characteristics. Inorganic electrolytes exhibit high ionic conductivity and mechanical strength, while polymer electrolytes provide flexibility, processability and good contact with the electrodes, reducing the electrode/solid electrolyte interface.

Despite significant improvement in solid electrolytes, there are several remaining challenges (Wang et al., 2014; Lopez et al., 2019; Zhao et al., 2020). For inorganic electrolytes, issues with grain boundary resistance, chemical and electrochemical stability with the electrodes, high cost and lack of processability need to be addressed. Plus, inorganic electrolytes are typically brittle. As a result, they do not compensate for volume change of electrodes during charge and discharge. For polymer electrolytes, its practical application remains hindered by low ionic conductivity at ambient temperature (Agapov and Sokolov, 2011; Wang et al., 2014; Manthiram et al., 2017; Liu et al., 2019; Zhao et al., 2020). Their low ionic conductivity renders them incapable of achieving the charging and discharging rates required in practical utilization. Therefore, developing solid electrolytes that meet all the requirements for the realization of high-performance all-solid-state battery technologies is the key to revolutionize modern electrochemical energy storage devices (Liu et al., 2019).

An efficient way to address the performance issues of solid electrolytes is to hybridize two or more component for combined advantages of each component. Hybrid solid-state electrolytes (HSEs) may combine the advantages of inorganic and polymer electrolytes while overcoming the disadvantages of each component when used separately, as shown in **Figure 1**. The main strategy of HSEs is to disperse high-surface-area inorganic fillers into a polymer matrix, which is the focus of this review. Other morphologies include using ceramic as the matrix, fiber mat and so on. Compared to inorganic and polymer electrolytes, hybrid electrolytes exhibit a combined advantage of each component including high ionic conductivity, good mechanical properties from inorganic component as well as reduced interfacial resistance from polymer component. The up-to-date performance metrics of ionic conductivity, transference number, and electrochemical stability of recently developed

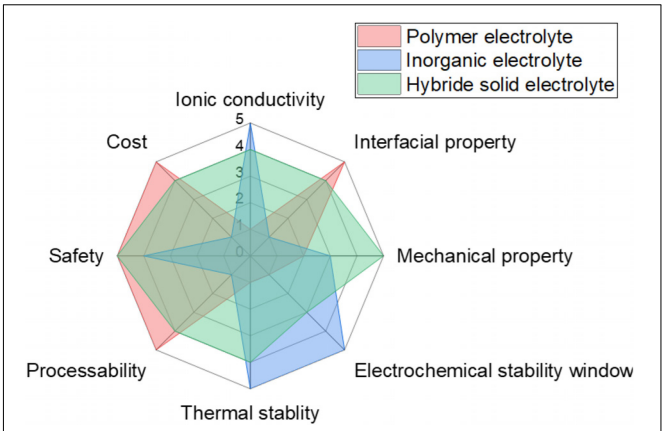

FIGURE 1 | Ranking of properties of solid electrolytes (5 = best, 1 = worst).

HSEs are summarized in **Table 1**. To date, a number of inorganic fillers have been utilized, such as inert fillers (Al_2O_3, SiO_2, TiO_2, $LiNbO_3$, and $BaTiO_3$) and active fillers consisting of metal oxides or sulfides (Appetecchi and Passerini, 2000; Adebahr et al., 2003; Kumar, 2004; Zhao et al., 2016a). It is essential to summarize the state-of-the-art progress of HSEs based on the most recently available publications. A brief overview of solid-state electrolytes is provided, and are divided into three categories: inorganic electrolytes, polymer electrolytes, and hybrid electrolytes. Furthermore, the performance of various HSE systems is discussed in detail, along with ion transport mechanisms and fabrication methods. Despite many studies, current HSEs still have relatively low ambient ionic conductivity ($<10^{-3}$ S/cm), poor interfacial stability, and high interfacial resistance, which greatly restrict the performance of the LIBs. In the end of this review, the current challenge and perspective of HSEs are discussed.

HYBRID SOLID ELECTROLYTES

Polymer Matrix

Polymers are widely used as solid electrolytes. Polymer electrolytes are attracting increasing interest because of their flexibility, processability, high safety, and scalability. Polymer electrolytes have been studied for use in a variety of high energy and power density batteries, including lithium-ion, lithium-sulfur, and lithium-air rechargeable batteries (Kim J. G. et al., 2015; Sun et al., 2017). With the incorporation of lithium salts, the ionic conductivity of solid-state polymer electrolytes can reach 10^{-6} to 10^{-5} S/cm at room temperature (Wang et al., 2016; Meabe et al., 2019). With the covalent attachment of anions to the polymer backbone, single lithium ion conducting polymer electrolytes show a lower ionic conductivity of 10^{-7} to 10^{-6} S/cm at room temperature (Cao et al., 2017, 2020; Zhang H. et al., 2017). Recent study demonstrated the remarkably high Li^+ conductivity of 5.84×10^{-4} S/cm at 25°C (Ahmed et al., 2019). Due to its flexible nature and good adhesive properties,

TABLE 1 | Summary of recent HSE performance.

Composite		Ionic conductivity (S/cm)	Transference number	Electrochemical stability Vs. Li^+/Li	References
Polymer	**Filler**				
PEO	$Li_{1.5}Al_{0.5}Ge_{1.5}(PO_4)_3$	1×10^{-5} (R.T.)		Up to 4.75 V	Jung et al., 2015
	vertically aligned $Li_{1.5}Al_{0.5}Ge_{1.5}(PO_4)_3$	1.67×10^{-4} (R.T.); 1.11×10^{-3} (60°C)	0.56	1–4.5 V	Wang et al., 2019
	$Li_{1.3}Al_{0.3}Ti_{1.7}(PO_4)_3$	1.9×10^{-4} (40°C)			Nairn et al., 1996
	vertically aligned $Li_{1.3}Al_{0.3}Ti_{1.7}(PO_4)_3$	5.2×10^{-5} (R.T.)		−0.5 to 5V	Zhai et al., 2017
	$Li_{10}GeP_2S_{12}$	2.2×10^{-4} (R.T.) (70% $Li_{10}GeP_2S_{12}$)	0.91 (90% $Li_{10}GeP_2S_{12}$)		Zheng et al., 2019
	$Li_{10}GeP_2S_{12}$	2.2×10^{-4} (R.T.) (1% $Li_{10}GeP_2S_{12}$)		0–5.7 V (1% $Li_{10}GeP_2S_{12}$)	Zhao et al., 2016b
	Li_6PS_5Cl	10^{-3} (R.T.)			Zhang J. et al., 2019
	nanofiber $Li_{0.33}La_{0.557}TiO_3$	2.4×10^{-4} (R.T.)		Up to 5.0 V	Zhu et al., 2018a
	3D $Li_{0.33}La_{0.557}TiO_3$ network	1.8×10^{-4} (R.T.)	0.33	Up to 4.5 V	Wang et al., 2018
	$Li_7La_3Zr_2O_{12}$ nanowires	2.4×10^{-4} (R.T.)		Up to 5.5 V	Zhu et al., 2018a
	tetragonal $Li_7La_3Zr_2O_{12}$	4.45×10^{-4} (55°C)		0–5 V	Choi et al., 2015
	$Li_{6.4}La_3Zr_{1.4}Ta_{0.6}O_{12}$ with solid plasticizer succinonitrile	1.22×10^{-4} (30°C)	0.41	Up to 5.5 V	Zha et al., 2018
	3D network of $Li_{1.4}Al_{0.4}Ti_{1.6}(PO_4)_3$/PAN enhanced PEO	6.5×10^{-4} (60°C)	0.32	0.5–5 V	Li D. et al., 2018
PAN	$Li_{0.33}La_{0.557}TiO_3$	2.4×10^{-4} (R.T.)		Up to 4.7 V	Liu et al., 2015
PVDF-HPF	$Li_7La_3Zr_2O_{12}$	7.63×10^{-4} (30°C)	0.61	Up to 5.3 V	Zhang et al., 2018
Poly(propylene carbonate)	$Li_{6.75}La_3Zr_{1.75}Ta_{0.25}O_{12}$	5.2×10^{-4} (20°C)	0.75	Up to 4.6 V	Zhang J. et al., 2017
Poly(vinyl carbonate)	$Li_{10}SnP_2S_{12}$	2.0×10^{-4} (R.T.)	0.6	Up to 4.5 V	Ju et al., 2018

polymer electrolytes components can form good contact with the electrodes. These unique electrochemical properties highlight the promise of polymer electrolytes for solid-state battery applications. The polymers commonly used as electrolytes include poly(ethylene oxide) (PEO), poly(carbonate) (PC), poly(siloxane), poly(acrylonitrile) (PAN), and poly(vinylidene fluoride) (PVDF). For many polymer electrolytes, ion mobility is strongly coupled to the segmental motion of the polymer chains, limiting the achievable ambient conductivity (Wang et al., 2014; Porcarelli et al., 2016). In addition, the crystalline phase of polymers (e.g., PEO) generally hinders ion transport below the melting point ($T_m \sim 65°C$ for PEO) (Xue et al., 2015). To reduce the degree of crystallinity and the glass-transition temperature (T_g) of polymers, a variety of methods have been explored, including polymer blends, copolymerization and crosslinking (Soo, 1999; Wen et al., 2000; Fullerton-Shirey and Maranas, 2009; Lopez et al., 2019; Cao et al., 2020).

Among polymer electrolytes, PEO-based polymer electrolytes are most extensively studied due to its faster polymer dynamics at ambient temperature and excellent capability to solvate various salts (Lopez et al., 2019). Salt-doped PEO exhibits reasonable ionic conductivity as an HSEs component due to its low glass transition temperature (∼-30°C with salts), (Senthil Kumar et al., 2014) remaining in a rubbery state at room temperature. Additionally, PEO demonstrates an outstanding ability to solvate large concentration of lithium salts (Berthier et al., 1983; Karan et al., 2008) and it may have favorable interactions with inorganic fillers (Croce et al., 1999; Malathi and Tamilarasan, 2014). The ether oxygen atoms in PEO act as a Lewis base to coordinate with the Li-ion (Meyer, 1998). The coordination of PEO with the Li-ion creates pseudo ionic crosslinks that restrict the movement of Li^+ and slows down the segmental motion of the polymer chains when the concentration of salt becomes high (typically above EO:Li = 12) (Lehmann et al., 2019). The restricted segmental motion of the PEO chains results in an increase in T_g and a reduction in ionic conductivity. The low Li transference number in PEO also originates from the strong coordination of the Li-ion by the ether oxygens. As a result, large anions like trifluoromethanesulfonyl imide ($TFSI^-$) moves faster than the small cation. Another weakness of PEO is its high crystallinity (>60%), originating from its linear structure. Due to these properties, the room temperature ionic conductivity of PEO with Li salts is low (10^{-6} S/cm), 3–4 orders of magnitude lower than that of commercial liquid electrolytes (Wright, 1975; Lee et al., 2005). To decrease the crystallinity and improve the mechanical properties of PEO, crosslinking has been adopted. The network structure with short PEO chains between crosslinking helps to decrease the crystallinity of PEO; however, the mobility of the polymer segments is also restricted, such that the ionic conductivity is often reduced (Maccallum et al., 1984). Another commonly used method to decrease the crystallinity of PEO, is to add inorganic or organic plasticizers to the polymer,

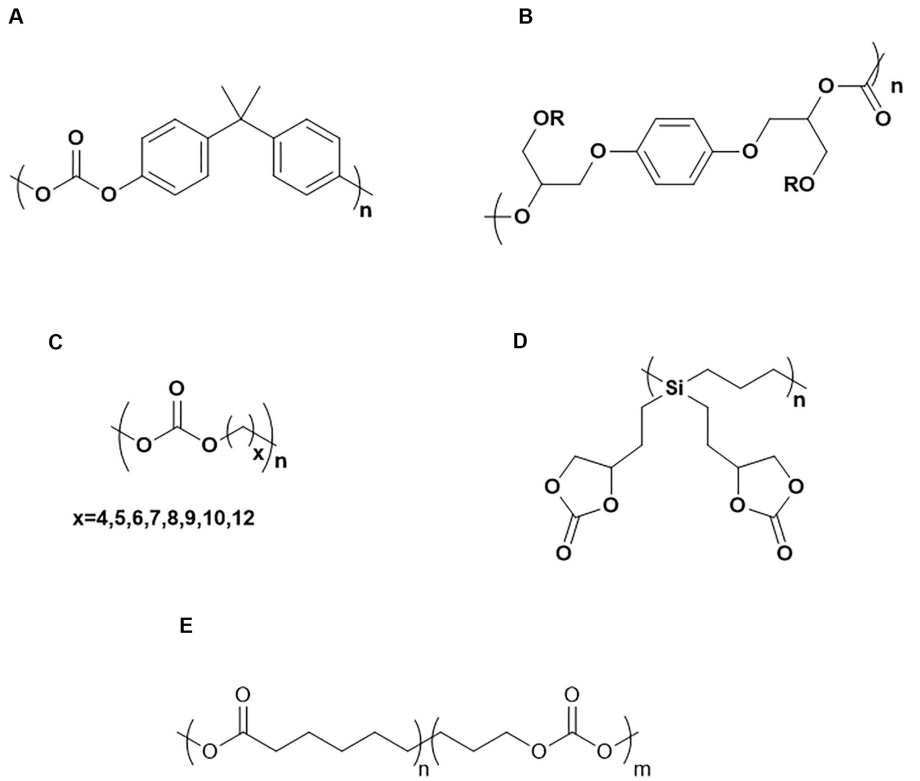

SCHEME 1 | Chemical structure of **(A)** PC made from Bisphenol A, **(B)** PC made from hydroquinone group, **(C)** APC with different length of CH_2, **(D)** PolySBDC, **(E)** Poly(carbonate-*co*-ester).

which was first proposed in Liang (1973). PEO with organic plasticizers typically exhibits worse mechanical properties than neat PEO (Quartarone et al., 1998). On the other hand, PEO with inorganic fillers usually shows improved mechanical and thermal stability (Weston and Steele, 1982). In addition to fillers, polymer blending can improve the mechanical strength of a PEO electrolyte. PEO/P(VDF-HFP)/LLZTO electrolyte shows largely enhanced tensile strength of 3.5 MPa and Young's modulus of 53.5 MPa (∼10 times higher than that of PEO/LLZTO SPE) (Wang T. et al., 2020). This approach of polymer–polymer hybrid solid electrolytes provides another avenue to enhance the mechanical property and overall electrolyte properties.

PCs have also drawn attention for use as solid electrolytes. The advantage of PCs includes their high dielectric constant and ability to dissolve lithium salts. Spectroscopic techniques and molecular dynamics simulations indicate that both of the oxygen atoms in PC (carbonyl group oxygen and alkoxy oxygen) can coordinate with Li^+ (Matsumoto et al., 2013; Ong et al., 2015). As a commercially available polymeric material, PC made from bisphenol A (**Scheme 1A**) exhibits high strength, toughness, and good durability. However, bisphenol A PC without any modifications cannot be utilized as an HSE, due to its low ambient temperature ionic conductivity of 7×10^{-9} S/cm (Spiegel et al., 2000). The T_g of PCs made from bisphenol A is typically above 100°C (i.e., T_g of Lexan is 145°C) (Yang and Yetter, 1994) due to the rigid phenol group in the backbone. Therefore, the mobility of polymer chains is limited at room temperature, resulting in its low ionic conductivity. Matsumoto et al. (2013) synthesized a PC by utilizing hydroquinone in place of bisphenol A (**Scheme 1B**) and by adding plasticizers. Although the conductivity (1.5×10^{-6} S/cm at 30°C) is still not satisfactory, the transference number was improved. The Li-ion transference number was above 0.5, higher than that of PEO (transference number is only 0.2–0.5) (Evans et al., 1987; Pożyczka et al., 2017). The weaker coordinating interaction of both the carbonyl oxygen and alkoxy oxygen groups in PC with Li^+ compared with that of the ether oxygen in PEO contributes to the higher Li-ion transference number. With the introduction of aliphatic groups into the PC backbone, a highly flexible PC can be fabricated. Meabe et al. (2017) synthesized a series of PCs with $(CH_2)_x$ where x = 4, 5, 6, 7, 8, 9, 10, and 12 (**Scheme 1C**). The results showed that the solid electrolyte made from PCs with $(CH_2)_x$ exhibited an optimal conductivity and lowest T_g when x = 7. With the addition of 80 wt% LiTFSI, the conductivity of low molecular weight poly(dodecamethylene carbonate) can reach 1×10^{-4} S/cm at room temperature (Meabe et al., 2017). An alternative method to incorporate a carbonate group into a polymer is via sidechain instead of in the backbone. For example, poly-1,1-di[2- (2,4-dioxa-3-pentanoyl)ethyl]silacyclobutane (polySBDC) (**Scheme 1D**), exhibited a significantly decreased T_g (−25°C) with the ionic conductivity reaching 1.2×10^{-4} S/cm at 30°C (Matsumoto et al., 2016). Copolymerization of PC with a polyester (carbonate:

ester = 80: 20) achieved a room temperature ionic conductivity of 4.1×10^{-5} S/cm (**Scheme 1E**) (Mindemark et al., 2015).

PAN is the first polymer to be used as a solid electrolyte that contains the nitrile group. The nitrogen atom in PAN is considered to have the ability to coordinate with Li^+ due to its strong electronegativity. In fact, nitrile groups can be found in liquid electrolytes and additives. PAN (**Scheme 2A**) is a semi-crystalline polymer at room temperature with a T_g of ∼80°C. Based on these thermal properties, PAN was not expected to have high ionic conductivity, because the PAN chains are less flexible than that of PEO. PAN exhibited an ionic conductivity of 6.5×10^{-7} S/cm with 20 wt% of $LiClO_4$ at room temperature (Yang et al., 1996). The main challenge for PAN is its limited solubility in organic solvents. Dimethylformamide (DMF) and dimethyl sulfoxide (DMSO) are commonly used to dissolve PAN. Since they are high boiling point solvents, it is very challenging to remove them from a solvent-cast polymer electrolyte. As a result, the residual solvent trapped in the polymer matrix significantly affects the Li^+ transport and electrochemical stability of the solid electrolyte (Gutmann, 1976). Forsyth et al. (2000) utilized a hot-press method to prepare solvent-free PAN films. With 72 wt% $LiCF_3SO_3$, its conductivity reached 2×10^{-6} S/cm at 65°C (Forsyth et al., 2000). To make the nitrile-based polymer more soluble, a methyl group can be introduced into the backbone. Poly(methacrylonitrile) (PMAN) (**Scheme 2B**) can be dissolved in acetone. The film contained no residual solvent with the use of the low boiling point casting solvent. The reported conductivity of PMAN is $\sim 10^{-5}$ S/cm at 75°C. However, the PMAN film has a high T_g (110°C), which limits its performance at room temperature (Saunier et al., 2002). Another strategy to improve the solubility of PAN is to incorporate PAN with other polymer segments. Florjañczyk et al. reported a copolymer of PAN with butyl acrylate (**Scheme 2C**). The butyl acrylate group makes it possible to prepare the electrolyte using a solvent casting method with acetonitrile. In addition, the T_g of the copolymer decreases to 42–44°C and shows a high capability of dissolving lithium salts (Florjañczyk et al., 2004, 2005).

Fillers

Many types of inorganic materials such as perovskite-type, garnet-type, sodium superionic conductor (NASICON)-type, amorphous oxides, and sulfide materials have been developed as a LIB electrolyte (Inaguma et al., 1993; Zheng et al., 2018). As reported, perovskite-type [e.g., $Li_{0.34(1)}La_{0.51(1)}TiO_{2.94(2)}$ (LLTO)] (Inaguma et al., 1993) and garnet-type [e.g., $Li_5La_3M_2O_{12}$ (M = Nb or Tb) and $Li_6ALa_2M_2O_{12}$ (A = Ca, Sr or Ba; M = Nb or Ta)] (Geiger et al., 2011; Murugan et al., 2011) solid electrolytes exhibit high ionic conductivity of $> 10^{-3}$ S/cm at room temperature. NASICON-type materials generally have an $AM_2(PO_4)_3$ formula (A = Li, Na, or K; M = Ge, Zr, or Ti) (Thangadurai and Weppner, 2006). For this type of solid electrolyte, their ionic conductivity can be improved by the substitution of the metal (Ge, Zr, or Ti) by Hf or Sn (Martinez-Juarez et al., 1995). Among all inorganic solid electrolytes, sulfide-type solid electrolytes (i.e., Li_2S-SiS_2) are another popular electrolyte and investigated due to exhibiting some of the highest reported ionic conductivities. Kamaya et al. reported that the ionic conductivity of a Li_3PS_4 crystal was significantly increased to 2.2×10^{-3} S/cm at room temperature by doping with phosphorus and germanium (Kamaya et al., 2011). In addition, their wide electrochemical stability window could be beneficial for use in high-voltage solid-state batteries (Chen et al., 2018b). However, the major drawback of inorganic materials, whether amorphous or crystalline, is their brittleness, making large scale production quite challenging. Furthermore, maintaining good contact between the electrolyte and electrodes is difficult because of their lack of flexibility and volume changes during charging and discharging (Muramatsu et al., 2011). Therefore, by using polymer as the matrix with inorganic fillers, the interfacial property between the electrolyte and electrode will be significantly improved, thus improving the overall battery performance.

In HSEs, inorganic fillers play an important role in determining the performance of the battery. In the following section, we divide the polymer-inorganic composite electrolyte into two categories based on the function of the filler; inert fillers, with no bulk Li-ion conduction, and active fillers usually with high bulk Li-ion conduction.

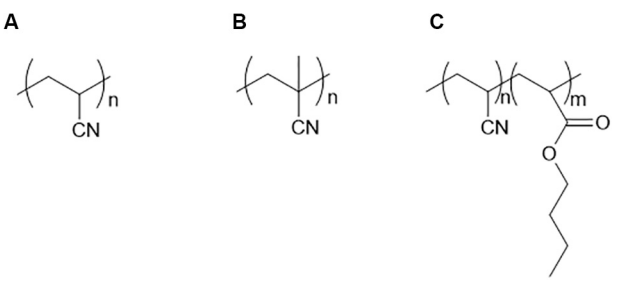

SCHEME 2 | Chemical structure of **(A)** PAN, **(B)** PMAN, **(C)** Copolymer of acrylonitrile and butyl acrylate.

Inert Fillers

Inert fillers do not conduct Li^+ themselves. Ceramic nanoparticles utilized in HSEs include Al_2O_3, TiO_2, and SiO_2 (Croce et al., 1998). Even though ceramic oxides do not participate in ion conduction directly, it was reported that ionic conductivity increased with the addition of the ceramic filler over a wide temperature range (30–100°C) (Croce et al., 1998). In hybrid electrolytes, the inorganic fillers not only act as solid plasticizers to inhibit the crystallization kinetics of the polymer segments but also promote ion mobility. Lin et al. (2016) reported that the crystallinity of PEO was highly decreased by SiO_2 via the *in situ* hydrolysis method compared to the blending method, attributing to their much stronger chemical/mechanical interactions between monodispersed 12 nm diameter SiO_2 nanospheres and PEO chains, and thus facilitates polymer segmental motion for ionic conduction. This led to good ionic conductivity (1.2×10^{-3} S/cm at 60°C, 4.4×10^{-5} S/cm at 30°C). Besides the ionic conductivity, incorporating inert fillers with the polymer electrolyte was also reported to widen the electrochemical stability window up to 5.5 V (Lin et al., 2016).

Weston and Steele (1982) firstly studied the effects of incorporating inert Al_2O_3 fillers to a $LiClO_4$/PEO electrolyte in 1982. From then on, inert fillers with different sizes as well as surface functionalities have been extensively investigated attributing to the important role of the fillers surfaces/interfaces in improving conductivity. The interfacial area is strongly dependent on the size and content of inert fillers.

Ceramic nanoparticles influence not only the electrochemical properties but also the mechanical properties of polymer electrolytes. Ramesh et al. (2007) studied the effect of SiO_2 on the mechanical properties of a poly(vinyl chloride)- PEO polymer electrolyte. The Young's modulus increased from 500 to 2300 Pa with the addition of 10% SiO_2 (Ramesh et al., 2007). Wen et al. investigated the effect of $BaTiO_3$ on a PEO-poly(propylene oxide) crosslinked amorphous polymer. With 10% $BaTiO_3$, the tensile strength improved from 1.42 to 2.12 MPa at 80°C (Wen et al., 2003).

Another interesting direction of the inert filler is the interaction between the functional group on the inert filler surface and the polymer chains. Liu et al. studied the interaction between the −OH/H functional group on the SiO_2, Li^+, and the PEO chains. It was concluded that with SiO_2, the ionic conductivity of PEO was not improved. Instead, the transference number was highly increased up to 0.56. The results were ascribed to the hydrogen bond between the -OH/H functional group on the SiO_2 surface and the PEO chain. The hydrogen bonding provided a free space around the SiO_2 particle and the free space would favor an absorption-like process. The anion, which contains -F elements, was trapped in the free space. Thus, the mobility of the anion was hindered (Liu et al., 2004).

Active Fillers

Active fillers participate in ionic conductivity. Metal oxides or sulfides are promising lithium-ion conductors. Li-ion transport in an active filler composite system is complex, and the proposed mechanisms are discussed in Section "Hybrid Solid Electrolytes." In this section, we provide an overview of several active fillers and their electrochemical performance.

$Li_{1+x}Al_xTi_{2-x}(PO_4)_3$ (LATP) and $Li_{1+x}Al_xGe_{2-x}(PO_4)_3$ (LAGP) are superionic conductors with the same structure as NASICON, but in Li-ion conducting form (Xu et al., 2004). When the Ti/Ge elements are partially substituted with Al, the ionic conductivity can be elevated from 10^{-4} S/cm to 10^{-3} S/cm for LATP (Aono, 1990; Xu et al., 2006) and 10^{-2} S/cm for LAGP (Kumar et al., 2009) at room temperature. The use of $Li_{1.3}Al_{0.3}Ti_{1.7}(PO_4)_3$ as an active filler in a PEO matrix was first reported in Nairn et al. (1996). With a 66% LATP loading in PEO (w/w), the ionic conductivity was increased to 10^{-4} S/cm at 40°C, two orders of magnitude higher than pure PEO. Wang et al. further systemically studied $Li_{1+x}Al_xTi_{2-x}(PO_4)_3$/PEO composites with varied Li/EO ratios, amount of x in LATP, and LATP/PEO weight ratios (Wang Y.-J. et al., 2006). At a fixed EO to Li ratio of EO/Li = 8, the ionic conductivity of $Li_{1+x}Al_xTi_{2-x}(PO_4)_3$ reaches its maximum value when $x = 0.5$. For PEO-$Li_{1.3}Al_{0.3}Ti_{1.7}(PO_4)_3$, ($x = 0.3$) composite, the maximum ionic conductivity (10^{-6} S/cm at room temperature) occurs when EO/Li = 16. The presence of LATP was found to suppresses the crystallinity of PEO at low loadings (5 wt%) but the degree of PEO crystallinity increases with increasing addition of LATP. In addition, compared to the randomly dispersed LATP, it was found that a vertically aligned structure of LATP in PEO can enhance the ionic conductivity to 5.2×10^{-5} S/cm (Zhai et al., 2017). A similar strategy was applied to LAGP with PEO. The room temperature ionic conductivity increased 6 times for a composite with an aligned ceramic structure (1.7×10^{-4} S/cm) compared to the randomly dispersed one (2.7×10^{-5} S/cm). The aligned composite electrolyte in a Li//$LiFePO_4$ cell showed a capacity retention (above 85% after 400 cycles) at 0.6 C (Wang et al., 2019). Li et al. fabricated a 3-dimensional fiber network consisting of LATP and PAN, which they embedded into a PEO matrix. The LATP/PAN/PEO composite electrolyte exhibited an electrochemical stability window of 5 volts and a 10.7 MPa tensile strength (Li D. et al., 2018). LAGP has higher ionic conductivity than LATP because LAGP has a lower resistance at the interface with the polymer (Mariappan et al., 2012). Jung et al. (2015) studied a LAGP-PEO composite electrolyte with different weight ratios. It was found that with 60% (w/w) LAGP, the cells showed the lowest electrode-electrolyte interfacial resistance and best rate capability (Jung et al., 2015).

Perovskites are another family of inorganic ionic conductors, among which $Li_{3x}La_{2/3-x}TiO_3$ (LLTO) is the most commonly used. $Li_{0.34}La_{0.51}TiO_{2.94}$ exhibits an ionic conductivity of 10^{-5} S/cm at room temperature, which was first reported in Inaguma et al. (1993). LLTO nanowire and nanoparticle PAN composite electrolytes were studied by Liu et al. (2015). An LLTO nanowire/PAN composite showed improved ionic conductivity compared to the one with dispersed nanoparticles at the same ceramic loading, due to the continuous conductive networks formed by the nanowires. The same strategy was also applied to PEO-based composite, resulting in an increased ionic conductivity of 2.4×10^{-4} S/cm at room temperature (Zhu et al., 2018a).

Garnet type inorganic ion conductors are also commonly used in composite electrolytes. $Li_7La_3Zr_2O_{12}$ (LLZO) is a promising material for use in Li-ion batteries. With an LLZO loading of 52.5% (w/w), the ionic conductivity of PEO-based HSE can achieve 10^{-4} S/cm at 55°C (Choi et al., 2015). Further studies have developed integrated all-solid-state batteries based on this composite electrolyte. The batteries exhibited stable performance in a Li//$LiFePO_4$ cell. When LLZO was placed in a PVDF-HFP matrix, the electrochemical stability window was widened (Zhang et al., 2018). A derivative material of LLZO was fabricated by the partial substitution of Zr by Ta (LLZTO) and was also studied as a composite electrolyte. However, there was little improvement in the ionic conductivity of the LLZTO/PEO composite electrolyte (1.9×10^{-5} S/cm) compared to the LLZO/PEO composite (1.0×10^{-5} S/cm) at 30°C (Choi et al., 2015; Zha et al., 2018). With the utilization of a poly(propylene carbonate) matrix instead of PEO, the conductivity of an LLZTO/poly(propylene carbonate) composite was improved to 5.2×10^{-4} S/cm at 21°C (Zhang J. et al., 2017).

In addition to the oxides mentioned above, sulfides are another class of inorganic ionic conductors, and the various types are comprehensively reviewed by Chen et al. (2018c).

Compared with oxides, S^{2-} has a larger ionic radius and lower electronegativity, thus, providing a weaker association with Li^+. The ionic conductivity of sulfides is generally higher than oxides. One of the highest reported ionic conductivities (10^{-2} S/cm at room temperature) of a sulfide-based inorganic electrolyte is for $Li_{10}GeP_2S_{12}$. The high ionic conductivity is attributed to the formation of anisotropic Li^+ diffusion pathway in the $Li_{10}GeP_2S_{12}$ crystalline structure. The combination of sulfides with a polymer not only show improved ionic conductivity but also have an extended electrochemical stability window of 5.7 V (Zhao et al., 2016b). A study utilizing high loadings (95 wt%) of a $78Li_2S–22P_2S_5$ glass type ceramic compared the performance of HSEs with PVDF and PEO polymer matrices (Zhang et al., 2020). While PVDF provided a higher ionic conductivity (4.54×10^{-4} S/cm) than PEO (1.27×10^{-4} S/cm) at room temperature, the LiTFSI salt was found to be inhomogeneously distributed in the PVDF composite. The composites achieved a charge/discharge capacity of 566 mA h/g for the PVDF and 725 mA h/g for the PEO in a Li//sulfur-carbon nanotube cell after 100 cycles.

ION CONDUCTION MECHANISMS IN HYBRID SOLID ELECTROLYTES

Ion conduction mechanisms in inorganic solid electrolytes are quite straightforward and generally occurs by ion hopping. The ions diffuse through the connected available vacant and interstitial sites in the crystal. The ionic conductivity of the solid electrolytes is determined by the concentration and distribution of the defects. In polymer electrolytes, the current understanding of ion conduction is the combination of ion movement with local polymer segmental motion and ion jumping over some potential energy barrier if the segmental motion is slow (Gibbs and DiMarzio, 1958; Cohen and Turnbull, 1959; Fan et al., 2018; Bocharova and Sokolov, 2020). The addition of inorganic fillers to the polymer electrolytes has proven to be an effective way to increase its ionic conductivity (Chen and Vereecken, 2019; Dirican et al., 2019). Recent efforts on explaining how ceramic fillers positively enhance the ionic conductivity is described below.

Ionic Conduction With Inert Fillers

Current understanding of the effects of the inert fillers, such as micro/nanoparticles, Al_2O_3 (Weston and Steele, 1982; Croce et al., 1998, 1999, 2000; Appetecchi et al., 2000), SiO_2 (Fan et al., 2003; Tominaga et al., 2005; Wang X.-L. et al., 2006; Tominaga and Endo, 2013), TiO_2 (Croce et al., 1999, 2000; Appetecchi et al., 2000; Croce et al., 2000), ZrO_2 (Croce et al., 2006), molecular sieves (Munichandraiah et al., 1995; Xi et al., 2004), and ferroelectric materials, has focused on two mechanisms: (1) the promotion of salt dissociation to create more free Li-ions by acting as centers of Lewis acid-base interactions; (2) the suppression of polymer crystallization.

The first hypothesis, the Lewis acid-base theory, was first proposed by Wieczorek in 1995 to explain the interactions between inorganic filler, polymer, and salt (Przyluski et al., 1995; Wieczorek et al., 1995, 1996). With the Lewis acid-base theory, the explanation is that in HSEs systems, the Li-ion is considered as a Lewis acid, and the solvating groups of polymers and ClO^{4-} anions act as Lewis bases. The fillers can be considered a Lewis acid or base, depending on their surface chemistry (**Figure 2**). Hence, several acid-base interactions are occurring in these systems. An acidic surface can attract the polymer solvating groups or ClO^{4-}, leading to free associated Li^+ cations. The addition of a basic surface attracts Li-ions and polymer functional groups, improving the dissociation of Li^+-ClO^{4-} ion pairs. Croce et al. added superacid ZrO_2 to a PEO/$LiBF_4$ complex. The Li-ion transference number was greatly improved as the acidic surface of the ceramic filler demonstrated a higher affinity toward ClO^{4-} than that of Li^+, promoting the separation Li^+-ClO^{4-} ion pairs (Croce et al., 2001).

In PEO-based electrolyte systems, studies have shown that the crystallization of the polymer is suppressed with the addition of inert fillers, which further increases the ionic conductivity (Bouchet et al., 2013; Hanson et al., 2013; Khurana et al., 2014; Das and Ghosh, 2015; Zhu et al., 2018a). Ion transport in PEO is strongly coupled to segmental dynamics, and freezing of segmental motion in crystalline phase suppresses ionic conductivity. The addition of inert fillers suppresses the crystallinity of PEO, which leads to increased segmental dynamics, resulting in a higher conductivity. Researchers have shown that the addition of γ-$LiAlO_2$ filler into PEO-based electrolyte greatly reduces the crystallization rate, increasing ionic conductivity, and the lithium/electrolyte interfacial stability (Hu et al., 2007; Tan et al., 2016).

However, Lewis interactions and polymer crystallinity are not the full picture of ion conduction mechanisms in HSEs with inert fillers. Marcinek et al. (2000) have shown that the ionic conductivity for a PEG-based electrolyte increases with the addition of neutral, acidic, or basic inert filler Al_2O_3 (Croce et al., 2001). The ionic conductivities of the electrolytes for acidic and basic surfaces are similar, and both are higher than the one with a neutral surface. However, the trend of the fraction of ion pairs measured for the electrolytes in the order of acidic > neutral > basic surface is inconsistent with the trend of the fraction of free ions. Fan et al. added fumed-silica particles into PEG-based electrolytes with lithium salts, leading to a better conductivity of the composite electrolyte. However, no conductivity differences were observed between the non-polar PEG with modified polar PEG electrolytes (Fan, 1997). Hanson et al. (2013) reported theoretical results of atomistic molecular dynamics simulations to study lithium ion diffusivities in PEO/TiO_2 and observed that the lithium ion diffusivities decrease with increased particle loading. Those contradictions may indicate the involvement of other factors or ion conduction mechanisms functioning in parallel, which are not yet fully revealed.

Ionic Conduction With Active Fillers

The ion conduction mechanisms in HSEs with active fillers are complicated, as not only the active fillers can influence the polymer chain structure, but also it can create additional Li^+ pathways within the composites. The pathways include active

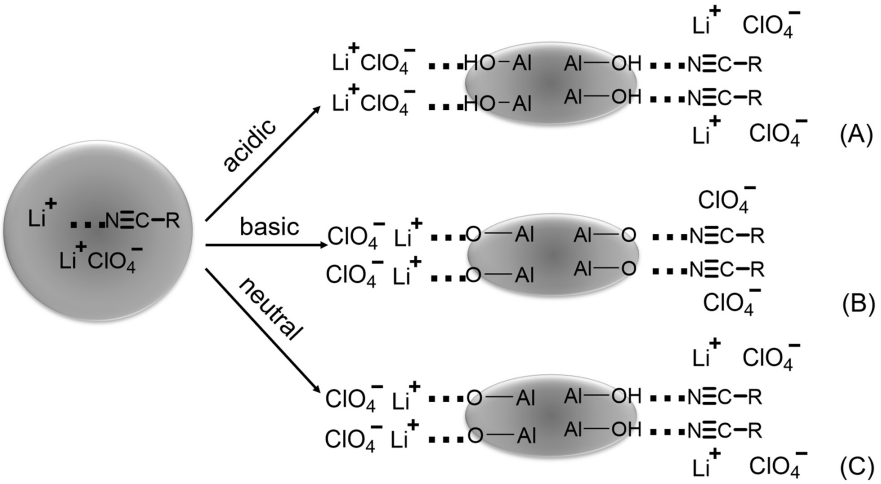

FIGURE 2 | Schematic demonstration of the Lewis acid-base dissociation effects of **(A)** Lewis acidic, **(B)** Lewis basic, and **(C)** neutral surface groups on ionic conductivity. Reprinted with permission from reference Wang et al. (2003). Copyright 2003 The Electrochemical Society, Inc.

filler, polymer, and polymer/active filler interface. Many studies have shown the new Li^+ pathways created by the active fillers such as LLZO (Murugan et al., 2007; Tao et al., 2017), LLTO (Le et al., 2015; Liu et al., 2015), and LATP (Goodenough et al., 1976; Aono, 1990; Chen X. C. et al., 2019; Peng et al., 2020), are the main reasons for the increase in ionic conductivity. These pathways, together with Li-ion concentration and ion mobility, determine the ionic conductivity of HSEs.

To understand the Li^+ diffusion pathway, Zheng et al. (2016) took advantage of high-resolution ^6Li NMR to investigate Li^+ ion transportation in different phases of an HSE. The method builds on the basis that ^6Li replaces ^7Li during Li^+ transport. Using a composite electrolyte with a mixture of PEO/$LiClO_4$ polymer matrix and LLZO (50 wt%), the authors confirmed the presence of three ways of Li-ion transport (Li^+ in the polymer phase, ceramic phase, and polymer-ceramic interface) within the material. Furthermore, by evaluating changes in the ^6Li amount before and after electrochemical cycling tests revealed that Li^+ diffusion in PEO-based electrolyte with LLZO (50 wt%) active filler preferred the pathway through the LLZO ceramic phase (Grey and Dupré, 2004; Bhattacharyya et al., 2010; Ilott et al., 2014). Yang et al. (2017) utilized a similar method to investigate the Li^+ pathway in the electrolyte of PAN/$LiClO_4$/LLZO nanowire. The results showed a strong interaction between LLZO nanowires and the PAN polymer chains. Cycle tests demonstrated that the Li^+ preferred to diffuse through the PAN-nanowire interface instead of the polymer or ceramic phase in HSEs with a low concentration of LLZO filler. In another study of PEO/$LiClO_4$/LATP HSEs, it has been shown that the ionic conductivity started to decrease beyond 4 vol% of LATP filler. The decrease was attributed to the agglomeration of nanoparticles that decreases volume ratio of the interface. Roman et al. studied the particle size effects on the ionic conductivity and found that the ionic conductivity increases as the particle size decreases, which is consistent with the prediction of the continuum percolation model (Roman, 1990). Zheng and coworkers did a systematic investigation on the compositional dependence of the three main factors for ionic conductivity, including ion mobility, ion transport pathways, and active ion concentration (Zheng and Hu, 2018). As shown in PEO (LiTFSI)/LLZO, with LLZO concentrations of 5 wt%, 20 wt%, and 50 wt% system in **Figure 3**, although active ion concentration increases with the addition of more ceramic filler, the actual fraction of Li^+ participating in the conduction does not show the same trend. At low contents of LLZO (5 and 20 wt%), with the increase of LLZO content, ion mobility increases, and ion transport is primarily through the PEO phase. At high LLZO content (50 wt%), a percolated network is formed by LLZO, through which most of the ion transport occurs. The 50 wt% LLZO composite showed notably lower ionic conductivity compared to the other composites, due to LLZO aggregation blocking the ion transport pathway though PEO and the high activation energy required for a Li-ion to move from one discrete LLZO particle to another or to the PEO phase. In general, the battery performance increases with increasing the loading of the fillers, when the loading ratio is small. Once the filler loading reaches certain level, the performance will not improve any more or even deteriorates due to filler aggregation.

PREPARATION OF HYBRID SOLID ELECTROLYTES

Hybrid solid electrolytes have been widely studied as promising electrolytes systems due to the synergetic effects of each component, which provide new opportunities to develop high-performance batteries with improved safety (Shim et al., 2014; Yue et al., 2016; Zhang et al., 2018). For HSEs, various preparation methods including casting, electrospinning, and *in situ* polymerization are utilized. Optimization of the preparation method is critical for enabling HSEs to achieve high

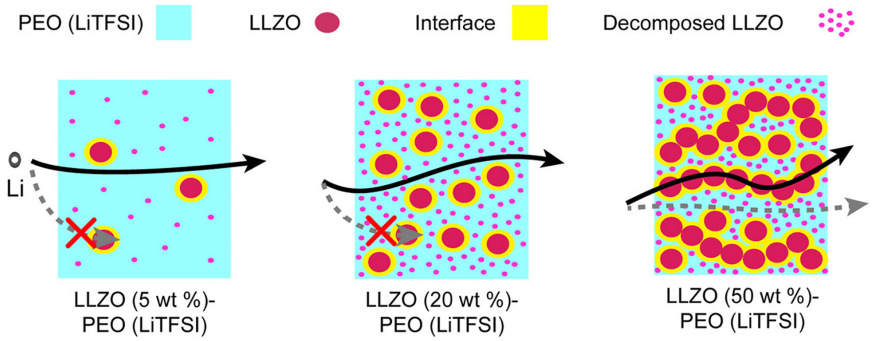

FIGURE 3 | Schematic of Li-ion pathways for PEO (LiTFSI)/LLZO with LLZO concentrations of 5 wt%, 20 wt%, and 50 wt%. Reprinted with the permission from reference Zheng and Hu (2018). Copyright 2018 American Chemical Society.

performance characteristics such as good interfacial contact and the formation of ion-conduction pathways (Kim J.-K. et al., 2015; Manthiram et al., 2017; Liu et al., 2018). As such, the various fabrication methods employed in the preparation of HSEs are discussed in the following sections.

Casting

Casting is one of the common techniques used to prepare polymer films and their composites, and is applied in a variety of fields (Zhu et al., 2012, 2014). In a typical preparation method, a polymer is dissolved in a suitable solvent together with a salt and inorganic material to prepare a slurry and is then cast on a substrate to fabricate the HSE film. The films can be obtained after drying the slurry in a (vacuum) oven under certain conditions. For example, a facile tape casting method was performed by Chen et al. to prepare a thin solid electrolyte with improved interfacial contact between the HSE and the electrode, achieving a high-performance solid-state battery. As a result, the cell with such a structural design could deliver an initial capacity of 125 mAh/g at a current density of 0.1 C for the fabricated Li//$LiFePO_4$ cell at room temperature (Chen X. et al., 2019).

To further solve the interfacial issue, isostatic processing, in which equal pressure is applied in all directions on the substrate, has been recognized as a promising method. By using this approach, good mechanical contact, as well as the enhancement of ionic transference, could be assured. For example, Afyon et al. (2019) utilized garnet-type solid electrolytes of LLZO for assembling solid-state battery cells and composite electrodes as well. Generally, LLZO was prepared based on a modified sol-gel synthesis-combustion approach. Sub-micron-sized particles were obtained at 650°C (Afyon et al., 2019). The resultant LLZO electrolyte pellets had relative densities of ∼87% and ionic conductivities of $\sim 0.5 \times 10^{-3}$ S/cm at room temperature. A composite of antimony nanoparticles, carbon black, LLZO electrolyte powder, and PVDF was tape-casted onto sintered thin LLZO pellets with a thickness of 300–400 μm. The dried solid-state electrodes were then pressed at a force of 1000 kN onto the solid electrolyte to ensure good contact at the interface of electrode/LLZO. Additionally, this method is scalable, as shown in **Figure 4**.

Electrospinning

Electrospinning has been recognized as one of the promising approaches to produce functional one-dimensional (1D) nanomaterials, which provide unique properties including high surface-to-volume ratio, good flexibilities, and large porosity (Zhu et al., 2015, 2016a,e; Li et al., 2018a,b; Zhu J. et al., 2019). The open porous structure and nanosized fibers may provide good ion transport path, benefiting the electrochemical performance of the prepared cells. The basic setup of electrospinning is shown in **Figure 5A**, which includes a syringe, a syringe pump, a high-voltage supplier, and a collector (Zhu et al., 2016c). Zhu et al. designed and prepared a PEO-based HSE with 1D ceramic LLTO nanofibers, showing a good ionic conductivity of 2.4×10^{-4} S/cm at room temperature (Zhu P. et al., 2019). Briefly, LLTO precursor nanofibers were first fabricated via electrospinning using poly(vinylpyrrolidone) as the polymer matrix followed by heat-treatment. The effect of treatment temperature on the morphology of the prepared LLTO has also been studied. As can be seen from **Figures 5B,C**, the average diameter of the LLTO nanofibers treated at 800°C is around 110 nm with a good fibrous shape. **Figure 5D** shows the TEM images of the individual LLTO nanofibers. The high-resolution TEM image indicates a lattice spacing of ∼0.27 nm, as shown in **Figure 5E**, which is ascribed to the (110) plane of LLTO. The resultant LLTO calcined at 800°C was mixed with PEO to prepare the LLTO/PEO solid-state composite electrolyte using acetonitrile as the casting solvent. It exhibits a high ionic conductivity of 2.4×10^{-4} S/cm at room temperature and a large electrochemical stability window of up to 5.0 V vs. Li/Li^+.

Spray Coating

Spray coating is a facile and scalable processing method to manufacture composite electrolyte films. Pandian et al. (2018) used aqueous spray coating to fabricate composite electrolyte films with high ceramic loadings (>50 vol% ceramic). In the spray coating process, slurry containing the polymer electrolyte and ceramic particles are delivered through the spray nozzle onto the substrate and forms a thin layer of composite. The thin layer is allowed to dry on the heated substrate before the next layer is delivered. The spraying-drying procedure is

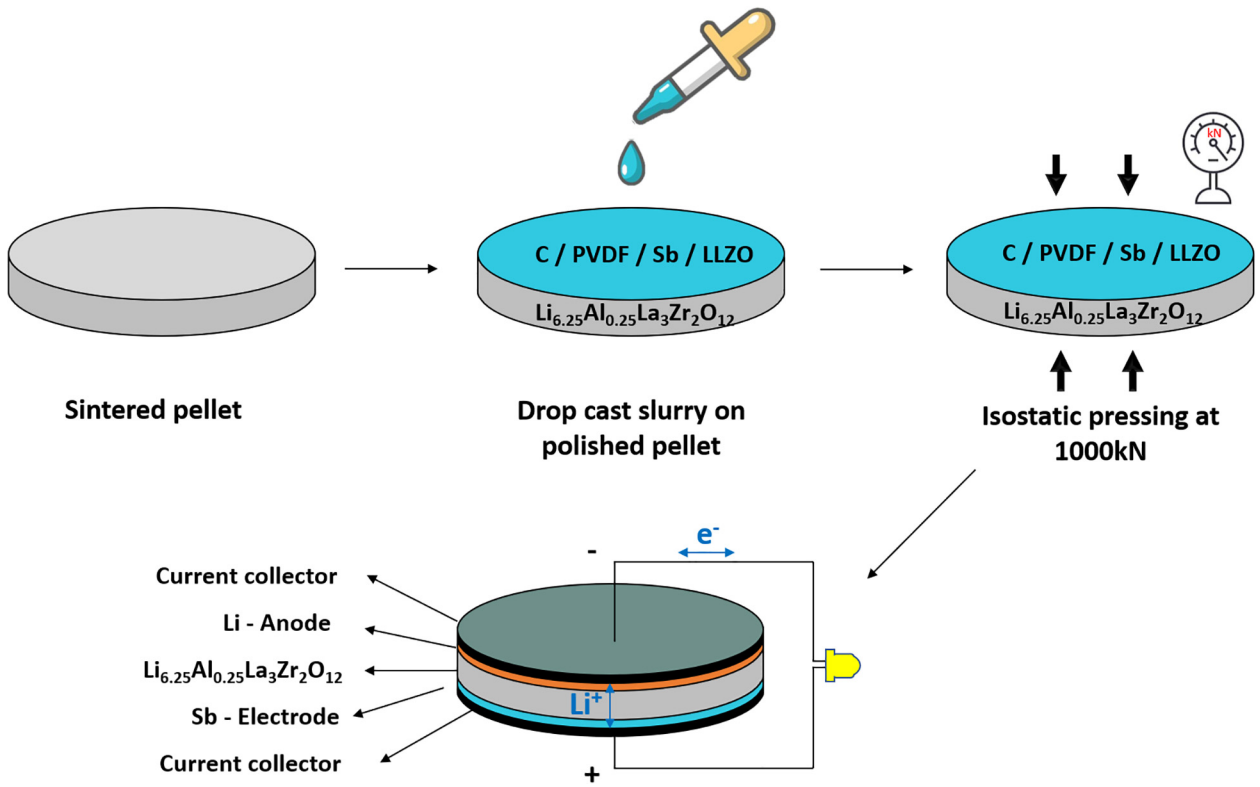

FIGURE 4 | Schematic image showing the deposition of the electrode to prepare an all-solid-state battery. Reprinted with permission from reference Afyon et al. (2019). Copyright 2019 Royal Society of Chemistry.

repeated until the desired thickness is reached. This method creates a film that is large, crack-free and three-dimensionally uniform, even with very high ceramic loadings. The thickness can be precisely controlled from a few micrometers to hundreds of micrometers. Comparatively conventional casting methods lead to crack formation when the ceramic loadings are high, due to segregation of the ceramics during drying. Furthermore, using aqueous slurry is a green process that is less expensive, more environmentally friendly which makes it attractive for commercialization.

In situ Polymerization

In situ polymerization to prepare HSEs provides several advantages including solvent-free preparation and improved contact with electrodes (Zhou et al., 2015, 2017; Suk et al., 2016; Chen et al., 2018a; Duan et al., 2018). Generally, a precursor containing a curable monomer, an initiator, lithium salts, and other additives is cured under certain conditions (i.e., thermal, UV irradiation, etc.) to synthesize HSEs. For example, Zhou et al. synthesized a solid-state electrolyte based on nitrile materials for achieving high-performance LIBs. **Figure 6** exhibits the synthesis route. Briefly, *in situ* polymerizing the cyanoethyl polyvinyl alcohol (PVA-CN) was performed to prepare this hierarchical structure, which was dissolved in succinonitrile (SN) and then mixed with two lithium salts (LiTFSI and $LiPF_6$) at a weight ratio of 5:1 to generate a slurry. The prepared slurry was further poured into a PAN nanofiber membrane and put into a cell. After heating the cell at 70°C for 6 h, a crosslinked 3D framework structure filled by SN−based solid electrolyte could be fabricated. In this work, $LiPF_6$ was used as an initiator for the polymerization of PVA-CN, and LiTFSI could provide charge carrier due to its low dissociation and large anionic radius. A conductivity of 4.49×10^{-4} S/cm could be achieved. The assembled cells used $LiFePO_4$ and lithium foil as the cathode and the anode, respectively, with the above-mentioned solid thin film as the electrolyte. An initial discharge capacity of 147 mAh/g for such cells achieved at a current density of 0.1 C. A capacity retention of 97% was obtained even at the 100th cycle, indicating a relatively stable electrochemical performance (Zhou et al., 2015).

Hybrid Methods

The above approaches can be combined to prepare unique composite solid electrolytes that take advantage of the benefits of each technique (Yan et al., 2019, 2020). For instance, Yan et al. used electrospinning to manufacture $Li_{6.28}La_3Al_{0.24}Zr_2O_{12}$ (LLAZO) nanofibers, which were then modified with silane functional groups (denoted as s@LLAZO) with different reaction times. The goal was to investigate the effect of silane functionalization on eliminating agglomeration of LLAZO during the casting process. In this study, a new type of hybrid solid electrolyte composed of s@LLAZO nanofibers and poly(ethylene glycol) diacrylate (PEGDA) was prepared

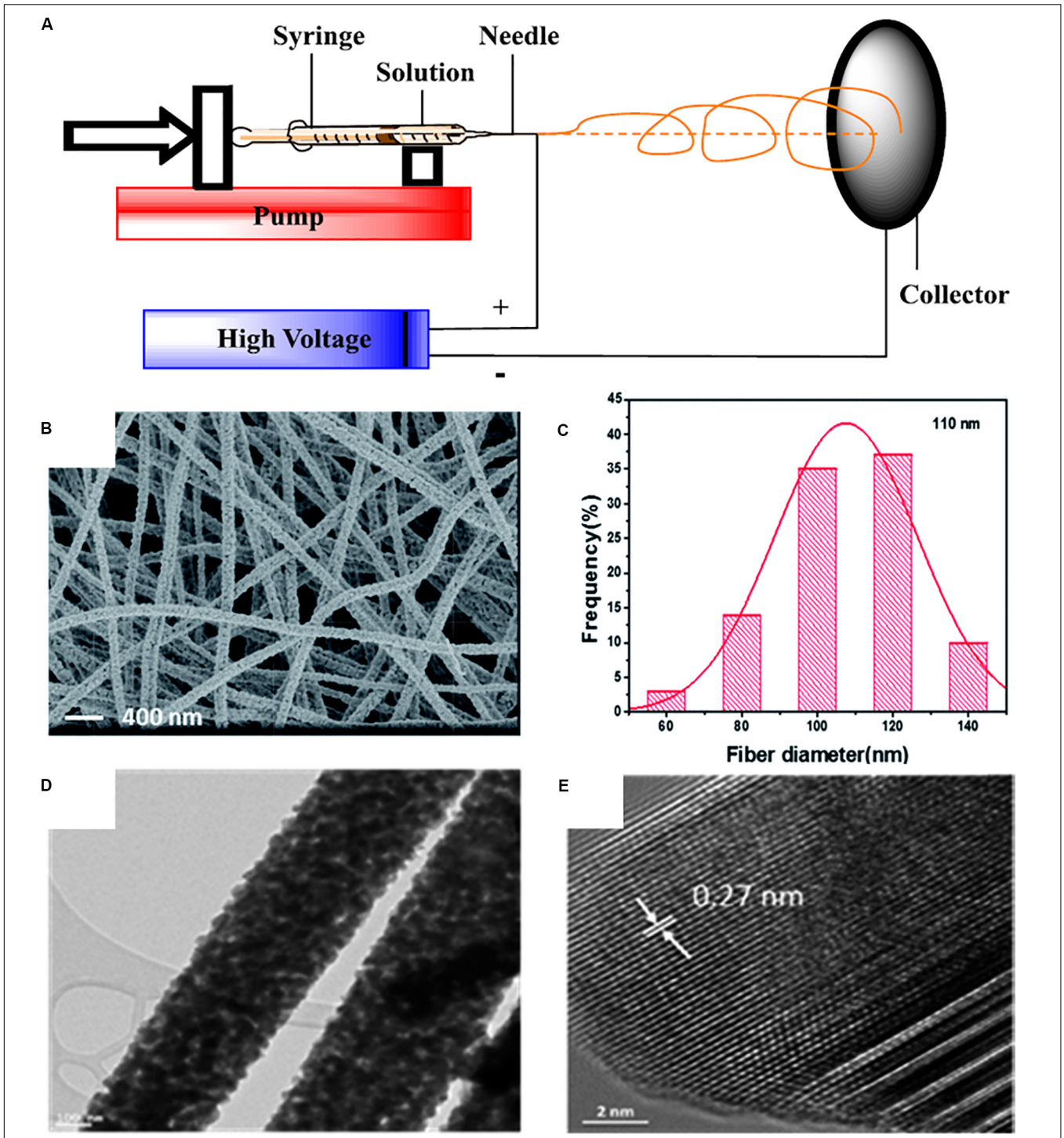

FIGURE 5 | (A) Schematic illustration of the setup of electrospinning. Reprinted with permission from reference Zhu et al. (2016c). Copyright 2016 Elsevier. **(B)** SEM images of the prepared LLTO nanofibers and **(C)** the corresponding diameter distribution. **(D)** Low- and **(E)** high-resolution TEM images of the LLTO nanofibers. Reprinted with permission from reference Zhu et al. (2018a). Copyright 2018 Royal Society of Chemistry.

and developed (**Figure 7**). As a result, the silane coupling agent could eliminate the agglomeration effect, which ensured high ionic conductivity and large lithium transference number of the s@LLZAO-PEGDA electrolyte, demonstrating a wider electrochemical stability window and better cycling stability for the cells with such electrolytes. $LiNi_{1/3}Mn_{1/3}Co_{1/3}O_2$ was also fabricated to be used as the cathode material for the cells. The high voltage cells with an HSE of s@LLZAO-PEGDA with

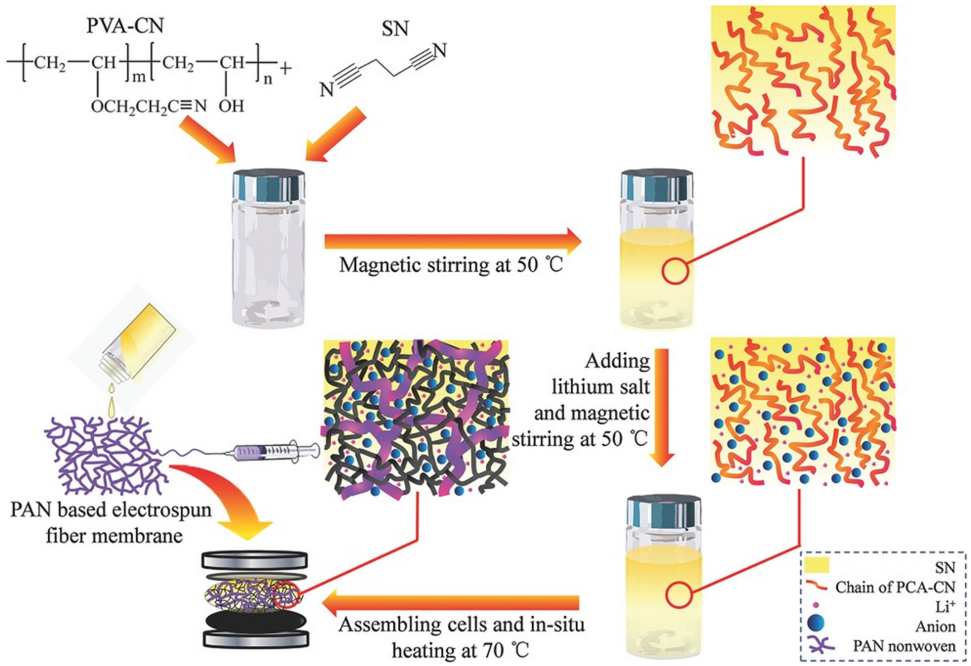

FIGURE 6 | Schematic image showing the procedure for the *in situ* synthesis of solid-state electrolyte based on nitrile materials. Reference Zhou et al. (2015). Copyright 2015 John Wiley and Sons.

$LiNi_{1/3}Mn_{1/3}Co_{1/3}O_2$ exhibited a stable capacity of 110 mAh/g after 250 cycles at a current density of 0.5 C at room temperature and with a high capacity retention of 97%. The excellent capacity retention was due to the good ionic conductivity of 3.9×10^{-4} S/cm and large transference number of 0.61 for the prepared hybrid electrolytes (Yan et al., 2020).

In another example, Palmer et al. (2020) used a novel spray coating – partially sintering method to create a three-dimensionally interconnected ceramic network using a doped LATP ceramic ($LIGCG^{TM}$). The ceramic network is then backfilled with a crosslinkable PEO-based polymer electrolyte to form the composite. The resulting composite has a very high ceramic loading (77 wt% or 61 vol%) and an ionic conductivity of 3.5×10^{-5} S/cm at 20°C with an activation energy of 0.43 eV. X-ray tomography verified that the composite is a bicontinuous structure with a connected ceramic phase and a connected polymer phase. The main ion transport pathway is through the ceramic network as the ionic conductivity scales proportionally with the volume fraction of the ceramic network. Owing to the interconnected structure of the ceramic and the polymer, the composite electrolyte exhibits much improved mechanical strength compared to the neat polymer electrolyte and decreased brittleness compared to the neat ceramic electrolyte.

CURRENT CHALLENGES AND PERSPECTIVES

In this review, we have highlighted three types of solid electrolytes; inorganic, polymer, and HSEs. HSEs can be the most promising solid-state electrolytes for LIBs, attributed to their good mechanical properties, excellent processability, low flammability, wide electrochemical stability window, and ease of scalability. In particular, HSEs incorporating different matrix components and fillers, common processing methods, and ion transport mechanisms were discussed in details. In recent years, the performance of LIBs with composite solid electrolytes has been greatly enhanced. The improved properties of HSEs have come close to being adequate for their potential use in LIBs.

Looking to the future, solid-state LIBs may become even more important in personal portable electronics, electric vehicles, and stationary storage devices. To promote the practical application and commercialization of solid-state batteries, the performance of HSEs for LIBs still needs to be improved. Current issues of HSEs include unsatisfactory ionic conductivity ($<10^{-3}$ S/cm at room temperature), poor interfacial stability, and high interfacial resistance, which greatly restrict the performance of these electrolytes.

Inorganic-type electrolytes allow for the realization of high power density LIBs, attributed to the high ionic conductivity of these electrolytes. However, inorganic-type electrolytes are brittle, have low adhesion to electrodes, and are difficult to manufacture, especially using current battery manufacturing processes, which limits their practical application. Polymer electrolytes are easy to process, are flexible and have good adhesion to electrodes, while their ionic conductivity is far from satisfactory. Therefore, HSEs developed by the mixing of an inorganic filler with a polymer matrix have attracted much attention. Many HSEs demonstrate better ionic conductivity than that of the polymer electrolyte matrix itself. Nonetheless, the

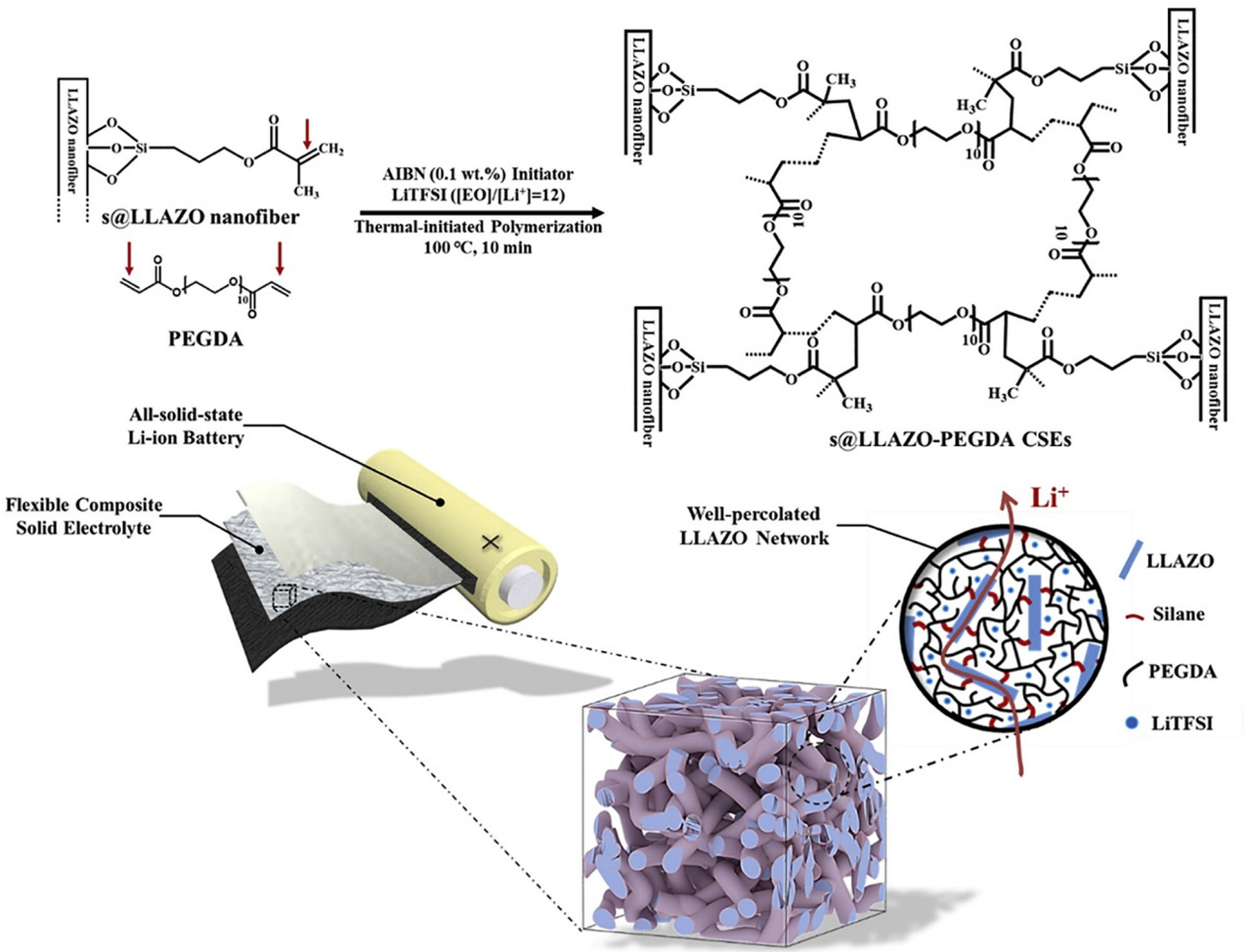

FIGURE 7 | Schematic illustration of the synthesis process of s@LLAZO-PEGDA composite solid electrolytes with percolated s@LLAZO network within the composite electrolyte. Reprinted with permission from reference Yan et al. (2020). Copyright 2020 Elsevier.

mixing of filler and matrix still needs improvement to increase ionic conductivity of composite electrolytes. Constructing a good dispersion method and strengthening the interaction between filler and the polymer may contribute to the improvement of ionic conductivity. Another factor is that insufficient investigation into the ion conduction mechanisms in HSEs is, restricting well-articulated development of novel fillers, polymers, and their composite. Continuous Li-ion transport channels between interconnected polymer matrix and filler are also in need of an in-depth study. In addition, the electrolyte/electrode interface has a great impact on the internal resistance of a battery. Significant advancements need to be made to improve the interfacial contact between the electrolyte and electrodes in order to achieve high performance of solid-state batteries.

Our perspective on the future research directions of HSEs for solid-state LIBs is to develop safe, highly stable, and conductive composite polymer electrolytes. A fundamental understanding of the mechanisms of ion transport, the interfacial properties between the polymer and filler, and between the electrolyte and electrodes may facilitate further molecular design to address these issues.

The future focus of HSE development should include:

(i) Understand the underlying mechanisms of ion transport in HSEs. A variety of proposed mechanisms of ion transport through an HSE are discussed in section "Ion conduction mechanisms in hybrid solid electrolytes" in detail. As discussed, the dominant mechanism depends on several factors, including the type of filler (inert or active) and filler loading. By developing a deeper understanding of each mechanism and the molecular interactions that cause transition from one mechanism to another is instrumental in the rational design of new HSE materials. Designing HSE materials on the molecular level may allow for greater interactions between polymer and filler that may be essential in increasing the ionic conductivity of the HSEs. Computational simulations would assist in the investigation of ion transport mechanisms and the polymer-filler interactions.

(ii) Improve the interfacial property between the polymer matrix and fillers, which is pivotal in obtaining a solid-state electrolyte with high conductivity and processability. The polymer-filler interface can influence the crystallinity and morphology of the polymer chain and provide a path for ion transportation through the HSE. Furthermore, with active fillers, controlling the interface between the active ceramic particle and the polymer is crucial for marrying the high conductivity of conductive ceramics with the flexibility of a polymer. Treatment and functionalization of filler's surfaces might provide significant enhancement of interfacial transport. A greater understanding of the structure-property relationships that control the polymer/filler interface may allow for the rational design of materials to create a stable interface. The nanostructure of HSEs could be investigated by TEM. In addition, typical polymer composite characterization techniques including, differential scanning calorimetry, rheology, broadband dielectric spectroscopy, and X-ray diffraction, would assist in gaining an in-depth understanding of the interfacial behavior between matrix and filler.

(iii) The design and synthesis of novel polymer matrices would open new avenues for improving the performance of HSEs. The optimal combination of matrix and filler would allow for high ionic conductivity and stability to be achieved. Novel polymer electrolytes designed specifically for a composite system is a field that researchers have rarely explored. Single ion conducting polymers, namely polyelectrolytes where the anions are covalently tethered to the polymer backbone and the lithium ions are the only mobile species, shows potential of increasing the lithium transference number. Considerable improvements in battery performance has been achieved by the introduction of single ion conducting polymers and the optimization of the macromolecular architecture via random and block copolymerization with various monomers. Therefore, a promising direction for HSE development is the use of a single ion conducting polymer as the matrix material.

(iv) Design of HSEs that are compatible with next-generation high energy density anodes and cathodes. In commercial LIBs, some commonly used cathode materials are lithium cobalt oxide, lithium iron phosphate (LFP), and lithium nickel manganese cobalt (NMC). The anode typically consists of graphite, but new anode materials of a significantly higher energy density are currently under investigation, including lithium metal. Both the anode and cathode require the solid electrolyte to exhibit a certain amount of flexibility and adhesion to ensure low interfacial resistance at the electrode/electrolyte interface. While the use of a lithium metal anode requires a strong solid electrolyte to resist puncture by lithium dendrites. HSEs can provide both requirements of flexibility and mechanical strength that opens the avenue for the use of a lithium metal anode that is not realizable with liquid electrolytes.

(v) Advanced simulations and computations would provide insight and a path to an in-depth understanding of ion transport, the interaction between polymer and filler, and interactions between electrode and electrolyte. By taking advantage of advanced computing simulations and calculations, researchers will be able to make informed decisions on new materials design and selection, and the potential combinations of fillers and polymers that may lead to improved performance of HSEs.

AUTHOR CONTRIBUTIONS

LH wrote the manuscript with support from ML, JZ, TL, ZZ, XT, C-TH, PC, and XC. AS and TS helped supervise the project. All authors contributed to the article and approved the submitted version.

FUNDING

This research was supported by the U.S. Department of Energy, Office of Science, Basic Energy Sciences, Materials Sciences and Engineering Division.

ACKNOWLEDGMENTS

This manuscript has been authored by UT-Battelle, LLC under Contract No. DE-AC05-00OR22725 with the U.S. Department of Energy. The United States Government retains and the publisher, by accepting the article for publication, acknowledges that the United States Government retains a non-exclusive, paid-up, irrevocable, world-wide license to publish or reproduce the published form of this manuscript, or allow others to do so, for United States Government purposes. The Department of Energy will provide public access to these results of federally sponsored research in accordance with the DOE Public Access Plan (http://energy.gov/downloads/doe-public-access-plan). XC acknowledges support from U.S. Department of Energy (DOE), Office of Energy Efficiency and Renewable Energy for the Vehicle Technologies Office's Advanced Battery Materials Research Program as well as Office of Science, Basic Energy Sciences, Materials Sciences and Engineering Division.

REFERENCES

Adebahr, J., Byrne, N., Forsyth, M., MacFarlane, D. R., and Jacobsson, P. (2003). Enhancement of ion dynamics in PMMA-based gels with addition of TiO_2 nano-particles. *Electrochim. Acta* 48, 2099–2103. doi: 10.1016/S0013-4686(03)00191-9

Afyon, S., Kravchyk, K. V., Wang, S., Broek, J. V. D., Hänsel, C., Kovalenko, M. V., et al. (2019). Building better all-solid-state batteries with Li-garnet solid electrolytes and metalloid anodes. *J. Mater. Chem. A* 7, 21299–21308.

Agapov, A. L., and Sokolov, A. P. (2011). Decoupling ionic conductivity from structural relaxation: a way to solid polymer electrolytes? *Macromolecules* 44, 4410–4414. doi: 10.1021/ma2001096

Ahmed, F., Choi, I., Rahman, M. M., Jang, H., Ryu, T., Yoon, S., et al. (2019). Remarkable conductivity of a self-healing single-Ion conducting polymer electrolyte, poly(ethylene-co-acrylic lithium (fluoro sulfonyl)imide), for all-solid-state li-Ion batteries. *ACS Appl. Mater. Interf.* 11, 34930–34938. doi: 10.1021/acsami.9b10474

Aono, H. (1990). Ionic conductivity of solid electrolytes based on lithium titanium phosphate. *J. Electrochem. Soc.* 137:1023. doi: 10.1149/1.2086597

Appetecchi, G. B., Croce, F., Persi, L., Ronci, F., and Scrosati, B. (2000). Transport and interfacial properties of composite polymer electrolytes. *Electrochim. Acta* 45, 1481–1490. doi: 10.1016/S0013-4686(99)00363-1

Appetecchi, G. B., and Passerini, S. (2000). PEO-carbon composite lithium polymer electrolyte. *Electrochim. Acta* 45, 2139–2145. doi: 10.1016/S0013-4686(99)00437-5

Berthier, C., Gorecki, W., Minier, M., Armand, M. B., Chabagno, J. M., and Rigaud, P. (1983). Microscopic investigation of ionic conductivity in alkali metal salts-poly(ethylene oxide) adducts. *Solid State Ionics* 11, 91–95. doi: 10.1016/0167-2738(83)90068-1

Bhattacharyya, R., Key, B., Chen, H., Best, A. S., Hollenkamp, A. F., and Grey, C. P. (2010). In situ NMR observation of the formation of metallic lithium microstructures in lithium batteries. *Nat. Mater.* 9, 504–510. doi: 10.1038/nmat2764

Bocharova, V., and Sokolov, A. P. (2020). Perspectives for polymer electrolytes: a view from fundamentals of ionic conductivity. *Macromolecules* 53, 4141–4157. doi: 10.1021/acs.macromol.9b02742

Bouchet, R., Maria, S., Meziane, R., Aboulaich, A., Lienafa, L., Bonnet, J.-P., et al. (2013). Single-ion BAB triblock copolymers as highly efficient electrolytes for lithium-metal batteries. *Nat. Mater.* 12, 452–457. doi: 10.1038/nmat3602

Cao, P.-F., Li, B., Yang, G., Zhao, S., Townsend, J., Xing, K., et al. (2020). Elastic Single-Ion conducting polymer electrolytes: toward a versatile approach for intrinsically stretchable functional polymers. *Macromolecules* 53, 3591–3601. doi: 10.1021/acs.macromol.9b02683

Cao, P.-F., Wojnarowska, Z., Hong, T., Carroll, B., Li, B., Feng, H., et al. (2017). A star-shaped single lithium-ion conducting copolymer by grafting a POSS nanoparticle. *Polymer* 124, 117–127. doi: 10.1016/j.polymer.2017.07.052

Chen, S., Wang, J., Zhang, Z., Wu, L., Yao, L., Wei, Z., et al. (2018a). In-situ preparation of poly(ethylene oxide)/Li_3PS_4 hybrid polymer electrolyte with good nanofiller distribution for rechargeable solid-state lithium batteries. *J. Power Sources* 387, 72–80. doi: 10.1016/j.jpowsour.2018.03.016

Chen, S., Wen, K., Fan, J., Bando, Y., and Golberg, D. (2018b). Progress and future prospects of high-voltage and high-safety electrolytes in advanced lithium batteries: from liquid to solid electrolytes. *J. Mater. Chem. A* 6, 11631–11663. doi: 10.1039/C8TA03358G

Chen, S., Xie, D., Liu, G., Mwizerwa, J. P., Zhang, Q., Zhao, Y., et al. (2018c). Sulfide solid electrolytes for all-solid-state lithium batteries: structure, conductivity, stability and application. *Energy Storage Mater.* 14, 58–74. doi: 10.1016/j.ensm.2018.02.020

Chen, X., He, W., Ding, L.-X., Wang, S., and Wang, H. (2019). Enhancing interfacial contact in all solid state batteries with a cathode-supported solid electrolyte membrane framework. *Energy Environ. Sci.* 12, 938–944. doi: 10.1039/C8EE02617C

Chen, X., and Vereecken, P. M. (2019). Solid and solid-like composite electrolyte for lithium ion batteries: engineering the Ion conductivity at interfaces. *Adv. Mater. Interf.* 6:1800899. doi: 10.1002/admi.201800899

Chen, X. C., Sacci, R. L., Osti, N. C., Tyagi, M., Wang, Y., Palmer, M. J., et al. (2019). Study of segmental dynamics and ion transport in polymer–ceramic composite electrolytes by quasi-elastic neutron scattering. *Mol. Syst. Design Eng.* 4, 379–385. doi: 10.1039/C8ME00113H

Choi, J.-H., Lee, C.-H., Yu, J.-H., Doh, C.-H., and Lee, S.-M. (2015). Enhancement of ionic conductivity of composite membranes for all-solid-state lithium rechargeable batteries incorporating tetragonal $Li_7La_3Zr_2O_{12}$ into a polyethylene oxide matrix. *J. Power Sources* 274, 458–463. doi: 10.1016/j.jpowsour.2014.10.078

Cohen, M. H., and Turnbull, D. (1959). Molecular transport in liquids and glasses. *J. Chem. Phys.* 31, 1164–1169. doi: 10.1063/1.1730566

Croce, F., Appetecchi, G. B., Persi, L., and Scrosati, B. (1998). Nanocomposite polymer electrolytes for lithium batteries. *Nature* 394, 456–458. doi: 10.1038/28818

Croce, F., Curini, R., Martinelli, A., Persi, L., Ronci, F., Scrosati, B., et al. (1999). Physical and chemical properties of nanocomposite polymer electrolytes. *J. Phys. Chem. B* 103, 10632–10638. doi: 10.1021/jp992307u

Croce, F., Persi, L., Ronci, F., and Scrosati, B. (2000). Nanocomposite polymer electrolytes and their impact on the lithium battery technology. *Solid State Ionics* 135, 47–52. doi: 10.1016/S0167-2738(00)00329-5

Croce, F., Persi, L., Scrosati, B., Serraino-Fiory, F., Plichta, E., and Hendrickson, M. A. (2001). Role of the ceramic fillers in enhancing the transport properties of composite polymer electrolytes. *Electrochim. Acta* 46, 2457–2461. doi: 10.1016/S0013-4686(01)00458-3

Croce, F., Settimi, L., and Scrosati, B. (2006). Superacid ZrO_2-added, composite polymer electrolytes with improved transport properties. *Electrochem. Commun.* 8, 364–368. doi: 10.1016/j.elecom.2005.12.002

Das, S., and Ghosh, A. (2015). Ion conduction and relaxation in PEO-LiTFSI-Al_2O_3 polymer nanocomposite electrolytes. *J. Appl. Phys.* 117:174103. doi: 10.1063/1.4919721

Dirican, M., Yan, C., Zhu, P., and Zhang, X. (2019). Composite solid electrolytes for all-solid-state lithium batteries. *Mater. Sci. Eng. R Rep.* 136, 27–46. doi: 10.1016/j.mser.2018.10.004

Duan, H., Yin, Y.-X., Zeng, X.-X., Li, J.-Y., Shi, J.-L., Shi, Y., et al. (2018). In-situ plasticized polymer electrolyte with double-network for flexible solid-state lithium-metal batteries. *Energy Storage Mater.* 10, 85–91. doi: 10.1016/j.ensm.2017.06.017

Evans, J., Vincent, C. A., and Bruce, P. G. (1987). Electrochemical measurement of transference numbers in polymer electrolytes. *Polymer* 28, 2324–2328. doi: 10.1016/0032-3861(87)90394-6

Famprikis, T., Canepa, P., Dawson, J. A., Islam, M. S., and Masquelier, C. (2019). Fundamentals of inorganic solid-state electrolytes for batteries. *Nat. Mater.* 18, 1278–1291. doi: 10.1038/s41563-019-0431-3

Fan, J. (1997). Composite electrolytes prepared from fumed silica, polyethylene oxide oligomers, and lithium salts. *J. Electrochem. Soc.* 144:399. doi: 10.1149/1.1837423

Fan, L., Nan, C.-W., and Zhao, S. (2003). Effect of modified SiO_2 on the properties of PEO-based polymer electrolytes. *Solid State Ionics* 164, 81–86. doi: 10.1016/j.ssi.2003.08.004

Fan, L., Wei, S., Li, S., Li, Q., and Lu, Y. (2018). Recent progress of the solid-state electrolytes for high-energy metal-based batteries. *Adv. Energy Mater.* 8:1702657. doi: 10.1002/aenm.201702657

Florjańczyk, Z., Zygadło-Monikowska, E., Affek, A., Tomaszewska, A., Łasińska, A., Marzantowicz, M., et al. (2005). Polymer electrolytes based on acrylonitrile–butyl acrylate copolymers and lithium bis(trifluoromethanesulfone)imide. *Solid State Ionics* 176, 2123–2128. doi: 10.1016/j.ssi.2004.08.046

Florjańczyk, Z., Zygadło-Monikowska, E., Wieczorek, W., Ryszawy, A., Tomaszewska, A., Fredman, K., et al. (2004). Polymer-in-salt electrolytes based on acrylonitrile/butyl acrylate copolymers and lithium salts. *J. Phys. Chem. B* 108, 14907–14914. doi: 10.1021/jp049195d

Forsyth, M., Sun, J., Macfarlane, D. R., and Hill, A. J. (2000). Compositional dependence of free volume in PAN/$LiCF_3SO_3$ polymer-in-salt electrolytes and the effect on ionic conductivity. *J. Polym. Sci. Part B Polym. Phys.* 38, 341–350. doi: 10.1002/(sici)1099-0488(20000115)38:2<341::Aid-polb6<3.0.Co;2-s

Fu, K., Li, Y., Dirican, M., Chen, C., Lu, Y., Zhu, J., et al. (2014). Sulfur gradient-distributed CNF composite: a self-inhibiting cathode for binder-free lithium–sulfur batteries. *Chem. Commun.* 50, 10277–10280. doi: 10.1039/C4CC04970E

Fullerton-Shirey, S. K., and Maranas, J. K. (2009). Effect of $LiClO_4$ on the structure and mobility of PEO-based solid polymer electrolytes. *Macromolecules* 42, 2142–2156. doi: 10.1021/ma802502u

Ge, Y., Jiang, H., Fu, K., Zhang, C., Zhu, J., Chen, C., et al. (2014). Copper-doped Li4Ti5O12/carbon nanofiber composites as anode for high-performance sodium-ion batteries. *J. Power Sources* 272, 860–865. doi: 10.1016/j.jpowsour.2014.08.131

Geiger, C. A., Alekseev, E., Lazic, B., Fisch, M., Armbruster, T., Langner, R., et al. (2011). Crystal chemistry and stability of "$Li_7La_3Zr_2O_{12}$" garnet: a fast lithium-Ion conductor. *Inorg. Chem.* 50, 1089–1097. doi: 10.1021/ic101914e

Gibbs, J. H., and DiMarzio, E. A. (1958). Nature of the glass transition and the glassy state. *J. Chem. Phys.* 28, 373–383. doi: 10.1063/1.1744141

Goodenough, J. B., Hong, H. Y. P., and Kafalas, J. A. (1976). Fast Na^+-ion transport in skeleton structures. *Mater. Res. Bull.* 11, 203–220. doi: 10.1016/0025-5408(76)90077-5

Grey, C. P., and Dupré, N. (2004). NMR studies of cathode materials for lithium-Ion rechargeable batteries. *Chem. Rev.* 104, 4493–4512. doi: 10.1021/cr020734p

Gutmann, V. (1976). Empirical parameters for donor and acceptor properties of solvents. *Electrochim. Acta* 21, 661–670. doi: 10.1016/0013-4686(76)85034-7

Hanson, B., Pryamitsyn, V., and Ganesan, V. (2013). Mechanisms underlying Ionic mobilities in nanocomposite polymer electrolytes. *ACS Macro Lett.* 2, 1001–1005. doi: 10.1021/mz400234m

Hsueh, L., and Bennion, D. N. (1971). EMF measurements of sodium activity in sodium amalgam with beta-alumina. *J. Electrochem. Soc.* 118:1128. doi: 10.1149/1.2408260

Hu, L., Tang, Z., and Zhang, Z. (2007). New composite polymer electrolyte comprising mesoporous lithium aluminate nanosheets and PEO/$LiClO_4$. *J. Power Sources* 166, 226–232. doi: 10.1016/j.jpowsour.2007.01.028

Ilott, A. J., Trease, N. M., Grey, C. P., and Jerschow, A. (2014). Multinuclear in situ magnetic resonance imaging of electrochemical double-layer capacitors. *Nat. Commun.* 5:4536. doi: 10.1038/ncomms5536

Inaguma, Y., Liquan, C., Itoh, M., Nakamura, T., Uchida, T., Ikuta, H., et al. (1993). High ionic conductivity in lithium lanthanum titanate. *Solid State Commun.* 86, 689–693. doi: 10.1016/0038-1098(93)90841-A

Janek, J., and Zeier, W. G. (2016). A solid future for battery development. *Nat. Energy* 1:16141. doi: 10.1038/nenergy.2016.141

Ju, J., Wang, Y., Chen, B., Ma, J., Dong, S., Chai, J., et al. (2018). Integrated interface strategy toward room temperature solid-state lithium batteries. *ACS Appl. Mater. Interf.* 10, 13588–13597. doi: 10.1021/acsami.8b02240

Jung, Y.-C., Lee, S.-M., Choi, J.-H., Jang, S. S., and Kim, D.-W. (2015). All solid-state lithium batteries assembled with hybrid solid electrolytes. *J. Electrochem. Soc.* 162, A704–A710. doi: 10.1149/2.0731504jes

Kamaya, N., Homma, K., Yamakawa, Y., Hirayama, M., Kanno, R., Yonemura, M., et al. (2011). A lithium superionic conductor. *Nat. Mater.* 10, 682–686. doi: 10.1038/nmat3066

Karan, N. K., Pradhan, D. K., Thomas, R., Natesan, B., and Katiyar, R. S. (2008). Solid polymer electrolytes based on polyethylene oxide and lithium trifluoro- methane sulfonate (PEO–$LiCF_3SO_3$): ionic conductivity and dielectric relaxation. *Solid State Ionics* 179, 689–696. doi: 10.1016/j.ssi.2008.04.034

Khurana, R., Schaefer, J. L., Archer, L. A., and Coates, G. W. (2014). Suppression of lithium dendrite growth using cross-linked polyethylene/Poly(ethylene oxide) electrolytes: a new approach for practical lithium-metal polymer batteries. *J. Am. Chem. Soc.* 136, 7395–7402. doi: 10.1021/ja502133j

Kim, J. G., Son, B., Mukherjee, S., Schuppert, N., Bates, A., Kwon, O., et al. (2015). A review of lithium and non-lithium based solid state batteries. *J. Power Sources* 282, 299–322. doi: 10.1016/j.jpowsour.2015.02.054

Kim, J.-K., Scheers, J., Park, T. J., and Kim, Y. (2015). Superior Ion-conducting hybrid solid electrolyte for all-solid-state batteries. *ChemSusChem* 8, 636–641. doi: 10.1002/cssc.201402969

Kumar, B. (2004). From colloidal to composite electrolytes: properties, peculiarities, and possibilities. *J. Power Sources* 135, 215–231. doi: 10.1016/j.jpowsour.2004.04.038

Kumar, B., Thomas, D., and Kumar, J. (2009). Space-charge-mediated superionic transport in lithium Ion conducting glass–ceramics. *J. Electrochem. Soc.* 156:A506. doi: 10.1149/1.3122903

Kummer, J. T., and Neill, W. (1968). *Secondary Battery Employing Molten Alkali Metal Reactant*. Google Patents US3404035A.

Lagadec, M. F., Zahn, R., and Wood, V. (2019). Characterization and performance evaluation of lithium-ion battery separators. *Nat. Energy* 4, 16–25. doi: 10.1038/s41560-018-0295-9

Le, H. T. T., Kalubarme, R. S., Ngo, D. T., Jadhav, H. S., and Park, C.-J. (2015). Bi-layer lithium phosphorous oxynitride/aluminium substituted lithium lanthanum titanate as a promising solid electrolyte for long-life rechargeable lithium–oxygen batteries. *J. Mater. Chem. A* 3, 22421–22431. doi: 10.1039/C5TA06374D

Lee, H., Oh, P., Kim, J., Cha, H., Chae, S., Lee, S., et al. (2019). Advances and prospects of sulfide all-solid-state lithium batteries via one-to-one comparison with conventional liquid lithium Ion batteries. *Adv. Mater.* 31:1900376. doi: 10.1002/adma.201900376

Lee, Y. M., Seo, J. E., Choi, N.-S., and Park, J.-K. (2005). Influence of tris(pentafluorophenyl) borane as an anion receptor on ionic conductivity of LiClO4-based electrolyte for lithium batteries. *Electrochim. Acta* 50, 2843–2848. doi: 10.1016/j.electacta.2004.11.058

Lehmann, M. L., Yang, G., Gilmer, D., Han, K. S., Self, E. C., Ruther, R. E., et al. (2019). Tailored crosslinking of Poly(ethylene oxide) enables mechanical robustness and improved sodium-ion conductivity. *Energy Storage Mater.* 21, 85–96. doi: 10.1016/j.ensm.2019.06.028

Li, D., Chen, L., Wang, T., and Fan, L.-Z. (2018). 3D fiber-network-reinforced bicontinuous composite solid electrolyte for dendrite-free lithium metal batteries. *ACS Appl. Mater. Interf.* 10, 7069–7078. doi: 10.1021/acsami.7b18123

Li, Y., Zhu, J., Shi, R., Dirican, M., Zhu, P., Yan, C., et al. (2018a). Ultrafine and polar ZrO_2-inlaid porous nitrogen-doped carbon nanofiber as efficient polysulfide absorbent for high-performance lithium-sulfur batteries with long lifespan. *Chem. Eng. J.* 349, 376–387. doi: 10.1016/j.cej.2018.05.074

Li, Y., Zhu, J., Zhu, P., Yan, C., Jia, H., Kiyak, Y., et al. (2018b). Glass fiber separator coated by porous carbon nanofiber derived from immiscible PAN/PMMA for high-performance lithium-sulfur batteries. *J. Membr. Sci.* 552, 31–42. doi: 10.1016/j.memsci.2018.01.062

Liang, C. C. (1973). Conduction characteristics of the lithium iodide-aluminum oxide solid electrolytes. *J. Electrochem. Soc.* 120:1289. doi: 10.1149/1.2403248

Lin, D., Liu, W., Liu, Y., Lee, H. R., Hsu, P.-C., Liu, K., et al. (2016). High ionic conductivity of composite solid polymer electrolyte via in situ synthesis of monodispersed SiO_2 nanospheres in poly(ethylene oxide). *Nano Lett.* 16, 459–465. doi: 10.1021/acs.nanolett.5b04117

Liu, W., Liu, N., Sun, J., Hsu, P.-C., Li, Y., Lee, H.-W., et al. (2015). Ionic conductivity enhancement of polymer electrolytes with ceramic nanowire fillers. *Nano Lett.* 15, 2740–2745. doi: 10.1021/acs.nanolett.5b00600

Liu, X., Li, X., Li, H., and Wu, H. B. (2018). Recent progress of hybrid solid-state electrolytes for lithium batteries. *Chem. Eur. J.* 24, 18293–18306. doi: 10.1002/chem.201803616

Liu, Y., Lee, J. Y., and Hong, L. (2004). In situ preparation of poly(ethylene oxide)–SiO_2 composite polymer electrolytes. *J. Power Sources* 129, 303–311. doi: 10.1016/j.jpowsour.2003.11.026

Liu, Y., Zhu, Y., and Cui, Y. (2019). Challenges and opportunities towards fast-charging battery materials. *Nat. Energy* 4, 540–550. doi: 10.1038/s41560-019-0405-3

Lopez, J., Mackanic, D. G., Cui, Y., and Bao, Z. (2019). Designing polymers for advanced battery chemistries. *Nat. Rev. Mater.* 4, 312–330. doi: 10.1038/s41578-019-0103-6

Luo, L., Li, D., Zang, J., Chen, C., Zhu, J., Qiao, H., et al. (2017). Carbon-coated magnesium ferrite nanofibers for lithium-Ion battery anodes with enhanced cycling performance. *Energy Technol.* 5, 1364–1372. doi: 10.1002/ente.201600686

Luo, L., Xu, W., Xia, Z., Fei, Y., Zhu, J., Chen, C., et al. (2016). Electrospun ZnO–SnO_2 composite nanofibers with enhanced electrochemical performance as lithium-ion anodes. *Ceram. Int.* 42, 10826–10832. doi: 10.1016/j.ceramint.2016.03.211

Maccallum, J. R., Smith, M. J., and Vincent, C. A. (1984). The effects of radiation-induced crosslinking on the conductance of $LiClO_4$·PEO electrolytes. *Solid State Ionics* 11, 307–312. doi: 10.1016/0167-2738(84)90022-5

Malathi, M. T., and Tamilarasan, K. (2014). Synthesis and characterization of polyethylene oxide based nano composite electrolyte. *Sadhana* 39, 999–1007.

Manthiram, A., Yu, X., and Wang, S. (2017). Lithium battery chemistries enabled by solid-state electrolytes. *Nat. Rev. Mater.* 2:16103. doi: 10.1038/natrevmats.2016.103

Marcinek, M., Bac, A., Lipka, P., Zalewska, A., Żukowska, G., Borkowska, R., et al. (2000). Effect of filler surface group on ionic interactions in PEG-$LiClO_4$-Al_2O_3 composite polyether electrolytes. *J. Phys. Chem. B* 104, 11088–11093. doi: 10.1021/jp0021493

Mariappan, C. R., Gellert, M., Yada, C., Rosciano, F., and Roling, B. (2012). Grain boundary resistance of fast lithium ion conductors: comparison between a lithium-ion conductive Li–Al–Ti–P–O-type glass ceramic and a $Li_{1.5}Al_{0.5}Ge_{1.5}P_3O_{12}$ ceramic. *Electrochem. Commun.* 14, 25–28. doi: 10.1016/j.elecom.2011.10.022

Martinez-Juarez, A., Rojo, J. M., Iglesias, J. E., and Sanz, J. (1995). Reversible monoclinic-rhombohedral transformation in $LiSn_2(PO_4)_3$ with NASICON-type structure. *Chem. Mater.* 7, 1857–1862. doi: 10.1021/cm00058a016

Matsumoto, K., Kakehashi, M., Ouchi, H., Yuasa, M., and Endo, T. (2016). Synthesis and properties of polycarbosilanes having 5-membered cyclic

carbonate groups as solid polymer electrolytes. *Macromolecules* 49, 9441–9448. doi: 10.1021/acs.macromol.6b01516

Matsumoto, M., Uno, T., Kubo, M., and Itoh, T. (2013). Polymer electrolytes based on polycarbonates and their electrochemical and thermal properties. *Ionics* 19, 615–622. doi: 10.1007/s11581-012-0796-7

Meabe, L., Huynh, T. V., Mantione, D., Porcarelli, L., Li, C., O'Dell, L. A., et al. (2019). UV-cross-linked poly(ethylene oxide carbonate) as free standing solid polymer electrolyte for lithium batteries. *Electrochim. Acta* 302, 414–421. doi: 10.1016/j.electacta.2019.02.058

Meabe, L., Lago, N., Rubatat, L., Li, C., Müller, A. J., Sardon, H., et al. (2017). Polycondensation as a versatile synthetic route to aliphatic polycarbonates for solid polymer electrolytes. *Electrochim. Acta* 237, 259–266. doi: 10.1016/j.electacta.2017.03.217

Meyer, W. H. (1998). Polymer electrolytes for lithium-Ion batteries. *Adv. Mater.* 10, 439–448. doi: 10.1002/(sici)1521-4095(199804)10:6<439::Aid-adma439<3.0.Co;2-i

Mindemark, J., Sun, B., Törmä, E., and Brandell, D. (2015). High-performance solid polymer electrolytes for lithium batteries operational at ambient temperature. *J. Power Sources* 298, 166–170. doi: 10.1016/j.jpowsour.2015.08.035

Munichandraiah, N., Scanlon, L. G., Marsh, R. A., Kumar, B., and Sircar, A. K. (1995). Influence of zeolite on electrochemical and physicochemical properties of polyethylene oxide solid electrolyte. *J. Appl. Electrochem.* 25, 857–863. doi: 10.1007/BF00233905

Muramatsu, H., Hayashi, A., Ohtomo, T., Hama, S., and Tatsumisago, M. (2011). Structural change of Li_2S–P_2S_5 sulfide solid electrolytes in the atmosphere. *Solid State Ionics* 182, 116–119. doi: 10.1016/j.ssi.2010.10.013

Murugan, R., Ramakumar, S., and Janani, N. (2011). High conductive yttrium doped $Li_7La_3Zr_2O_{12}$ cubic lithium garnet. *Electrochem. Commun.* 13, 1373–1375. doi: 10.1016/j.elecom.2011.08.014

Murugan, R., Thangadurai, V., and Weppner, W. (2007). Fast lithium Ion conduction in garnet-Type $Li_7La_3Zr_2O_{12}$. *Angewandte Chem. Int. Ed.* 46, 7778–7781. doi: 10.1002/anie.200701144

Nairn, K., Forsyth, M., Every, H., Greville, M., and MacFarlane, D. R. (1996). Polymer-ceramic ion-conducting composites. *Solid State Ionics* 8, 589–593. doi: 10.1016/0167-2738(96)00212-3

Ong, M. T., Verners, O., Draeger, E. W., van Duin, A. C. T., Lordi, V., and Pask, J. E. (2015). Lithium Ion solvation and diffusion in bulk organic electrolytes from first-principles and classical reactive molecular dynamics. *J. Phys. Chem. B* 119, 1535–1545. doi: 10.1021/jp508184f

Palmer, M. J., Kalnaus, S., Dixit, M. B., Westover, A. S., Hatzell, K. B., Dudney, N. J., et al. (2020). A three-dimensional interconnected polymer/ceramic composite as a thin film solid electrolyte. *Energy Storage Mater.* 26, 242–249. doi: 10.1016/j.ensm.2019.12.031

Pandian, A. S., Chen, X. C., Chen, J., Lokitz, B. S., Ruther, R. E., Yang, G., et al. (2018). Facile and scalable fabrication of polymer-ceramic composite electrolyte with high ceramic loadings. *J. Power Sources* 390, 153–164. doi: 10.1016/j.jpowsour.2018.04.006

Peng, J., Xiao, Y., Clarkson, D. A., Greenbaum, S. G., Zawodzinski, T. A., and Chen, X. C. (2020). A Nuclear magnetic resonance study of cation and anion dynamics in polymer–ceramic composite solid electrolytes. *ACS Appl. Polym. Mater.* 2, 1180–1189. doi: 10.1021/acsapm.9b01068

Pomerantseva, E., Bonaccorso, F., Feng, X., Cui, Y., and Gogotsi, Y. (2019). Energy storage: the future enabled by nanomaterials. *Science* 366:eaan8285. doi: 10.1126/science.aan8285

Porcarelli, L., Gerbaldi, C., Bella, F., and Nair, J. R. (2016). Super soft all-ethylene oxide polymer electrolyte for safe all-solid lithium batteries. *Sci. Rep.* 6:19892. doi: 10.1038/srep19892

Pożyczka, K., Marzantowicz, M., Dygas, J. R., and Krok, F. (2017). IONIC CONDUCTIVITY AND LITHIUM TRANSFERENCE NUMBER OF POLY(ETHYLENE OXIDE):LiTFSI SYSTEM. *Electrochim. Acta* 227, 127–135. doi: 10.1016/j.electacta.2016.12.172

Przyluski, J., Siekierski, M., and Wieczorek, W. (1995). Effective medium theory in studies of conductivity of composite polymeric electrolytes. *Electrochim. Acta* 40, 2101–2108. doi: 10.1016/0013-4686(95)00147-7

Quartarone, E., Mustarelli, P., and Magistris, A. (1998). PEO-based composite polymer electrolytes. *Solid State Ionics* 110, 1–14. doi: 10.1016/S0167-2738(98)00114-3

Ramesh, S., Winie, T., and Arof, A. K. (2007). Investigation of mechanical properties of polyvinyl chloride–polyethylene oxide (PVC–PEO) based polymer electrolytes for lithium polymer cells. *Eur. Polym. J.* 43, 1963–1968. doi: 10.1016/j.eurpolymj.2007.02.006

Roman, H. E. (1990). A continuum percolation model for dispersed ionic conductors. *J. Phys. Condensed Matter* 2, 3909–3917. doi: 10.1088/0953-8984/2/17/002

Saunier, J., Chaix, N., Alloin, F., Belières, J. P., and Sanchez, J. Y. (2002). Electrochemical study of polymethacrylonitrile electrolytes: conductivity study of polymer/salt complexes and plasticized polymer electrolytes. Part I. *Electrochim. Acta* 47, 1321–1326. doi: 10.1016/S0013-4686(01)00852-0

Senthil Kumar, R., Raja, M., Anbu Kulandainathan, M., and Manuel Stephan, A. (2014). Metal organic framework-laden composite polymer electrolytes for efficient and durable all-solid-state-lithium batteries. *RSC Adv.* 4, 26171–26175. doi: 10.1039/C4RA03147D

Shim, J., Kim, D.-G., Lee, J. H., Baik, J. H., and Lee, J.-C. (2014). Synthesis and properties of organic/inorganic hybrid branched-graft copolymers and their application to solid-state electrolytes for high-temperature lithium-ion batteries. *Polym. Chem.* 5, 3432–3442. doi: 10.1039/C4PY00123K

Soo, P. P. (1999). Rubbery block copolymer electrolytes for solid-state rechargeable lithium batteries. *J. Electrochem. Soc.* 146:32. doi: 10.1149/1.1391560

Spiegel, E. F., Adamic, K. J., Williams, B. D., and Sammells, A. F. (2000). Solvation of lithium salts within single-phase dimethyl siloxane bisphenol-A carbonate block copolymer. *Polymer* 41, 3365–3369. doi: 10.1016/S0032-3861(99)00535-2

Suk, J., Lee, Y. H., Kim, D. Y., Kim, D. W., Cho, S. Y., Kim, J. M., et al. (2016). Semi-interpenetrating solid polymer electrolyte based on thiol-ene cross-linker for all-solid-state lithium batteries. *J. Power Sources* 334, 154–161. doi: 10.1016/j.jpowsour.2016.10.008

Sun, C., Liu, J., Gong, Y., Wilkinson, D. P., and Zhang, J. (2017). Recent advances in all-solid-state rechargeable lithium batteries. *Nano Energy* 33, 363–386. doi: 10.1016/j.nanoen.2017.01.028

Tan, R., Gao, R., Zhao, Y., Zhang, M., Xu, J., Yang, J., et al. (2016). Novel organic–inorganic hybrid electrolyte to enable $LiFePO_4$ Quasi-solid-state Li-Ion batteries performed highly around room temperature. *ACS Appl. Mater. Interf.* 8, 31273–31280. doi: 10.1021/acsami.6b09008

Tao, X., Liu, Y., Liu, W., Zhou, G., Zhao, J., Lin, D., et al. (2017). Solid-state lithium–sulfur batteries operated at 37 °C with composites of nanostructured $Li_7La_3Zr_2O_{12}$/Carbon foam and polymer. *Nano Lett.* 17, 2967–2972. doi: 10.1021/acs.nanolett.7b00221

Thangadurai, V., and Weppner, W. (2006). Recent progress in solid oxide and lithium ion conducting electrolytes research. *Ionics* 12, 81–92. doi: 10.1007/s11581-006-0013-7

Tominaga, Y., Asai, S., Sumita, M., Panero, S., and Scrosati, B. (2005). Fast ionic conduction in PEO-based composite electrolyte filled with ionic liquid-modified mesoporous silica. *Electrochem. Solid State Lett.* 8:A22. doi: 10.1149/1.1828354

Tominaga, Y., and Endo, M. (2013). Ion-conductive properties of polyether-based composite electrolytes filled with mesoporous silica, alumina and titania. *Electrochim. Acta* 113, 361–365. doi: 10.1016/j.electacta.2013.09.117

Varzi, A., Raccichini, R., Passerini, S., and Scrosati, B. (2016). Challenges and prospects of the role of solid electrolytes in the revitalization of lithium metal batteries. *J. Mater. Chem. A* 4, 17251–17259. doi: 10.1039/C6TA07384K

Wang, A., Xu, H., Zhou, Q., Liu, X., Li, Z., Gao, R., et al. (2016). A new all-solid-state hyperbranched star polymer electrolyte for lithium Ion batteries: synthesis and electrochemical properties. *Electrochim. Acta* 212, 372–379. doi: 10.1016/j.electacta.2016.07.003

Wang, T., Zhang, R., Wu, Y., Zhu, G., Hu, C., Wen, J., et al. (2020). Engineering a flexible and mechanically strong composite electrolyte for solid-state lithium batteries. *J. Energy Chem.* 46, 187–190. doi: 10.1016/j.jechem.2019.10.010

Wang, X., Kerr, R., Chen, F., Goujon, N., Pringle, J. M., Mecerreyes, D., et al. (2020). Toward high-energy-density lithium metal batteries: opportunities and challenges for solid organic electrolytes. *Adv. Mater.* 32:e1905219. doi: 10.1002/adma.201905219

Wang, X., Zhai, H., Qie, B., Cheng, Q., Li, A., Borovilas, J., et al. (2019). Rechargeable solid-state lithium metal batteries with vertically aligned ceramic nanoparticle/polymer composite electrolyte. *Nano Energy* 60, 205–212. doi: 10.1016/j.nanoen.2019.03.051

Wang, X., Zhang, Y., Zhang, X., Liu, T., Lin, Y.-H., Li, L., et al. (2018). Lithium-salt-rich PEO/$Li_{0.3}La_{0.557}TiO_3$ interpenetrating composite electrolyte with three-dimensional ceramic nano-backbone for all-solid-state lithium-Ion batteries. *ACS Appl. Mater. Interf.* 10, 24791–24798. doi: 10.1021/acsami.8b06658

Wang, X.-L., Mei, A., Li, M., Lin, Y., and Nan, C.-W. (2006). Effect of silane-functionalized mesoporous silica SBA-15 on performance of PEO-based composite polymer electrolytes. *Solid State Ionics* 177, 1287–1291. doi: 10.1016/j.ssi.2006.06.016

Wang, Y., Fan, F., Agapov, A. L., Saito, T., Yang, J., Yu, X., et al. (2014). Examination of the fundamental relation between ionic transport and segmental relaxation in polymer electrolytes. *Polymer* 55, 4067–4076. doi: 10.1016/j.polymer.2014.06.085

Wang, Y.-J., Pan, Y., and Kim, D. (2006). Conductivity studies on ceramic $Li_{1.3}Al_{0.3}Ti_{1.7}(PO_4)_3$-filled PEO-based solid composite polymer electrolytes. *J. Power Sources* 159, 690–701. doi: 10.1016/j.jpowsour.2005.10.104

Wang, Z., Huang, X., and Chen, L. (2003). Understanding of effects of nano-Al_2O_3 particles on ionic conductivity of composite polymer electrolytes. *Electrochem. Solid State Lett.* 6:E40. doi: 10.1149/1.1615352

Wen, Z., Itoh, T., Ichikawa, Y., Kubo, M., and Yamamoto, O. (2000). Blend-based polymer electrolytes of poly(ethylene oxide) and hyperbranched poly[bis(triethylene glycol)benzoate] with terminal acetyl groups. *Solid State Ionics* 134, 281–289. doi: 10.1016/S0167-2738(00)00707-4

Wen, Z., Itoh, T., Uno, T., Kubo, M., and Yamamoto, O. (2003). Thermal, electrical, and mechanical properties of composite polymer electrolytes based on cross-linked poly(ethylene oxide-co-propylene oxide) and ceramic filler. *Solid State Ionics* 160, 141–148. doi: 10.1016/S0167-2738(03)00129-2

Weston, J. E., and Steele, B. C. H. (1982). Effects of inert fillers on the mechanical and electrochemical properties of lithium salt-poly(ethylene oxide) polymer electrolytes. *Solid State Ionics* 7, 75–79. doi: 10.1016/0167-2738(82)90072-8

Wieczorek, W., Florjanczyk, Z., and Stevens, J. R. (1995). Composite polyether based solid electrolytes. *Electrochim. Acta* 40, 2251–2258. doi: 10.1016/0013-4686(95)00172-B

Wieczorek, W., Stevens, J. R., and Florjañczyk, Z. (1996). Composite polyether based solid electrolytes. The Lewis acid-base approach. *Solid State Ionics* 85, 67–72. doi: 10.1016/0167-2738(96)00042-2

Wright, P. V. (1975). Electrical conductivity in ionic complexes of poly(ethylene oxide). *Br. Polym. J.* 7, 319–327. doi: 10.1002/pi.4980070505

Xi, J., Miao, S., and Tang, X. (2004). Selective transporting of lithium Ion by shape selective molecular sieves ZSM-5 in PEO-based composite polymer electrolyte. *Macromolecules* 37, 8592–8598. doi: 10.1021/ma048849d

Xiao, Y., Wang, Y., Bo, S.-H., Kim, J. C., Miara, L. J., and Ceder, G. (2020). Understanding interface stability in solid-state batteries. *Nat. Rev. Mater.* 5, 105–126. doi: 10.1038/s41578-019-0157-5

Xu, X., Wen, Z., Gu, Z., Xu, X., and Lin, Z. (2004). Lithium ion conductive glass ceramics in the system $Li_{1.4}Al_{0.4}(Ge1\text{-}xTi_x)1.6(PO_4)_3$ (x=0–1.0). *Solid State Ionics* 171, 207–213. doi: 10.1016/j.ssi.2004.05.009

Xu, X., Wen, Z., Yang, X., Zhang, J., and Gu, Z. (2006). High lithium ion conductivity glass-ceramics in Li_2O–Al_2O_3–TiO_2–P_2O_5 from nanoscaled glassy powders by mechanical milling. *Solid State Ionics* 177, 2611–2615. doi: 10.1016/j.ssi.2006.04.010

Xue, Z., He, D., and Xie, X. (2015). Poly(ethylene oxide)-based electrolytes for lithium-ion batteries. *J. Mater. Chem. A* 3, 19218–19253. doi: 10.1039/C5TA03471J

Yan, C., Zhu, P., Jia, H., Du, Z., Zhu, J., Orenstein, R., et al. (2020). Garnet-rich composite solid electrolytes for dendrite-free, high-rate, solid-state lithium-metal batteries. *Energy Storage Mater.* 26, 448–456. doi: 10.1016/j.ensm.2019.11.018

Yan, C., Zhu, P., Jia, H., Zhu, J., Selvan, R. K., Li, Y., et al. (2019). High-performance 3-D fiber network composite electrolyte enabled with Li-Ion conducting nanofibers and amorphous PEO-based cross-linked polymer for ambient all-solid-state lithium-metal batteries. *Adv. Fiber Mater.* 1, 46–60. doi: 10.1007/s42765-019-00006-x

Yang, C. R., Perng, J. T., Wang, Y. Y., and Wan, C. C. (1996). Conductive behaviour of lithium ions in polyacrylonitrile. *J. Power Sources* 62, 89–93. doi: 10.1016/S0378-7753(96)02414-7

Yang, H., and Yetter, W. (1994). Miscibility studies of high Tg polyester and polycarbonate blends. *Polymer* 35, 2417–2421. doi: 10.1016/0032-3861(94)90781-1

Yang, T., Zheng, J., Cheng, Q., Hu, Y.-Y., and Chan, C. K. (2017). Composite polymer electrolytes with $Li_7La_3Zr_2O_{12}$ garnet-type nanowires as ceramic fillers: mechanism of conductivity enhancement and role of doping and morphology. *ACS Appl. Mater. Interf.* 9, 21773–21780. doi: 10.1021/acsami.7b03806

Yanilmaz, M., Lu, Y., Zhu, J., and Zhang, X. (2016). Silica/polyacrylonitrile hybrid nanofiber membrane separators via sol-gel and electrospinning techniques for lithium-ion batteries. *J. Power Sources* 313, 205–212. doi: 10.1016/j.jpowsour.2016.02.089

Yue, L., Ma, J., Zhang, J., Zhao, J., Dong, S., Liu, Z., et al. (2016). All solid-state polymer electrolytes for high-performance lithium ion batteries. *Energy Storage Mater.* 5, 139–164. doi: 10.1016/j.ensm.2016.07.003

Zha, W., Chen, F., Yang, D., Shen, Q., and Zhang, L. (2018). High-performance $Li_{6.4}La_3Zr_{1.4}Ta_{0.6}O_{12}$/Poly(ethylene oxide)/Succinonitrile composite electrolyte for solid-state lithium batteries. *J. Power Sources* 397, 87–94. doi: 10.1016/j.jpowsour.2018.07.005

Zhai, H., Xu, P., Ning, M., Cheng, Q., Mandal, J., and Yang, Y. (2017). A flexible solid composite electrolyte with vertically aligned and connected Ion-conducting nanoparticles for lithium batteries. *Nano Lett.* 17, 3182–3187. doi: 10.1021/acs.nanolett.7b00715

Zhang, C., Feng, Y., Han, Z., Gao, S., Wang, M., and Wang, P. (2019). Electrochemical and structural analysis in all-solid-state lithium batteries by analytical electron microscopy: progress and perspectives. *Adv. Mater.* 29:e1903747. doi: 10.1002/adma.201903747

Zhang, H., Li, C., Piszcz, M., Coya, E., Rojo, T., Rodriguez-Martinez, L. M., et al. (2017). Single lithium-ion conducting solid polymer electrolytes: advances and perspectives. *Chem. Soc. Rev.* 46, 797–815. doi: 10.1039/C6CS00491A

Zhang, J., Zang, X., Wen, H., Dong, T., Chai, J., Li, Y., et al. (2017). High-voltage and free-standing poly(propylene carbonate)/$Li_{6.75}La_3Zr_{1.75}Ta_{0.25}O_{12}$ composite solid electrolyte for wide temperature range and flexible solid lithium ion battery. *J. Mater. Chem. A* 5, 4940–4948. doi: 10.1039/C6TA10066J

Zhang, J., Zheng, C., Lou, J., Xia, Y., Liang, C., Huang, H., et al. (2019). Poly(ethylene oxide) reinforced Li6PS5Cl composite solid electrolyte for all-solid-state lithium battery: enhanced electrochemical performance, mechanical property and interfacial stability. *J. Power Sources* 412, 78–85. doi: 10.1016/j.jpowsour.2018.11.036

Zhang, W., Nie, J., Li, F., Wang, Z. L., and Sun, C. (2018). A durable and safe solid-state lithium battery with a hybrid electrolyte membrane. *Nano Energy* 45, 413–419. doi: 10.1016/j.nanoen.2018.01.028

Zhang, Y., Chen, R., Wang, S., Liu, T., Xu, B., Zhang, X., et al. (2020). Free-standing sulfide/polymer composite solid electrolyte membranes with high conductance for all-solid-state lithium batteries. *Energy Storage Mater.* 25, 145–153. doi: 10.1016/j.ensm.2019.10.020

Zhao, Q., Stalin, S., Zhao, C.-Z., and Archer, L. A. (2020). Designing solid-state electrolytes for safe, energy-dense batteries. *Nat. Rev. Mater.* 5, 229–252. doi: 10.1038/s41578-019-0165-5

Zhao, Y., Huang, Z., Chen, S., Chen, B., Yang, J., Zhang, Q., et al. (2016a). A promising PEO/LAGP hybrid electrolyte prepared by a simple method for all-solid-state lithium batteries. *Solid State Ionics* 295, 65–71. doi: 10.1016/j.ssi.2016.07.013

Zhao, Y., Wu, C., Peng, G., Chen, X., Yao, X., Bai, Y., et al. (2016b). A new solid polymer electrolyte incorporating Li10GeP2S12 into a polyethylene oxide matrix for all-solid-state lithium batteries. *J. Power Sources* 301, 47–53. doi: 10.1016/j.jpowsour.2015.09.111

Zheng, F., Kotobuki, M., Song, S., Lai, M. O., and Lu, L. (2018). Review on solid electrolytes for all-solid-state lithium-ion batteries. *J. Power Sources* 389, 198–213. doi: 10.1016/j.jpowsour.2018.04.022

Zheng, J., and Hu, Y.-Y. (2018). New insights into the compositional dependence of Li-Ion transport in polymer–ceramic composite electrolytes. *ACS Appl. Mater. Interf.* 10, 4113–4120. doi: 10.1021/acsami.7b17301

Zheng, J., Tang, M., and Hu, Y. Y. (2016). Lithium ion pathway within $Li_7La_3Zr_2O_{12}$−polyethylene oxide composite electrolytes. *Angewandte Chem. Int. Ed.* 55, 12538–12542.

Zheng, J., Wang, P., Liu, H., and Hu, Y.-Y. (2019). Interface-enabled Ion conduction in $Li_{10}GeP_2S_{12}$–Poly(ethylene Oxide) hybrid electrolytes. *ACS Appl. Energy Mater.* 2, 1452–1459. doi: 10.1021/acsaem.8b02008

Zhou, D., He, Y.-B., Liu, R., Liu, M., Du, H., Li, B., et al. (2015). In situ synthesis of a hierarchical all-solid-state electrolyte based on nitrile materials for high-performance lithium-Ion batteries. *Adv. Energy Mater.* 5:1500353. doi: 10.1002/aenm.201500353

Zhou, D., Liu, R., Zhang, J., Qi, X., He, Y.-B., Li, B., et al. (2017). In situ synthesis of hierarchical poly(ionic liquid)-based solid electrolytes for high-safety lithium-ion and sodium-ion batteries. *Nano Energy* 33, 45–54. doi: 10.1016/j.nanoen.2017.01.027

Zhu, J., Chen, C., Lu, Y., Ge, Y., Jiang, H., Fu, K., et al. (2015). Nitrogen-doped carbon nanofibers derived from polyacrylonitrile for use as anode material in sodium-ion batteries. *Carbon* 94, 189–195. doi: 10.1016/j.carbon.2015.06.076

Zhu, J., Chen, C., Lu, Y., Zang, J., Jiang, M., Kim, D., et al. (2016a). Highly porous polyacrylonitrile/graphene oxide membrane separator exhibiting excellent anti-self-discharge feature for high-performance lithium–sulfur batteries. *Carbon* 101, 272–280. doi: 10.1016/j.carbon.2016.02.007

Zhu, J., Ge, Y., Kim, D., Lu, Y., Chen, C., Jiang, M., et al. (2016b). A novel separator coated by carbon for achieving exceptional high performance lithium-sulfur batteries. *Nano Energy* 20, 176–184. doi: 10.1016/j.nanoen.2015.12.022

Zhu, J., Lee, C.-H., Joh, H.-I., Kim, H. C., and Lee, S. (2012). Synthesis and properties of polyimide composites containing graphene oxide via in-situ polymerization. *Carbon Lett.* 13, 230–235.

Zhu, J., Lim, J., Lee, C.-H., Joh, H.-I., Kim, H. C., Park, B., et al. (2014). Multifunctional polyimide/graphene oxide composites via *in situ* polymerization. *J. Appl. Polymer Sci.* 131:40177. doi: 10.1002/app.40177

Zhu, J., Lu, Y., Chen, C., Ge, Y., Jasper, S., Leary, J. D., et al. (2016c). Porous one-dimensional carbon/iron oxide composite for rechargeable lithium-ion batteries with high and stable capacity. *J. Alloys Compounds* 672, 79–85. doi: 10.1016/j.jallcom.2016.02.160

Zhu, J., Yanilmaz, M., Fu, K., Chen, C., Lu, Y., Ge, Y., et al. (2016d). Understanding glass fiber membrane used as a novel separator for lithium–sulfur batteries. *J. Membr. Sci.* 504, 89–96. doi: 10.1016/j.memsci.2016.01.020

Zhu, J., Yildirim, E., Aly, K., Shen, J., Chen, C., Lu, Y., et al. (2016e). Hierarchical multi-component nanofiber separators for lithium polysulfide capture in lithium–sulfur batteries: an experimental and molecular modeling study. *J. Mater. Chem. A* 4, 13572–13581. doi: 10.1039/C6TA04577D

Zhu, J., Zhu, P., Yan, C., Dong, X., and Zhang, X. (2019). Recent progress in polymer materials for advanced lithium-sulfur batteries. *Prog. Polym. Sci.* 90, 118–163. doi: 10.1016/j.progpolymsci.2018.12.002

Zhu, P., Yan, C., Dirican, M., Zhu, J., Zang, J., Selvan, R. K., et al. (2018a). $Li_{0.33}La_{0.557}TiO_3$ ceramic nanofiber-enhanced polyethylene oxide-based composite polymer electrolytes for all-solid-state lithium batteries. *J. Mater. Chem. A* 6, 4279–4285. doi: 10.1039/C7TA10517G

Zhu, P., Yan, C., Zhu, J., Zang, J., Li, Y., Jia, H., et al. (2019). Flexible electrolyte-cathode bilayer framework with stabilized interface for room-temperature all-solid-state lithium-sulfur batteries. *Energy Storage Mater.* 17, 220–225. doi: 10.1016/j.ensm.2018.11.009

Zhu, P., Zang, J., Zhu, J., Lu, Y., Chen, C., Jiang, M., et al. (2018b). Effect of reduced graphene oxide reduction degree on the performance of polysulfide rejection in lithium-sulfur batteries. *Carbon* 126, 594–600. doi: 10.1016/j.carbon.2017.10.063

Zhu, P., Zhu, J., Yan, C., Dirican, M., Zang, J., Jia, H., et al. (2018c). In situ polymerization of nanostructured conductive polymer on 3D sulfur/carbon nanofiber composite network as cathode for high-performance lithium–sulfur batteries. *Adv. Mater. Interf.* 5:1701598. doi: 10.1002/admi.201701598

Conflict of Interest: The authors declare that the research was conducted in the absence of any commercial or financial relationships that could be construed as a potential conflict of interest.

frontiers in Energy Research

MINI REVIEW
published: 04 September 2020
doi: 10.3389/fenrg.2020.585795

Application of Carbon Nanotube-Based Materials as Interlayers in High-Performance Lithium-Sulfur Batteries: A Review

Huijie Wei[1], Yong Liu[1,2], Xiaoliang Zhai[1], Fei Wang[1], Xinyuan Ren[3], Feng Tao[1], Tengfei Li[1], Guangxin Wang[1] and Fengzhang Ren[1]**

[1] Provincial and Ministerial Co-construction of Collaborative Innovation Center for Non-ferrous Metal New Materials and Advanced Processing Technology, Henan Key Laboratory of Non-Ferrous Materials Science and Processing Technology, School of Materials Science and Engineering, Henan University of Science and Technology, Luoyang, China, [2] National Joint Engineering Research Center for Abrasion Control and Molding of Metal Materials, Henan Key Laboratory of High-Temperature Structural and Functional Materials, Henan University of Science and Technology, Luoyang, China, [3] School of Art and Design, Henan University of Science and Technology, Luoyang, China

OPEN ACCESS

Edited by:
Kai Zhu,
Harbin Engineering University, China

Reviewed by:
Yan-Bing He,
Tsinghua University, China
Xunhui Xiong,
South China University of Technology, China
Hongshuai Hou,
Central South University, China

***Correspondence:**
Yong Liu
liuyong209@haust.edu.cn
Fengzhang Ren
renfz@haust.edu.cn

Specialty section:
This article was submitted to Electrochemical Energy Conversion and Storage, a section of the journal Frontiers in Energy Research

Received: 21 July 2020
Accepted: 14 August 2020
Published: 04 September 2020

Citation:
Wei H, Liu Y, Zhai X, Wang F, Ren X, Tao F, Li T, Wang G and Ren F (2020) Application of Carbon Nanotube-Based Materials as Interlayers in High-Performance Lithium-Sulfur Batteries: A Review. Front. Energy Res. 8:585795. doi: 10.3389/fenrg.2020.585795

With the ever-increasing demands of electrochemical energy storage, lithium–sulfur (Li–S) batteries have drawn more attention because of their superior theoretical energy density and high specific capacity. However, practical applications of Li–S batteries suffer from problems such as low conductivity of sulfur and discharged products, severe polysulfide shuttling effect, and large volume change of sulfur during cycling, resulting in sluggish rate performance, and unsatisfactory cycle life. Various nanostructured carbon materials have been served as barrier layers to overcome these problems. In particular, carbon nanotubes (CNTs) with unique 1D nanostructure, have been introduced to Li–S batteries as the intermediate layers because of its superior flexibility, excellent electrical conductivity, and good chemical stability. Moreover, CNTs and CNTs-based barrier layers could also curb lithium polysulfides shuttling. In the minireview, we summarize recent works of CNTs-based materials as modifying interlayers for Li–S batteries. In addition, the strategies to enhance electrochemical performances of the batteries are summarized and discussed. Finally, the challenges and prospects for future research of CNTs-based materials as interlayer are proposed. We hope this review will be useful for designing and fabricating high-performance Li–S batteries and boost their practical applications.

Keywords: lithium–sulfur batteries, carbon nanotubes, CNTs-based materials, interlayer, lithium polysulfides

INTRODUCTION

Nowadays, electric energy storage technology and equipment are gradually becoming a critical issue with the development of society (Wang F. et al., 2018; Wang R. et al., 2020; Liu et al., 2019a,b; Wu et al., 2019a; Zhao X. et al., 2019; Zhao et al., 2020; Li et al., 2020f; Ma et al., 2020b; Pan K. et al., 2020). In recent years, various electrochemical energy storage systems have been extensively studied (Ma et al., 2013, 2017, 2019; Luo et al., 2017; Chen H. et al., 2018; Guo et al., 2019, 2020; Liu et al., 2019c, 2020; Song C. et al., 2020; Wang F. et al., 2020; Yu et al., 2020; Zou P. et al., 2020). Among them, Li–S batteries have become one of the most promising candidates for next-generation electrochemical energy storage owing to their high theoretical specific capacity (1675 mAh g^{-1}) and superior theoretical specific

energy density (2600 Wh Kg^{-1}), together with non-toxicity, low cost and environmental friendliness of sulfur (Yu et al., 2018; Gao et al., 2020).

However, there are some challenges for Li–S batteries to overcome, including the electrical insulating characteristic of sulfur and the discharge product (Li_2S_2/Li_2S), the large volumetric change of sulfur during the charge/discharge process (approximately 80%), as well as the notorious shuttle effect caused by dissolved lithium polysulfides (LiPSs) (Huang et al., 2015; Cao et al., 2019; Chen Y.T. et al., 2019).

To address these problems, researchers have made considerable effort with regard to cathode and separator modification (Wang X. et al., 2019; Wei et al., 2019; Li et al., 2020a), optimization of electrolytes (Ding et al., 2016), and lithium metal anode protection and stabilization (Paolella et al., 2019; Pei et al., 2019). Among them, the interlayers could selectively control the shuttle effect of polysulfides, while not disturbing the Li^+ transfer. As a superior type of carbon material, carbon nanotubes (CNTs) have been intensively investigated as intermediate layers due to their excellent mechanical durability and high electrical conductivity as well as stable chemical properties. Together with other materials, CNTs-based interlayers are receiving considerable attentions for Li–S batteries in recent years (Wang et al., 2017; Jiang et al., 2018; Li et al., 2018; Son et al., 2019). For example, Yao M. et al. (2018) reported the multifunctional layer consisting of MnO_2 and multi-walled CNTs modified polypropylene (PP) separator could tightly attract polysulfides and promote the transfer of electrons and ions, which could enhance the electrochemical performance of Li–S batteries. Li et al. (2018) designed and constructed a MoS_2/CNTs interlayer to insert between separator and cathode, exhibited an optimized cycle performance and excellent rate capability. Some reviews also discussed recent developments on the interlayer materials for Li–S batteries. For instance, Chen et al. reviewed on interlayer design of Li–S batteries by coating and inserting different types of carbon-based materials (Chen L. et al., 2020). Furthermore, Jiao et al. reviewed recent articles regarding to the interlayers for Li–S batteries including carbon-based interlayers (Jiao et al., 2019); Pang and co-workers reviewed on recent research work on CNT-based materials for Li–S batteries (Zheng et al., 2019). However, there is still a lack of review to exclusively cover the state-of-the-art developments of CNTs-based interlayer materials for Li–S batteries.

Herein, we provide an overview on carbon nanotubes-based materials as inter-layers of Li–S batteries. Their nano/microstructure and electrochemical performances are summarized. In addition, some reasonable suggestion on their design and development are proposed to facilitate breakthroughs. We hope this review could attract more attentions to CNTs-based interlayer materials for Li–S batteries and boost their practical applications.

MWCNTs

CNTs can be regarded as the curled graphene sheets, and they could be classified into two catagories, including multi-walled CNTs (MWCNTs) and single-walled CNTs (SWCNTs) (Kumar S. et al., 2018; Ali et al., 2019). MWCNTs could be seen as the collection of multiple curled graphene sheets. Compared to SWCNTs, they are cheaper and easier to fabricate. Moreover, they remains the merits of high conductivity, low thermal expansion coefficient and stable structure (Zheng et al., 2019). For interlayers for Li–S batteries, MWCNTs are used mainly in two ways, (1) as the coating layer on separator (Cheng et al., 2016; Wang J. et al., 2018); (2) as the self-supporting film (Kim H.M. et al., 2016; Wang X. et al., 2020). The electrochemical performances of Li–S batteries with MWCNTs-based interlayers are summarized in **Table 1**.

Separator-Based Interlayer

As an essential part of Li–S batteries, separators could separate the cathode and anode and prevent the internal short circuit. However, the pore size (∼100 nm) of commercial separators is much larger than the average size of long-chained polysulfides, which may cause the soluble polysulfides to easily migrate to the anodes, leading to notorious shuttle effect (Li et al., 2020d). To prevent the shuttling of dissolved polysulfides, various MWCNTs-based materials have been developed to modify separators to provide physical entrapment and chemical adsorption for LiPSs, enhancing the electrochemical performances of Li–S batteries (Chang et al., 2015; Tan et al., 2018; Li et al., 2019e; Xiang et al., 2019).

Pure MWCNTs

As the most common CNT materials, MWCNTs have been intensively applied as interlayer coated on separator for Li–S batteries. For example, Chung and Manthiram (2014) developed a MWCNT-coated separator as a barrier to anchor dissolved LiPSs, as shown in **Figure 1A**. The MWCNTs layer not only act as an upper current collector for rapidly electron transport and high sulfur utilization but also serve as a filter to trap and adsorb LiPSs. Meanwhile, the porous network of MWCNTs layer is conducive to electrolyte infiltration and electron/ion diffusion. Hence, the cell with MWCNTs-coated separator exhibited a superior long-term cycling performance. After 150 cycles, the cell with MWCNT layer delivered a specific capacity of 881, 809, and 798 mAh g^{-1} at 0.2, 0.5, and 1 C, respectively. After that, researchers have paid more attention on carbon nanotubes modified separator to improve the performance of Li–S batteries. For instance, Ponraj et al. (2017) synthesized a hydroxyl-functionalized carbon nanotube (CNTOH) coated on the separator, which could address the poor electronic conductivity of active materials and mitigate the diffusion and migration of LiPSs in Li–S batteries owing to the good conductivity and hydroxyl groups of CNTOH.

MWCNTs-Based Composites

Nano-composite materials normally have a better performance than single-component materials due to the synergistic effect of different components, which have attracted extensive attention from researchers in recent years (Luo Y. et al., 2018; Guan B. et al., 2019; Kim et al., 2020; Ma et al., 2020a; Wang W. et al., 2020). Many types of MWCNTs-based composites,

TABLE 1 | Electrochemical performance of Li–S batteries employing CNT-based materials as interlayer.

Materials	Mass load (mg cm^{-2})	Sulfur contents (wt%)/loading (mg cm^{-2})	Current density	Cycle number	Initial capacity (mAh g^{-1})	Post-cycle capacity (mAh g^{-1})	References
Modify separator							
MWCNT	0.17	70/2	C/5	150	1324	881	Chung and Manthiram, 2014
DWCNT	0.00477	60/1.5–2	0.1 C	100	598	508	Sun et al., 2020
o-MWCNT	0.4	90/5	0.1 A g^{-1}	50	1105	925	Cheng et al., 2016
PAN/SiO_2-MWCNT	3.44	70/1–1.2	0.2 C	100	1182	741	Zhu et al., 2016
MWCNT/GO/MWCNT	0.23	70/7	0.2 C	200	1290	620	Chang et al., 2017
CNT	–	–/–	1 C	500	684	361	Liu et al., 2017
aCNT	∼0.15	67/1.5	0.5 C	500	1306	621	Huang et al., 2018
CNTOH	1.34	70/3	0.5 C	400	1056	∼591	Ponraj et al., 2017
OCNT	–	-/1.5	0.5 C	400	1034.9	∼732	Kim et al., 2018
CNT	(5	80/1.3	1 C	200	968	∼670	Manoj et al., 2018a
AB/MWCNT	–	70/3.2	1.6 A g^{-1}	200	1500	662	Tian et al., 2018
CNT/PVP	0.4	70/1–1.2	0.1 C	100	1226	887	Li et al., 2019c
Ni@NG-CNTs	0.6	70/1–1.2	1 C	800	1144.2	655.5	Zuo et al., 2019
Co-NCNTs	0.23	70/1.8	0.2 C	200	1251.4(20^{th})	857.7	Wei et al., 2020
SCL	0.25	70/1.35–1.55	1 C	400	1073	700.4	Geng et al., 2020
MoS_2@CNT	–	77.5/–	1 C	500	∼690	∼670	Jeong et al., 2017
Sb_2S_3/CNT	0.4	65/1.0	1 C	1000	∼720	373	Yao S. et al., 2018
SnS_2/CNT	0.4	78/1.4	2 C	800	∼782	555	Jiang et al., 2019
NSCNTs/MoS2	0.5	88.3/2.2	1 C	1000	1024	814	Xiang et al., 2019
SWCNT	0.13	80/3.0	0.2 C	100	953	713	Chang et al., 2016
PANiNF/MWCNT	0.01	60/1.4	0.2 C	100	1020	709	Chang et al., 2015
MCNT@PEG	0.26	60/1.6	0.5 C	200	1283	727	Wang et al., 2015
MWCNT/PEG	0.12	78/6.5	0.2 C	300	1206	630	Luo et al., 2016
PEI/MWCNT)	–	75/1.1	2 C	300	819	∼590	Lee Y.-H. et al., 2018
PEDOT: PSS-CNT	–	80/–	0.2 C	–	950	–	Manoj et al., 2018b
PAMAM-CNTs	0.34	60/0.6–0.8	2 C	1200	1050	573	Li et al., 2020c
MWCNT/SPANI	0.4	72/5	0.1 A g^{-1}	100	∼1127	913	Shi et al., 2018
PDAAQ/K-FGF/MWCNT/CTAB	–	70/1.8	1 C	200	1361	968	Kiai and Kizil, 2019
CNT/AC	–	70/–	0.2 C	200	1495.6	742	Guo et al., 2017
G@CNT	0.33	60/1.4	0.2 C	200	1231.3	935.1	Wu et al., 2017
CNT/CH	0.35	75/1.2	0.5 C	200	894	826	Jiang et al., 2018
MWCNT/NCQD	0.15	60/1.3–1.5	0.5 C	1000	1330.8	507.9	Pang et al., 2018
PC/MWCNT	0.51	70/1.6–1.7	0.5 C	200	911	659	Tan et al., 2018
G/CNT	0.17	75/1.7–2	0.5 C	100	∼913.5	813	Gao et al., 2019b
GO/CNT	–	60/1.1	0.2 C	50	1591.56	1003	Lee et al., 2019
EB	0.2	70/1.8	0.2 C	100	950 (25^{th})	980	Lu et al., 2019
Co/NCNS/CNT	0.2	80/2	2 C	1000	972.4	∼486	Song C.L. et al., 2020
CNT/Al_2O_3	–	60/1	0.2 C	100	1282	807.8	Xu Q. et al., 2015
Al_2O_3/CNT	–	70/1.0–1.2	0.2 C	100	1096	760.4	Chen X. et al., 2020
Fe_3O_4@C/CNTO	0.288	65/1.5	2 C	1000	∼833	335	Du et al., 2020
CNTs@FeOOH	–	55/0.8	3.2 A g^{-1}	350	1121.9	556	Li et al., 2020e
$MgBO_2$(OH)/CNT	0.3	70/1.1	0.5 C	200	924	785	Kong L. et al., 2017
CNT@TiO_2	0.7	66.4/1.7	0.1 C	200	1351	803	Yang et al., 2017
TiO_2/CNTs	0.3	70/1.5	1 C	250	1036.9	763	Guan Y. et al., 2019
MWCNTs @TiO_2	–	60/0.8–1.0	838 mA g^{-1}	600	1083	610	Ding et al., 2018
Ni-MOF/MWCNTs	0.36	60/1.58	0.5 C	300	1358	1183	Lee D.H. et al., 2018
CNT/ZrO_2	–	50/1.5	0.1 C	120	1207	685	Liu et al., 2018
MoO_3@CNT	0.577	60/1	0.3 C	200	1251	755	Luo L. et al., 2018
CNT/MoP_2	0.34	50/1.2	0.2 C	100	1223	905	Luo Y. et al., 2018

(Continued)

TABLE 1 | Continued

Materials	Mass load (mg cm^{-2})	Sulfur contents (wt%)/loading (mg cm^{-2})	Current density	Cycle number	Initial capacity (mAh g^{-1})	Post-cycle capacity (mAh g^{-1})	References
CNT@ZIF	0.9	70.2/1.2	0.2 C	100	1588.4	870.3	Wu et al., 2018
COF-CNT	–	80/2	1 A g^{-1}	500	1068	621	Wang J. et al., 2020
MoS_2/CNT	0.25	50/1.4	0.5 C	500	1237	648	Yan et al., 2018
MWCNTs/MnO_2	0.20–0.48	60/1,4	1 C	500	∼880	∼610	Yao M. et al., 2018
TiO_2/CNT	–	73/2	1 C	200	936	557	Chen A. et al., 2019
TiO_2/CNT	–	70/0.86	0.2 C	100	1247	627	Chen P. et al., 2020
TiS_2/CNT	0.6	69.7/2	0.5 C	100	1012	848	Pan S. et al., 2020
MWCNTs/CeO_2	0.15	60/1.8–2.0	0.2 C	300	898.3	520.7	Zhu et al., 2020
Sc_2O_3@CNT	0.17	65/1.5	1 C	500	1037	788	Xu et al., 2020
Co_2B@CNT	–	72.45/3.6	0.2 C	200	1430	1283	Guan B. et al., 2019
PCCNT/Ni_2P	0.8	78.8/1.1–1.2	1 C	500	1067	654.2	Guang et al., 2019
Ce-MOF/CNT	0.4	80/2.5	1 C	800	1021.8	838.8	Hong et al., 2019
CNTs/MXene	0.16	70/0.8–2.5	1 C	600	987	614	Li et al., 2019a
$Ti_3C_2T_x$/CNTs	0.016	70/1.2	1 C	200	760	640	Li et al., 2020b
TiO/MWCNT	0.7	60/1.4–1.6	0.5 C	200	1527.2	1033.8	Li et al., 2019e
Ta_2O_5/CNT-O	–	80/1.5	0.2 C	100	1230.7	932.6	Li et al., 2019f
CNTs/Fe_3O_4	0.38	72/1.4	1 C	1000	∼750	651	Sun et al., 2019b
MnO_2/CNT	0.35	70/0.8	1 C	500	843.7	∼574	Wang Y. et al., 2019
Co/NCNS/CNT	0.2	80/2	2 C	1000	972.4	434	Song C.L. et al., 2020
B-CNT	0.06	70/2.4–2.5	0.2 C	500	∼675	509	Chung et al., 2016
Gr-CNT-Ni	0.2	64/7.68	0.2 C	100	849	549	Kumar G.G. et al., 2018
W-V_2O_5-G/CNT	0.11	75/1.7–2	0.5 C	200	∼910	815	Gao et al., 2019a
HfO_2/CNT	0.087	75/1.80–2.22	1 C	500	∼1060	721	Kong et al., 2018
ACNTs	–	90/2.2–2.5	0.5 C	1400	897	713	Chen M. et al., 2018
Freestanding interlayer							
MWCNT/RGO	1	70/1.5–1.8	1 C	350	908	611	Sun et al., 2018
MWCNT	0.83–1.1	70/–	0.2 C	50	∼1420	962	Su and Manthiram, 2012
GF/CNT	0.54	70/1.6	0.2 C	230	1111.7	802.8	Lee and Kim, 2015
DF/PCW	–	56/1.8–2.7	1 C	100	1113	1040.6	Hwang et al., 2016
MWCNT	1.95	80/3	0.5 C	100	851	∼664	Kim H.M. et al., 2016
CNT	∼0.256	60/–	0.5 C	500	872	460	Sun et al., 2016
CNTs	1.0	70/0.974	0.25 C	100	1658	556	Li et al., 2017
CNT	0.45	45/4	0.5 C	80	∼1160	981	Xie et al., 2017
CNTs	1	-/3	1 C	200	943	802	Peng et al., 2019
SMAP	–	70/–	1 C	200	849	806	Rui et al., 2019
C-C-N-Co	0.45	70/1	0.5 C	100	∼1060	787	Li et al., 2020g
UPHC	–	60/1.5–2.0	0.5 C	300	704.5	608.8	Wang X. et al., 2020
SWCNT	–	70/–	0.1 C	50	1674	1052	Kaiser et al., 2015
PAA-SWNT	0.82	65/2.7	1 C	200	∼770	573	Kim J.H. et al., 2016
SWCNT	1	50/1.0–1.2	0.8 A g^{-1}	1500	1034	408	Jin et al., 2018
SWCNT/rGO	0.1	60/1	1 A g^{-1}	80	773	∼605	Hao J. et al., 2019
PEDOT:PSS-CNT	0.7	60/2	0.5 C	50	793	690	Wang et al., 2017
GO/CNT	1.1	70/1	0.2 C	300	1370	671	Huang et al., 2016
CNTs/RGO	0.34	70/2	4 C	600	∼765	597	Liu et al., 2016
MWCNTs/RGO	1	70/1.5–1.8	0.2 C	100	1224	854	Sun et al., 2018
CNTF	5–7.6	80/1.3	1 C	200	542	384	Manoj et al., 2019
G/CNT	0.2	50/2.46	2 C	500	∼460	445	Shi et al., 2019
CNTP/TiO_2	–	70/0.98	0.5 C	250	∼1575	575.8	Xu G. et al., 2015
G/M@CNT	0.104	60–80/1.11–1.37	1 C	2500	∼1065	293	Kong W. et al., 2017
MoS_2/CNTP	0.04	70/3.4	0.5 C	100	1233	850	Li et al., 2018
CNF@VS_2/CNT@GN	1.9	60/1	1 C	1145	1138.4	605	Wang L. et al., 2018

(Continued)

TABLE 1 | Continued

Materials	Mass load (mg cm^{-2})	Sulfur contents (wt%)/loading (mg cm^{-2})	Current density	Cycle number	Initial capacity (mAh g^{-1})	Post-cycle capacity (mAh g^{-1})	References
Fe_3C-C-CNTs	–	–/1.5	0.2 C	100	1243	870.2	Wang S. et al., 2020
CeF_3/CNTs	0.8–2	90/1.2–1.4	0.2 C	100	1015	951	Zou K. et al., 2020
Pd_3Co/MWCNTs	–	60/1	2 C	300	953	752	Cho et al., 2019
Pt@CNT	–	60/0.7	0.5 C	400	1120	660	Ding et al., 2019
MWCNTs-OH	–	70/2–2.3	1 C	500	601	516	Huang et al., 2019
MTO-CNT	0.06	65/1.1–3	0.5 C	500	931.7	634.6	Li et al., 2019b
SiO_2/AP	–	87/–	1 C	200	∼1087	1039	Li et al., 2019d
BTO/C	–	60/0.94	0.2 C	200	∼1201	908	Son et al., 2019
ZnO/CNT/RGO	0.85	–/1.7	0.2 C	150	1061	768	Sun et al., 2019a

o-MWCNT, oxidized multiwall carbon nanotube; PAN/SiO_2-MWCNT, poly-acrylonitrile/silica-MWCNT; aCNT, activated carbon nanotube; AB/MWCNT, acetylene black/MWCNT; SCL, sandwich-structure composite carbon layer (a N-doped mesoporous carbon sandwiched between two carbon nanotube); NSCNTs/MoS_2, nitrogen and sulfur codoped carbon nanotubes/MoS_2; SWCNT, single-walled carbon nanotube; MWCNT/PEG, MWCNT/polyethylene glycol; MWCNT/SPANI, MWCNT/sulfonated polyaniline; SMAP, nano-SnO_2/MWCNTs/aramid paper; PDAAQ/K-FGF/MWCNT/CTAB, poly 1,5-diaminoanthraquinone/potassium functionalized graphene/MWCNT/cetyltrimethyl-ammonium-bromide; CNT/AC, CNT/active carbon; PAMAM-CNTs, poly(amidoamine)-modified multiwalled carbon nanotubes; COF-CNT, Covalent organic frameworks-CNT; CNT/CH, CNT/chitosan; MWCNT/NCQD, MWCNT/N-doped carbon quantum dot; PC/MWCNT, porous carbon/MWCNT; EB, the mixture of H_xMnO_{2+x} nanosheets, graphene and CNTs; PCCNT/Ni_2P, P-doped carbon (PC) wrapped carbon nanotubes/Ni_2P; Ta_2O_5/CNT-O, Ta_2O_5/oxidized multi-walled carbon nanotubes; MTO-CNTs, mesoporous TiO_2-carbon nanotubes; Gr-CNT-Ni, graphene-CNT-nickel; C-C-N-Co, single-atom cobalt-anchored nitrogen-doped carbon nanosheets and dual network of carbon nanotube-cellulose nanofiber hybrid; UPHC, ultraviolet polymerized PVDF-HFP with the addition of MWCNTs; ACNTs, N, B, S tri-doped active carbon nanotubes; PEDOT:PSS-CNT, poly(3,4-ethylenedioxythiophene):polystyrene sulfonate–carbon nanotube; PAA-SWNT, poly(acrylic acid) coated single-walled carbon nanotube; CNTF, acid-functionalized carbon nanotubes; CNTP/TiO_2, carbon-nanotube paper/TiO_2; SiO_2/AP, nano-SiO_2 and multi-walled carbon nanotubes and aramid paper; BTO/C, $BaTiO_3$/CNT; NMC/CNT, N-doped mesoporous carbon/CNT; Co/NCNS/CNT, Co/nitrogen-doped carbon nanosheets/CNT. The symbol "-" in the table means that there is no relevant information in the reference.

such as MWCNTs/carbonaceous material composites, MWCNTs/polymer composites and MWCNTs/metal-based compound composites have been applied as interlayer coated on separator for Li–S batteries. For example, Pang et al. (2018) fabricated a MWCNT/N-doped carbon quantum dots (NCQDs) composites as coating layer onto the separator for Li–S batteries (**Figure 1B**). The NCQDs with large surface area and rich oxygenated functional groups could be regarded as an efficient adsorbent for LiPSs, meanwhile, MWCNTs are beneficial to enhance the conductivity of composites. Therefore, the cell with MWCNT/NCQDs-coated separators displayed an excellent electrochemical performance, as well as an average self-discharge value of ∼11% after resting for 48 h, which is lower than that with the pristine MWCNTs-modified separator (**Figure 1B**).

MWCNTs/Polymer composites have also been fabricated to trap LiPSs through physical obstructing and chemical bonding in Li–S batteries (Chang et al., 2015; Luo et al., 2016; Lee Y.-H. et al., 2018). For Lee Y.-H. et al. (2018) instance, developed a spiderweb separator consisting of three functional nanomats with good mechanical properties and excellent electrical conductivity. In this sandwich-type separator, MWCNT-wrapped polyetherimide (PEI/MWCNT) nanomats were used as the top and bottom layer, and the PVIm[TFSI]/poly(vinylidene fluoride-co-hexafluoropropylene) (PVDF-HFP) with a polyethylene (PE) nanomat was the middle layer (**Figure 1C**). When tested in Li–S batteries, the cell with this composites separator exhibited higher discharge capacity and more stable cycling performance than that with pristine PE separator (Lee Y.-H. et al., 2018).

Metal-based compounds are mainly including metal oxides (Ding et al., 2018; Luo L. et al., 2018), metal sulfides (Jeong et al., 2017; Xiang et al., 2019), metal phosphides (Luo Y. et al., 2018), metal borides (Guan B. et al., 2019), metal hydroxides (Kong L. et al., 2017) and metal-organic frameworks (MOFs) (Lee D.H. et al., 2018; Wu et al., 2018), which could offer a polar chemical interaction with LiPSs and curb polysulfides shuttling in Li–S batteries. For instance, Hong et al. (2019) fabricated cerium-MOFs/MWCNTs composites as coating material on separators for Li–S batteries at a high sulfur loading of 6 mg cm^{-2}, the cell with the modified separators could deliver an initial specific capacity of 993.5 mAh g^{-1} at 0.1 C, and the specific capacity of 886.4 mAh g^{-1} was retained after 200 cycles (**Figure 1D**). The superior electrochemical performance is ascribed that Ce-MOFs/MWCNTs can mitigate the transmission and diffusion of polysulfides and boost the efficient catalytic conversion of LiPSs, owing to their uniformly dispersed catalytic active sites and large specific surface area as well as good electronic conductivity. Yao S. et al. (2018) successfully exfoliated a 2D antimony sulfides (Sb_2S_3) sheets and combined them with MWCNTs (Sb_2S_3/MWCNTs) to modify the Celgard PP separator (**Figure 1E**). With Sb_2S_3/MWCNTs modified separator, the Li–S cell exhibited a low average capacity decay rate (∼0.049% per cycle after cycling 1000 cycles at 1 C), indicated that the Sb_2S_3/MWCNTs has a strong interaction with polysulfides which was confirmed by the first-principle calculation.

Free-Standing Interlayer

In addition to coating MWCNTs-based materials onto the separator to curb the shuttling of lithium polysulfides, another alternative strategy is to insert a self-supporting interlayer between the cathode and separator (Wang et al., 2017; Sun et al., 2018). The self-supported interlayers are usually much thicker than the modified-separators interlayers, and they are supposed

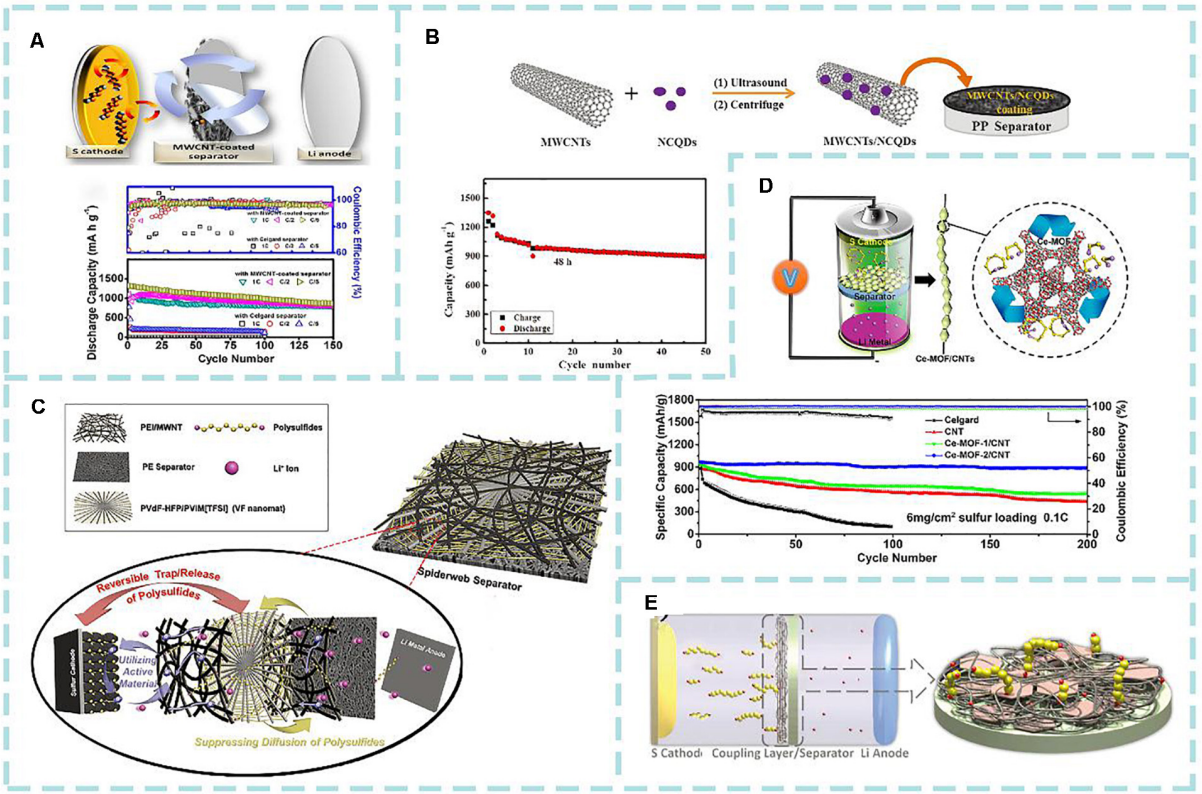

FIGURE 1 | (A) Mechanism of multi-walled carbon nanotubes (MWCNTs)-coated separator for Li–S batteries and the corresponding cycling performance; **(B)** Schematic diagram of MWCNTs/N-doped carbon quantum dots (MWCNTs/NCQDs)-coated separator preparation process and the cycle performance of the Li–S battery with MWCNTs/NCQDs-coated separator; **(C)** Schematic illustration of spiderweb separator and its application in Li–S batteries; **(D)** Scheme of Ce-MOFs/CNTs as coating materials in Li–S battery and the corresponding cyclic performance; **(E)** Schematic configuration of the Li–S cell with a Sb_2S_3/CNTs coated membrane. **(A)** Reproduced with permission. Chung and Manthiram (2014) Copyright 2014, American Chemical Society. **(B)** Reproduced with permission. Pang et al. (2018) Copyright 2018, Wiley-VCH. **(C)** Reproduced with permission. Lee Y.-H. et al. (2018) Copyright 2018, Wiley-VCH. **(D)** Reproduced with permission. Hong et al. (2019) Copyright 2019, American Chemical Society. **(E)** Reproduced with permission. Yao S. et al. (2018) Copyright 2018, Wiley-VCH.

to have the characteristics of strong chemical and/or physical adsorption toward polysulfides, good container for polysulfides and good electronic conductor. Also, the interlayer should allow smooth Li-ion diffusion. Therefore, with the insertion of interlayers, the LiPSs could be blocked at the cathode side, and the Li^+ diffusion and electron tranfer could also be promoted (Huang et al., 2016).

Pure MWCNTs

Because of intrinsic interweaving properties of CNTs, it is easy to prepare freestanding CNT interlayers with good flexibility and high porosity. Manthiram (Su and Manthiram, 2012) firstly fabricated a freestanding MWCNTs membrane by ultrasonic dispersion of synthesized MWCNTs, followed by a facile vacuum filtration (**Supplementary Figure S1A**). With the insertion of this freestanding interlayer, interfacial resistance in cathode was greatly reduced, and the intermediate polysulfides was efficiently localized at cathode side. The enhanced cycling performance of Li–S battery with MWCNTs interlayers could be ascribed that MWCNTs can prevent the undesirable migration and diffusion of polysulfides (Su and Manthiram, 2012). After that, many other interlayers based on MWCNTs have been explored for Li–S batteries (Lee and Kim, 2015; Sun et al., 2016). For instance, Kim H.M. et al. (2016) prepared a self-assembled MWCNTs membrane by mixing MWCNTs and electrolyte, followed by being applied to the top of sulfur electrode (**Supplementary Figure S1B**). The self-assembled MWCNTs membrane has more tightly interwoven structure and denser than bare MWCNTs interlayer. When tested in Li–S batteries, after 100 cycles at 0.5 C, the surface of the self-assembled MWCNTs interlayer only has tiny pores and more densely packed shape than that of bare MWCNTs interlayer. The enhanced electrochemical performance of the cell with self-assembled MWCNTs interlayer could be attributed to efficiently hinder polysulfide diffusion and enhance sulfur utilization through supplying polysulfide capturing sites (Kim H.M. et al., 2016).

MWCNTs-Based Composites

Owing to the abundance of functional groups, large specific surface area, and excellent electrical conductivity, graphene has attracted more interest in energy storage materials fields

(Wu et al., 2019b; Ma et al., 2020c; Sui et al., 2020). In Li–S batteries, many researchers combined graphene with MWCNTs as barrier materials to inhibit polysulfides migration (Sun et al., 2018; Shi et al., 2019). For instance, Huang et al. synthesized a freestanding graphene oxide/MWCNTs (GO/MWCNTs) film through combining MWCNTs with GO sheets (Huang et al., 2016), which exhibited high electronic conductivity and strong ability to immobilize LiPSs in Li–S batteries, resulting in improved electrochemical performance. The cell with GO/MWCNTs depicted an outstanding initial specific capacity of 1370 mAh g^{-1} at 0.1 C. After 300 cycles at 0.2 C, it still maintained a discharge capacity of 671 mAh g^{-1}, and the corresponding capacity decay rate was about 0.043% per cycle. More recently, Shi et al. (2019) reported a three-dimensional graphene/multi-walled carbon nanotube aerogels (G/MWCNTs) as self-supporting interlayer to improve the performance of Li–S cells. As displayed in **Supplementary Figure S1D**, this 3D G/MWCNTs aerogels with a 3D interconnected porous network were fabricated by the rapid reduction of graphene oxide/MWCNTs aerogel via self-propagating combustion. Cross-linked MWCNTs with graphene can give the membrane good mechanical flexibility and abundant pores, so that it can prevent the damage of interlayer during battery assembly and has more active sites to anchor polysulfides by chemical interaction and physical confinement.

In addition to combining with graphene, some researchers also combined MWCNTs with polar materials such as metal oxides (Xu G. et al., 2015; Kong W. et al., 2017; Kong et al., 2018; Li et al., 2019b), metal sulfides (Li et al., 2018; Wang L. et al., 2018), and metal catalyst (Cho et al., 2019; Ding et al., 2019), which could have produced strong chemical interactions with polysulfides. For instance, Wang L. et al. (2018) integrated a multicomponent sandwich structure interlayer as freestanding interlayer inserting between the sulfur cathode and separator, and the Li–S cell has been displayed outstanding electrochemical performance. In the structure, CNF is used as a scaffold to support CNT and vanadium disulfide compounds (VS_2/CNT), and covered a graphene layer onto it in the end. As shown in **Supplementary Figure S1C**, the CNT containing VS_2 had stronger adsorption ability toward polysulfides than pure CNT, suggesting that the polar V–S bonds in VS_2 promote the adsorption toward polysulfide. With the introduction of VS_2/CNT, the interlayer exhibited excellent synergetic effects to trap LiPSs and suppress the self-discharge effect (Wang L. et al., 2018).

SWCNTs

SWCNTs can be regarded as an ideal scaffold to anchor polysulfides in Li–S batteries due to their relatively uniform diameters and excellent mechanical and electrical properties, which could allow fast electron transfer (Zhao et al., 2012; Fang et al., 2017). Many efforts have been devoted to SWCNTs-based materials as interlayer for Li–S batteries (Kaiser et al., 2015; Chang et al., 2016; Hao J. et al., 2019). For example, Kaiser et al. (2015) synthesized a refined and interwoven structured SWCNTs freestanding film as the barrier layer, and inserted it between sulfur cathode and separator, which could effectively restrain polysulfides, enhancing the electrochemical performance of Li–S batteries.

Later, Kim J.H. et al. (2016) fabricated a polymer-coated single-wall carbon nanotube membrane (PAA-SWCNTs) as functional interlayer, which could efficiently restrain the diffusion of polysulfides via physical blocking of SWCNTs scaffold and hydrogen-bonding interaction of PAA. Moreover, SWCNTs films can act as second current collector to smooth the transfer of electron and Li^+. As a result, due to the synergic effect of PAA-SWCNT interlayer, the assembled cell exhibited an initial capacity of 770 mAh g^{-1}, it still retained a capacity of 573 mAh g^{-1} after 200 cycles at 1 C.

Apart from combined polymer with SWCNT, there are also researchers combined rGO with SWCNT as intermediate layer to anchor polysulfides (Hao J. et al., 2019). The composite membrane not only improve the internal electronic conductivity but also efficiently anchor polysulfides, resulting in an improved performance in Li–S batteries.

CONCLUSION AND OUTLOOK

In summary, we briefly review the recent development of CNT-based materials, including heteroatom-doped CNTs, carbonaceous materials/CNT composites, and metal-based materials/

CNT composites, as interlayers for Li–S batteries. Their nano/microstructure and electrochemical performances are intensively discussed. As we can see, even though the electrochemical properties of Li–S batteries with CNT-based interlayer have been significantly improved, several problems still exist and need to be addressed before practical application of Li–S batteries.

1. As mentioned above, CNTs-based materials are beneficial to immobilize the LiPSs when it is designed as an intercept layer, however, it should be noted that these materials could just relieve the shuttle effect to a certain degree physically or chemically, and the active materials still be possible to shuttle to the anode during the cycling. Moreover, the sulfur loading is normally about 1–2 mg cm^{-2} in most of above-mentioned work, and the highest loading does not exceed 10 mg cm^{-2}. With gradually increased sulfur loading, despite the existence of intercept layers, the issues of active material loss and polysulfide shuttling are severe. Hence, it is imperative to develop new materials which have strong binding energy and interactions with polysulfides.
2. The mechanism of CNTs-based materials for immobilization and catalytic conversion of LiPSs and their phase transformation during cycling are not clear enough, and still need to be explored. In-operando techniques, such as *in situ* electron microscopy, and *in situ* X-ray

technique, as well as synchron X-ray based techniques, are very helpful to obtain time dependent information. So, more research using in-operando techniques need to conduct to get insight understanding of the CNTs-based materials as interlayers for Li–S batteries.

3. Another issue to be tackled for practical application is lithium metal anode for lithium–sulfur batteries. There is always a problem in battery systems in which lithium metal exists: the formation and growth of lithium dendrites and the resulting low Coulombic efficiency and volume changes (Wang Y. et al., 2018; Wang G. et al., 2020; Zhao Q. et al., 2019). Therefore, in order to obtain a stable and safe lithium anode, a suitable electrolyte additive can be used. At present, the research on electrolyte additives has been highly advanced. Further, it is also possible to insert an artificial layer on the side of the lithium anode (Hao X. et al., 2019; Wang G. et al., 2020). However, there is little research on application of interlayers of CNTs-based composites in anodes, and this area requires further effort.
4. The reported literatures on CNTs-based materials coating layer/freestanding interlayers have developed many high-loading sulfur cathodes with excellent performances. However, the introduction of a coating/freestanding interlayer will increase the inactive weight ratio of the whole battery. Therefore, the direction to balance the relationship between the introduced CNTs-based interlayers and the total energy densities of batteries will be very important in the development of high-energy Li–S batteries.

AUTHOR CONTRIBUTIONS

YL and FR conceived the idea. HW and YL wrote the draft. All authors contributed to the writing, discussion, and revision of the final version of the manuscript.

FUNDING

This work was supported by the Program for Changjiang Scholars and Innovative Research Team in University (IRT_16R21), the Chinese 02 Special Fund (2017ZX02408003), the Scientific and Technological Project of Henan Province (182102210297), Open Fund of National Joint Engineering Research Center for Abrasion Control and Molding of Metal Materials (HKDNM201807), Eighth Postgraduate Innovation Foundation of Henan University of Science and Technology (CXJJ-2019-KJ01), Science Foundation for Youths of Henan University of Science and Technology (2013QN006), the Student Research Training Plan of Henan University of Science and Technology (2020026), and the National Undergraduate Innovation and Entrepreneurship Training Program (202010464031).

SUPPLEMENTARY MATERIAL

The Supplementary Material for this article can be found online at: https://www.frontiersin.org/articles/10.3389/fenrg.2020.585795/full#supplementary-material

REFERENCES

Ali, S., Rehman, S. A. U., Luan, H.-Y., Farid, M. U., and Huang, H. (2019). Challenges and opportunities in functional carbon nanotubes for membrane-based water treatment and desalination. *Sci. Total Environ.* 646, 1126–1139. doi: 10.1016/j.scitotenv.2018.07.348

Cao, D. X., Jiao, Y. C., Cai, Q. F., Han, D. D., Zhang, Q., Ma, Y., et al. (2019). Stable lithium-sulfur full cells enabled by dual functional and interconnected mesocarbon arrays. *J. Mater. Chem. A* 7, 3289–3297. doi: 10.1039/c8ta10351h

Chang, C.-H., Chung, S.-H., and Manthiram, A. (2015). Ultra-lightweight PANiNF/MWCNT-functionalized separators with synergistic suppression of polysulfide migration for Li-S batteries with pure sulfur cathodes. *J. Mater. Chem. A* 3, 18829–18834. doi: 10.1039/c5ta05053g

Chang, C.-H., Chung, S.-H., and Manthiram, A. (2016). Effective Stabilization of a High-Loading Sulfur Cathode and a Lithium-Metal Anode in Li-S Batteries Utilizing SWCNT-Modulated Separators. *Small* 12, 174–179. doi: 10.1002/smll.201502505

Chang, C.-H., Chung, S.-H., Nanda, S., and Manthiram, A. (2017). A rationally designed polysulfide-trapping interface on the polymeric separator for high-energy Li-S batteries. *Mater. Today Energy* 6, 72–78. doi: 10.1016/j.mtener.2017.09.001

Chen, A., Liu, W., Yan, J., and Liu, K. (2019). A novel separator modified by titanium dioxide nanotubes/carbon nanotubes composite for high performance lithium-sulfur batteries. *Funct. Mater. Lett.* 12:1950016. doi: 10.1142/s1793604719500164

Chen, H., Zhang, B., Wang, X., Dong, P., Tong, H., Zheng, J.-C., et al. (2018). CNT-Decorated Na3V2(PO4)(3) Microspheres as a high-rate and cycle-stable cathode material for sodium ion batteries. *ACS Appl. Mater. Interfaces* 10, 3590–3595. doi: 10.1021/acsami.7b16402

Chen, L., Yu, H., Li, W., Dirican, M., Liu, Y., and Zhang, X. (2020). Interlayer design based on carbon materials for lithium-sulfur batteries: a review. *J. Mater. Chem. A* 8, 10709–10735. doi: 10.1039/d0ta03028g

Chen, M., Zhao, S., Jiang, S., Huang, C., Wang, X., Yang, Z., et al. (2018). Suppressing the polysulfide shuttle effect by heteroatom-doping for high-performance lithium-sulfur batteries. *ACS Sustain. Chem. Eng.* 6, 7545–7557. doi: 10.1021/acssuschemeng.8b00273

Chen, P., Wang, Z., Zhang, B., Zhao, J., Liu, H., Guo, X., et al. (2020). Multi-functional TiO2 nanosheets/carbon nanotubes modified separator enhanced cycling performance for lithium-sulfur batteries. *Int. J. Energy Res.* 44, 3231–3240. doi: 10.1002/er.5171

Chen, X., Huang, Y., Li, J., Wang, X., Zhang, Y., Guo, Y., et al. (2020). Bifunctional separator with sandwich structure for high-performance lithium-sulfur batteries. *J. Colloid Interface Sci.* 559, 13–20. doi: 10.1016/j.jcis.2019.10.001

Chen, Y. T., Abbas, S. A., Kaisar, N., Wu, S. H., Chen, H. A., Boopathi, K. M., et al. (2019). Mitigating metal dendrite formation in lithium-sulfur batteries via morphology-tunable Graphene oxide interfaces. *ACS Appl. Mater. Interfaces* 11, 2060–2070. doi: 10.1021/acsami.8b18379

Cheng, X., Wang, W., Wang, A., Yuan, K., Jin, Z., Yang, Y., et al. (2016). Oxidized multiwall carbon nanotube modified separator for high performance lithium-sulfur batteries with high sulfur loading. *RSC Adv.* 6, 89972–89978. doi: 10.1039/c6ra14581g

Cho, S. H., Cho, S. M., Bae, K. Y., Kim, B. H., Son, B. D., and Yoon, W. Y. (2019). Improving electrochemical properties of Lithium-Sulfur batteries by adding a catalyst-embedded interlayer. *Electrochim. Acta* 315, 33–40. doi: 10.1016/j.electacta.2019.05.062

Chung, S.-H., Han, P., and Manthiram, A. (2016). A polysulfide-trapping interface for electrochemically stable sulfur cathode development. *ACS Appl. Mater. Interfaces* 8, 4709–4717. doi: 10.1021/acsami.5b12012

Chung, S.-H., and Manthiram, A. (2014). High-performance Li-S batteries with an ultra-lightweight MWCNT-Coated separator. *J. Phys. Chemi. Lett.* 5, 1978–1983. doi: 10.1021/jz5006913

Ding, H., Zhang, Q., Liu, Z., Wang, J., Ma, R., Fan, L., et al. (2018). TiO2 quantum dots decorated multi-walled carbon nanotubes as the multifunctional separator for highly stable lithium sulfur batteries. *Electrochim. Acta* 284, 314–320. doi: 10.1016/j.electacta.2018.07.167

Ding, N., Zhou, L., Zhou, C., Geng, D., Yang, J., Chien, S. W., et al. (2016). Building better lithium-sulfur batteries: from LiNO3 to solid oxide catalyst. *Sci. Rep.* 6:33154.

Ding, X., Pan, Z., Liu, N., Li, L., Wang, X., Xu, G., et al. (2019). Freestanding carbon nanotube film for flexible Straplike Lithium/sulfur batteries. *Chem. A Eur. J.* 25, 3775–3780. doi: 10.1002/chem.201806408

Du, J., Ahmed, W., Xu, J., Zhang, M., Zhang, Z., Zhang, X., et al. (2020). Chainmail Catalyst of Fe3O4@C/CNTO-modified celgard separator with low metal loading for high-performance lithium-sulfur batteries. *Chemistryselect* 5, 3757–3762. doi: 10.1002/slct.202000366

Fang, R., Li, G., Zhao, S., Yin, L., Du, K., Hou, P., et al. (2017). Single-wall carbon nanotube network enabled ultrahigh sulfur-content electrodes for high-performance lithium-sulfur batteries. *Nano Energy* 42, 205–214. doi: 10.1016/j.nanoen.2017.10.053

Gao, F., Yan, X., Li, X., Qiao, Y., Shang, H., Zhang, Y., et al. (2019a). A new finding on the enhancement of the ability of polysulfide adsorption of V2O5 by Doping Tungsten in Lithium-Sulfur Batteries. *Energy Technol.* 7:1900405. doi: 10.1002/ente.201900405

Gao, F., Yan, X., Wei, Z., Qu, M., and Fan, W. (2019b). Graphene/carbon nanotubes composite as a polysulfide trap for lithium-sulfur batteries. *Int. J. Electrochem. Sci.* 14, 3301–3314. doi: 10.20964/2019.04.16

Gao, G., Feng, W., Su, W., Wang, S., Chen, L., Li, M., et al. (2020). Preparation and Modification of MIL-101(Cr) Metal organic framework and its application in lithium-sulfur batteries. *Int. J. Electrochem. Sci.* 15, 1426–1436. doi: 10.20964/2020.02.26

Geng, Y., Ma, Z., Su, L., Sang, L., Ding, F., and Shao, G. (2020). A sandwich-structure composite carbon layer coated on separator to trap polysulfides for high-performance lithium sulfur batteries. *J. Alloys Compd.* 815:152189. doi: 10.1016/j.jallcom.2019.152189

Guan, B., Zhang, Y., Fan, L., Wu, X., Wang, M., Qiu, Y., et al. (2019). Blocking Polysulfide with Co2B@CNT via "Synergetic Adsorptive Effect" toward Ultrahigh-Rate Capability and Robust Lithium-Sulfur Battery. *ACS Nano* 13, 6742–6750. doi: 10.1021/acsnano.9b01329

Guan, Y., Li, W., Xie, X., Qu, W., Shen, J., Fu, K., et al. (2019). Preparation of TiO2/CNTs composite coated separator and its application in Li-S battery. *Chem. J. Chin. Univ. Chin.* 40, 536–541.

Guang, Z., Huang, Y., Chen, X., Sun, X., Wang, M., Feng, X., et al. (2019). Three-dimensional P-doped carbon skeleton with built-in Ni2P nanospheres as efficient polysulfides barrier for high-performance lithium-sulfur batteries. *Electrochim. Acta* 307, 260–268. doi: 10.1016/j.electacta.2019.03.190

Guo, D., Yang, M., Li, Y., Xue, Y., Liu, G., Wu, N., et al. (2020). Hydrogel-derived VPO4/porous carbon framework for enhanced lithium and sodium storage. *Nanoscale* 12, 3812–3819. doi: 10.1039/d0nr00460j

Guo, X., Zhang, Y.-Z., Zhang, F., Li, Q., Anjum, D. H., Liang, H., et al. (2019). A novel strategy for the synthesis of highly stable ternary SiOx composites for Li-ion-battery anodes. *J. Mater. Chem. A* 7, 15969–15974. doi: 10.1039/c9ta04062e

Guo, Y., Xiao, J., Hou, Y., Wang, Z., and Jiang, A. (2017). Carbon nanotube doped active carbon coated separator for enhanced electrochemical performance of lithium-sulfur batteries. *J. Mater. Sci. Mater. Electron.* 28, 17453–17460. doi: 10.1007/s10854-017-7679-7

Hao, J., Pan, Y., Chen, W., Zhu, X., Zhou, Y., and Chou, S. (2019). Improving the Li-S battery performance by applying a combined interface engineering approach on the Li2S cathode. *J. Mater. Chem. A* 7, 27247–27255. doi: 10.1039/c9ta10301e

Hao, X., Zhao, Q., Su, S., Zhang, S., Ma, J., Shen, L., et al. (2019). Constructing Multifunctional Interphase between Li1.4Al0.4Ti1.6(PO4)(3) and Li Metal by Magnetron Sputtering for Highly Stable Solid-State Lithium Metal Batteries. *Adv. Energy Mater.* 9:1901604. doi: 10.1002/aenm.201901604

Hong, X.-J., Song, C.-L., Yang, Y., Tan, H.-C., Li, G.-H., Cai, Y.-P., et al. (2019). Cerium based metal-organic frameworks as an efficient separator coating catalyzing the conversion of polysulfides for high performance lithium-sulfur batteries. *ACS Nano* 13, 1923–1931.

Huang, J.-Q., Chong, W. G., Zheng, Q., Xu, Z.-L., Cui, J., Yao, S., et al. (2018). Understanding the roles of activated porous carbon nanotubes as sulfur support and separator coating for lithium-sulfur batteries. *Electrochim. Acta* 268, 1–9. doi: 10.1016/j.electacta.2018.02.096

Huang, J.-Q., Xu, Z.-L., Abouali, S., Garakani, M. A., and Kim, J.-K. (2016). Porous graphene oxide/carbon nanotube hybrid films as interlayer for lithium-sulfur batteries. *Carbon* 99, 624–632. doi: 10.1016/j.carbon.2015.12.081

Huang, J. Q., Zhuang, T. Z., Zhang, Q., Peng, H. J., Chen, C. M., and Wei, F. (2015). Permselective graphene oxide membrane for highly stable and anti-self-discharge lithium-sulfur batteries. *ACS Nano* 9, 3002–3011. doi: 10.1021/nn507178a

Huang, Y., Sun, X., Wang, J., Li, X., Chen, W., Wei, C., et al. (2019). Hydroxylated sandwich-structure interlayer as a polysulfide reservoir for lithium-sulfur battery. *J. Alloys Compd.* 776, 187–193. doi: 10.1016/j.jallcom.2018.10.146

Hwang, J.-Y., Kim, H. M., Lee, S.-K., Lee, J.-H., Abouimrane, A., Khaleel, M. A., et al. (2016). High-energy, high-rate, lithium-sulfur batteries: synergetic effect of hollow TiO2-webbed carbon nanotubes and a dual functional carbon-paper interlayer. *Adv. Energy Mater.* 6:1501480. doi: 10.1002/aenm.201501480

Jeong, Y. C., Kim, J. H., Kwon, S. H., Oh, J. Y., Park, J., Jung, Y., et al. (2017). Rational design of exfoliated 1T MoS2@CNT-based bifunctional separators for lithium sulfur batteries. *J. Mater. Chem. A* 5, 23909–23918. doi: 10.1039/c7ta08153g

Jiang, S., Chen, M., Wang, X., Wu, Z., Zeng, P., Huang, C., et al. (2018). MoS2-Coated N-doped Mesoporous Carbon Spherical Composite Cathode and CNT/Chitosan modified separator for advanced lithium sulfur batteries. *ACS Sustain. Chem. Eng.* 6:16828. doi: 10.1021/acssuschemeng.8b04157

Jiang, S., Chen, M., Wang, X., Zeng, P., Li, Y., Liu, H., et al. (2019). A tin disulfide nanosheet wrapped with interconnected carbon nanotube networks for application of lithium sulfur batteries. *Electrochim. Acta* 313, 151–160. doi: 10.1016/j.electacta.2019.05.001

Jiao, L., Wu, S., Tao, Y., Lv, W., Zhang, C., Ling, G., et al. (2019). Interlayers for lithium-based batteries. *Energy Storage Mater.* 23, 112–136.

Jin, Q., Zhang, N., Zhu, C. C., Gao, H., and Zhang, X. T. (2018). Rationally designing S/Ti3C2Tx as a cathode material with an interlayer for high-rate and long-cycle lithium-sulfur batteries. *Nanoscale* 10, 16935–16942. doi: 10.1039/c8nr05749d

Kaiser, M. R., Wang, J., Liang, X., Liu, H.-K., and Dou, S.-X. (2015). A systematic approach to high and stable discharge capacity for scaling up the lithium-sulfur battery. *J. Power Sources* 279, 231–237. doi: 10.1016/j.jpowsour.2014.12.098

Kiai, M. S., and Kizil, H. (2019). Enhanced performance of Li-S battery with polymer doped potassium functionalized graphene interlayers as effective polysulfide barrier. *J. Electroanal. Chem.* 851:113405. doi: 10.1016/j.jelechem.2019.113405

Kim, D. S., Bae, J., Kwon, S. H., Hur, J., Lee, S. G., and Kim, I. T. (2020). Synergistic effect of antimony-triselenide on addition of conductive hybrid matrix for high-performance lithium-ion batteries. *J. Alloys Compd.* 828:154410. doi: 10.1016/j.jallcom.2020.154410

Kim, H. M., Hwang, J.-Y., Manthiram, A., and Sun, Y.-K. (2016). High - performance lithium-sulfur batteries with a self-assembled multiwall carbon nanotube interlayer and a robust electrode electrolyte interface. *ACS Appl. Mater. Interfaces* 8, 983–987. doi: 10.1021/acsami.5b10812

Kim, J. H., Seo, J., Choi, J., Shin, D., Carter, M., Jeon, Y., et al. (2016). Synergistic ultrathin functional polymer-coated carbon nanotube interlayer for high performance lithium-sulfur batteries. *ACS Appl. Mater. Interfaces* 8, 20092–20099. doi: 10.1021/acsami.6b06190

Kim, P. J. H., Kim, K., and Pol, V. G. (2018). Towards highly stable lithium sulfur batteries: surface functionalization of carbon nanotube scaffolds. *Carbon* 131, 175–183. doi: 10.1016/j.carbon.2018.01.100

Kong, L., Peng, H.-J., Huang, J.-Q., Zhu, W., Zhang, G., Zhang, Z.-W., et al. (2017). Beaver-dam-like membrane: a robust and sulphifilic MgBO2(OH)/CNT/PP nest separator in Li-S batteries. *Energy Storage Mater.* 8, 153–160. doi: 10.1016/j.ensm.2017.05.009

Kong, W., Wang, D., Yan, L., Luo, Y., Jiang, K., Li, Q., et al. (2018). Ultrathin HfO2-modified carbon nanotube films as efficient polysulfide barriers for Li-S batteries. *Carbon* 139, 896–905. doi: 10.1016/j.carbon.2018.07.063

Kong, W., Yan, L., Luo, Y., Wang, D., Jiang, K., Li, Q., et al. (2017). Ultrathin MnO2/Graphene Oxide/Carbon nanotube interlayer as efficient polysulfide-trapping shield for high-performance Li-S batteries. *Adv. Funct. Mater.* 27:1606663. doi: 10.1002/adfm.201606663

Kumar, G. G., Chung, S.-H., Kumar, T. R., and Manthiram, A. (2018). Three-dimensional graphene-carbon nanotube-Ni hierarchical architecture as a polysulfide trap for lithium-sulfur batteries. *ACS Appl. Mater. Interfaces* 10, 20627–20634. doi: 10.1021/acsami.8b06054

Kumar, S., Nehra, M., Kedia, D., Dilbaghi, N., Tankeshwar, K., and Kim, K.-H. (2018). Carbon nanotubes: a potential material for energy conversion and storage. *Prog. Energy Combust. Sci.* 64, 219–253. doi: 10.1016/j.pecs.2017.10.005

Lee, C.-L., and Kim, I.-D. (2015). A hierarchical carbon nanotube-loaded glass-filter composite paper interlayer with outstanding electrolyte uptake properties for high-performance lithium-sulphur batteries. *Nanoscale* 7, 10362–10367. doi: 10.1039/c5nr02637g

Lee, D. H., Ahn, J. H., Park, M.-S., Eftekhari, A., and Kim, D.-W. (2018). Metal-organic framework/carbon nanotube-coated polyethylene separator for improving the cycling performance of lithium-sulfur cells. *Electrochim. Acta* 283, 1291–1299. doi: 10.1016/j.electacta.2018.07.031

Lee, D. K., Kim, S. J., Kim, Y.-J., Choi, H., Kim, D. W., Jeon, H.-J., et al. (2019). Graphene oxide/carbon nanotube bilayer flexible membrane for high-performance Li-S batteries with superior physical and electrochemical properties. *Adv. Mater. Interfaces* 6:1801992. doi: 10.1002/admi.201801992

Lee, Y.-H., Kim, J.-H., Kim, J.-H., Yoo, J.-T., and Lee, S.-Y. (2018). Spiderweb-mimicking anion-exchanging separators for Li-S batteries. *Adv. Funct. Mater.* 28:1870293. doi: 10.1002/adfm.201870293

Li, J., Jiang, Y., Qin, F., Fang, J., Zhang, K., and Lai, Y. (2018). Magnetron-sputtering MoS2 on carbon paper and its application as interlayer for high-performance lithium sulfur batteries. *J. Electroanal. Chem.* 823, 537–544. doi: 10.1016/j.jelechem.2018.07.006

Li, M., Feng, W., and Wang, X. (2020a). Complex hollow structures of Cobalt(II) sulfide as a cathode for lithium-sulfur batteries. *Int. J. Electrochem. Sci.* 15, 526–534. doi: 10.20964/2020.01.77

Li, M., Wahyudi, W., Kumar, P., Wu, F., Yang, X., Li, H., et al. (2017). Scalable approach to construct free-standing and flexible carbon networks for lithium-sulfur battery. *ACS Appl. Mater. Interfaces* 9, 8047–8054.

Li, N., Cao, W., Liu, Y., Ye, H., and Han, K. (2019a). Impeding polysulfide shuttling with a three-dimensional conductive carbon nanotubes/MXene framework modified separator for highly efficient lithium-sulfur batteries. *Colloids Surf. A Physicochem. Eng. Aspects* 573, 128–136. doi: 10.1016/j.colsurfa.2019.04.054

Li, N., Chen, Z., Chen, F., Hu, G., Wang, S., Sun, Z., et al. (2019b). From interlayer to lightweight capping layer: rational design of mesoporous TiO2 threaded with CNTs for advanced Li-S batteries. *Carbon* 143, 523–530. doi: 10.1016/j.carbon.2018.11.064

Li, N., Ma, X., Ye, H., Wang, S., and Han, K. (2019c). Carbon nanotube-modified separator for lithium-sulfur batteries: effects of mass loading and adding polyvinylpyrrolidone on electrochemical performance. *J. Phys. Chem. Solids* 134, 69–76. doi: 10.1016/j.jpcs.2019.05.045

Li, N., Xie, Y., Peng, S., Xiong, X., and Han, K. (2020b). Ultra-lightweight Ti3C2Tx MXene modified separator for Li-S batteries: thickness regulation enabled polysulfide inhibition and lithium ion transportation. *J. Energy Chem.* 42, 116–125. doi: 10.1016/j.jechem.2019.06.014

Li, R., Sun, X., Zou, J., He, Q., and Xu, Y. (2019d). New-type SiO2/AP interlayer for inhibiting shuttle effect of Li-S battery. *Mater. Res. Express* 6:1801992.

Li, S., Zhang, H., Chen, W., Zou, Y., Yang, H., Yang, J., et al. (2020c). Toward commercially viable Li-S batteries: overall performance improvements enabled by a multipurpose interlayer of hyperbranched polymer-grafted carbon nanotubes. *ACS Appl. Mater. Interfaces* 12, 25767–25774. doi: 10.1021/acsami.0c03182

Li, S., Zhang, W., Zheng, J., Lv, M., Song, H., and Du, L. (2020d). Inhibition of polysulfide shuttles in Li-S batteries: modified separators and solid-state electrolytes. *Adv. Energy Mater.* 28:2000779. doi: 10.1002/aenm.202000779

Li, Y., Li, X., Hao, Y., Kakimov, A., Li, D., Sun, Q., et al. (2020e). β-FeOOH interlayer with abundant oxygen vacancy toward boosting catalytic effect for lithium sulfur batteries. *Front. Chem.* 8:309. doi: 10.3389/fchem.2020.00309

Li, Y., Zhai, X., Liu, Y., Wei, H., Ma, J., Chen, M., et al. (2020f). WO3-based materials as electrocatalysts for hydrogen evolution reaction. *Front. Mater.* 7:105. doi: 10.3389/fmats.2020.00105

Li, Y., Zhou, P., Li, H., Gao, T., Zhou, L., Zhang, Y., et al. (2020g). A freestanding flexible single-atom cobalt-based multifunctional interlayer toward reversible and durable lithium-sulfur batteries. *Small Methods* 4:1900701. doi: 10.1002/smtd.201900701

Li, Z., Tang, L., Liu, X., Song, T., Xu, Q., Liu, H., et al. (2019e). A polar TiO/MWCNT coating on a separator significantly suppress the shuttle effect in a lithium-sulfur battery. *Electrochim. Acta* 310, 1–12. doi: 10.1016/j.electacta.2019.04.057

Li, Z., Xu, J., Wang, J., Niu, D., Hu, S., and Zhang, X. (2019f). Well-dispersed amorphous Ta2O5 chemically grafted onto multi-walled carbon nanotubes for high-performance lithium sulfur battery. *Int. J. Electrochem. Sci.* 14, 6628–6642. doi: 10.20964/2019.07.39

Liu, B., Wang, S., Wu, X., Liu, Z., Gao, Z., Li, C., et al. (2018). Carbon nanotube/zirconia composite-coated separator for a high-performance rechargeable lithium-sulfur battery. *AIP Adv.* 8:105315. doi: 10.1063/1.5044486

Liu, B., Wu, X., Wang, S., Tang, Z., Yang, Q., Hu, G.-H., et al. (2017). Flexible carbon nanotube modified separator for high-performance lithium-sulfur batteries. *Nanomaterials* 7:196. doi: 10.3390/nano7080196

Liu, G., Cui, J., Luo, R., Liu, Y., Huang, X., Wu, N., et al. (2019a). 2D MoS2 grown on biomass-based hollow carbon fibers for energy storage. *Appl. Surf. Sci.* 469, 854–863. doi: 10.1016/j.apsusc.2018.11.067

Liu, G., Wu, H.-H., Meng, Q., Zhang, T., Sun, D., Jin, X., et al. (2020). Role of the anatase/TiO2(B) heterointerface for ultrastable high-rate lithium and sodium energy storage performance. *Nanoscale Horiz.* 5, 150–162. doi: 10.1039/c9nh00402e

Liu, M., Yang, Z., Sun, H., Lai, C., Zhao, X., Peng, H., et al. (2016). A hybrid carbon aerogel with both aligned and interconnected pores as interlayer for high-performance lithium-sulfur batteries. *Nano Res.* 9, 3735–3746. doi: 10.1007/s12274-016-1244-1

Liu, Y., Wang, H., Yang, K., Yang, Y., Ma, J., Pan, K., et al. (2019b). Enhanced Electrochemical Performance of Sb2O3 as an Anode for Lithium-Ion Batteries by a Stable Cross-Linked Binder. *Appl. Sci. Basel* 9:2677. doi: 10.3390/app9132677

Liu, Y., Wang, Y., Wang, F., Lei, Z., Zhang, W., Pan, K., et al. (2019c). Facile synthesis of antimony tungstate nanosheets as anodes for lithium-ion batteries. *Nanomaterials* 9:1689. doi: 10.3390/nano9121689

Lu, Q., Zou, X., Ran, R., Zhou, W., Liao, K., and Shao, Z. (2019). An "electronegative" bifunctional coating layer: simultaneous regulation of polysulfide and Li-ion adsorption sites for long-cycling and "dendrite-free", Li-S batteries. *J. Mater. Chem. A* 7, 22463–22474. doi: 10.1039/c9ta07999h

Luo, L., Chung, S.-H., and Manthiram, A. (2016). A trifunctional multi-walled carbon nanotubes/polyethylene glycol (MWCNT/PEG)-coated separator through a layer-by-layer coating strategy for high-energy Li-S batteries. *J. Mater. Chem. A* 4, 16805–16811. doi: 10.1039/c6ta07709a

Luo, L., Qin, X., Wu, J., Liang, G., Li, Q., Liu, M., et al. (2018). An interwoven MoO3@CNT scaffold interlayer for high-performance lithium-sulfur batteries. *J. Mater. Chem. A* 6, 8612–8619. doi: 10.1039/c8ta01726c

Luo, R., Lu, Y., Hou, X., Yu, Q., Peng, T., Yan, H., et al. (2017). Encapsulation of Se/C into ultra-thin Ni(OH)(2) nanosheets as cathode materials for lithium-selenium batteries. *J. Solid State Electrochem.* 21, 3611–3618. doi: 10.1007/s10008-017-3696-y

Luo, Y., Luo, N., Kong, W., Wu, H., Wang, K., Fan, S., et al. (2018). Multifunctional interlayer based on molybdenum diphosphide catalyst and carbon nanotube film for lithium-sulfur batteries. *Small* 14:1702853. doi: 10.1002/smll.201702853

Ma, J., Guo, X., Xue, H., Pan, K., Liu, C., and Pang, H. (2020a). Niobium/tantalum-based materials: synthesis and applications in electrochemical energy storage. *Chem. Eng. J.* 380:122428. doi: 10.1016/j.cej.2019.122428

Ma, J., Ren, F., Wang, G., Xiong, Y., Li, Y., and Wen, J. (2017). Electrochemical performance of melt-spinning Al-Mg-Sn based anode alloys. *Int. J. Hydrogen Energy* 42, 11654–11661. doi: 10.1016/j.ijhydene.2017.02.185

Ma, J., Wei, H., Liu, Y., Ren, X., Li, Y., Wang, F., et al. (2020b). Application of Co3O4-based materials in electrocatalytic hydrogen evolution reaction: a review. *Int. J. Hydrogen Energy* 45, 21205–21220. doi: 10.1016/j.ijhydene.2020.05.280

Ma, J., Wen, J., Li, Q., and Zhang, Q. (2013). Electrochemical polarization and corrosion behavior of Al-Zn-In based alloy in acidity and alkalinity solutions. *Int. J. Hydrogen Energy* 38, 14896–14902. doi: 10.1016/j.ijhydene.2013.09.046

Ma, J., Zhang, Y., Qin, C., Ren, F., and Wang, G. (2020c). Effects of polystyrene sulfonate/graphene and Mn3O4/graphene on property of aluminum(zinc)-air batteries. *Int. J. Hydrogen Energy* 45, 13025–13034. doi: 10.1016/j.ijhydene.2020.02.222

Ma, X., Xiong, X., Zou, P., Liu, W., Wang, F., Liang, L., et al. (2019). General and Scalable Fabrication of Core-Shell Metal Sulfides@C Anchored on 3D N-Doped Foam toward Flexible Sodium Ion Batteries. *Small* 15:1903259. doi: 10.1002/smll.201903259

Manoj, M., Ashraf, C. M., Jasna, M., Anilkumar, K. M., Jinisha, B., Pradeep, V. S., et al. (2019). Biomass-derived, activated carbon-sulfur composite cathode with a bifunctional interlayer of functionalized carbon nanotubes for lithium-sulfur cells. *J. Colloid Interface Sci.* 535, 287–299. doi: 10.1016/j.jcis.2018.09.096

Manoj, M., Jasna, M., Anilkumar, K. M., Abhilash, A., Jinisha, B., Pradeep, V. S., et al. (2018a). Sulfur-polyaniline coated mesoporous carbon composite in combination with carbon nanotubes interlayer as a superior cathode assembly for high capacity lithium-sulfur cells. *Appl. Surf. Sci.* 458, 751–761. doi: 10.1016/j.apsusc.2018.07.113

Manoj, M., Jasna, M., and Jayalekshmi, S. (2018b). "Activated Carbon-Sulfur composite with PEDOT: PSS-CNT interlayer as cathode material for Lithium-Sulfur batteries," in *Proceedings of the PIE 10725 Low-Dimensional Materials and Devices*, Vol. 1075, eds N. P. Kobayashi, A. A. Talin, M. S. Islam, and A. V. Davydov (San Diego, CA: SPIE).

Pan, K., Wang, F., Wei, S., Siyal, S. H., Ren, Y., Xu, L., et al. (2020). Low-temperature solution synthesis and characterization of enhanced titanium dioxide photocatalyst on tailored mesoporous γ-Al2O3 support. *Compos. Commun.* 19, 82–89. doi: 10.1016/j.coco.2020.02.009

Pan, S., Yin, Z., Cheng, Q., Zhang, G., Yu, X., Pan, Z., et al. (2020). Bifunctional TiS 2 /CNT as efficient polysulfide barrier to improve the performance of lithium -sulfur battery. *J. Alloys Compd.* 832:154947. doi: 10.1016/j.jallcom.2020.154947

Pang, Y., Wei, J., Wang, Y., and Xia, Y. (2018). Synergetic Protective Effect of the Ultralight MWCNTs/NCQDs modified separator for highly stable lithium-sulfur batteries. *Adv. Energy Mater.* 8:e1702288.

Paolella, A., Demers, H., Chevallier, P., Gagnon, C., Girard, G., Delaporte, N., et al. (2019). A platinum nanolayer on lithium metal as an interfacial barrier to shuttle effect in Li-S batteries. *J. Power Sources* 427, 201–206. doi: 10.1016/j.jpowsour.2019.04.078

Pei, F., Fu, A., Ye, W., Peng, J., Fang, X., Wang, M.-S., et al. (2019). Robust lithium metal anodes realized by Lithiophilic 3D porous current collectors for constructing high-energy lithium-sulfur batteries. *ACS Nano* 13, 8337–8346. doi: 10.1021/acsnano.9b03784

Peng, Y., Wen, Z., Liu, C., Zeng, J., Wang, Y., and Zhao, J. (2019). Refining Interfaces between Electrolyte and Both Electrodes with Carbon Nanotube Paper for High-Loading Lithium-Sulfur Batteries. *ACS Appl. Mater. Interfaces* 11, 6986–6994. doi: 10.1021/acsami.8b19866

Ponraj, R., Kannan, A. G., Ahn, J. H., Lee, J. H., Kang, J., Han, B., et al. (2017). Effective Trapping of Lithium Polysulfides using a functionalized carbon nanotube-coated separator for lithium-sulfur cells with enhanced cycling stability. *ACS Appl. Mater. Interfaces* 9, 38445–38454. doi: 10.1021/acsami.7b10641

Rui, L. I., Sun, X., Huang, Y., Zou, J., He, Q., and Xu, Y. (2019). SMAP interlayer for inhibiting shuttle effect of lithium-sulfur battery. *Vacuum* 168:108820. doi: 10.1016/j.vacuum.2019.108820

Shi, H., Zhao, X., Wu, Z.-S., Dong, Y., Lu, P., Chen, J., et al. (2019). Free-standing integrated cathode derived from 3D graphene/carbon nanotube aerogels serving as binder-free sulfur host and interlayer for ultrahigh volumetric-energy-density lithium-sulfur batteries. *Nano Energy* 60, 743–751. doi: 10.1016/j.nanoen.2019.04.006

Shi, L., Zeng, F., Cheng, X., Lam, K. H., Wang, W., Wang, A., et al. (2018). Enhanced performance of lithium-sulfur batteries with high sulfur loading utilizing ion selective MWCNT/SPANI modified separator. *Chem. Eng. J.* 334, 305–312. doi: 10.1016/j.cej.2017.08.015

Son, B. D., Cho, S. H., Bae, K. Y., Kim, B. H., and Yoon, W. Y. (2019). Dual functional effect of the ferroelectricity embedded interlayer in lithium sulfur battery. *J. Power Sources* 419, 35–41. doi: 10.1016/j.jpowsour.2019.02.014

Song, C., Feng, W., Wang, X., and Shi, Z. (2020). Enhanced electrochemical performance of Li1.2Mn0.54Ni0.13Co0.13O2 cathode material with bamboo essential oil. *Ionics* 26, 661–672. doi: 10.1007/s11581-019-03233-9

Song, C.-L., Li, G.-H., Yang, Y., Hong, X.-J., Huang, S., Zheng, Q.-F., et al. (2020). 3D catalytic MOF-based nanocomposite as separator coatings for high-performance Li-S battery. *Chem. Eng. J.* 381:122701. doi: 10.1016/j.cej.2019.122701

Su, Y.-S., and Manthiram, A. (2012). A new approach to improve cycle performance of rechargeable lithium-sulfur batteries by inserting a free-standing MWCNT interlayer. *Chem. Commun.* 48, 8817–8819. doi: 10.1039/c2cc33945e

Sui, D., Xu, L., Zhang, H., Sun, Z., Kan, B., Ma, Y., et al. (2020). A 3D cross-linked graphene-based honeycomb carbon composite with excellent confinement effect of organic cathode material for lithium-ion batteries. *Carbon* 157, 656–662. doi: 10.1016/j.carbon.2019.10.106

Sun, L., Kong, W., Li, M., Wu, H., Jiang, K., Li, Q., et al. (2016). Cross-stacked carbon nanotube film as an additional built-in current collector and adsorption layer for high-performance lithium sulfur batteries. *Nanotechnology* 27:075401. doi: 10.1088/0957-4484/27/7/075401

Sun, X., Huang, Y., Chen, M., and Dou, W. (2018). Double interlayers to improve cycle performance for Li-S batteries by Using Multiwall carbon nanotubes/reduced graphene oxide. *Ind. Eng. Chem. Res.* 57, 6741–6745. doi: 10.1021/acs.iecr.8b01360

Sun, Z., Guo, Y., Li, B., Tan, T., and Zhao, Y. (2019a). ZnO/carbon nanotube/reduced graphene oxide composite film as an effective interlayer for lithium/sulfur batteries. *Solid State Sci.* 95:105924. doi: 10.1016/j.solidstatesciences.2019.06.013

Sun, Z., Wang, T., Zhang, Y., Kempa, K., and Wang, X. (2019b). Boosting the electrochemical performance of lithium/sulfur batteries with the carbon nanotube/Fe3O4 coated by carbon modified separator. *Electrochim. Acta* 327:134843.

Sun, Z., Xie, C., Fan, Z., Shen, F., Yin, Y., Niu, C., et al. (2020). Ultrathin dense double-walled carbon nanotube membrane for enhanced lithium-sulfur batteries. *J. Nanopart. Res.* 22:160.

Tan, L., Li, X., Wang, Z., Guo, H., Wang, J., and An, L. (2018). Multifunctional separator with porous carbon/multi-walled carbon nanotube coating for advanced lithium-sulfur batteries. *Chemelectrochem* 5, 71–77. doi: 10.1002/celc.201700986

Tian, W., Xi, B., Mao, H., Zhang, J., Feng, J., and Xiong, S. (2018). Systematic Exploration of the Role of a Modified Layer on the Separator in the Electrochemistry of Lithium-Sulfur Batteries. *ACS Appl. Mater. Interfaces* 10, 30306–30313. doi: 10.1021/acsami.8b08438

Wang, A., Xu, G., Ding, B., Chang, Z., Wang, Y., Dou, H., et al. (2017). Highly conductive and lightweight composite film as polysulfide reservoir for high-performance lithium-sulfur batteries. *Chemelectrochem* 4, 362–368. doi: 10.1002/celc.201600579

Wang, F., Liu, Y., Wei, H., Wang, G., Ren, F., Liu, X., et al. (2020). Graphene induced growth of Sb_2 WO_6 nanosheets for high- performance pseudocapacitive lithium -ion storage. *J. Alloys Compd.* 839:155614. doi: 10.1016/j.jallcom.2020.155614

Wang, F., Liu, Y., Zhao, Y., Wang, Y., Wang, Z., Zhang, W., et al. (2018). Facile synthesis of two-dimensional porous MgCo2O4 nanosheets as anode for lithium-ion batteries. *Appl. Sci. Basel* 8:22. doi: 10.3390/app8010022

Wang, G., Chen, C., Chen, Y., Kang, X., Yang, C., Wang, F., et al. (2020). Self-stabilized and strongly adhesive supramolecular polymer protective layer enables ultrahigh-rate and large-capacity lithium-metal anode. *Angew. Chem. Int. Ed.* 59, 2055–2060. doi: 10.1002/anie.201913351

Wang, G., Lai, Y., Zhang, Z., Li, J., and Zhang, Z. (2015). Enhanced rate capability and cycle stability of lithium-sulfur batteries with a bifunctional MCNT@PEG-modified separator. *J. Mater. Chem. A* 3, 7139–7144. doi: 10.1039/c4ta07133f

Wang, J., Qin, W., Zhu, X., and Teng, Y. (2020). Covalent organic frameworks (COF)/CNT nanocomposite for high performance and wide operating temperature lithium-sulfur batteries. *Energy* 199:117372. doi: 10.1016/j.energy.2020.117372

Wang, J., Sun, X., Chen, W., Li, X., Huang, Y., Wei, C., et al. (2018). Electrochemical performance of hydroxylated multi-walled carbon nanotube sandwich separator in lithium-sulfur battery. *Chem. J. Chin. Univ. Chin.* 39, 1782–1789.

Wang, L., He, Y.-B., Shen, L., Lei, D., Ma, J., Ye, H., et al. (2018). Ultra-small self-discharge and stable lithium-sulfur batteries achieved by synergetic effects of multicomponent sandwich-type composite interlayer. *Nano Energy* 50, 367–375. doi: 10.1016/j.nanoen.2018.05.043

Wang, R., Cao, X., Zhao, D., Zhu, L., Xie, L., Liu, J., et al. (2020). Wet-chemistry synthesis of Li4Ti5O12 as anode materials rendering high-rate Li-ion storage. *Int. J. Energy Res.* 44, 4211–4223. doi: 10.1002/er.5020

Wang, S., Li, X., Zhang, Y., Zheng, W., Dai, Y., and He, G. (2020). Highly efficient polysulfide trapping and ion transferring within a hierarchical porous membrane interlayer for high-energy lithium-sulfur batteries. *ACS Appl. Energy Mater.* 3, 5050–5057. doi: 10.1021/acsaem.0c00629

Wang, W., Sun, K., and Liu, H. (2020). Effects of different aluminum sources on morphologies and properties of ceramic floor tiles from red mud. *Construct. Build. Mater.* 241:118119. doi: 10.1016/j.conbuildmat.2020.118119

Wang, X., Hao, X., Cai, D., Zhang, S., Xia, X., and Tu, J. (2020). An ultraviolet polymerized 3D gel polymer electrolyte based on multi-walled carbon nanotubes doped double polymer matrices for lithium-sulfur batteries. *Chem. Eng. J.* 382:122714. doi: 10.1016/j.cej.2019.122714

Wang, X., Yang, C., Xiong, X., Chen, G., Huang, M., Wang, J.-H., et al. (2019). A robust sulfur host with dual lithium polysulfide immobilization mechanism for long cycle life and high capacity Li-S batteries. *Energy Storage Mater.* 16, 344–353. doi: 10.1016/j.ensm.2018.06.015

Wang, Y., Liu, W., Liu, R., Pan, P., Suo, L., Chen, J., et al. (2019). Inhibiting polysulfide shuttling using dual-functional nanowire/nanotube modified layers for highly stable lithium-sulfur batteries. *New J. Chem.* 43, 14708–14713. doi: 10.1039/c9nj03320c

Wang, Y., Wang, Z., Lei, D., Lv, W., Zhao, Q., Ni, B., et al. (2018). Spherical Li Deposited inside 3D Cu Skeleton as Anode with Ultrastable Performance. *ACS Appl. Mater. Interfaces* 10, 20244–20249. doi: 10.1021/acsami.8b04881

Wei, H., Ding, Y., Li, H., Zhang, Q., Hu, N., Wei, L., et al. (2019). MoS2 quantum dots decorated reduced graphene oxide as a sulfur host for advanced lithium-sulfur batteries. *Electrochim. Acta* 327:134994. doi: 10.1016/j.electacta.2019.134994

Wei, L., Li, W., Zhao, T., Zhang, N., Li, L., Wu, F., et al. (2020). Cobalt nanoparticles shielded in N-doped carbon nanotubes for high areal capacity Li-S batteries. *Chem. Commun.* 56, 3007–3010. doi: 10.1039/c9cc08218b

Wu, F., Zhao, S., Chen, L., Lu, Y., Su, Y., Jia, Y., et al. (2018). Metal-organic frameworks composites threaded on the CNT knitted separator for suppressing the shuttle effect of lithium sulfur batteries. *Energy Storage Mater.* 14, 383–391. doi: 10.1016/j.ensm.2018.06.009

Wu, H., Huang, Y., Zhang, W., Sun, X., Yang, Y., Wang, L., et al. (2017). Lock of sulfur with carbon black and a three-dimensional graphene@carbon nanotubes coated separator for lithium-sulfur batteries. *J. Alloys Compd.* 708, 743–750. doi: 10.1016/j.jallcom.2017.03.047

Wu, N., Qiao, X. G., Shen, J. K., Liu, G. L., Sun, T., Wu, H., et al. (2019a). Anatase inverse opal TiO2-x@N-doped C induced the dominant pseudocapacitive effect for durable and fast lithium/sodium storage. *Electrochim. Acta* 299, 540–548. doi: 10.1016/j.electacta.2019.01.040

Wu, N., Shen, J., Sun, L., Yuan, M., Shao, Y., Ma, J., et al. (2019b). Hierarchical N-doped graphene coated 1D cobalt oxide microrods for robust and fast lithium storage at elevated temperature. *Electrochim. Acta* 310, 70–77. doi: 10.1016/j.electacta.2019.04.115

Xiang, K., Wen, X., Hu, J., Wang, S., and Chen, H. (2019). Rational fabrication of nitrogen and sulfur Codoped Carbon Nanotubes/MoS2 for high-performance lithium-sulfur batteries. *Chemsuschem* 12, 3602–3614. doi: 10.1002/cssc.201900929

Xie, K., Yuan, K., Zhang, K., Shen, C., Lv, W., Liu, X., et al. (2017). Dual functionalities of carbon nanotube films for dendrite-free and high energy-high power lithium-sulfur batteries. *ACS Appl. Mater. Interfaces* 9, 4605–4613. doi: 10.1021/acsami.6b14039

Xu, G., Yuan, J., Tao, X., Ding, B., Dou, H., Yan, X., et al. (2015). Absorption mechanism of carbon-nanotube paper-titanium dioxide as a multifunctional barrier material for lithium-sulfur batteries. *Nano Res.* 8, 3066–3074. doi: 10.1007/s12274-015-0812-0

Xu, J., Zhang, Q., Liang, X., Yan, J., Liu, J., and Wu, Y. (2020). A multifunctional separator based on scandium oxide nanocrystal decorated carbon nanotubes for high performance lithium-sulfur batteries. *Nanoscale* 12, 6832–6843. doi: 10.1039/d0nr00160k

Xu, Q., Hu, G. C., Bi, H. L., and Xiang, H. F. (2015). A trilayer carbon nanotube/Al2O3/polypropylene separator for lithium-sulfur batteries. *Ionics* 21, 981–986. doi: 10.1007/s11581-014-1263-4

Yan, L., Luo, N., Kong, W., Luo, S., Wu, H., Jiang, K., et al. (2018). Enhanced performance of lithium-sulfur batteries with an ultrathin and lightweight MoS2/carbon nanotube interlayer. *J. Power Sources* 389, 169–177. doi: 10.1016/j.jpowsour.2018.04.015

Yang, L., Li, G., Jiang, X., Zhang, T., Lin, H., and Lee, J. Y. (2017). Balancing the chemisorption and charge transport properties of the interlayer in lithium-sulfur batteries. *J. Mater. Chem. A* 5, 12506–12512. doi: 10.1039/c7ta01352c

Yao, M., Wang, R., Zhao, Z., Liu, Y., Niu, Z., and Chen, J. (2018). A flexible all-in-one lithium-sulfur battery a flexible all-in-one lithium-sulfur battery. *Acs Nano* 12, 12503–12511. doi: 10.1021/acsnano.8b06936

Yao, S., Cui, J., Huang, J.-Q., Lu, Z., Deng, Y., Chong, W. G., et al. (2018). Novel 2D Sb2S3 Nanosheet/CNT coupling layer for exceptional polysulfide recycling performance. *Adv. Energy Mater.* 8:1800710. doi: 10.1002/aenm.201800710

Yu, M., Yin, Z., Yan, G., Wang, Z., Guo, H., Li, G., et al. (2020). Synergy of interlayer expansion and capacitive contribution promoting sodium ion storage in S, N-Doped mesoporous carbon nanofiber. *J. Power Sources* 449:227514. doi: 10.1016/j.jpowsour.2019.227514

Yu, Q., Luo, R., Bai, X., Yang, W., Lu, Y., Hou, X., et al. (2018). Rational design of double-confined Mn2O3/S@Al2O3 nanocube cathodes for lithium-sulfur batteries. *J. Solid State Electrochem.* 22, 849–858. doi: 10.1007/s10008-017-3818-6

Zhao, M.-Q., Liu, X.-F., Zhang, Q., Tian, G.-L., Huang, J.-Q., Zhu, W., et al. (2012). Graphene/Single-Walled Carbon Nanotube Hybrids: one-step catalytic growth and applications for high-rate Li-S batteries. *ACS Nano* 6, 10759–10769. doi: 10.1021/nn304037d

Zhao, Q., Hao, X. G., Su, S. M., Ma, J. B., Hu, Y., Liu, Y., et al. (2019). Expanded-graphite embedded in lithium metal as dendrite-free anode of lithium metal batteries. *J. Mater. Chem. A* 7, 15871–15879. doi: 10.1039/c9ta04240g

Zhao, X., Chen, H., Kong, F., Zhang, Y., Wang, S., Liu, S., et al. (2019). Fabrication, characteristics and applications of carbon materials with different morphologies and porous structures produced from wood liquefaction: a review. *Chem. Eng. J.* 364, 226–243. doi: 10.1016/j.cej.2019.01.159

Zhao, Y., Wei, S., Wang, F., Xu, L., Liu, Y., Lin, J., et al. (2020). Hatted 1T/2H-Phase MoS2 on Ni3S2 Nanorods for Efficient Overall Water Splitting in Alkaline Media. *Chem. A Eur. J.* 26, 2034–2040. doi: 10.1002/chem.201904307

Zheng, M., Chi, Y., Hu, Q., Tang, H., Jiang, X., Zhang, L., et al. (2019). Carbon nanotube-based materials for lithium-sulfur batteries. *J. Mater. Chem. A* 7, 17204–17241.

Zhu, J., Yildirim, E., Aly, K., Shen, J., Chen, C., Lu, Y., et al. (2016). Hierarchical multi-component nanofiber separators for lithium polysulfide capture in lithium-sulfur batteries: an experimental and molecular modeling study. *J. Mater. Chem. A* 4, 13572–13581. doi: 10.1039/c6ta04577d

Zhu, W., Zhang, Z., Wei, J., Jing, Y., Guo, W., Xie, Z., et al. (2020). A synergistic modification of polypropylene separator toward stable lithium-sulfur battery. *J. Membr. Sci.* 597:117646. doi: 10.1016/j.memsci.2019.117646

Zou, K., Li, N., Dai, X., Jing, W., Shi, M., Lu, C., et al. (2020). Lightweight Freestanding CeF3 Nanorod/Carbon Nanotube Composite Interlayer for Lithium-Sulfur Batteries. *ACS Appl. Nano Mater.* 3, 5732–5742. doi: 10.1021/acsanm.0c00920

Zou, P., Lin, Z., Fan, M., Wang, F., Liu, Y., and Xiong, X. (2020). Facile and efficient fabrication of Li3PO4-coated Ni-rich cathode for high-performance lithium-ion battery. *Appl. Surf. Sci.* 504:144506. doi: 10.1016/j.apsusc.2019.144506

Zuo, X., Zhen, M., and Wang, C. (2019). Ni@N-doped graphene nanosheets and CNTs hybrids modified separator as efficient polysulfide barrier for high-performance lithium sulfur batteries. *Nano Res.* 12, 829–836. doi: 10.1007/s12274-019-2298-7

Conflict of Interest: The authors declare that the research was conducted in the absence of any commercial or financial relationships that could be construed as a potential conflict of interest.

frontiers in Energy Research

ORIGINAL RESEARCH
published: 06 October 2020
doi: 10.3389/fenrg.2020.00207

High Mass-Loading Sulfur-Composite Cathode for Lithium-Sulfur Batteries

*Nurzhan Baikalov[1,2], Nurassyl Serik[2], Sandugash Kalybekkyzy[1,2], Indira Kurmanbayeva[1,3], Zhumabay Bakenov[1,2,3] and Almagul Mentbayeva[1,2]**

[1] National Laboratory Astana, Nazarbayev University, Nur-Sultan, Kazakhstan, [2] School of Engineering and Digital Sciences, Nazarbayev University, Nur-Sultan, Kazakhstan, [3] Institute of Batteries LLC, Nur-Sultan, Kazakhstan

This research aimed to increase the mass loading of sulfur in the composite electrode in order to increase the energy density of the lithium-sulfur (Li-S) cell. This requires designing the electrode with the use of conductive agents to maintain the conductivity of the sulfur composite. Therefore, the composite of sulfur with polyacrylonitrile (PAN) and carbon nanotubes (CNT) was synthesized by heating. Following that, the mass loading of sulfur was increased by using several layers of carbon fiber paper (CFP) with a large free space as a three-dimensional current collector. As a result of the heat treatment and formation of covalent bonding between pyrolyzed PAN and sulfur, uniform distribution and enhanced conductivity were achieved, while CNT maintained structural integrity, acting as an interwoven network. Due to these advantages, the mass loading of sulfur was increased up to 5 mg cm^{-2} while maintaining a high initial specific capacity of 1400 mAh g^{-1} and stable cyclability.

Keywords: lithium-sulfur battery, composite cathode, 3D current collector, carbon fiber paper, mass loading

OPEN ACCESS

Edited by:
Yan-Bing He,
Tsinghua University, China

Reviewed by:
Huiqi Wang,
North University of China, China
Guangmin Zhou,
Tsinghua University, China
Bin Wang,
China Academy of Engineering Physics, China

****Correspondence:***
Almagul Mentbayeva
almagul.mentbayeva@nu.edu.kz

Specialty section:
This article was submitted to Electrochemical Energy Conversion and Storage, a section of the journal Frontiers in Energy Research

Received: *25 May 2020*
Accepted: *03 August 2020*
Published: *06 October 2020*

Citation:
Baikalov N, Serik N, Kalybekkyzy S, Kurmanbayeva I, Bakenov Z and Mentbayeva A (2020) High Mass-Loading Sulfur-Composite Cathode for Lithium-Sulfur Batteries. Front. Energy Res. 8:207. doi: 10.3389/fenrg.2020.00207

INTRODUCTION

The development of electric vehicles and portable devices require high power and high energy density batteries. In this regard, among the existing energy storage systems, lithium-ion batteries (LIBs) play a key role since they offer the highest power density among all known secondary batteries. Also, LIBs have important advantages such as good rate capability and long cycle life. However, the energy and power densities of conventional LIBs are reaching limited theoretical values and cannot fulfill the requirements of the new generation of portable devices and electric vehicles (Ye et al., 2016). It is mainly due to the low theoretical capacity of currently available intercalated cathode materials such as $LiCoO_2$ and $LiNi_{1/3}Co_{1/3}Mn_{1/3}O_2$ (about 150 mAh g^{-1} and 188 mAh g^{-1}, respectively) (Shin et al., 2011; Li M. et al., 2017). In addition, these transition metals are expensive and toxic. Therefore, alternative cathodes offering higher capacity with inexpensive, abundant, and environmentally friendly resources have to be developed (Nie et al., 2015).

A promising replacement for intercalated cathode materials is sulfur, since it has a high theoretical specific capacity and a high gravimetric energy density (1672 mAh g^{-1} and 2600 Wh kg^{-1}, respectively) (Shin et al., 2011). Moreover sulfur has several advantages associated with low cost, environmental friendliness, and abundant resources (Hara et al., 2015; Zeng et al., 2015). However, lithium-sulfur (Li-S) battery implementation is hindered by several difficulties related to the low conductivity of sulfur and the complexity of the redox process (Li M. et al., 2017). Firstly, sulfur has low ionic and electrical conductivity (5×10^{-30} S cm^{-1}) (Nie et al., 2015).

Another problem is the formation of polysulfides, intermediate products of sulfur reduction and its dissolution in the electrolytes (Yang et al., 2014; Li et al., 2018). Polysulfides shuttle back and forth during the redox reaction leading to the loss of the active material, thus generating free space in the cathode and increasing viscosity of the liquid electrolyte (Ould Ely et al., 2018). Then polysulfides precipitate at the anode side in the form of low order lithium sulfides (Li_2S_2 and Li_2S) (Kalybekkyzy et al., 2019). The reduction to Li_2S causes large volume expansion, which leads to non-linear discharge and charge of the cell and limited cyclability (Ma and Xu, 2018; Rajkumar et al., 2019). All these issues generate rapid capacity fade, low coulombic efficiency, and low power capability.

Various strategies were addressed in order to solve the aforementioned problems such as the fabrication of composite materials using conductive polymers like polypyrrole (Zhang et al., 2012), polyaniline (Yuan et al., 2009), polyacrylonitrile (PAN) (Wang et al., 2003), carbon additives such as multi-walled carbon nanotubes (MWCNTs) (Zhang Y. et al., 2014), graphene (Li et al., 2019), graphene oxide (Peng et al., 2018), and porous carbon (Li T. et al., 2017). These efforts are generally aimed at to improve the electrical conductivity of sulfur and limit polysulfides dissolution into the electrolyte (Bakenov et al., 2017). The group of Wang was among the first to work on the fabrication of molecular-level sulfur composites, where they synthesized a sulfur-dehydrogenated polyacrylonitrile (S/DPAN) composite by heating the mixture of sulfur and PAN at 280–300°C (Wang et al., 2003). The fixing of sulfur by a conductive polymer skeleton improved cyclability and capacity of the Li-S battery (Wang et al., 2003). Covalent bonding between sulfur and cyclized conductive DPAN in some degree maintains polysulfide dissolution (Zhang et al., 2012). Also, it was investigated that the addition of conductive hosts such as graphene (Yin et al., 2012), porous carbon (Li T. et al., 2017), and carbon nanotubes (Guo et al., 2011) to the mixture of S/DPAN further improves the electrochemical performance of the electrode (Peng et al., 2017b). However, the addition of inactive conductive materials into the composite decreases the sulfur content, which in turn affects the energy density of Li-S batteries (Zhao et al., 2015).

An increase in the amount of inactive materials (polymer, carbon) significantly reduces the weight content of sulfur, resulting in low mass loading. Low mass loading of sulfur notably decreases the energy density (Peng et al., 2017a). Moreover, conventional thin 2D metallic foil (Al) current collectors are incapable of providing high mass loading of sulfur ($\leq$2 mg cm^{-2}) (Cheng et al., 2016). Therefore, alternative current collectors which enable high mass loading of sulfur need to be developed. There have been numerous attempts to increase mass loading and the areal capacity of sulfur using three-dimensional (3D) structures on metallic current collectors (Yu et al., 2018), freestanding carbon materials [including carbon nanotubes (Ye et al., 2016), doped carbon nanofibers (Song et al., 2017), 3D graphene composite foams (Lu et al., 2014)], structural confinement using hollow carbon nanofibers (Chung et al., 2016; Chung and Manthiram, 2018), and electro-spun 3D carbon nanofibers (Kalybekkyzy et al., 2020). These approaches are mainly based on the confinement of sulfur in conductive hosts, which enables them to limit polysulfide dissolution and thus, increases the lifetime of batteries. Among these candidates 3D carbon current collectors such as carbon fiber paper (CFP) attracts a lot of attention due to its good electrical conductivity, high mechanical and chemical stability, low density, and low cost (Yuan et al., 2009; Suktha et al., 2015).

Herein we report a simple and efficient preparation method for high mass loading sulfur composite cathodes by designing micro- and nano-level 3D carbon networks. It was achieved through synthesis of S/DPAN/CNT composite cathodes by heat treatment in an argon atmosphere, where covalent bonding between pyrolyzed PAN and sulfur diminished polysulfide dissolution, while CNT maintained structural integrity, acting as a nanoscale interwoven network and ensured electron transfer within and between the S/DPAN granules (Mentbayeva et al., 2016). Then S/DPAN/CNT was impregnated into the voids of the commercial CFP, which in its turn was used in several layers to provide bulk electron conductivity at the macro-level. As a result, mass loading of sulfur was increased up to 5 mg cm^{-2}.

EXPERIMENTAL PART

Chemicals

Sulfur (98%, GOST 127.1, Tengizchevroil, Kazakhstan), polyacrylonitrile (average Mr = 150,000, J&K Scientific), multi-walled carbon nanotubes (CNT, >95%, OD: 10–20 nm, US Research Nanomaterials, Inc.), N-methyl-pyrrolidone (NMP) (>99%, Sigma-Aldrich), and polyvinylidene fluoride (PVdF, 100%, Arkema, MTI Corp.).

Preparation of S/DPAN/CNT Composite Cathode

Sulfur was manually ground and mixed with PAN at the mass ratio of 4:1 with the addition of different amounts of CNT (1–4 wt% of total mass) as illustrated in **Figure 1**. After that, the mixture was heated in a tube furnace at 300°C with different durations of time (3 h and 40 min) in the argon atmosphere to form the S/DPAN/CNT composite.

Physical-Chemical Characterization

X-ray diffraction (XRD, Rigaku SmartLab) was used in the structure analysis. The morphology of the samples were analyzed using scanning electron microscopy (FåSEM-EDS Auriga, Crossbeam 540), Raman spectroscopy (HORIBA Scientific, France), and Fourier transform infrared spectroscopy (Nicolet iS10 FT-IR Spectrometer); the sulfur content of composites was analyzed using elemental chemical analysis (CHNS, Vario Micro Cube, Elementar).

Electrochemical Characterization

The electrochemical performance was analyzed using a CR2032 coin type cell configuration assembled in an argon filled glovebox (MasterLab, MBraun). Lithium metal disks were used as an anode, a porous polypropylene membrane (Celgard 2400) served as a separator and the electrolyte consisted of 1 M $LiPF_6$

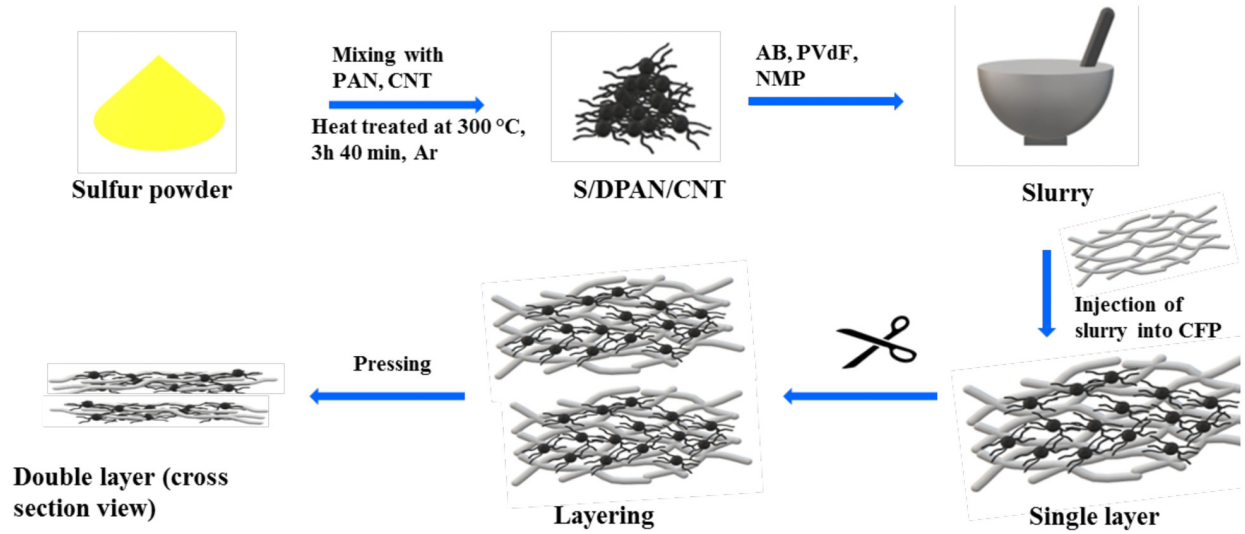

FIGURE 1 | A schematic representation illustrating the preparation and injection process of sulfur composites into 3D current collector.

in ethylene carbonate/dimethyl carbonate/diethylene carbonate (EC:DMC:DEC, in volumetric ratio of 1:1:1 Targray). The area of the electrode was 1.77 cm^2. Firstly, two drops of the electrolyte were applied onto the cathode, then the separator was placed onto the surface of the cathode and the electrolyte was dropped again. Cathodes were prepared using the slurry-casting method as illustrated in **Figure 1**. For that S/DPAN/CNT composite, acetylene black and PVdF were dispersed in N-methyl-2-pyrrolydone (NMP) in the mass ratio of 8:1:1. The prepared slurry was cast as a thin layer on CFP to fill voids using Doctor Blade. The slurry-loaded CFP was cut into two pieces and one was placed on another to obtain a double layered cathode. For a comparison, a thin layer of slurry was cast onto carbon-coated Al foil. Both samples were dried under vacuum at the 60°C for 12 h. The mass loading of sulfur was about 1.0 mg cm^{-2} in the S/DPAN/CNT cathode on the Al foil current collector and about 3.5–5 mg cm^{-2} in cathodes on the double layered CFP. The prepared cells were galvanostatically cycled in a voltage range of 1.0–3.0 V vs. Li^+/Li using the multichannel battery tester (BT-2000, Arbin Instruments Inc.) and the specific capacity was calculated based on the mass of the sulfur in the electrode. A cyclic voltammogram (CV) was received at a potential range from 1 to 3 V vs. Li^+/Li at a scan rate of 0.1 mV s^{-1} (VMP3 potentiostat/galvanostat, Bio-Logic Instruments). All the electrochemical measurements were carried out at room temperature.

RESULTS AND DISCUSSION

Composite cathodes with increased mass loading of sulfur were prepared by simple slurry casting of a S/DPAN/CNT composite on CFP and layering it as shown in **Figure 1**. The slurry-loaded CFPs were layered in a wet condition to increase the amount of sulfur per the unit of electrode area and were dried in a pressed condition to ensure better contact between layers. The three dimensional structure of the low-weight CFP allowed it to hold a high amount of the S/DPAN/CNT composite, and carbon fibers ensured a high bulk conductivity of the electrode (Suktha et al., 2015). The addition of small amounts of CNT into the composite in the stage of heat treatment improved the electron conduction within the composite spheres.

The morphology of the synthesized S/DPAN/CNT composite was investigated by SEM analysis. **Figure 2A** shows the S/DPAN/CNT composite with 50 wt% sulfur and 3 wt% CNT content which has spherical S/DPAN particles interconnected with CNT. Additionally, the distribution of S, C, and N elements in the composite was analyzed by the SEM/EDS. **Figure 2B** shows the mapping of S, C, and N elements in the S/DPAN/CNT composite, which illustrates the homogenous distribution of sulfur within the composite (**Figure 2B**).

Figure 3 represents the XRD patterns of the pure components and synthesized composites. It can be seen that CNT shows an intensive peak at about 27°, which can be indexed as the C (002) reflection of the hexagonal graphitic structure, while PAN and sulfur exhibit high crystallinity (16.5° on PAN and sharp peaks between 10° and 60° S, respectively) (Wang et al., 2015). The XRD patterns of the heat-treated S/DPAN/CNT composite exhibits no peak of crystalline PAN, which was dehydrogenated and probably bound with sulfur during the heat treatment (Chung et al., 2016). The sulfur exhibits two different phase forms according to the XRD analysis which are crystalline and amorphous. The sharp peaks of crystalline sulfur with lower intensity (labelled by star) can still be observed in the S/DPAN/CNT composite with a sulfur content of 54 wt%, while they completely disappeared in the case of the S/DPAN/CNT composite with 50 wt% of sulfur. These sharp peaks are related to the excess sulfur which is not bound with the polymer matrix and remains crystalline on its surface (Wang et al., 2015). The detailed structure information about the S/DPAN composite has

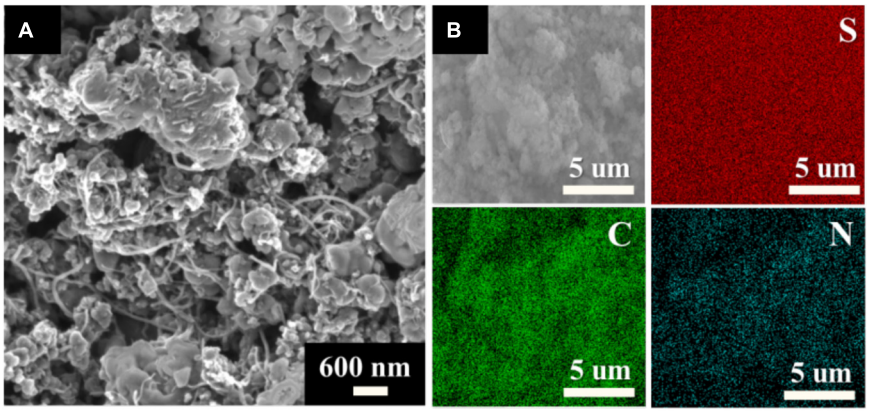

FIGURE 2 | SEM images of S/DPAN/CNT composite. **(A)** high resolution image of S/DPAN/CNT composite; **(B)** C, S, N element distributions in S/DPAN/CNT composite.

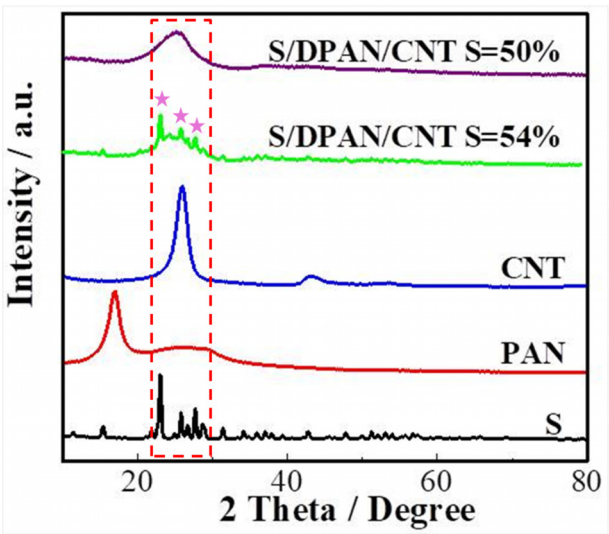

FIGURE 3 | XRD results of S/DPAN/CNT composites.

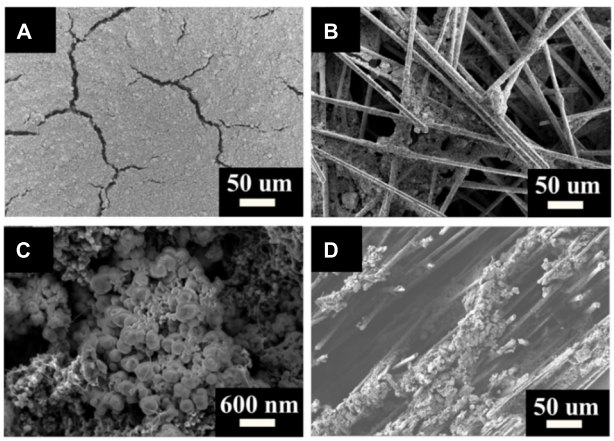

FIGURE 4 | SEM images of S/DPAN/CNT cathodes. **(A)** S/DPAN/CNT cathode on Al foil, **(B,C)** low and high magnification S/DPAN/CNT cathode on CFP current collector, and **(D)** cross-section view of S/DPAN/CNT cathode on CFP current collector.

been explored and described previously in literature (Wang et al., 2015). Thereby, sulfur bound to the dehydrogenated PAN and converted to an amorphous state, which represents embedding into the heterocyclic structure of PAN (Konarov et al., 2014). Also, the sharp peak of CNT is weakened and overlapped with a broad peak of the amorphous S/DPAN. Therefore, in further experiments S/DPAN/CNT with 50 wt% sulfur was used.

The signals of the C–S and S–S bonds were analyzed by Raman spectra shown in **Supplementary Figure S1**. The elemental sulfur has strong sharp characteristic peaks according to the reports (Yu et al., 2004), which are very weak in the S/DPAN/CNT composite, and some peaks have completely disappeared. The appeared new peaks at 309, 380, 930, and 1149 cm^{-1} indicate the presence of chemical bonding between cyclized PAN and elemental sulfur (Yu et al., 2004). In the higher frequency region of the Raman spectra (above 1200 cm^{-1}), two dominant peaks emerged which are related to carbon-based materials after pyrolysis of the polymer. The broad peak centered at 1520 cm^{-1}, often referred as G band, is due to a graphite-like structure, and 1320 cm^{-1} is due to a disordered structure or D band. The FTIR spectra of the composite was also analyzed to investigate the cyclization of PAN and interaction of sulfur with pyrolyzed PAN (**Supplementary Figure S2**). The FTIR spectrum of PAN has characteristic peaks of –CN and $–CH_2$ groups at 2244 cm^{-1} and 1454 cm^{-1}, while in the spectrum of S/DPAN/CNT several new peaks appeared. The peaks at 1485 cm^{-1} and 1351 cm^{-1} correspond to –C = C double bond and –CH deformation, respectively and the peaks at 1413 cm^{-1} and 800 cm^{-1} attribute to the cyclized structure of polymer (Kalybekkyzy et al., 2019). Moreover, the two new weak peaks detected at 663 cm^{-1} and 509 cm^{-1} belong to C–S and S–S stretching vibrations, indicating that sulfur can be chemically bonded with dehydrogenated PAN (DPAN) (Zhang Y.Z. et al., 2014). According to the reports, elemental sulfur is inactive in IR,

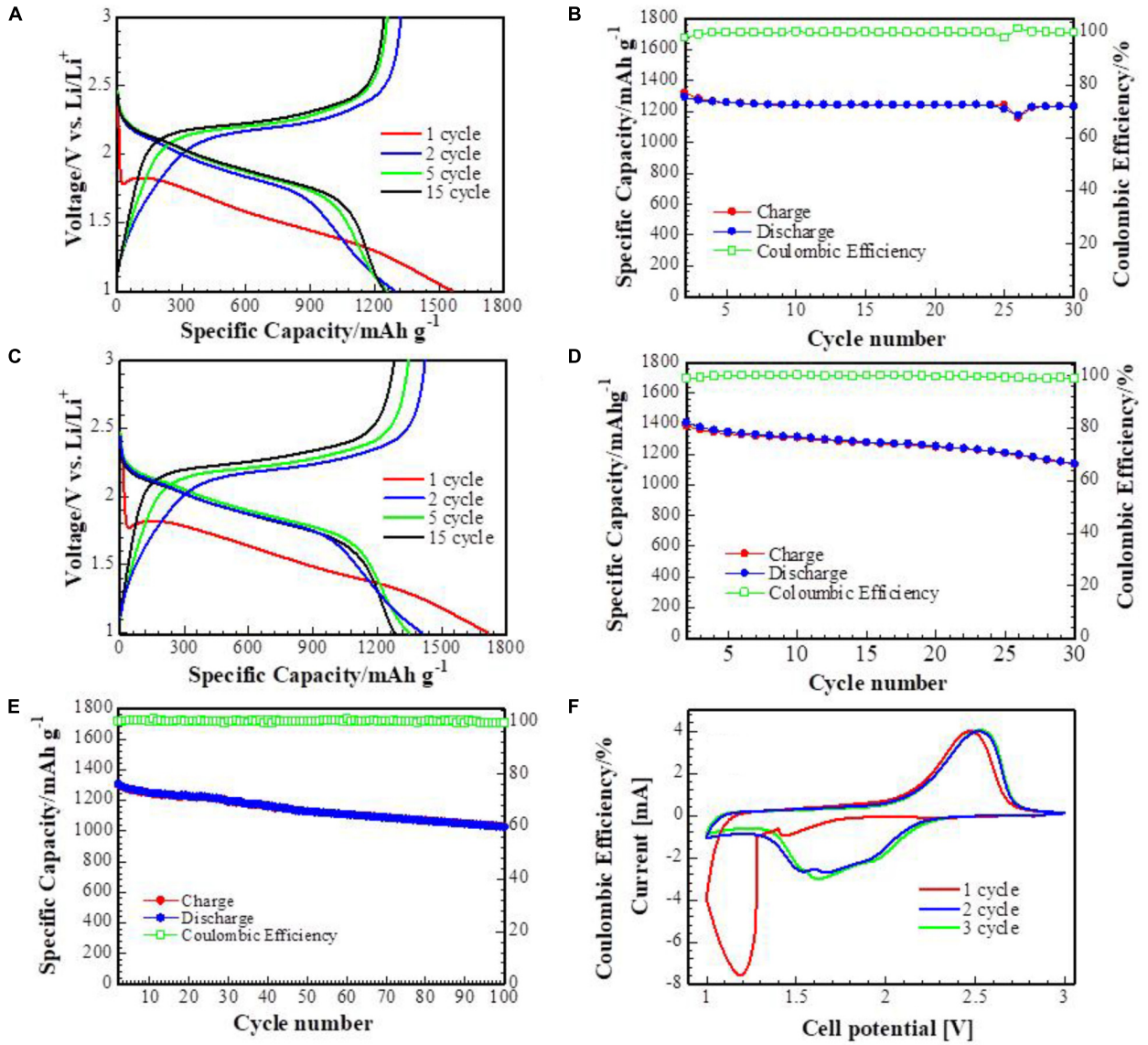

FIGURE 5 | Potential profiles and cycle performance of S/DPAN/CNT composite cathodes. **(A,B)** cathodes on Al current collector. **(C,D)** cathodes on CFP current collector at 0.1C, **(E)** longer cycling performance of S/DPAN/CNT on CFP current collector **(F)** CV profiles (0.1 mV s^{-1}) of the cells with S/DPAN/CNT cathode.

the vibration at 509 cm^{-1} can only be caused by the stretching of S–S bonds in the compound-state (Yu et al., 2004). Additionally, the peak at 930 cm^{-1} corresponds to the ring breathing in which a C-S bond is also included together with the side chain of the S–S ring (Wang et al., 2012; Chen et al., 2019). Therefore, these characteristic peaks verify the structure of C-S and S-S bonds after the dehydrogenation reaction.

The morphology of the S/DPAN/CNT cathodes on Al foil and CFP was analyzed by SEM as shown in **Figure 4**. The SEM image of the S/DPAN/CNT composite cathode on an Al foil current collector (**Figure 4A**), indicate that the slurry was homogeneously distributed onto the surface of the current collector, while cracks of 7 μm in width appeared on its surface due to solvent evaporation. In the case of the CFP current collector (**Figures 4B,C**), the main part of the composite cathode was loaded into the large free space between interconnected carbon fibers. Moreover, the complete filling of the free space between the layers of CFP can be confirmed by the cross-section SEM image (**Figure 4D**). A SEM image with higher magnification (**Figure 4C**) shows that hundreds of nanometers in size particles of S/DPAN are bridged with CNTs and the small particles of a conductive agent (AB, 10 wt%). Also, mapping of the elements in the S/DPAN/CNT composite cathode on CFP illustrates the homogenous distribution of S, C, and N elements within the electrode (**Supplementary Figure S3**).

Electrochemical performance of the S/DPAN/CNT composite cathode with different amounts of CNT (1–4%) was tested using a carbon coated Al foil current collector

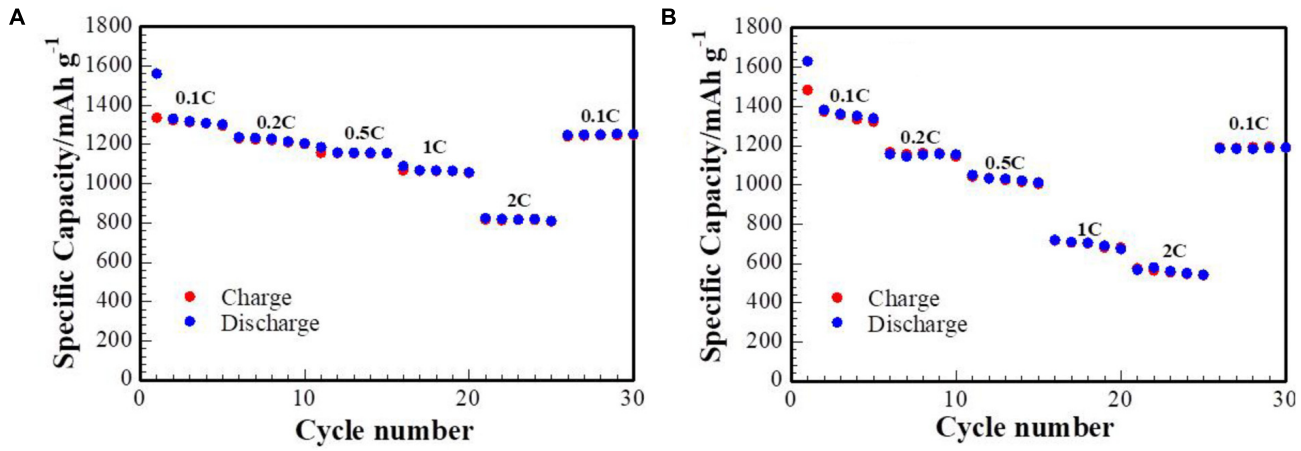

FIGURE 6 | Rate capability test of cells with S/DPAN/CNT composite cathodes. **(A)** cathode on Al foil current collector (mass loading 1.0 mg cm^{-2}). **(B)** Cathode on CFP current collector (mass loading 4.0 mg cm^{-2}).

(**Supplementary Figure S4**) with an equal sulfur content (50%) and mass loading of 1.0 mg cm^{-2}. The S/DPAN/CNT composite cathode with 3% CNT showed the highest capacity retention and lower polarization among other composite cathodes. However, increasing the amount of CNT up to 4% shows no improvement in electrochemical performance. Comparative analysis of the EIS data was performed on the electrodes with equal mass loading of sulfur of 1.0 mg cm^{-2} (**Supplementary Figure S5**). Increasing the content of CNT led to a smaller charge transfer resistance which could refer to the conductivity improvement due to the addition of highly conductive CNT (Mentbayeva et al., 2016; Li T. et al., 2017). Therefore, the S/DPAN/CNT composite cathode with 3 wt% CNT was used in further experiments.

Figures 5A–E represent galvanostatic charge-discharge and cyclability of Li-S cells with the S/DPAN/CNT with 3 wt% CNT composite cathode on the Al and CFP current collectors. The composite cathode on Al foil with sulfur mass loading of 1 mg cm^{-2} delivers a high discharge capacity of 1350 mAh g^{-1} at the 2nd cycle at 0.1C. At the first 30 cycles the cells performed stable capacity retention with a high coulombic efficiency of about 100%. At the same time the cathode on the CFP current collector showed similar specific capacity at the 2nd, 5th, and 15th cycles when the mass loading of sulfur was increased up to 5 mg cm^{-2}. Similar electrochemical results of the composite cathode on CFP compared to the cathode on the Al foil can be explained in terms of the high conductivity of long carbon fibers (Suktha et al., 2015), which ensures the electrode integrity while large voids of CFP provides mechanical support to accommodate volume change, and CNT maintains structural integrity and faster electron conduction at the micro level (Peng et al., 2017b; Qin et al., 2017). The longer cycling performance of the cell with the S/DPAN/CNT composite cathode on the CFP current collector and sulfur mass loading of 4 mg cm^{-2} is illustrated in **Figure 5E**. It can be seen that the cell maintained a stable capacity of 1030 mAh g^{-1} at the 100th cycle.

Figure 5F illustrates CV curves of the cathode on the CFP current collector. The composite cathode exhibits a large reduction peak at 1.2 V vs. Li^+/Li. This peak slightly moves to the higher voltage at the next cycle. A large polarization between the reduction and oxidation peaks during the first cycles could stem from the generation of the solid electrolyte interface (SEI) on the anode surface (Zhang et al., 2013). During the following cycles a large oxidation peak at 2.5 V vs. Li^+/Li and two reduction peaks at 1.7 and 1.6 V presented, which can be explained by the formation of long-chain lithium polysulfides and low-order lithium sulfides (Zhang et al., 2013).

Figure 6 represents the rate step-progressive test of batteries with S/DPAN/CNT (3 wt% CNT) composite cathodes on both Al foil and CFP current collectors, where cells were galvanostatically cycled at current densities ranging from 0.1C up to 2C. At the lower current densities of 0.1C, 0.2C, 0.5C, and 1C stable capacities of 1340, 1215, 1160, 1050 mAh g^{-1}, respectively, were achieved, while the 2C capacity of 791 mAh g^{-1} was obtained for the cathode on the Al foil current collector. Then the initial capacity of 1245 mAh g^{-1} was regenerated when the current density was lowered back to 0.1C. In comparison, the cathode on the CFP current collector with mass loading of sulfur at 4.0 mg cm^{-2} showed stable capacities of 1345, 1150, 1010, 650, 570 mAh g^{-1}, respectively. High capacity retention can be observed when the current density was lowered back to 0.1C. Thus, the CFP fibers provide better conductivity and better active material utilization was achieved at high cycling rates.

Increasing the mass loading of sulfur should go along with the addition of conductive agents in order to provide sufficient bulk conductivity. As described above the addition of 3% CNT significantly lowers the charge transfer resistance (**Supplementary Figure S5**). Consequently, the entrapping of composite cathodes into a 3D structured CFP current collector and the addition of small amounts of CNT to the composite

remarkably improves the electron conduction of the cathode, which enables a reasonable C rate performance of the cathode with mass loading as high as 4 mg cm^{-2}.

The post-cycling morphology of the S/DPAN/CNT composite cathode on the CFP current collector after 30 cycles of discharge and charge processes was analyzed using SEM (**Supplementary Figure S6**). A SEM image with high magnification clearly shows the agglomeration of the particles, which can be explained by the irreversible formation of low order lithium sulfides due to the partial loss of contact between the composite cathode and current collector (Pan et al., 2015). This is one of the reasons of the capacity decay of the cell upon cycling. In general, there are minor changes in surface morphology. Particles are equally distributed between long carbon fibers, which can be explained by the strong adhesion and stability of the composite.

CONCLUSION

To sum up, a S/DPAN/CNT composite cathode with 1–4% CNT and 50 wt% sulfur content was synthesized by manual mixing of sulfur, PAN, and CNT followed by heating in an argon atmosphere. Composites with 3 wt% CNT showed better electrochemical performance among other composites (1–4 wt% CNT). The results of both Raman and FTIR spectra of the composite showed the interaction of sulfur with PAN (S-C bond) and cyclization of PAN. Fixing sulfur to a pyrolyzed PAN structure can diminish the dissolution of polysulfides, while CNT acts as interwoven network and maintains structural integrity. Injection of S/DPAN/CNT into double layered CFP allowed for obtaining a high mass loading (5.0 mg cm^{-2}) sulfur composite cathode with initial capacity of 1400 mAh g^{-1}. The cells with a mass loading of sulfur of 4 mg cm^{-2} showed stable capacity retention up to 100 cycles and a stable rate capability, due to improved bulk conductivity of the cathode by carbon fibers and CNT.

DATA AVAILABILITY STATEMENT

All datasets presented in this study are included in the article/**Supplementary Material**.

AUTHOR CONTRIBUTIONS

AM: conceptualization, methodology, validation, data curation, writing – original draft, and supervision. NB: writing – original draft, data curation, and writing – review and editing. NS: validation, investigation, and visualization. SK: investigation, recourses, and visualization. IK: investigation and recourses. ZB: writing – review and editing, and funding acquisition.

FUNDING

This work was supported by the Faculty development competitive research grant #080420FD1906 from Nazarbayev University and by the State Target Program #BR05236524 from the Ministry of Education and Science of the Republic of Kazakhstan.

ACKNOWLEDGMENTS

The authors thank the Shared Facility of Nazarbayev University for access to laboratory equipment.

SUPPLEMENTARY MATERIAL

The Supplementary Material for this article can be found online at: https://www.frontiersin.org/articles/10.3389/fenrg.2020.00207/full#supplementary-material

REFERENCES

Bakenov, Z., Yashiro, H., Sun, Y.-K., Myung, S.-T., and Konarov, A. (2017). Effect of carbon-sulphur bond in a sulphur/dehydrogenated polyacrylonitrile/reduced graphene oxide composite cathode for lithium-sulphur batteries. *J. Power Sources* 355, 140–146. doi: 10.1016/j.jpowsour.2017.04.063

Chen, X., Peng, L., Wang, L., Yang, J., Hao, Z., Xiang, J., et al. (2019). Ether-compatible sulfurized polyacrylonitrile cathode with excellent performance enabled by fast kinetics via selenium doping. *Nat. Commun.* 10, 1–9. doi: 10.1038/s41467-019-08818-6

Cheng, X.-B., Huang, J.-Q., Zhang, Q., Xu, W.-T., Peng, H.-J., Wang, D.-W., et al. (2016). 3D carbonaceous current collectors: the origin of enhanced cycling stability for high-sulfur-loading lithium-sulfur batteries. *Adv. Funct. Mater.* 26, 6351–6358. doi: 10.1002/adfm.201602071

Chung, S. H., Chang, C. H., and Manthiram, A. (2016). A carbon-cotton cathode with ultrahigh-loading capability for statically and dynamically stable lithium-sulfur batteries. *ACS Nano* 10, 10462–10470. doi: 10.1021/acsnano.6b06369

Chung, S. H., and Manthiram, A. (2018). Rational design of statically and dynamically stable lithium–sulfur batteries with high sulfur loading and low electrolyte/sulfur ratio. *Adv. Mater.* 30, 1–9. doi: 10.1002/adma.201705951

Guo, J., Xu, Y., and Wang, C. (2011). Sulfur-impregnated disordered carbon nanotubes cathode for lithium-sulfur batteries. *Nano Lett.* 11, 4288–4294. doi: 10.1021/nl202297p

Hara, T., Konarov, A., Mentbayeva, A., Kurmanbayeva, I., and Bakenov, Z. (2015). High mass-loading of sulfur-based cathode composites and polysulfides stabilization for rechargeable lithium/sulfur batteries. *Front. Energy Res.* 3:22. doi: 10.3389/fenrg.2015.00022

Kalybekkyzy, S., Mentbayeva, A., Kahraman, M. V., Zhang, Y., and Bakenov, Z. (2019). Flexible S/DPAN/KB Nanofiber Composite as Binder-Free Cathodes for Li-S Batteries. *J. Electrochem. Soc.* 166, A5396–A5402. doi: 10.1149/2.0571903jes

Kalybekkyzy, S., Mentbayeva, A., Yerkinbekova, Y., Baikalov, N., Kahraman, M. V., and Bakenov, Z. (2020). Electrospun 3D structured carbon current collector for Li/S batteries. *Nanomaterials* 10, 1–13. doi: 10.3390/nano10040745

Konarov, A., Gosselink, D., Doan, T. N. L., Zhang, Y., Zhao, Y., and Chen, P. (2014). Simple, scalable, and economical preparation of sulfur-PAN composite cathodes for Li/S batteries. *J. Power Sources* 259, 183–187. doi: 10.1016/j.jpowsour.2014.02.078

Li, G., Wang, S., Zhang, Y., Li, M., Chen, Z., and Lu, J. (2018). Revisiting the Role of Polysulfides in Lithium–sulfur batteries. *Adv. Mater.* 30, 1–19. doi: 10.1002/adma.201705590

Li, H., Wang, J., Zhang, Y., Wang, Y., Mentbayeva, A., and Bakenov, Z. (2019). Synthesis of carbon coated Fe3O4 grown on graphene as effective sulfur-host

materials for advanced lithium/sulfur battery. *J. Power Sources* 437, 226901. doi: 10.1016/j.jpowsour.2019.226901

Li, M., Carter, R., Douglas, A., Oakes, L., and Pint, C. L. (2017). Sulfur Vapor-Infiltrated 3D Carbon Nanotube foam for binder-free high areal capacity Lithium-Sulfur battery composite cathodes. *ACS Nano* 11, 4877–4884. doi: 10.1021/acsnano.7b01437

Li, T., Bo, H., Cao, H., Lai, Y., Liu, Y., and Huang, Z. (2017). Effects of carbon hosts on electrochemical properties of lithium-sulfur batteries. *Int. J. Electrochem. Sci.* 12, 5731–5741. doi: 10.20964/2017.06.41

Lu, S., Chen, Y., Wu, X., Wang, Z., and Li, Y. (2014). Three-dimensional sulfur/graphene multifunctional hybrid sponges for lithium-sulfur batteries with large areal mass loading. *Sci. Rep.* 4, 4–7. doi: 10.1038/srep04629

Ma, W., and Xu, Q. (2018). Lithium cobaltate: a novel host material enables high-rate and stable lithium–sulfur batteries. *Rare Met.* 37, 929–935. doi: 10.1007/s12598-018-1129-4

Mentbayeva, A., Belgibayeva, A., Umirov, N., Zhang, Y., Taniguchi, I., Kurmanbayeva, I., et al. (2016). High performance freestanding composite cathode for lithium-sulfur batteries. *Electrochim. Acta* 217, 242–248. doi: 10.1016/j.electacta.2016.09.082

Nie, Z., Zhang, J.-G., Browning, N. D., Li, Q., Mehdi, L. B., Xie, X., et al. (2015). High energy density Lithium-Sulfur Batteries: challenges of thick Sulfur Cathodes. *Adv. Energy Mater.* 5:1402290. doi: 10.1002/aenm.201402290

Ould Ely, T., Kamzabek, D., Chakraborty, D., and Doherty, M. F. (2018). Lithium–Sulfur batteries: state of the art and future directions. *ACS Appl. Energy Mater.* 1, 1783–1814. doi: 10.1021/acsaem.7b00153

Pan, J., Xu, G., Ding, B., Han, J., Dou, H., and Zhang, X. (2015). Enhanced electrochemical performance of sulfur cathodes with a water-soluble binder. *RSC Adv.* 5, 13709–13714. doi: 10.1039/c4ra15303k

Peng, H., Huang, J., Cheng, X., and Zhang, Q. (2017a). Review on high-loading and high-energy Lithium – Sulfur Batteries. 1700260, 1–54. doi: 10.1002/aenm.201700260

Peng, H., Wang, X., Zhao, Y., Tan, T., Mentbayeva, A., Bakenov, Z., et al. (2017b). Enhanced electrochemical performance of sulfur/polyacrylonitrile composite by carbon coating for lithium/sulfur batteries. *J. Nanoparticle Res.* 19:348. doi: 10.1007/s11051-017-4049-6

Peng, H., Wang, X., Zhao, Y., Tan, T., Bakenov, Z., and Zhang, Y. (2018). Synthesis of a flexible freestanding sulfur/polyacrylonitrile/graphene oxide as the cathode for lithium/sulfur batteries. *Polymers* 10, 1–10. doi: 10.3390/polym10040399

Qin, F., Wang, X., Zhang, K., Fang, J., Li, J., and Lai, Y. (2017). High areal capacity cathode and electrolyte reservoir render practical Li-S batteries. *Nano Energy* 38, 137–146. doi: 10.1016/j.nanoen.2017.05.037

Rajkumar, P., Diwakar, K., Subadevi, R., Gnanamuthu, R. M., and Sivakumar, M. (2019). Sulfur cloaked with different carbonaceous materials for high performance lithium sulfur batteries. *Curr. Appl. Phys.* 19, 902–909. doi: 10.1016/j.cap.2019.05.001

Shin, K.-H., Kim, K.-B., Jin, C.-S., Ahn, W., and Jung, K.-N. (2011). Synthesis and electrochemical properties of a sulfur-multi walled carbon nanotubes composite as a cathode material for lithium sulfur batteries. *J. Power Sources* 202, 394–399. doi: 10.1016/j.jpowsour.2011.11.074

Song, X., Wang, S., Bao, Y., Liu, G., Sun, W., Ding, L. X., et al. (2017). A high strength, free-standing cathode constructed by regulating graphitization and the pore structure in nitrogen-doped carbon nanofibers for flexible lithium-sulfur batteries. *J. Mater. Chem. A* 5, 6832–6839. doi: 10.1039/C7TA01171G

Suktha, P., Chiochan, P., Iamprasertkun, P., Wutthiprom, J., Phattharasupakun, N., Suksomboon, M., et al. (2015). High-Performance Supercapacitor of Functionalized Carbon Fiber Paper with High Surface ionic and bulk electronic conductivity: effect of organic functional groups. *Electrochim. Acta* 176, 504–513. doi: 10.1016/j.electacta.2015.07.044

Wang, B. J., Yang, J., Wan, C., Du, K., Xie, J., and Xu, N. (2003). Sulfur Composite Cathode Materials for Rechargeable Lithium Batteries. *Adv. Funct. Mater.* 13, 487–492. doi: 10.1002/adfm.200304284

Wang, J., He, Y. S., and Yang, J. (2015). Sulfur-based composite cathode materials for high-energy rechargeable lithium batteries. *Adv. Mater.* 27, 569–575. doi: 10.1002/adma.201402569

Wang, L., He, X., Li, J., Gao, J., Guo, J., Jiang, C., et al. (2012). Analysis of the synthesis process of sulphur-poly(acrylonitrile)-based cathode materials for lithium batteries. *J. Mater. Chem.* 22, 22077–22081. doi: 10.1039/c2jm30632h

Yang, C. P., Yin, Y. X., Ye, H., Jiang, K. C., Zhang, J., and Guo, Y. G. (2014). Insight into the effect of boron doping on sulfur/carbon cathode in lithium-sulfur batteries. *ACS Appl. Mater. Interfaces* 6, 8789–8795. doi: 10.1021/am501627f

Ye, X., Ma, J., Hu, Y. S., Wei, H., and Ye, F. (2016). MWCNT porous microspheres with an efficient 3D conductive network for high performance lithium-sulfur batteries. *J. Mater. Chem. A* 4, 775–780. doi: 10.1039/c5ta08991c

Yin, L., Wang, J., Lin, F., Yang, J., and Nuli, Y. (2012). Polyacrylonitrile/graphene composite as a precursor to a sulfur-based cathode material for high-rate rechargeable Li-S batteries. *Energy Environ. Sci.* 5, 6966–6972. doi: 10.1039/c2ee03495f

Yu, X., Deng, J., Lv, R., Huang, Z. H., Li, B., and Kang, F. (2018). A compact 3D interconnected sulfur cathode for high-energy, high-power and long-life lithium-sulfur batteries. *Energy Storage Mater.* 20, 1–10. doi: 10.1016/j.ensm.2018.11.029

Yu, X. G., Xie, J. Y., Yang, J., Huang, H. J., Wang, K., and Wen, Z. S. (2004). Lithium storage in conductive sulfur-containing polymers. *J. Electroanal. Chem.* 573, 121–128. doi: 10.1016/j.jelechem.2004.07.004

Yuan, L., Yuan, H., Qiu, X., Chen, L., and Zhu, W. (2009). Improvement of cycle property of sulfur-coated multi-walled carbon nanotubes composite cathode for lithium/sulfur batteries. *J. Power Sources* 189, 1141–1146. doi: 10.1016/j.jpowsour.2008.12.149

Zeng, F., Wang, W., Wang, A., Yuan, K., Jin, Z., and Yang, Y. (2015). Multidimensional Polycation β – Cyclodextrin Polymer as an E ff ective Aqueous Binder for High Sulfur Loading Cathode in Lithium – Sulfur Batteries. *ACS Appl. Mater. Interfaces* 7, 26257–26265. doi: 10.1021/acsami.5b08537

Zhang, Y., Bakenov, Z., Zhao, Y., Konarov, A., Doan, T. N. L., Malik, M., et al. (2012). One-step synthesis of branched sulfur/polypyrrole nanocomposite cathode for lithium rechargeable batteries. *J. Power Sources* 208, 1–8. doi: 10.1016/j.jpowsour.2012.02.006

Zhang, Y., Zhao, Y., Yermukhambetova, A., Bakenov, Z., and Chen, P. (2013). Ternary sulfur/polyacrylonitrile/Mg0.6Ni0.4O composite cathodes for high performance lithium/sulfur batteries. *J. Mater. Chem. A* 1, 295–301. doi: 10.1039/c2ta00105e

Zhang, Y. Z., Liu, S., Li, G. C., Li, G. R., and Gao, X. P. (2014). Sulfur/polyacrylonitrile/carbon multi-composites as cathode materials for lithium/sulfur battery in the concentrated electrolyte. *J. Mater. Chem. A* 2, 4652–4659. doi: 10.1039/c3ta14914e

Zhang, Y., Zhao, Y., Bakenov, Z., Tuiyebayeva, M., Konarov, A., and Chen, P. (2014). Synthesis of hierarchical porous sulfur/polypyrrole/multiwalled carbon nanotube composite cathode for lithium batteries. *Electrochim. Acta* 143, 49–55. doi: 10.1016/j.electacta.2014.07.148

Zhao, Y., Zhang, Y., Bakenova, Z., and Bakenov, Z. (2015). Carbon/Sulfur Composite Cathodes for Flexible Lithium/Sulfur batteries: status and prospects. *Front. Energy Res.* 3:2. doi: 10.3389/fenrg.2015.00002

Conflict of Interest: ZB and IK were employed by the company Institute of Batteries LLC.

The remaining authors declare that the research was conducted in the absence of any commercial or financial relationships that could be construed as a potential conflict of interest.

frontiers in Energy Research

ORIGINAL RESEARCH
published: 09 November 2020
doi: 10.3389/fenrg.2020.595481

Evaluating Sulfur-Composite Cathode Material with Lithiated Graphite Anode in Coin Cell and Pouch Cell Configuration

*Berik Uzakbaiuly[1], Almagul Mentbayeva[1,2,3], Aishuak Konarov[2,3], Indira Kurmanbayeva[1,2], Yongguang Zhang[4] and Zhumabay Bakenov[1,2,3]**

[1]National Laboratory Astana, Nazarbayev University, Nur-Sultan, Kazakhstan, [2]Department of Chemical and Materials Engineering, Nazarbayev University, Nur-Sultan, Kazakhstan, [3]Institute of Batteries LLC, Nur-Sultan, Kazakhstan, [4]Research Institute for Energy Equipment Materials, Hebei University of Technology, Tianjin, China

High-performance sulfur-composite cathode material, sulfur/polyacrylonitrile/ketjen black, was prepared by simple mixing and low-temperature heat treatment route. The cell made of the composite cathode and anode from metallic lithium or lithiated graphite was assembled in coin cell configuration. Half-cells retained about 70% of their initial capacity of 1,270 mAh g^{-1} after 150 cycles, while full-cells retained about 85% of the initial capacity of 1,500 mAh g^{-1} for over 150 cycles. Since coin cells do not reflect the true performance of a practical cell, the cathode composite was assembled with lithiated graphite anode in a 45 × 85 × 6 mm^3 pouch cell configuration. This cell retained about 81% of its initial capacity for over 100 cycles. At high cycling rates up to 1 C, the pouch cell demonstrated a moderate rate capability and exhibited good recovery and stable performance after high rate cycling. Also, the cell successfully passed safety tests such as overcharge, deep discharge, and mechanical short circuit tests.

Keywords: lithium sulfur battery, sulfur-composite cathode materials, Li-S coin and pouch cells, rechargeable battery, lithiated electrode for Li-S battery

OPEN ACCESS

Edited by:
Hyo-Jun Ahn, Gyeongsang National University, South Korea

Reviewed by:
Jae-Kwang Kim, Cheongju University, South Korea
Mehmet Kadri Aydinol, Middle East Technical University, Turkey

****Correspondence:***
Berik Uzakbaiuly
berik.uzakbaiuly@nu.edu.kz;
Zhumabay Bakenov
zbakenov@nu.edu.kz

Specialty section:
This article was submitted to Electrochemical Energy Conversion and Storage, a section of the journal Frontiers in Energy Research

Received: *16 August 2020*
Accepted: *29 September 2020*
Published: *09 November 2020*

Citation:
Uzakbaiuly B, Mentbayeva A, Konarov A, Kurmanbayeva I, Zhang Y and Bakenov Z (2020) Evaluating Sulfur-Composite Cathode Material with Lithiated Graphite Anode in Coin Cell and Pouch Cell Configuration. Front. Energy Res. 8:595481. doi: 10.3389/fenrg.2020.595481

INTRODUCTION

Li-ion batteries (LIBs) based upon nickel-rich layered transition metal oxide cathodes $LiNi_{1-x-y}Mn_xCo_yO_2$ (NMC, x + y < 0.5) and graphite anodes are ubiquitous cells of several battery manufacturers. LIBs deliver high energy density (> 200 Wh kg^{-1}) and stable cycle performance (> 1,000 cycles), as long as problems like flammable liquid electrolytes, overheating, extreme temperature failure, overcharge, and deep discharge are appropriately managed by designing a thorough battery management system (Rahimi-Eichi et al., 2013; Nitta et al., 2015). This, of course, along with increasing prices for nickel and cobalt, adds to the price of the battery at the pack level and the required progress toward the cost of energy storage < 100 USD kWh^{-1} for electric vehicles, unmanned aerial vehicles, and portable devices are still ongoing. In addition, in order to reach 500 Wh kg^{-1} energy density at the cell level, investigation of the possibilities of replacing graphite anode with Li-metal is one of the pursuits of many researchers (Albertus et al., 2017; Choudhury, 2019; Liu et al., 2019a; Yasin et al., 2019). However, the problems such as Li-metal consumption, dendrite formation, electrolyte contamination, and volume change upon cycling still have not been resolved entirely.

In order to enhance electrochemical performance, compensate the battery cost, and ensure safety at the cell level, various technologies are under development such as nonflammable polymer electrolytes (Croce et al., 1998; Wang et al., 2019; Wei et al., 2019), solid electrolytes (Liu et al., 2019b; Zhao et al., 2019), lithium/sulfur (Li/S) batteries (Aurbach et al., 2009; Liang et al., 2016; Seh et al., 2016), and others (Girishkumar et al., 2010; Omampuliyur et al., 2015). Li/S batteries are considered as next-generation batteries, which offer a high theoretical energy density of 2,500 Wh kg^{-1} with a very competitive price at the cell level (70 USD kWh^{-1}) (Hagen et al., 2015). Although several groups have claimed good capacity and cyclability with sulfur-composite cathode materials, many of them have used coin cell configuration whose properties cannot be translated into practical pouch cells (Cheng et al., 2017; Liu et al., 2019a). In coin cells, the electrolyte is overflooded (> 10 μL mg^{-1} of cathode), and the Li foil that is usually used as a counter electrode is very thick (> 250 μm), whereas in practical pouch cells, the electrolyte content should be limited and Li-metal should be as thin as possible in order to reach high energy densities of 500 Wh kg^{-1}. In addition, uneven current distribution in the practical cell causes Li dendrites to grow, which in turn may short-circuit the cell and hinders its long-term operation (Cheng et al., 2017). Therefore, a newly developed cathode material, after testing in a coin cell, needs to be tested in a pouch cell configuration to verify its practicality.

One of the most popular ways of a sulfur cathode material preparation is a formation of a sulfur-carbon composite. For example, a multiwalled carbon nanotube/nano-S cathode exhibits excellent electrochemical performance, but it is composed of expensive MWCNT and nano-S (Yuan et al., 2009). Several sulfur/conductive polymer/conductive carbon ternary composites have been developed and offer an inexpensive alternative, yet their properties can be further optimized (Liang et al., 2016). For instance, polypyrrole-coated sulfur/ketjen black (S/KB) with 1,047 mAh g^{-1} initial discharge capacity decays in the performance during cycling due to the dissolution of polysulfides (Nakamura et al., 2016). The composites of sulfur with conductive polymer-polyacrylonitrile have been intensely investigated because it exhibited a capability to accommodate the sulfur volume change upon cycling, prevent polysulfide dissolution, and act as conductivity enhancer (Wang et al., 2002; Peng et al., 2017). Moreover, sulfurized polyacrylonitrile composite offers stable specific capacity, which is very close to the theoretical value of elemental sulfur and the simpler reaction mechanism avoiding long-chain polysulfide reaction, and offers chemical compatibility with $LiPF_6$-carbonate-based electrolyte with high Coulombic efficiency and low self-discharge (Zhang, 2014; Hara et al., 2015). **Figure 1** shows the reaction mechanism of sulfur/polyacrylonitrile (S/PAN) composite after the first and subsequent cycles, which has been proposed by Wang et al. (2018). The S-S bond is cleaved in the first discharge process, and subsequent S/PAN becomes conjugative with thiyl radical. This radical structure forms an ion-coordination bond which enables a fast Li-ion transfer mechanism. In this work, a mixture of sulfur/polyacrylonitrile/conductive carbon has been utilized to fabricate a composite cathode material that was evaluated in coin cell and pouch cell configuration. Testing in pouch cell configuration offers valuable insight into the feasibility of the composites for full-scale battery application. Here, we prepared sulfur/polyacrylonitrile/ketjen black (S/PAN/KB) composite by simple mixing of sulfur, KB, and PAN, followed by heat treatment in Ar environment. The preparation procedure is simple and offers opportunities for the most industrially suitable scale-up methods.

The successfully prepared S/PAN/KB composite cathode was tested in coin cell configuration both in half-cell configuration using Li-metal anode and in full-cell configuration using lithiated graphite as the anode. The full-cell configuration showed better cycling performance than the half-cell one because of a stable solid electrolyte interface (SEI) layer formed at the prelithiated graphite anode. The initial discharge capacity of the cell was about 1,500 mAh $g^{-1,}$ which is about 90% of the theoretical capacity of the sulfur anode, and the cell showed very stable electrochemical performance.

As the behavior of a cell in a coin cell configuration is not the true indication of practical battery performance, Li-metal free pouch cells of 2000 mAh and 10,000 mAh capacities were constructed to conduct the tests in the most close to practical application conditions. On the verge of several sulfur-composite materials' development, our pouch cell revealed great promises and could deliver high-performance capabilities with the Coulombic efficiency of 100% over 100 cycles. The developed composite material is inexpensive, enables high utilization of sulfur, and is very suitable for pouch cell design.

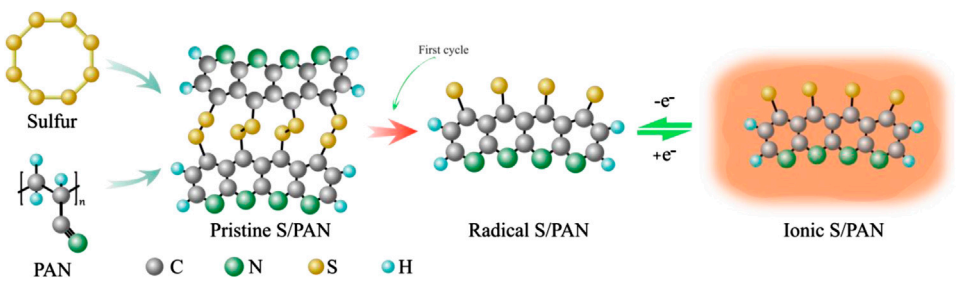

FIGURE 1 | S/PAN reaction mechanism with radical and ionic intermediates. Adapted with premission from Wang et al. (2018). Copyright (2018) American Chemical Society.

EXPERIMENTAL SECTION

Materials

Sulfur (98%, GOST 127.1, Tengizchevroil, Kazakhstan), polyacrylonitrile (average molecular weight 150,000, J&K Scientific), ketjen black (Akzo Nobel), and natural graphite (Hohsen Corp.) were used as received without further purification.

Material Synthesis and Cell Assembly

Sulfur, PAN, and KB were mixed in a weight ratio of 4 : 1 : 1.5 wt% using ball-mill (Pulverisette 7, Fritsch Inc.) and heat-treated at 300°C for 3 h in a tubular furnace in argon to form a molecular level composite S/PAN/KB. After heat treatment, the sulfur content in the S/PAN/KB composite cathode was about 47% as revealed by CHNS analysis (Vario Micro cube, Elementar Inc.). When a composite with a higher sulfur content value was prepared, the battery did not show good performance, and as a result, the S/PAN/KB composite prepared with a weight ratio of the components 4 : 1 : 1.5 was chosen for further characterization and cell assembly (Konarov et al., 2014; Mentbayeva et al., 2016).

Cell Assembly

The cathode slurry was prepared by dispersing 80 wt% of S/PAN/KB composite, 10 wt% of acetylene black (MTI, 99.5% purity), and 10 wt% polyvinylidene fluoride (PVDF, Kynar, HSV900) in N-methyl-2-pyrrolidone (NMP) (Sigma-Aldrich, 99.5% purity). The resulting slurry was drop-cast on aluminum foil (MTI) using the doctor blade technique. Afterward, the electrode sheet was vacuum-dried at 60°C for 12 h. Coin type cells were assembled in a glovebox (MasterLab, MBraun), using lithium metal discs (250 μm) as both counter (negative) and a reference electrode, porous polypropylene membrane as a separator (Celgard® 2,400), and 1 M $LiPF_6$ solution in ethylene carbonate/dimethyl carbonate/diethylene carbonate (EC : DMC : DEC, a volume ratio of 1 : 1 : 1, Targray) as a liquid electrolyte. The areal mass loading of the cathode was ~2 mg cm^{-2} with the electrolyte to the sulfur ratio of 30 ml g^{-1} (Mentbayeva et al., 2016). For a full-cell preparation, graphite anode was used.

Slurry preparation for graphite anode was the same as the above-described method. Graphite (80 wt%) was mixed with 10 wt% acetylene black and 10 wt% polyvinylidene fluoride in N-methyl-2-pyrrolidone, and the resulting slurry was cast on copper foil and then vacuum-dried. In order to lithiate the graphite, coin type cells (CR2032) were assembled using Li-metal as a counter electrode. After a few cycles, the charged cell was disassembled, and lithiated graphite was taken for further use. Graphite anode preparation for pouch cells was as follows. Double side coated electrodes were prepared by roll pressing single side graphite coated electrode and casting the graphite slurry on the other side followed by vacuum drying at 60°C for 12 h and roll pressing. Each side of the graphite anode was wetted with 20 μL cm^{-2} electrolyte and then sandwiched between two slides of Li foil and glass plates with applying a little pressure and placing into a glass container. The lithiated graphite preparation set was left in a glove box for 12 h and used for pouch cell assembly immediately after disassembling this set.

To assemble pouch cells, the electrode sheets with the dimensions 85 × 45 mm^2 for 2 Ah pouch cells and 165 × 135 mm^2 for 10 Ah pouch cells were used, and hence, vacuum mixer and vacuum coater were used in this case. Mass loading of sulfur was similar to that of the coin cell (2–2.2 mg cm^{-2}), and the mass loading of graphite was 10–12 mg cm^{-2} on each side of the electrode, which corresponded to an areal capacity of 3 mAh cm^{-2}. Pouch cells were assembled in the glovebox with 12 pairs of double side coated cathode and anode and then sealed in a pouch cell case under vacuum. All lithiation and cell assembly procedures were carried in an argon-filled glovebox (MasterLab, MBraun) with O_2 and H_2O values less than 0.1 ppm.

Characterization

Crystal structure analysis of the samples was carried out by X-ray diffraction (XRD, Rigaku SmartLab). The morphology of the materials was investigated using scanning electron microscopy (UHR FE-SEM SU9000, Hitachi Co.) with energy-dispersive spectroscopy (EDS), and the sulfur content was determined using chemical analysis (CHNS, Vario Micro cube, Elementar Inc.).

The electrochemical performance of the S/PAN/KB composite cathode was investigated using coin type (CR2032) and pouch cells. The cells were galvanostatically cycled at different current densities in a potential range of 1.0–3.0 V vs. Li/Li^+ on a multichannel battery tester (BT-2000, Arbin Instruments Inc.). Specific capacity and current density were calculated based on the weight of sulfur in the electrode. Cyclic voltammetry (CV) was conducted over a potential range from 1 to 3 V vs. Li/Li^+ at a scan rate of 0.1 mV s^{-1}. All electrochemical measurements were carried out at room temperature.

RESULTS AND DISCUSSION

As mentioned above, the S/PAN/KB composite with 47 wt% S was chosen for further characterization. The morphology of the S/PAN/KB cathode composite was studied by SEM. As can be seen in **Figure 2**, sulfur, nitrogen, and carbon distribution in the S/PAN/KB composite is very homogeneous, enabling electronically conductive media around low conductive sulfur. It can be seen that the composite has a particle size around 250 nm.

XRD data showed one broad peak at $2\theta = 25^{\circ}$, which revealed that the composite is amorphous in structure. This is in agreement with other reports which show the embedding of S into PAN structure (Wang et al., 2002; Konarov et al., 2014; Mentbayeva et al., 2016; Kalybekkyzy et al., 2019).

Charge/discharge profiles and cycling performance of the half-cell coin cell are presented in **Figures 3A,B**, respectively. The initial discharge capacity of the cell at 0.2 C was about 1700 mAh g^{-1}, which after an intrinsic initial irreversible capacity drop stabilized around 1,300 mAh g^{-1} for 100 cycles (Hara et al., 2015; Nakamura et al., 2016; Wang et al., 2018). The low potential discharge plateau at the first cycle ($\Delta V \sim -0.35$ V) and large initial discharge capacity is typical behavior for sulfurized polyacrylonitrile composite materials (Wang et al.,

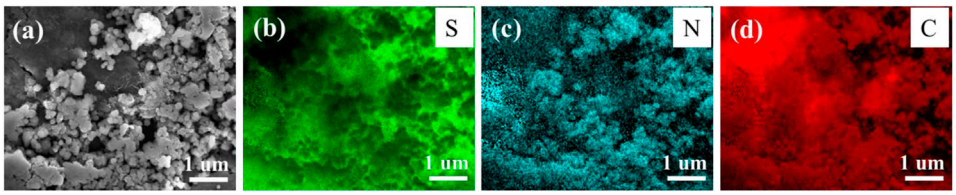

FIGURE 2 | (A) SEM-EDS image of S/PAN/KB composite, **(B)** sulfur, **(C)** nitrogen, and **(D)** carbon mapping of the composite.

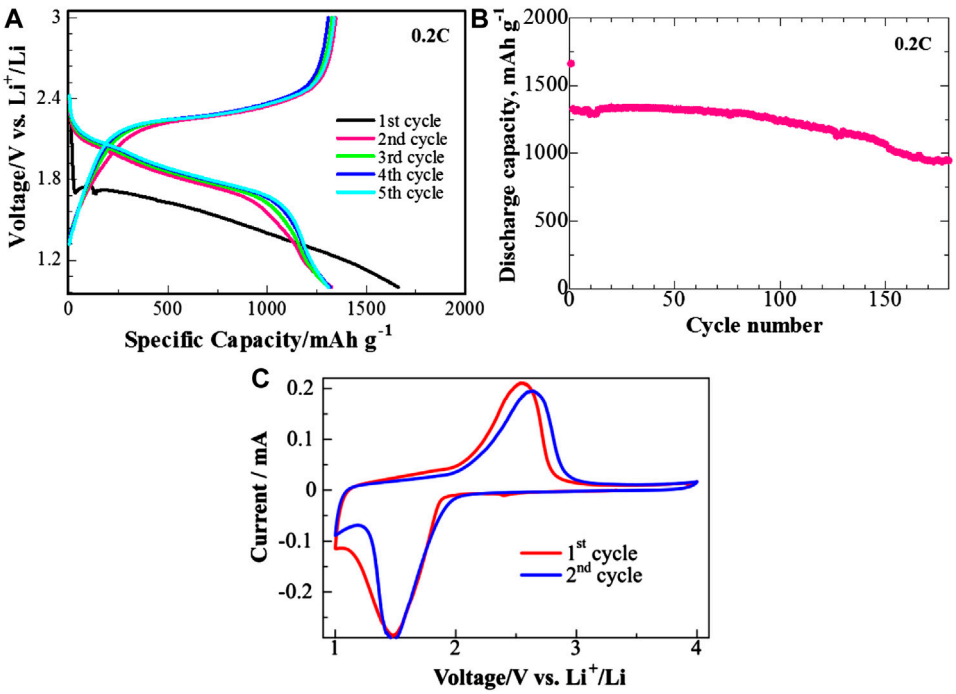

FIGURE 3 | (A) Charge/discharge profiles, **(B)** cyclability, and **(C)** cyclic voltammetry of the half-cell with S/PAN/KB cathode at 0.2 C. Coin type cells.

2018). After 150 cycles, the cells retained 70% of their initial discharge capacity, which demonstrates high cycle stability of the prepared composite cathode. The CV curves of the half-cell demonstrated one broad reduction peak around 1.5 V vs. Li/Li^+ in the first cycle which shifts to higher potentials upon further cycling and one broad oxidation peak around 2.5 V. This is typical behavior of the S/PAN-based cathode materials (Kalybekkyzy et al., 2019).

The half-cell exhibits a moderate rate capability, as can be seen in **Figure 4**. At 0.5 C (~800 mA g^{-1}), the discharge capacity around 1,200 mAh g^{-1} was observed, and when the cycling rate was returned back to a lower C rate of 0.2 C (~300 mA g^{-1}), the capacity was fully recovered, which means that this composite cathode can be used at different current densities.

The full-cell exhibited and enhanced cycling performance compared to the half-cell. **Figure 5A** illustrates charge/discharge profiles of the S/PAN/KB cathode composite assembled in the full-cell (lithium-ion) configuration, and it

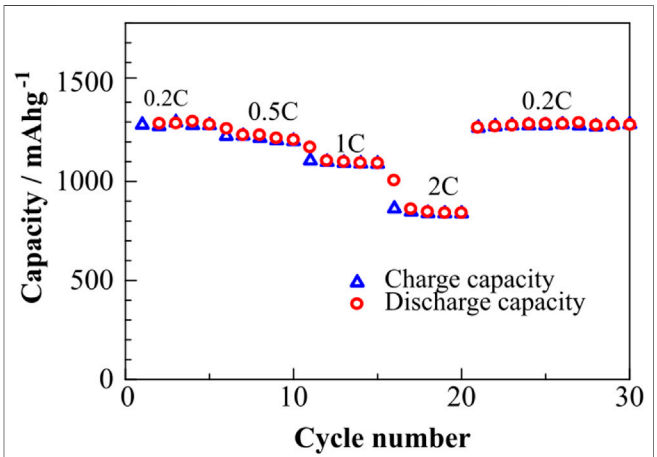

FIGURE 4 | Rate capability of half-cell containing S/PAN/KB composite assembled with Li-metal (0.2 C = 300 mA g^{-1} and 0.5 C = 800 mA g^{-1}).

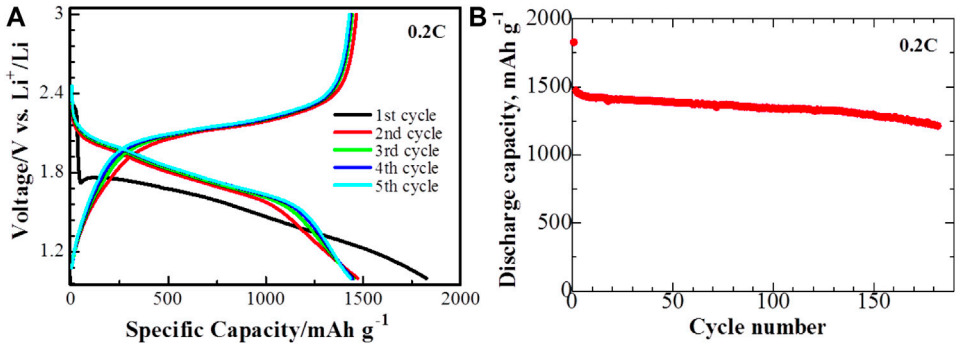

FIGURE 5 | (A) Charge/discharge profiles and **(B)** cyclability of S/PAN/KB full-cell at 0.2 C.

presents a very similar shape and tendency with the half-cell (with lithium metal anode) counterpart. Comparing the data of **Figure 3B** and **5B**, one can see that lithium-ion cell shows even better cycling performance than the Li-metal cell. This superior performance can be attributed to the fact that, with the lithiated graphite anode, a more stable SEI layer is formed, which relieves the capacity loss. Comparing Nyquist plots of half and full-cell, one can note that the full-cell exhibits more stable interfacial resistance than the half-cell (**Supplementary Figure S1**). Wu et al. (2018) have also observed similar behavior for half- and full-cell Li-S batteries with a customized ether-based electrolyte. In their work, an S-Li_xC full-cell was prepared, which showed a discharge capacity of 900 mAh g^{-1} after 400 cycles. Our full-cell in a coin cell version with a commercial carbonate-based electrolyte without any additives or modifications shows very stable performance for the initial 150 cycles (~1,500 mAh $(g\text{-}S)^{-1}$).

Various groups have reported full-cell configuration such as S-Li-Si (Ye et al., 2017), Li_2S-Si (Yang et al., 2010), Li_2S-C (Bresser et al., 2013; Jeong et al., 2013), and Li_2S-Sn (Hassoun et al., 2011) using coin cell configuration. However, a cathode preparation method with mixing and heat treatment developed in this work presents a simple and industrially scalable technique for pouch cell preparation.

Among the works reported on the fabrication of Li-S pouch cells, the best performing full-cell based on S-C cathode, Si-C anode, and LTFSI electrolyte has achieved a specific capacity of ~500 mAh g^{-1} after 400 cycles (Kang et al., 2016). In addition, OXIS energy claimed to have developed ~15 Ah/400 Wh kg^{-1} Li-S pouch cells (Li-metal anode and assembled with ether electrolyte) with a cycle life of 100 cycles (Fotouhi et al., 2017). Pouch cell with $LiPF_6$ electrolyte was fabricated using S-C composite electrode material with an initial discharge capacity of 1,000 mAh g^{-1}. However, no information about the cyclability of the cell was reported (Li et al., 2018). Here, we report the first practical pouch cell assembled in carbonate-based electrolytes with very stable performance.

Figure 6A shows the initial CV curve of a 2 Ah pouch cell at the scan rate of 0.1 mV s^{-1}. There is one broad reduction peak at 1.2 V and one oxidation peak at 2.6 V at the first cycle, which shifted toward a higher potential at the following cycle (dashed lines). The long-chain sulfur reaction mechanism is absent or very limited in S/PAN structure, and thus lithium polysulfides are merely formed in the electrolyte (Wang et al., 2018). This makes these systems very stable upon cycling. The CV data confirm that the pouch cell reaction mechanism reproduces the tendencies and behavior of those observed for the coin cell. To investigate the stability of the pouch cell in a wider potential range, overcharge and deep discharge tests were done by CV screening of the same cell in **Figure 6A** between 0.1 and 4.0 V (the cycles three to five, solid lines). Data shown in **Figure 6A** confirm that still only one oxidation and one reduction peaks appear in this wide potential range, except during the charge stage when the current starts to rise again around 4 V. This might be related to corrosion of a current collector (Al for cathode) after 4 V. However, the CV curves are reproducible during the cycles, which confirms sufficient stability of the system even during overcharge and deep discharge operations.

Figure 6B shows the charge/discharge potential profiles of the pouch cell at 0.1 C, and the typical behavior of sulfurized polyacrylonitrile was observed in this case as well (Wang et al., 2018). In the pouch cell, we had 24 layers of electrodes, which were placed in parallel to each other. The amount of the material in a pouch cell is much larger than in a coin cell; however, the geometry of the pouch cell is more preferable for current flow as it can be seen from the impedance spectroscopy results. The semicircle is very small in the case of a pouch cell, which indicates small resistance of the system (**Supplementary Figure S2**). Indeed, it is not comparable with coin cell (**Supplementary Figure S2**, inset), since the cells are very different in their structures and sizes. It should be noted that the applied areal current to the cell is estimated to be 160 mA, which is much larger than that of the coin cell counterparts (0.5–5 mA) (Cheng et al., 2017).

The cycling performance of the pouch cell is stable, as shown in **Figure 6C**. It delivers a high discharge capacity of 2000 mAh in the second cycle at 0.1 C. The cell could maintain 81% of its capacity (~1,630 mAh) after 100 cycles, as shown in **Figure 6C**, which is the highest reported value for Li-S full-cell assembled in the carbonate-based electrolyte. Capacity fading (or increase in the cell resistance) is attributed to the slight dissolution of S into the electrolyte. The system exhibited a high Coulombic efficiency

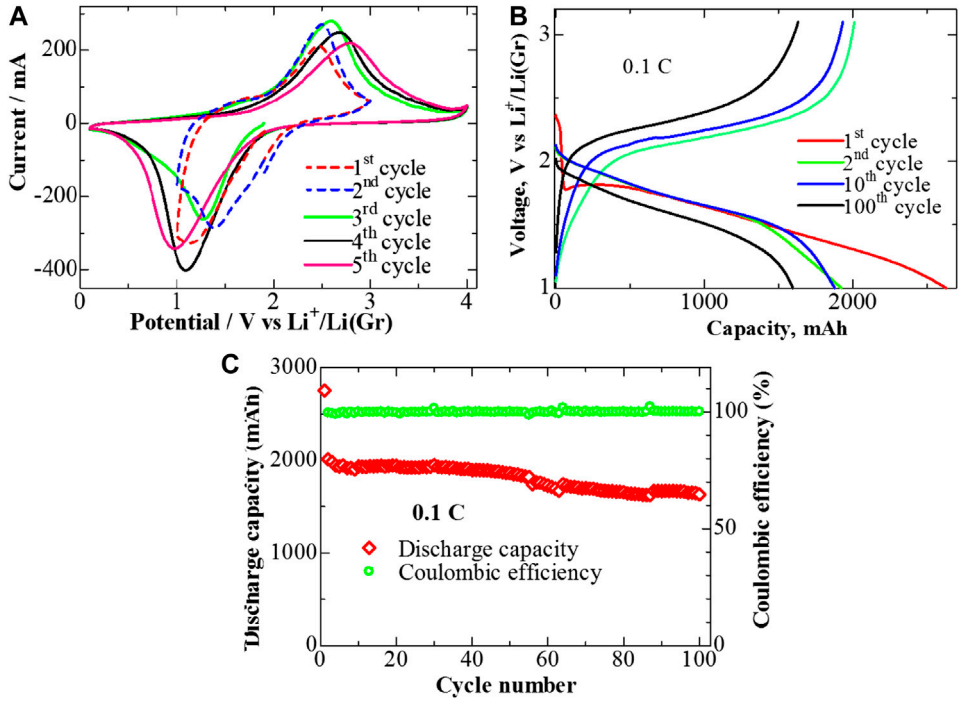

FIGURE 6 | CV curves at a scan rate 0.1 V s^{-1} within potential windows **(A)** 1–3 V and **(B)** 0.1–4 V vs. Li/Li^+; **(B)** charge/discharge profile; and **(C)** cyclability of the pouch cell within cutoff potentials 1–3 V vs. Li/Li^+.

of about 100% over 100 cycles, which could be attributed to the shuttle effect suppression in the hierarchical mesoporous and macroporous structure of the ternary composite prepared in this work.

Similar discharge characteristics could be observed for a 10 Ah pouch cell with the electrode areal dimensions of 135 × 165 mm. The cell could deliver a capacity of 10,640 mAh with a 0.1 C rate (**Supplementary Figure S3**). These results show the scalability of this system from the coin cell to the pouch cell configuration.

The rate capability studies of 2 Ah pouch cells have been carried out as presented in **Figure 7A**. It was galvanostatically charged at 0.2 C and discharged at various discharge rates up to 2 C. At 0.1 C rate, the cell exhibited an initial discharge capacity of 1950 mAh, at 0.2 C it exhibited an initial discharge capacity of 1750 mAh, and at 0.5 C, it exhibited an initial discharge capacity of 850 mAh. Although these values decreased gradually with the cycling rate, a reversible capacity of 280 mAh could be achieved even at 1 C rate, indicating a good rate performance of the system. This is attributed to a unique sulfur reaction mechanism with polyacrylonitrile. After cycling at 2 C with a delivered capacity of 50 mAh, the cell could recover its reversible capacity of about 1700 mAh when it was further cycled at 0.1 C. This is a good indicator of performance for practical pouch cells.

In addition, the self-discharge behavior studies of this cell were carried out, the results of which are shown in **Figure 7B**. After charging to 3 V, the cell retained a potential above 2 V for 30 days, which indicates good stability and low self-discharge of only 0.7 mV day^{-1}. In addition, overcharge, deep discharge, and short circuit tests have been carried out for the 2 Ah pouch cell (**Supplementary Figure S4**). During the tests, no seal leaks, fire, or explosion was detected and/or observed, but there was a swelling of the battery during overcharge (**Supplementary Figure S4(a)**). Therefore, it can be confirmed that our pouch cells comply with the safety requirements for lithium-ion batteries. In order to test the feasibility of the cell for potential device applications, a battery stack—a prototype of rechargeable batteries for a radio phone and drone—was assembled from 5 pouch cells of the dimensions of 85 × 45 × 6 mm^3 as shown in **Figure 8A**. Two Ah pouch cells of the same capacity were connected in series to obtain the required stack voltage of 10 V (~170 Wh L^{-1}). As shown in **Figure 8B**, the battery prototype exhibits a stable charge/discharge profile, and an average discharge potential was around 10 V suitable for the applications mentioned.

CONCLUSION

In conclusion, S/PAN/KB cathode composite was prepared by a very simple method of mixing and heat treatment. An optimized (heat treatment at 300°C for 3 h) S/PAN/KB cathode composite delivered a high capacity of 1,500 mAh/g when assembled with lithiated graphite in coin cell configuration. All cell components used for cell assembly, including carbonate electrolyte, were commercially available and were not customized or modified and are thus of a low cost. In order to show the practicality of the developed composite cathode and proposed approaches in this work, pouch cells with the cathode composite and lithiated

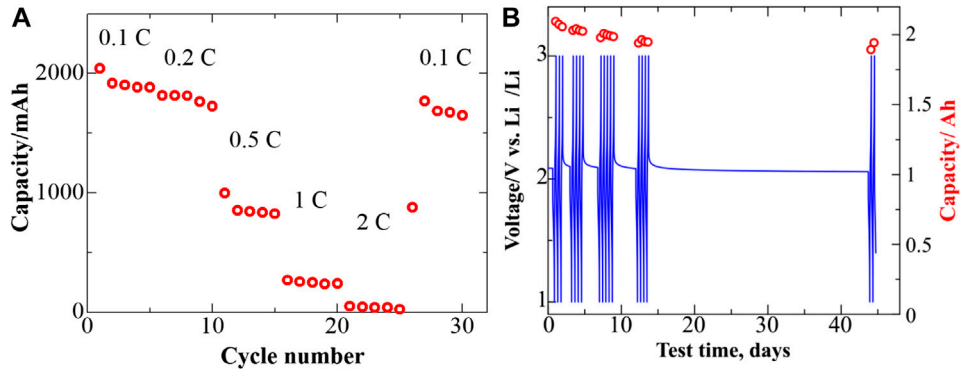

FIGURE 7 | (A) Rate performance and **(B)** self-discharge of 2 Ah Li-S pouch cell.

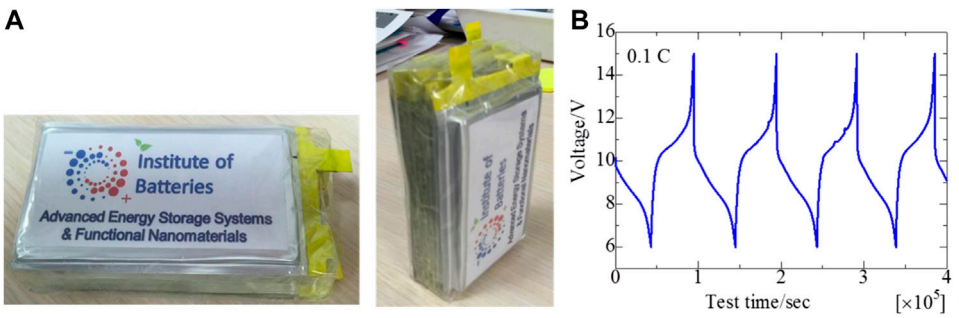

FIGURE 8 | (A) Photos of battery stack from five 2 Ah pouch cells connected in series and **(B)** the stack's cyclability.

graphite were assembled. The cell showed a stable capacity of 2000 mAh with 100% Coulombic efficiency over 100 cycles, and it has successfully passed the safety tests required for commercial batteries. This work demonstrates very feasible results for a Li-S practical full-cell and promising results toward its commercialization.

DATA AVAILABILITY STATEMENT

All datasets presented in this study are included in the article/ **Supplementary Material**.

AUTHOR CONTRIBUTIONS

YZ, AM, IK, AK, and ZB developed the project idea. ZB supervised the work. BU, AM, AK, IK, YZ, and ZB contributed to discussion and manuscript writing. BU, AM, AK, IK, and YZ contributed to experimental work.

FUNDING

This work was supported by the Subproject #157-2013 funded under the Technology Commercialization Project by the World Bank and the Government of the Republic of Kazakhstan and the Targeted Program from the Ministry of Education and Science of Kazakhstan BR05236524 "Innovative materials and systems for energy conversion and storage."

ACKNOWLEDGMENTS

The authors thank Professor Izumi Taniguchi from Tokyo Institute of Technology, Japan, for assistance in conducting the SEM-EDS measurements.

SUPPLEMENTARY MATERIAL

The Supplementary Material for this article can be found online at: https://www.frontiersin.org/articles/10.3389/fenrg.2020.595481/full#supplementary-material

REFERENCES

Albertus, P., Babinec, S., Litzelman, S., and Newman, A. (2017). Status and challenges in enabling the lithium metal electrode for high-energy and low-cost rechargeable batteries. *Nat. Energy.* 3 (1), 16–21. doi:10.1038/s41560-017-0047-2

Aurbach, D., Pollak, E., Elazari, R., Salitra, G., Kelley, C. S., and Affinito, J. (2009). On the surface chemical aspects of very high energy density, rechargeable Li-sulfur batteries. *J. Electrochem. Soc.* 156 (8), 694–702. doi:10.1149/1.3148721

Bresser, D., Passerini, S., and Scrosati, B. (2013). Recent progress and remaining challenges in sulfur-based lithium secondary batteries-a review. *Chem. Commun.* 49 (90), 10545–10562. doi:10.1039/c3cc46131a

Cheng, X.-B., Yan, C., Huang, J.-Q., Li, P., Zhu, L., Zhao, L., et al. (2017). The gap between long lifespan Li-S coin and pouch cells: the importance of lithium metal anode protection. *Energy Storage Mater.* 6, 18–25. doi:10.1016/j.ensm.2016.09.003

Choudhury, S. (2019). "A highly reversible room-temperature lithium metal battery based on cross-linked hairy nanoparticles," in *Rational design of nanostructured polymer electrolytes and solid–liquid Interphases for lithium batteries*. (Cham, Switzerland: Springer International Publishing), 35–57.

Croce, F., Appetecchi, G. B., Persi, L., and Scrosati, B. (1998). Nanocomposite polymer electrolytes for lithium batteries. *Nature* 394 (6692), 456–458. doi:10.1038/28818

Fotouhi, A., Auger, D. J., O'Neill, L., Cleaver, T., and Walus, S. (2017). Lithium-sulfur battery technology readiness and applications-a review. *Energies* 10 (12), 1937. doi:10.3390/en10121937

Girishkumar, G., McCloskey, B., Luntz, A. C., Swanson, S., and Wilcke, W. (2010). Lithium–air battery: promise and challenges. *J. Phys. Chem. Lett.* 1 (14), 2193–2203. doi:10.1021/jz1005384

Hagen, M., Hanselmann, D., Ahlbrecht, K., Maça, R., Gerber, D., and Tübke, J. (2015). Lithium-sulfur cells: the gap between the state-of-the-art and the requirements for high energy battery cells. *Adv. Energy Mater.* 5 (16), 1401986. doi:10.1002/aenm.201401986

Hara, T., Konarov, A., Mentbayeva, A., Kurmanbayeva, I., and Bakenov, Z. (2015). High mass-loading of sulfur-based cathode composites and polysulfides stabilization for rechargeable lithium/sulfur batteries. *Front. Energy Res.* 3, 7–12. doi:10.3389/fenrg.2015.00022

Hassoun, J., Sun, Y.-K., and Scrosati, B. (2011). Rechargeable lithium sulfide electrode for a polymer tin/sulfur lithium-ion battery. *J. Power Sources.* 196 (1), 343–348. doi:10.1016/j.jpowsour.2010.06.093

Jeong, S., Bresser, D., Buchholz, D., Winter, M., and Passerini, S. (2013). Carbon coated lithium sulfide particles for lithium battery cathodes. *J. Power Sources.* 235, 220–225. doi:10.1016/j.jpowsour.2013.01.084

Kalybekkyzy, S., Mentbayeva, A., Kahraman, M. V., Zhang, Y., and Bakenov, Z. (2019). Flexible S/DpAN/KB nanofiber composite as binder-free cathodes for Li-S batteries. *J. Electrochem. Soc.* 166 (3), A5396–A5402. doi:10.1149/2.0571903jes

Kang, H. S., Park, E., Hwang, J.-Y., Kim, H., Aurbach, D., Rosenman, A., et al. (2016). A scaled-up lithium (Ion)-sulfur battery: newly faced problems and solutions. *Adv. Mater. Technol.* 1 (6). doi:10.1002/admt.201670027

Konarov, A., Gosselink, D., Doan, T. N. L., Zhang, Y., Zhao, Y., and Chen, P. (2014). Simple, scalable, and economical preparation of sulfur-PAN composite cathodes for Li/S batteries. *J. Power Sources.* 259, 183–187. doi:10.1016/j.jpowsour.2014.02.078

Li, X., Banis, M., Lushington, A., Yang, X., Sun, Q., Zhao, Y., et al. (2018). A high-energy sulfur cathode in carbonate electrolyte by eliminating polysulfides via solid-phase lithium-sulfur transformation. *Nat. Commun.* 9 (1), 1–10. doi:10.1038/s41467-018-06877-9

Liang, J., Sun, Z.-H., Li, F., and Cheng, H.-M. (2016). Carbon materials for Li-S batteries: functional evolution and performance improvement. *Energy Storage Mater.* 2, 76–106. doi:10.1016/j.ensm.2015.09.007

Liu, J., Bao, Z., Cui, Y., Dufek, E. J., Goodenough, J. B., Khalifah, P., et al. (2019a). Pathways for practical high-energy long-cycling lithium metal batteries. *Nat. Energy.* 4 (3), 180–186. doi:10.1038/s41560-019-0338-x

Liu, Q., Yu, Q., Li, S., Wang, S., Zhang, L., Cai, B., et al. (2019b). Safe LAGP-based all solid-state Li metal batteries with plastic super-conductive interlayer enabled by *in-situ* solidification. *Energy Storage Mater.* 25, 613–620. doi:10.1016/j.ensm.2019.09.023

Mentbayeva, A., Belgibayeva, A., Umirov, N., Zhang, Y., Taniguchi, I., Kurmanbayeva, I., et al. (2016). High performance freestanding composite cathode for lithium-sulfur batteries. *Electrochim. Acta.* 217, 242–248. doi:10.1016/j.electacta.2016.09.082

Nakamura, N., Wu, Y., Yokoshima, T., Nara, H., Momma, T., and Osaka, T. (2016). Film properties of electropolymerized polypyrrole for a sulfur/ketjenblack cathode in lithium secondary batteries. *J. Electrochem. Soc.* 163 (5), A683–A689. doi:10.1149/2.0731605jes

Nitta, N., Wu, F., Lee, J. T., and Yushin, G. (2015). Li-ion battery materials: present and future. *Mater. Today.* 18, 252–264 doi:10.1016/j.mattod.2014.10.040

Omampuliyur, R. S., Bhuiyan, M., Han, Z., Jing, Z., Li, L., Fitzgerald, E. A., et al. (2015). Nanostructured thin film silicon anodes for Li-ion microbatteries. *J. Nanosci. Nanotechnol.* 15 (7), 4926–4933. doi:10.1166/jnn.2015.9831

Peng, H., Wang, X., Zhao, Y., Tan, T., Mentbayeva, A., Bakenov, Z., et al. (2017). Enhanced electrochemical performance of sulfur/polyacrylonitrile composite by carbon coating for lithium/sulfur batteries. *J. Nanoparticle Res.* 19 (10), 348. doi:10.1007/s11051-017-4049-6

Rahimi-Eichi, H., Ojha, U., Baronti, F., and Chow, M.-Y. (2013). Battery management system: an overview of its application in the smart grid and electric vehicles. *EEE Ind. Electron. Mag.* 7 (2), 4–16. doi:10.1109/mie.2013.2250351

Seh, Z. W., Sun, Y., Zhang, Q., and Cui, Y. (2016). Designing high-energy lithium-sulfur batteries. *Chem. Soc. Rev.* 45 (20), 5605–5634. doi:10.1039/c5cs00410a

Wang, J., Yang, J., Xie, J., and Xu, N. (2002). A novel conductive polymer-sulfur composite cathode material for rechargeable lithium batteries. *Adv. Mater.* 14 (13), 963–965. doi:10.1002/1521-4095(20020705)14:13/14<963::aid-adma963>3.0.co;2-p

Wang, Q., Zhang, H., Cui, Z., Zhou, Q., Shangguan, X., Tian, S., et al. (2019). Siloxane-based polymer electrolytes for solid-state lithium batteries. *Energy Storage Mater.* 23, 466–490. doi:10.1016/j.ensm.2019.04.016

Wang, W., Cao, Z., Elia, G. A., Wu, Y., Wahyudi, W., Abou-Hamad, E., et al. (2018). Recognizing the mechanism of sulfurized polyacrylonitrile cathode materials for Li-S batteries and beyond in Al-S batteries. *ACS Energy Lett.* 3 (12), 2899–2907. doi:10.1021/acsenergylett.8b01945

Wei, Z., Zhang, Z., Chen, S., Wang, Z., Yao, X., Deng, Y., et al. (2019). UV-cured polymer electrolyte for $LiNi0.85Co0.05Al0.1O_2$//Li solid state battery working at ambient temperature. *Energy Storage Mater.* 22, 337–345. doi:10.1016/j.ensm.2019.02.004

Wu, Y., Momma, T., Yokoshima, T., Nara, H., and Osaka, T. (2018). High performance sulfur graphite full cell for next generation sulfur Li-ion battery. *J. Power Sources.* 388, 5–10. doi:10.1016/j.jpowsour.2018.03.051

Yang, Y., McDowell, M. T., Jackson, A., Cha, J. J., Hong, S. S., and Cui, Y. (2010). New nanostructured Li2S/Silicon rechargeable battery with high specific energy. *Nano Lett.* 10 (4), 1486–1491. doi:10.1021/nl100504q

Yasin, G., Arif, M., Mehtab, T., Lu, X., Yu, D., Muhammad, N., et al. (2019). Understanding and suppression strategies toward stable Li metal anode for safe lithium batteries. *Energy Storage Mater.* 25, 644–678. doi:10.1016/j.ensm.2019.09.020

Ye, R., Bell, J., Patino, D., Ahmed, K., Ozkan, M., and Ozkan, C. S. (2017). Advanced sulfur-silicon full cell architecture for lithium ion batteries. *Sci. Rep.* 7 (1), 1–10. doi:10.1038/s41598-017-17363-5

Yuan, L., Yuan, H., Qiu, X., Chen, L., and Zhu, W. (2009). Improvement of cycle property of sulfur-coated multi-walled carbon nanotubes composite cathode for lithium/sulfur batteries. *J. Power Sources.* 189 (2), 1141–1146. doi:10.1016/j.jpowsour.2008.12.149

Zhang, S. (2014). Understanding of sulfurized polyacrylonitrile for superior performance lithium/sulfur battery. *Energies* 7 (7), 4588–4600. doi:10.3390/en7074588

Zhao, C.-Z., Zhao, B.-C., Yan, C., Zhang, X.-Q., Huang, J.-Q., Mo, Y., et al. (2019). Liquid phase therapy to solid electrolyte–electrode interface in solid-state Li metal batteries: a review. *Energy Storage Mater.* 24, 75–84. doi:1016/j.ensm.2019.07.026

Conflict of Interest: The authors declare that the research was conducted in the absence of any commercial or financial relationships that could be construed as a potential conflict of interest.

frontiers in Energy Research

ORIGINAL RESEARCH
published: 24 November 2020
doi: 10.3389/fenrg.2020.594857

Tackling xEV Battery Chemistry in View of Raw Material Supply Shortfalls

Duygu Karabelli[1], Steffen Kiemel[1], Soumya Singh[1], Jan Koller[2], Simone Ehrenberger[3], Robert Miehe[1], Max Weeber[1] and Kai Peter Birke[1,4]*

[1]Fraunhofer Institute for Manufacturing Engineering and Automation IPA, Stuttgart, Germany, [2]Fraunhofer Institute for Manufacturing Engineering and Automation IPA, Bayreuth, Germany, [3]Institute of Vehicle Concepts, German Aerospace Center (DLR), Stuttgart, Germany, [4]Institute for Photovoltaics, University of Stuttgart, Stuttgart, Germany

The growing number of Electric Vehicles poses a serious challenge at the end-of-life for battery manufacturers and recyclers. Manufacturers need access to strategic or critical materials for the production of a battery system. Recycling of end-of-life electric vehicle batteries may ensure a constant supply of critical materials, thereby closing the material cycle in the context of a circular economy. However, the resource-use per cell and thus its chemistry is constantly changing, due to supply disruption or sharply rising costs of certain raw materials along with higher performance expectations from electric vehicle-batteries. It is vital to further explore the nickel-rich cathodes, as they promise to overcome the resource and cost problems. With this study, we aim to analyze the expected development of dominant cell chemistries of Lithium-Ion Batteries until 2030, followed by an analysis of the raw materials availability. This is accomplished with the help of research studies and additional experts' survey which defines the scenarios to estimate the battery chemistry evolution and the effect it has on a circular economy. In our results, we will discuss the annual demand for global e-mobility by 2030 and the impact of Nickel-Manganese-Cobalt based cathode chemistries on a sustainable economy. Estimations beyond 2030 are subject to high uncertainty due to the potential market penetration of innovative technologies that are currently under research (e.g. solid-state Lithium-Ion and/or sodium-based batteries).

Keywords: xEV, Li-ion batteries, NMC chemistry, raw materials, circular economy, end-of-life, recycling

OPEN ACCESS

Edited by:
Jian Liu,
University of British Columbia Okanagan, Canada

Reviewed by:
Hossein Yadegari,
Imperial College London, United Kingdom
Fadwa Dababneh,
Applied Science Private University, Jordan

****Correspondence:***
Duygu Karabelli
duygu.kaus@ipa.fraunhofer.de

Specialty section:
This article was submitted to Electrochemical Energy Conversion and Storage, a section of the journal Frontiers in Energy Research

Received: *14 August 2020*
Accepted: *02 November 2020*
Published: *24 November 2020*

Citation:
Karabelli D, Kiemel S, Singh S, Koller J, Ehrenberger S, Miehe R, Weeber M and Birke KP (2020) Tackling xEV Battery Chemistry in View of Raw Material Supply Shortfalls. Front. Energy Res. 8:594857. doi: 10.3389/fenrg.2020.594857

INTRODUCTION

Since the commercial development of Li-ion cells in 1991 by Sony (Nishi, 2001), the Lithium-ion battery (LIB) market is continuously growing. The market for rechargeable LIBs is currently divided into three main segments: consumer electronics, electromobility (e-mobility) applications and stationary batteries. Within these listed segments, e-mobility is essential for achieving the climate targets. E-mobility essentially means much more than driving an Electric Vehicle (EV). E-bikes and e-scooters have gained popularity and they are increasingly materializing in our daily lives. The battery chemistry used in EVs can also be applied in other mobility solutions (Vezzini, 2014). However, expected lifetime of e-bikes and e-scooters are relatively shorter as compared to xEV due to the high cycle number at high C-rates in a short period of use (Oeser, 2018; Baeva et al., 2019).

EVs are strong contributors to the expanding market of Li-ion cells because an EV battery system is much larger in Ah as compared to consumer applications. Automotive traction batteries can contain up to 7,000–10,000 single cylindrical cells of the formats 18,650-type (18 mm diameter,

65 mm height) or 21,700-type (21 mm diameter, 70 mm height) (Quinn et al., 2018). In consequence, the global demand for raw materials of Li-ion cells will rise tremendously in the upcoming years. In case the local grid demands offer attractive return of investments, the stationary applications employing Li-ion cells would also be of great interest. In Australia, for example, Tesla has built up a 129 MWh stationary battery consisting of cylindrical cell modules, mainly same as those in the Tesla automobile (Perkins, 2018; Keck et al., 2019).

Nevertheless, what makes Li-ion so unique, why was it worth receiving the Nobel price of chemistry in 2019 (Manthiram, 2020), and will it be or stay the ruling battery technology? Indeed, the ingredients of success are quite uniquely called intercalation electrodes and Solid Electrolyte interphase (SEI) (Nishi, 2001; Handbuch Lithium-Ionen-Batterien, 2013; Pistoia, 2014; Luntz et al., 2015; Liu et al., 2016; Zubi et al., 2018). No question that some replications with mobile ions other than Li-ions are also feasible. However, the important discussion lies in the question if the replication can ever beat the original. The ideal intercalation principle allows to insert and extract ions into and from a lattice host structure without any volume changes. Indeed, such a "zero strain" material exists in reality, it is $Li_4Ti_5O_{12}$, capable to insert and extract three Li atoms with nearly zero strain expansion (about 0.2–0.3%) which results in achieving extremely high cycles with improved safety (Zaghib et al., 1999; Xu et al., 2017). One may argue that this is also due to the favorable voltage of about 1.5 V vs. Li^+/Li, which evidently suppresses electrolyte decomposition. However, the less the volume changes upon charge and discharge of an intercalation material, the better the expected cycle behavior. The volume expansion of the host materials also depends on the co-intercalation of solvent species. Similar to hydrogen, lithium offers very small ions. Smaller the ion, lesser the expected volume changes of the host lattice when the ions are inserted and extracted. In fact, any alternative to Li-ions should contain larger monovalent ions. If multivalent ions are anticipated, the discussion does not only include the size but also possibly much unfavorable diffusions coefficients than those of monovalent ions (Levi and Aurbach, 2005; Li et al., 2020). A similar uniqueness holds for the SEI. A breakthrough discovery was the fact that $LiAsF_6$ and $LiPF_6$ based electrolytes, dissolved in certain carbonate mixtures consisting of EC (ethylene carbonate), DMC (dimethylcarbonate), EMC (ethylmethylcarbonate) and DEC (diethylcarbonate), build SEIs on graphite electrodes (the negative one), which last a whole battery life with acceptable degradation (Aurbach et al., 1995; Peled and Menkin, 2017). Evidently, only $LiPF_6$ survived since $LiAsF_6$ was not feasible due to reasons of toxicity. But the most interesting aspect is that since 1991, around 95% of the electrolyte composition stayed unchanged, proving the uniqueness of this electrolyte system. So, any replication attempt with other mobile ions has to find a comparable electrolyte system at first. Cells employing so-called solid electrolytes (Zheng et al., 2018) are not in discussion to just replace the liquid electrolyte. The hope is to employ solid electrolytes in order to use metallic negative electrodes and improve the energy density. However, actual research results do not show that this option would be available in widespread commercial applications before 2030. It has to be additionally emphasized that tremendous production capacities (Giga-factories) (Kurland, 2019; Fan et al., 2020) and automotive V-Model life cycle (Kumar et al., 2009; Liu et al., 2016) will prevent any fast switch to other battery cell technologies. Hence, it is established that Li-ion technology will be prominent in the near future, however its chemistry and materials are uncertain.

Discussing the materials for all the battery components is not within the scope of this paper, thus the most challenging one is selected, the cathode (positive electrode). The negative electrode is somehow settled. Graphite has a potential near lithium, and only the combination of graphite and electrolyte allows long lasting SEIs, so no improvements are possible besides adding some silicon (Xiang et al., 2011; Chakrapani et al., 2012). The positive electrode, however, has still a tremendous tuning factor, if we look at the so-called 4 V materials. Particularly Nickel-Manganese-Cobalt (NMC) and Nickel-Cobalt-Aluminium (NCA) based electrodes have unified much advantages such as capacity, long life, acceptable safety, capacity (mAh/g), as well as voltage slope as function of the state of charge (SoC) which is very favorable for many applications (Barré et al., 2013; Thielmann et al., 2015; Dominko et al., 2019). Alternative cathode materials with higher capacity have often been discussed in the literature, such as manganese vanadates ($Mn(VO_3)_2{\cdot}yH_2O$) (Pillot, 2017), but they failed due to unfavorable voltage as function of the SoC as well as too low absolute mean values of the open circuit voltage vs. Li. Though $LiFePO_4$ is a very interesting and already successfully commercialized cathode candidate (Handbuch Lithium-Ionen-Batterien, 2013; Pillot, 2017; Zubi et al., 2018), it is rather a 3 V than a 4 V material. Hence, $LiFePO_4$ struggles in energy density over NMC.

In order to consequently optimize NMC, researchers started to tune the N:M:C 1:1:1 ($LiNi_{1/3}Mn_{1/3}Co_{1/3}O_2$) formulation to more Ni-rich ones such as 5:3:2 ($LiNi_{0.5}Mn_{0.3}Co_{0.2}O_2$), 6:2:2 ($LiNi_{0.6}Mn_{0.2}Co_{0.2}O_2$) and 8:1:1 ($LiNi_{0.8}Mn_{0.1}Co_{0.1}O_2$). The question then arises as to which of these compositions is the most favorable one, and if 8:1:1 is technically and commercially feasible (Kim et al., 2018). This shifts the frequently discussed raw material question from cobalt to nickel, especially in the time horizon of 2030.

In parallel, the handling and recycling of LIB from end-of-life (EoL) vehicles at the end of their service life is proving to be extremely challenging for battery manufacturers and recyclers. However, used batteries also offer economic opportunities. This is particularly true in an environment in which manufacturers of key components of e-mobility are trying to secure their access to raw materials of strategic economic importance in the long term. The materials and elements from LIBs of EVs can be an extremely valuable secondary source. In addition to material recycling, alternative recycling strategies such as reuse, repair and remanufacturing offer the possibility of extending the economically usable life of a battery system and at the same time mitigating the growing demand for resources for the production of energy storage systems.

Assuming a 10 years lifetime in automotive followed by a 10 years lifetime in stationary applications, those batteries have a time delay of 20 years for any recycling effort. In this context, one can ask when would these used batteries will be available for the

recycling strategies. Additionally, the automotive battery mass market is assumed to begin earliest in 2023 (Sonoc et al., 2015). This market cannot be the recycling driver in such a short run. This means, currently it is vital to discuss the available materials coming from consumer cells and small traction batteries (eg e-bikes, e-scooters, pedelecs and segways). In order to be able to evaluate the feasibility of such reverse supply chains at all, in the first step the potential return volumes from EoL batteries have to be estimated. In addition to the quantity as a function of time, other factors such as development in the battery performances (direct effect on the EoL), battery chemistry in the future as well as reuse and recycling costs have to be taken into consideration. On this basis, various recycling strategies could be predicted in accordance with the European waste regulations.

Taking into account that Li-ion will be the dominating system for a long time, and the battery demand and production capacities will be growing together along with the anticipated development of Ni-rich cathodes for Li-ion cells, we reduced the prominent questions to the following; First, the expected NMC compositions (until 2030) will be discussed including performance aspects such as cycling aging, safety and cost. Secondly, the question of raw material availability is explored, taking the competition with the steel industry into account. Lastly, it is discussed whether the various strategies for a circular economy (recycle, reuse, repair, remanufacture) can possibly reduce the market stress and contribute to raw material availability.

EVALUATION AND PROGNOSIS OF EXPERTS' SURVEY

The methodology consists of two-step analysis. Firstly, we perform an extensive literature study of the market shares of EV batteries, their chemistry and expected lifetime. The findings are further supported with expert opinions in order to predict the possible developments in the future. Secondly, we perform a criteria-based prognosis for the realistic scenarios of battery development until 2030. The complete survey consisted of 13 questions focused on battery lifetime, second life and future battery developments.

The literature study complements the finding from the experts and helps in verification. As a first step thematically matched experts (battery R&D scientists, recyclers, manufacturers, raw material experts, consultants etc.) were identified. We have then defined the necessary questions and scenarios in order to adequately evaluate the survey and to gain a deeper understanding of today's challenges, requirements and prospective expectations. Elicitation interviews took place in april 2020 by mailing them a questionnaire (see **Supplementary Material**).

Experts' Opinion on the Evolution of Li-Ion Battery Cathode Chemistry

Due to the various stakeholders' involvement, from the fields of producer-customer, raw material suppliers and recycling market, a target-oriented interdisciplinary survey must be conducted to identify future battery technologies and business developments.

Collectively, there is an estimation of global demand of 1,200 GWh battery capacity in the year 2030, which is projected to increase to 3.500 GWh by 2050 (Dolega, 2019). Zubi et al. reported around 1.5 Million of EV will be sold worldwide in 2020 and the LIB demand is expected to reach 240GWh in 2030 (including EV, PHEV and HEV) (Zubi et al., 2018). The rapid growth may lead to temporary shortages of lithium, nickel and cobalt under certain circumstances. Currently the primary state-of-the-art automotive Li-ion chemistries are $LiNi_{0.8}Co_{0.15}Al_{0.05}O_2$ (NCA), spinel $LiMn_2O_4$ (LMO), olivine $LiFePO_4$ (LFP), and layered $LiNi_{1-x-y}Mn_yCo_zO_2$ (NMC). Among these chemistries, NMC is assumed to have 60% of market share in the near future (Vaalma et al., 2018).

With reference to this large market share, this paper focuses on NMC chemistry evolution until 2030. A market report of Avicenne Energy (Pillot, 2017) on different NMC chemistries (NMC 811, NMC 622, etc.) for 2020 was used as reference. Also, we asked the experts to predict the expected changes in these chemistries until 2030, if a technologically progressive development is assumed (**Figure 1**). This progressive development can be realized if all the primary challenges (stable raw material prices, reaching higher energy density and capacity, improved safety and design) are overcome and the battery life cycle is technologically advanced.

NMC cathodes are also particularly robust and more durable than the NCA cathodes. Most EV manufacturers have already presented their near future plans on NMC cathode material. Batteries with Ni-Mn-Co ratio of 1:1:1 (NMC 111) are currently widely used (45% market share), but alternative ratios with NMC 532 and NMC 622 already exist. Some experts assume that in the future NMC 811 will have the highest market share compared to other ratios. In order to estimate the realistic market shares of different NMC chemistries, we have defined six important key characteristics for EV batteries:

- Raw material prices
- High energy density
- High capacity
- increase of temperature tolerance
- Stability (Safety)
- Reduction of battery weight

As a first step we asked experts to order these characteristics according to their influence on battery design and chemistry. Most of the experts agreed that the increasing raw material prices has the highest influence factor on the decision of battery chemistry. The resulting order of influence factors is shown in **Figure 2A**.

Increase in raw material costs has a direct impact on the cost of the battery and it is highly predictable that it can play an important role during the development of new battery chemistry. Higher nickel content brings higher capacity and energy content. For example, NMC 111 exhibits 160 mAh g^{-1} of a specific capacity where this value reaches to more than 200 mAh g^{-1} for NMC-811 (Schmuch et al., 2018). However, Ni-rich batteries become less stable and consequently show shorter cycle life. Furthermore, production is usually more expensive due

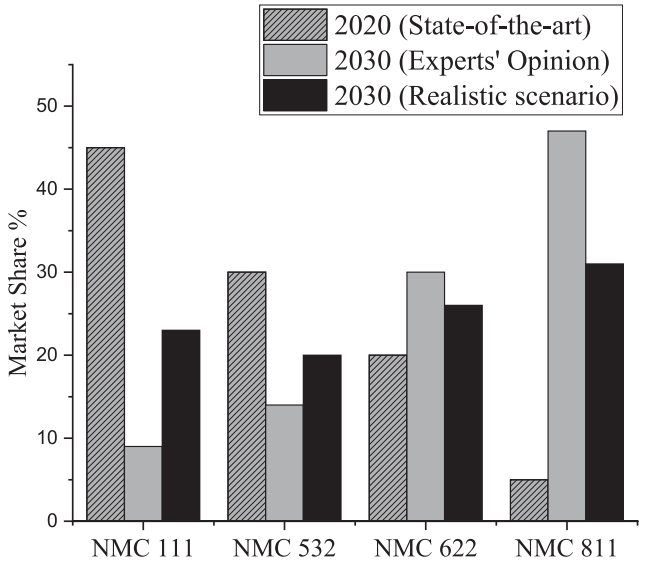

FIGURE 1 | Evolution of NMC Chemistry from 2020 to 2030 and the values according to realistic scenario calculations.

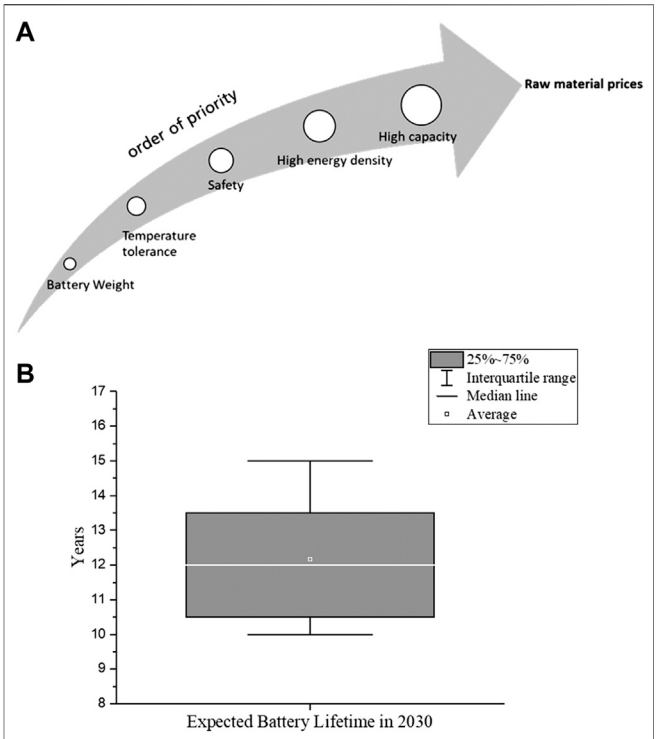

FIGURE 2 | (A) Impact of influence factors on battery chemistry developments **(B)** Expected battery lifetime in 2030 if the important influence factors are improved.

to need of extra additives and safety concerns (temperature tolerance, stability). Last but not least, the weight of the battery has also a direct impact on the performance of the EVs. Lighter battery results with lighter EV with extended driving range.

We gave certain statements and requested the experts' viewpoint (**Table 1**). Not every expert answered every question and some of them stayed "undecided." Specifically, we asked about the probability of achieving a battery with high performance and better safety with low cost in 2030.

Given the disagreement of the experts on raw material prices, we further analyze the potential of alternative end-of-life strategies to reduce fluctuations of raw material prices. For the rest of the statements, most of the experts believed that there will be a success for higher capacity, higher energy density, higher temperature tolerance, higher safety and lighter battery packs. The table above also summarizes the expected developments for Ni-rich cathodes.

Experts' Opinion on calendar lifetime of batteries

Most batteries used in EVs currently have a minimum warranty of 8-year (Neubauer and Pesaran, 2011; Skeete et al., 2020). According to answers of 24 experts, the average life of an EV battery in 2030 is estimated as 12.2 years assuming the development is technically progressive (**Figure 2B**). Based on many studies, the SoH of an EV battery is reduced to 80% after 8–10 years. External factors such as operating temperature, overcharge/discharge, high charge/discharge rates and improper charge/discharge cycles can negatively affect the SoH (Barré et al., 2013). The SoH indicates the condition of the battery system and characterizes its ability to meet the specified performance specifications. The specification of SoH is related to the performance values of a new battery system. Hereby we first asked experts to rank the influence of the individual factors on the life of a battery. After evaluation of expert answers, the following order was established: Temperature > SoC > range > C-Rate Cycle number.

Brief explanations of these factors and their impact the SoH and consequently the battery lifetime are given in **Supplementary Material**.

Thereby the operating temperature has a much greater effect on the SoH than the SoC range, C rate and number of cycles. In this case, it should be noted that for future developments, the battery materials must be more resistant to fluctuations in the operating temperature. In addition, the battery must be able to operate in a wider SoC range. According to the order of the influencing factors, weighting impact numbers were distributed from 1 (lowest impact) to 4 (highest impact).

Following the assignment of weightage to the influencing factors, the experts were asked to estimate the development potential of the respective factors until 2030. According to the majority of the experts, the higher C-rates capability and achieving high cycle numbers are estimated to have a high development potential, whereas the higher temperature resistance and broader SoC rate can still be a challenge (**Table 2**). A "score" is specified for each of the influencing factors in the table:

Table 1 | Statements on battery developments and expert answers.

Development until 2030:	Disagreed	Agreed	Undecided	Favoring Ni-rich Cathodes?
Raw material prices for battery material will rise	8	8	9	YES
The energy density of Battery Systems will increase	0	22	3	YES
The weight of Battery Systems is decrease	5	16	4	YES
The temperature tolerance of Battery Systems will increase	3	15	7	NO
The stability of Battery Systems will increase	1	16	8	NO
The capacity of Battery Systems is increase	4	20	1	YES

Table 2 | Battery life influencing factors and their development forecast.

Influencing factors	Development potential of the influencing factors until 2030	Score
Achieving higher cycle numbers	High	1
Increase in C-Rates	High	1
Broader SoC range	Medium	0.5
Increase of the temperature resistance	Medium	0.5

- Low Potential = 0
- Medium Potential = 0.5
- High Potential = 1

These scores together with impact numbers are used later in *Realistic Scenarios of Future Developments in Battery Technology* in order to calculate a realistic battery life expectancy.

Realistic Scenarios of Future Developments in Battery Technology

This section presents the individual results of the expert survey and the forecasting for the battery life and chemistry. Detailed calculations of realistic scenarios are given in the **Supplementary Material Sections 1–3**.

Taking into account the resulting weighting and the expected development of the influencing factors described in the previous section were used to calculate Realistic Development Potential (RDP) %. According to the described procedure (**Supplementary Material 1**), a RDP % is obtained as 65%. The difference between the progressive (Experts' opinion) and conservative (state-of-the-art) scenario is equal to 4.2 years. In this case, an expected life of lithium-ion battery systems in 2030 according to a calculated realistic is rounded to **11 years.**

As **Table 1** lists all relevant influencing factors and shows the estimations of the 25 experts for the future development, another RDP% for the battery chemistry can be calculated as 62.6% (**Supplementary Material 1**). The dominating answers are marked bold and the answers with "undecided" were neglected. Accordingly, realistic market shares can be seen in the last row of **Table 3**.

A realistic calculation was indispensable for analyzing the coherence of the answers. The answers obtained from experts had to be examined in terms of inner logic, consistency and plausibility. As a result, the realistic market share of NMC 111 can be forecasted still higher than the experts' opinion (**Figure 1** and **Table 5**).

Table 3 | NMC Chemistry market share (%) according to literature, experts and calculation.

NMC 111	NMC 532	NMC 622	NMC 811	Origin of the value
45	30	20	5	Literature [34]
9	14	30	47	Experts
–36	–16	10	42	Difference
22.5	**20**	**26.3**	**31.2**	**Realistic market share**

When we interpreted these numbers, it must be noted that, the dominant NMC lithium-ion cells with a simultaneous increase in the nickel content is already in progress today. Without the trend toward lithium-ion cells with reduced cobalt content, the demand for cobalt for global e-mobility would still be considerably high in the medium and long term.

RAW MATERIAL SITUATION AND POTENTIAL SHORTAGES

LIBs consist of several raw materials that are associated with medium or high supply risk (Helbig et al., 2018). As this work focusses on cell chemistries based on nickel-manganese-cobalt (NMC) cathodes, these materials have to be analyzed in detail. The same applies to lithium as it is considered an "important, substantial and probably critical metal" as well (Simon et al., 2015). Instead of a detailed material criticality assessment, a qualitative discussion of relevant factors concerning the four mentioned raw materials is conducted. Therefore, some generally acknowledged indicators (Benjamin Achzet, 2013) or describing the supply risk are discussed but not evaluated in detail. Additionally, the expected change in cell chemistry of LIBs is assessed in terms of its effect on the future sustainable supply of battery materials.

Recent developments in lithium ion technology aim on nickel rich cathodes. Starting from equal shares of nickel, manganese and cobalt (NMC 111) in the first generations of NMC-batteries, the share of nickel is increased while reducing the ones of manganese and cobalt. The stepwise progression went to the second generation of NMC cathodes with material shares of 50% nickel, 30% manganese, 20% cobalt (NMC 532) and 60% nickel, 20% manganese, 20% cobalt respectively (NMC 622) (Study on the review of the list of critical raw materials: Final report, 2017). The third generation, which is expected to become predominant

Table 4 | Material demand scenarios.

	Scope	Name of Scenario	Abbr.	Color Scheme
Material Demands in t=2020 [metric t]	Only Battery	Battery: Scenario 100% NMC 111	*1x*	—
		Battery: Scenario 100% NMC 811	*1y*	—
		Battery: Scenario Realistic Mix	*1z*	—
	All Applications	All: Scenario 100% NMC 111	*2x*	—
		All: Scenario 100% NMC 811	*2y*	—
		All: Scenario Realistic Mix	*2z*	—
Material Supply (annual mining rate) [metric t]				—

in the mobility sector within the next years, utilizes cathodes comprised of 80% nickel, 10% manganese and 10% cobalt (NMC 811) (McKinsey and Company, 2018). Beside an increase in battery capacity, the decrease of the manganese and cobalt shares in battery cathodes is often associated with an easing of the material supply situation for LIBs (Olivetti et al., 2017; Schmuch et al., 2018).

This is mainly due to the critical conditions of the cobalt supply chain. In 2018 around 70% of the cobalt mine production took place in the Democratic Republic of Congo. Not only the fact of the extreme concentration of the world's production but also the critical situation concerning the governance and living conditions of the Democratic Republic of Congo and other cobalt producing countries (eg China, Russia, and Madagascar) results in a high rating of cobalt's supply risk. This statement is based on the interpretation of indicators provided by the World Bank Group (world governance indicators–voice and accountability, -political stability and absence of violence, -control of corruption), the United Nations Development Program (Human Development Index) and the Fraser Institute (Policy Perception Index) (United Nations Development Program).

Manganese is rated with a medium criticality, mainly due to its above-average country concentration. While being far afield from the geographical concentration of mining operations for cobalt, the potential risk for cuts in the supply chain exists if political and/or civil commotions occur (Fortier et al., 2018). The accompanied political risk is also assessed as slightly above average (United Nations Development Program). Manganese has no promising substitutes for most of its main applications, which increases its supply risk significantly (Graedel et al., 2015). Manganese is abundant in Earth's crust, however only around 4.5% of the world's manganese resources are currently classified as reserves (Fortier et al., 2018). Moreover, it is currently recyclable and future technologies are not expected to contribute to a significant increase in demand prospectively (Graedel et al., 2011). Also, the fact that manganese is mainly mined as a host metal and not as a by-product, lowers its respective supply risk (Nassar et al., 2015).

Based on generally acknowledged indicators for evaluating the supply risk of materials, nickel receives the lowest rating of the four considered materials (Graedel et al., 2015). The country concentration is assessed as medium (Fortier et al., 2018) as well as the related political risk (except for the human development index, which receives a more critical rating. Same as for manganese, recycling pathways for nickel are widely established. Furthermore, the expected increase in demand for future technologies is rather low, compared to the demand for current conventional applications (especially steel production) (Marscheider-Weidemann et al., 2016; Schmuch et al., 2018).

Table 5 | Executive summary of the survey.

Number of Total Experts 25	Valid Answers for Battery Life	
	24	
	Valid Answers for NMC Evolution	
	25	
Battery Life (Years)	**Experts' Opinion**	**Realistic Scenario**
	12.2	**11**
Market Share %		
NMC 111	9	22.5
NMC 532	14	20
NMC 622	30	26.3
NMC 811	47	31.2

Same as for cobalt, lithium is characterized by a noticeable concentration of production. Australia (~61%) and Chile (~18%) dominate the world's supply (Fortier et al., 2018). However, stable governance conditions in most lithium mining countries compared to the ones of cobalt mining countries result in a lower political- and thus supply risk. This is again except for the Human Development Index, which is rated as critical (United Nations Development Program). Although not established on a large scale, at least some companies are able to recycle lithium from EoL products and improvement is expected in the future. The increase in demand for future technologies compared to the current mining output is rated as very critical (Fortier et al., 2018; Marscheider-Weidemann et al., 2016). This is mainly due to the expected market penetration of LIBs (Marscheider-Weidemann et al., 2016).

In order to estimate the consequences of a change in cell chemistry on the availability of the four assessed raw materials, a scenario analysis is conducted. The six scenarios represent different assumptions concerning material demand in year 2030. Scenarios 1x, 1y and 1z focus on the demand solely caused by increasing demand for LIBs, while scenarios 2x, 2y and 2z include the total demand for batteries and other applications. This is done in order to give an impression about the impact of increasing battery demand on the commodity market and the market power of competitors for available

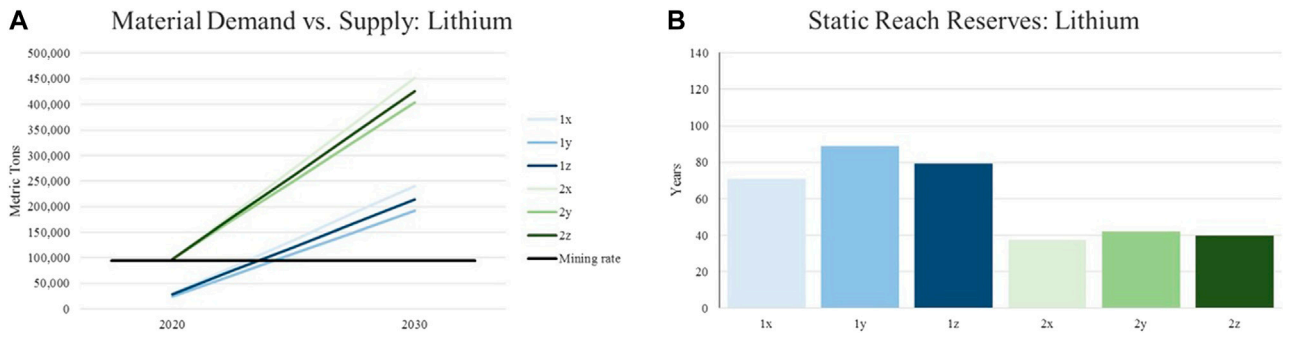

FIGURE 3 | Analysis of lithium raw material availability.

reserves. Also, this analysis indicates necessary increases in mining capacity. For each scope (only battery and all applications) there is one conservative scenario (100% NMC 111 in 2030: *1x* & *2x*), one progressive scenario (100% NMC 811 in 2030: *1y* & *2y*) and one realistic scenario which is based on the results of the expert interview introduced in **section 2.3.2** (*1z* and *2z*). The individual scenarios are depicted in **Table 1**. Each scenario is compared to the current mining rate in order to illustrate potential gaps between supply and demand. Due to reasons of simplification, it is assumed, that the annual mining rates and thus the material supply remains constant. Hence, this juxtaposition is intended to give a first glimpse on the magnitude of future demands in relation to current supply.

The future material demand for LIBs are calculated by considering the material inputs per kWh for each cell chemistry, the assumed shares of cell chemistries and the predicted battery capacity for automotive application in 2030. The material inputs per kWh of NMC 111, NMC 622 and NMC 811 are based on Olivetti et al. (2017), while the ones for NMC 532 are based on own assumptions (Olivetti et al., 2017). Further calculations are based on the average of predicted battery capacity from Campagnol et al. and Roland Berger GmbH (ref. **Table 6**). The two literatures have concordant predictions of future demands for LIBs, which is why the forecast of Zubi et al. is neglected in this work (Zubi et al., 2018).

The demand in the scenarios with the scope of including all applications of the respective material are composed of the projected demand for Li-Ion batteries in 2030, the current amounts used for the most prominent applications (Fortier et al., 2018) as well as the predicted demand for future technologies in 2035 (Bernhart, 2019). Hence, it is assumed, that the demand induced by the current main uses remain constant to today's level.

For illustrating potential shortages in supply, the annual material demand represented by the introduced scenarios are put in relation with currently identified reserves of the assessed materials. This is done in order to calculate the reach of material supply in years. Same as for the constant material supply, the world's reserves are expected to remain the same until 2030. Although this results in a certain inaccuracy, historic data from the United States Geological Survey concerning the reserves of various raw materials show that such a hypothesis is reasonable.

Table 6 | Literature - Li-Ion battery demand in 2030.

Literature Source	Name of Dataset	2020	2025	2030
		Battery Capacity [GWh]		
Campagnol et al. (2018)	Battery Capacity for Electric Mobility	—	735	1890
Roland Berger (2018)	Automotive Battery Cell Demand	213	794	1559
Average		213	~765	~1725

The following charts depict the described evaluation for the materials focused in this article (lithium, nickel, manganese, cobalt). The legend with the color scheme for the individual graphs can be found in **Figure 3** and **Table 4**.

It can be observed, that the lithium demand for traction batteries alone will surpass the current supply in each scenario before 2025. Although this seems very critical it needs to be stated, that lithium mining capacities are currently not utilized at full load. However, even by doubling the annual lithium supply, demands for Li-Ion batteries in the realistic scenario will exceed the available amount. In order to meet the total demands for lithium, the production capacity needs to be increased fourfold. Li-ion batteries account for nearly half of the world's demand for lithium. The static reach of lithium increases slightly due to lower material inputs per kWh in batteries with nickel-rich cathodes. However, the effect on the scope including all applications can be scored as low **Figure 4**.

Compared to the global demand, the nickel demand for LIBs are currently insignificant. However, increasing demands alongside with higher nickel contents in future battery systems will raise the share on the global demand from around 4% in 2020 to 34% (scenario 100% NMC 811) and 30% (realistic scenario) respectively. This illustrates the increasing market power of cathode- and/or battery manufacturers. Excessive current supply in the early twenties indicates the possibility of shortage in material availability and price increase. The change in battery chemistry has huge influence on the static reach of the nickel reserves. By supposing a complete market penetration of NMC 811 (*1y*) the static reach is cut in half compared to the conservative scenario (*1x*). Including the demands of the current main

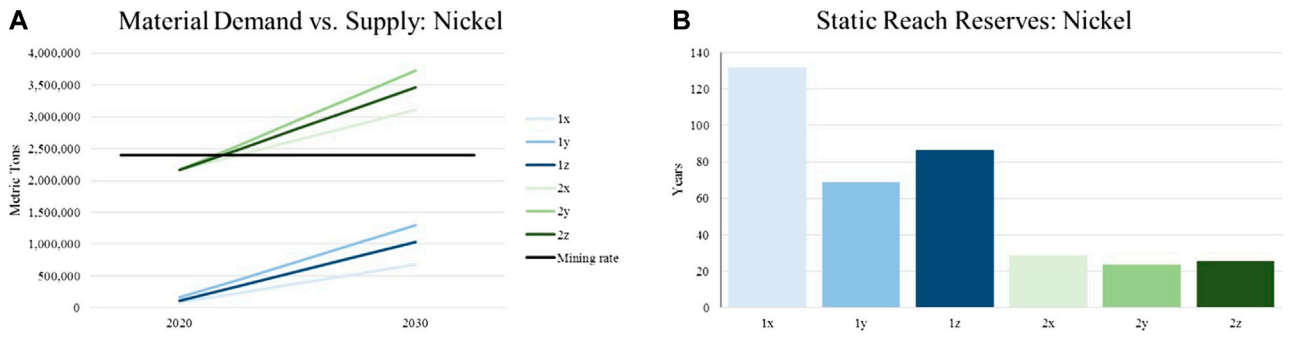

FIGURE 4 | Analysis of nickel raw material availability.

applications and future technologies with LIBs, the static reach of the nickel reserves approaches critical values of around 20 years **Figure 5**.

The demand for manganese in LIBs is insignificant compared to the global demand of all applications (mainly metallurgy). This pertains to each analyzed scenario. The change in battery chemistry has nearly no impact on the supply-demand ratio. Respectively, the static reach of manganese reserves in the scenarios with focus on battery demands (*1x, 1y, 1z*) is higher than any strategic planning horizon (notice the inconsistent *y*-axis). Although battery demand does not have a measurable effect, the static reach is decreased to around 40 years by incorporating all applications of manganese (*2x, 2y, 2z*). Hence, supposing there are shortfalls in manganese supply, the battery industry is in competition with strong market participants **Figure 6**.

As expected, the availability of cobalt is scored to be the most critical. Even by assuming the complete market penetration of NMC 811, the cobalt demand for traction batteries only surpasses the current supply (*1y*). The total demand for cobalt in the realistic scenario equals around 3.6 times the current mining rate (*2z*). By assuming a conservative scenario and thus NMC 111 to stay the predominant cathode, the demand is equivalent to 5.7 times the current supply (*2x*). By lowering the cobalt content in battery systems, the static reach of cobalt reserves can be extended from 8 (*2x*) to 22 (*2y*) years. The static reach in the realistic scenario amounts to 13 years which is assessed as highly critical.

As recycling bears the potential of easing the presented supply situation, the following section discusses the state-of-the-art recycling routes for LIBs.

CURRENT RECYCLING TECHNOLOGIES AND THEIR CONTRIBUTION TO REGAIN CRITICAL RAW MATERIALS

Recycling is a key element within the circular economy, to keep materials in a closed loop system and to reduce the demand for primary raw materials in production, which in turn reduces the supply risk of critical raw materials. The increasing number of LIBs collected from EVs at their EoL raises the need for recycling. Recycling of LIBs typically includes pre-treatment processes, pyrometallurgical and or hydrometallurgical processes (Mossali et al., 2020).

Pre-Treatment Processes

Pre-treatment processes comprise various activities before either hydrometallurgical or pyrometallurgical processes or mixtures of both are applied to recycle LIBs (Li et al., 2018; Velázquez-Martínez et al., 2019; Mossali et al., 2020). Main objectives according to 55 are improvement of recovery rate, management of safety issues, reduction of scrap volumes and energy consumption and enrichment of the metallic fraction.

As a prerequisite for an efficient recycling and due to the increasing variety of LIBs, they are first sorted and classified regarding battery type and battery chemistry (Melin, 2019). To prevent risks like short circuiting or spontaneous combustion during handling and manipulation, LIBs are then discharged (Hanisch et al., 2015; Li and et al., 2018; Mossali et al., 2020). This is usually done by immersing the LIB in salt solutions (Wang et al., 2017; Zheng et al., 2018; Mossali et al., 2020). 60 describe alternatives like connecting the LIBs to resistors to collect the residual energy or stimulating a controlled short circuit (Hanisch et al., 2015; Mossali et al., 2020).

For the recycling of battery systems, these are generally completely disassembled for processing to enable a material recovery of individual cells and to decrease the volume of the product to be treated (Mossali et al., 2020). Because of the high variety of LIBs, this is usually done manually, however research is focusing on possibilities to automate this process to reduce time and costs (Melin, 2019; Mossali et al., 2020). The cells are further dismantled manually to separate cathode, anode and other components or by mechanical separation (Zheng et al., 2018). Binder materials such as polyvinylidene fluoride (PVDF) or polytetrafluoroethylene (PTFE) make it difficult to separate the cathode material from the substrate (aluminum foil). There are different methods to solve this issue, eg ultrasonic-assisted separation, thermal treatment or a solvent dissolution method (Gaines, 2018; Melin, 2019). Besides thermal and chemical pre-treatments, mechanical and physical pre-treatments are the most used technique at industrial level, which allows to segregate valuable materials and to reduce scrap volumes (Mossali et al., 2020). Mechanical pre-treatments are based on differences in the physical properties and do not alter the cell chemistry

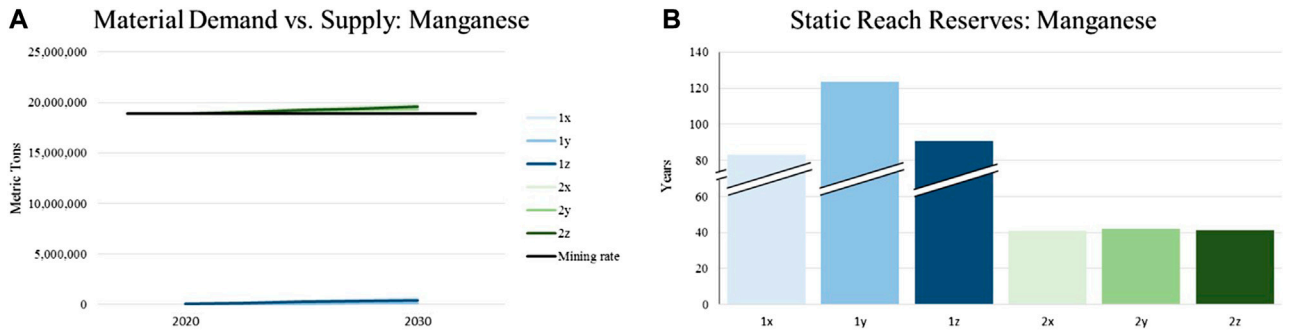

FIGURE 5 | Analysis of manganese raw material availability.

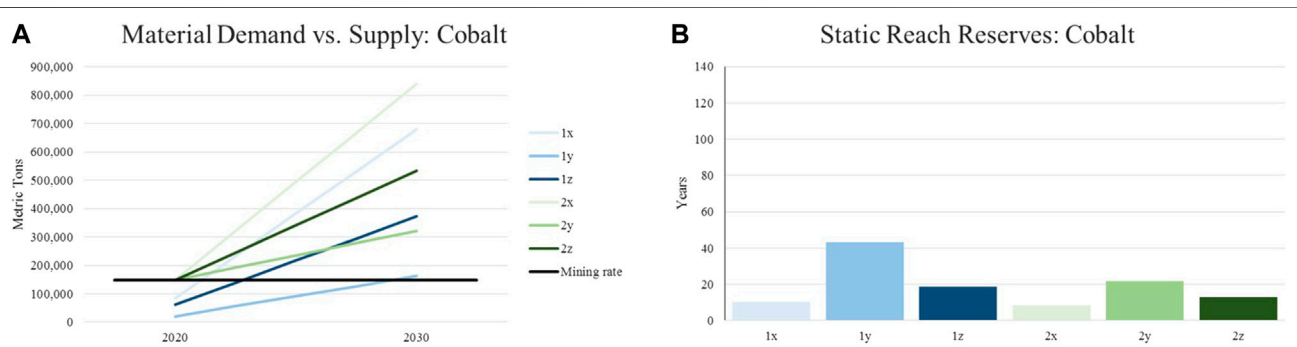

FIGURE 6 | Analysis of cobalt raw material availability.

(Velázquez-Martínez et al., 2019). Crushing, shredding and grinding is used to segregate current collector foils and organic materials from the active leachable powder. The increased surface enables a more efficient dissolution of metals during acid leaching in the following hydrometallurgical process (Hanisch et al., 2015; Mossali et al., 2020). However, mechanical pre-treatments like shredding mix up the anode and cathode materials at the start of the process, which makes it more complex in the downstream processes (Harper et al., 2019).

Pyrometallurgical Recycling

Pyrometallurgical processes are the most mature battery recycling technology, even if this process was not intended for use in recycling of spent LIBs during their initial design (Baltac and Slater, 2019; Fan et al., 2020). The simple operation and the ability to recycle different battery chemistries simultaneously are one of the main advantages of this recycling scheme (Baltac and Slater, 2019; Fan et al., 2020). However, according to Dunn et al. using pyrometallurgy recycling for LMO, LFP and NMC batteries does not reduce green house gases, since the emissions from primary production of their virgin materials are lower (Joulié et al., 2014).

For pyrometallurgical recycling, LIBs are dismantled either to module or cell level, without the need for a prior passivation step. They are fed to a high-temperature shaft furnace, together with a slag forming agent (Gaines, 2014; Harper t al., 2019) Within the high-temperature furnaces where the batteries are placed, redox reactions are activated to smelt and purify valuable metals, which are reduced and recovered in the form of alloys (Lv et al., 2018; Zheng et al., 2018; Velázquez-Martínez et al., 2019). During the process, the heat of burning materials (eg electrolytes, plastics, wires) can be re-used to reduce the energy consumption (Gaines, 2014; Gaines, 2018; Baltac and Slater, 2019; Harper et al., 2019). Output of the pyrometallurgical process are a metallic alloy fraction, slag and gases (Harper et al., 2019). High temperature facilitates oxidation and reduction reactions resulting in a mixed metal alloy containing copper, cobalt, nickel and iron (Gaines, 2018; Baltac and Slater, 2019; Harper et al., 2019; Fan et al., 2020; Mossali et al., 2020). The alloy can be separated through hydrometallurgical processes (Harper et al., 2019). The resulting furnace slag consists of ashes and burnt components, primarily containing aluminum, lithium, silicon, calcium, iron and manganese, which was present in the cathode material (Gaines, 2014; Baltac and Slater, 2019; Harper et al., 2019). In general, the aluminum and lithium in the slag is not recovered, since it is not economically viable (Gaines, 2018; Mossali et al., 2020). Instead, the slag can be reused eg as cement additive (Hanisch et al., 2012; Gaines, 2018). For a comprehensive description of recycling processes regarding lithium recovery including method, efficiency and quality (Shin et al., 2005). To avoid the release of potentially toxic by-

products, gas clean-up steps are necessary (Gaines, 2014). Despite disadvantages of the pyrometallurgical process, like high capital costs, production of toxic gases, high-energy consumption and limited number of reclaimed materials, it remains a frequently used, economical process for the extraction of high-value transition metals as cobalt and nickel (Gaines, 2014; Joulié et al., 2014; Chen et al., 2015; Harper et al., 2019; Mossali et al., 2020).

Hydrometallurgical Recycling

Hydrometallurgical processes are used after pre-treatments, in which battery packs are dismantled and cells further fragmented, eg by shredding (Baltac and Slater, 2019). Leaching is one of the key processes in which the ions are dissolved out of a solid like the active cathodic powder by using acids, resulting in a mixture of ionic species in solution (Gaines, 2018; Lv et al., 2018; Yao et al., 2018; Baltac and Slater, 2019; Harper et al., 2019; Mossali et al., 2020). Main operating parameters are temperature, acid and reducing agent concentration and species, reaction time and solid/liquid ratio (Li et al., 2018; Harper et al., 2019; Mossali et al., 2020). The metals in the solution can be recovered in high rates using a series of chemical methods like precipitation, solvent extraction and electrolytic deposition resulting in separated elements, which can be eg used to produce new cathode material (Gaines, 2018; Yao et al., 2018; Baltac and Slater, 2019). Due to their similar properties, cobalt and nickel ions are difficult to separate from each other (Gaines, 2018).

In general, the main advantages of hydrometallurgical processes compared with pyrometallurgical processes are higher recovery efficiency of valuable metals, especially Li, lower energy consumption, less production of toxic gases and lower capital costs (Lv et al., 2018; Fan et al., 2020; Mossali et al., 2020). Main drawbacks of using hydrometallurgical processes for LIB recycling are high dependency on pre-treatments and used technologies, emissions associated with the used chemicals and difficulty to process different battery chemistries and battery at once (Baltac and Slater, 2019; Mossali et al., 2020). This is due to the fact that each recycling sequence has to be optimized for a certain battery chemistry, to ensure high recovery of materials and favourable economics (Baltac and Slater, 2019). While the use of strong acids is connected with possible health issues and contamination of the environment, and also increases process costs and complexity, current studies propose the use of biodegradable organic acids (Gaines, 2018; Harper et al., 2019; Mossali et al., 2020).

Direct recycling

Direct, mechanical or physical recycling processes are a new recycling technology, which is still under development and are not yet used on an industrial scale (Baltac and Slater, 2019; Harper et al., 2019). Without using thermal or chemical energy, the recycling process focuses on reusing components or materials in new batteries, e.g. by the separation of components from the active material powder of shredded cells ("black mass") (Gaines, 2018; Shi et al., 2018; Harper et al., 2019). Other forms of direct recycling comprise e.g. the use of supercritical CO_2 to extract the electrolyte from battery cells (Mayyas et al., 2019) or the recovery of components like casing and wiring for further processing (Baltac and Slater, 2019).

It is important to highlight, that the recycling processes described above are not just alternatives to each other, but can be used in different combinations and with multiple variations in each design (Managing End-of-Life Li-ion Batteries: Battery Recycling Technologies: Innovative Technologies for the Recovery and Reuse of Valuable Metals from End-of-Life Lithium-ion Batteries, 2020). Due to the complex structure of LIBs, recycling processes were designed with the aim to recover different components (Fan et al., 2020). Generally, hydrometallurgy processes are used after the pyrometallurgy process to recover metals like Co. or Ni from the alloy. More than 90% Ni and Co. are recoverable from the molten alloy, for Cu the recovery rate is lower and Li and Al are part of the furnace slag (Fan et al., 2020; Managing End-of-Life Li-ion Batteries: Battery Recycling Technologies: Innovative Technologies for the Recovery and Reuse of Valuable Metals from End-of-Life Lithium-ion Batteries, 2020). A cost-intensive recovery of about 50–60% of Li is possible. Hydrometallurgical recycling allows a recovery rate of around 95% regarding Ni and Co. as salts, while Cu can be recovered up to 100% and Li by around 90%. Other components are recoverable by up to 80%. To achieve these high rates, the leaching processes are usually tailored for specific battery chemistries and extensive pre-treatment processes are necessary. In the future, hydrometallurgical recycling processes require an efficient and more rapid removal of impurities, to increase the purity of the recovered materials (Fan et al., 2020; Managing End-of-Life Li-ion Batteries: Battery Recycling Technologies: Innovative Technologies for the Recovery and Reuse of Valuable Metals from End-of-Life Lithium-ion Batteries, 2020).

CONCLUSION

An executive summary of the survey and this study are collected in **Table 5**. The investigated scenarios of this paper demonstrate a strong market growth in the e-mobility sector. As a result, a rapid increase in LIB production capacities is foreseeable. It is evident that no competitive alternatives to Li-ion technology will arise until 2030 regarding commercialization and mass production. Hence, a significant growth in supply for their key elements (Li, Ni and Co.) is required. As a consequence of the extremely dynamic development of e-mobility, which nowadays includes e-bikes and e-scooters with shorter lifetimes, the raw material demand will tremendously accelerate. Estimations beyond 2030 are subject to high uncertainty due to the potential market penetration of innovative technologies that are currently under research (eg solid-state Lithium-Ion and/or sodium-based batteries).

The results of this paper show that the annual demand for global e-mobility by 2030 will boost the battery production to about 1725 GWh (LIB) and that Ni will be the dominating raw material. LIBs are now and in the coming years driven by higher nickel contents. Among the various NMC subgroups, NMC 111 has currently the highest demand. The present situation concerning battery demand and market shares of the

respective cell chemistries corresponds to a yearly nickel demand of 4% of the annual global mining production. In the progressive scenario in which NMC cathode demand is solely met by NMC 811 chemistries, the demand for nickel in year 2030 would increase to 34% of the current mining production.

Although NMC 111 may still have a notable market share in the near future, the trend toward NMC and NCA battery cells with a high nickel and low cobalt content is clear and will be responsible for an accelerated depletion of nickel reserves by 2050. However, further research incorporating dynamic supply is recommended. Additionally, a battery grade nickel production requires a specific supply chain, meaning not all nickel resources are feasible for LIBs production. Taking into account that remarkable LIB recycling will take place beyond 2030, since enough cells must be present and second life is envisaged before recycling, potential shortages and tremendous cost uncertainties of Ni are the consequences. This makes the parallel search for alternative Ni-free battery technologies indispensable from now.

DATA AVAILABILITY STATEMENT

The original contributions presented in the study are included in the article/**Supplementary Material**, further inquiries can be directed to the corresponding author.

AUTHOR CONTRIBUTIONS

All authors listed have made a substantial, direct, and intellectual contribution to the work and approved it for publication.

FUNDING

This study was supported by "Ministry of the Environment, Climate Protection and the Energy Sector Baden-Württemberg," with a Grant No 017-100035|B7.R| and managed by the Project Management Agency Karlsruhe (PTKA).

ACKNOWLEDGMENTS

The authors gratefully acknowledge the contributions of the participating technical experts listed in **Supplementary Material**.

SUPPLEMENTARY MATERIAL

The Supplementary Material for this article can be found online at: https://www.frontiersin.org/articles/10.3389/fenrg.2020.594857/full#supplementary-material

REFERENCES

Aurbach, D., Zaban, A., Schechter, A., Ein-Eli, Y., Zinigrad, E., and Markovsky, B. (1995). The study of electrolyte solutions based on ethylene and diethyl carbonates for rechargeable Li batteries: I . Li metal anodes. *J. Electrochem. Soc.* 142(9), 2873. doi:10.1149/1.2048658

Baeva, S., Shterev, V., Yochev, K., and Hinov, N. (2019). Route optimization for long durability battery life during e-bike cycling. *AIP Conf. Proc.* 2172(1), 80017. doi:10.1063/1.5133575

Baltac, S., and Slater, S. (2019). *Batteries on wheels: the role of battery electric cars in the EU power system and beyond.* Cambridge, United Kingdom: Element Energy Ltd.

Barré, A., Deguilhem, B., Grolleau, S., Gérard, M., Suard, F., and Riu, D. (2013). A review on lithium-ion battery ageing mechanisms and estimations for automotive applications. *J. Power Sources.* 241, 680–689. doi:10.1016/j.jpowsour.2013.05.040

Benjamin Achzet, C. H. (2013). "How to evaluate raw material supply risks—an overview. *Resour. Pol.* 38(4), 435–447. doi:10.1016/j.resourpol.2013.06.003

Bernhart, W. (2019). Zukunftsmarkt batterie-recycling: verpasst Europa: (wieder) den Anschluss?. Available at: https://www.rolandberger.com/de/Point-of-View/Zukunftsmarkt-Batterie-Recycling-Verpasst-Europa-(wieder)-den-Anschluss.html (accessed July 18 2020)

Chakrapani, V., Rusli, F., Filler, M. A., and Kohl, P. A. (2012). Silicon nanowire anode: improved battery life with capacity-limited cycling. *J. Power Sources.* 205, 433–438. doi:10.1016/j.jpowsour.2012.01.061

Chen, X., Chen, Y., Zhou, T., Liu, D., Hu, H., and Fan, S. (2015). Hydrometallurgical recovery of metal values from sulfuric acid leaching liquor of spent lithium-ion batteries. *Waste Manag.* 38, 349–356. doi:10.1016/j.wasman.2014.12.023

Dolega, P. (2019). "Gigafactories für Lithium-Ionen-Zellen, Rohstoffbedarfe für die globale Elektromobilität bis 2050". 2019.

Dominko, R., Fichtner, M., Perraud, S., Tarascon, J.-M., Vegge, T., and Winter, M. (2019). Inventing the batteries of the future. Available at: https://www.energie-rs2e.com/en/news/inventing-sustainable-batteries-future

Fan, E., Li, L., Wang, Z., Lin, J., Huang, Y., Yao, Y., et al. (2020). Sustainable recycling technology for Li-ion batteries and beyond: challenges and future prospects. *Chem. Rev.* 120, 7020–7063. doi:10.1021/acs.chemrev.9b00535

Fortier, S. M., Hammarstrom, J. H., Ryker, S. J., Day, W. C., and Seal, R. R. (2018). USGS Critical Minerals Review. *Mining Eng.* 71, 35.

Managing end-of-life Li-ion batteries: battery recycling technologies. in *Innovative technologies for the recovery and reuse of valuable metals from end-of-life lithium-ion batteries.* Santa Clara, CA

Gaines, L. (2018). Lithium-ion battery recycling processes: research towards a sustainable course. *Sustainable Materials and Technologies.* 17, e00068. doi:10.1016/j.susmat.2018.e00068

Gaines, L. (2014). The future of automotive lithium-ion battery recycling: charting a sustainable course. *Sustainable Materials and Technologies.* 1-2, 2–7. doi:10.1016/j.susmat.2014.10.001

Graedel, T. E., Allwood, J., Birat, J.-P., Buchert, M., Hagelüken, C., Reck, B. K., et al. (2011). What do we know about metal recycling rates?. *J. Ind. Ecol.* 15(3), 355–366. doi:10.1111/j.1530-9290.2011.00342.x

Graedel, T. E., Harper, E. M., Nassar, N. T., Nuss, P., and Reck, B. K. (2015). Criticality of metals and metalloids. *Proceedings of the National Academy of Sciences of the United States of America.* 112(14), 4257–4262. doi:10.1073/pnas.1500415112

Graedel, T. E., Harper, E. M., Nassar, N. T., and Reck, B. K. (2015). On the materials basis of modern society. *Proc. Natl. Acad. Sci. Unit. States Am.* 112 (20), 6295–6300. doi:10.1073/pnas.1312752110

Handbuch lithium-ionen-batterien. Berlin: Springer Vieweg, (2013).

Hanisch, C., Haselrieder, W., and Kwade, A. (2012). "Recycling von Lithium-Ionen-Batterien – das Projekt LithoRec," in *Recycling und Rohstoffe.* (Neuruppin: TK-Verl.), 691-698.

Hanisch, C., Loellhoeffel, T., Diekmann, J., Markley, K. J., Haselrieder, W., and Kwade, A. (2015). Recycling of lithium-ion batteries: a novel method to separate coating and foil of electrodes. *J. Clean. Prod.* 108, 301–311. doi:10.1016/j.jclepro.2015.08.026

Harper, G., Sommerville, R., Kendrick, E., Driscoll, L., Slater, P., Stolkin, R., et al. (2019). Recycling lithium-ion batteries from electric vehicles. *Nature.* 575(7781), 75–86. doi:10.1038/s41586-019-1682-5

Helbig, C., Bradshaw, A. M., Wietschel, L., Andrea, T., and Tuma, A. (2018). Supply risks associated with lithium-ion battery materials. *J. Clean. Prod.* 172, 274–286. doi:10.1016/j.jclepro.2017.10.122

Marscheider-Weidemann, F., Langkau, S., Hummen, T., Erdmann, L., Tercero Espinoza, L., Angerer, G., et al. (2016). *Rohstoffe für Zukunftstechnologien 2016: Auftragsstudie.* Hannover: DERA.

Joulié, M., Laucournet, R., and Billy, E. (2014). Hydrometallurgical process for the recovery of high value metals from spent lithium nickel cobalt aluminum oxide based lithium-ion batteries. *J. Power Sources.* 247, 551–555. doi:10.1016/j.jpowsour.2013.08.128

Keck, F., Lenzen, M., Vassallo, A., and Li, M. (2019). The impact of battery energy storage for renewable energy power grids in Australia. *Energy.* 173, 647–657. doi:10.1016/j.energy.2019.02.053

Kim, J., Lee, H., Cha, H., Yoon, M., Park, M., and Cho, J. (2018). Prospect and reality of Ni-rich cathode for commercialization. *Adv. Energy Mater.* 8 (6), 1702028. doi:10.1002/aenm.201702028

Kumar, M., Yoo, J., and Hong, S. (2009). Enhancing AUTOSAR methodology to a cotsbased development process via mapping to V-Model," in IEEE international Symposium on industrial embedded SystemsSIES '09., Lausanne, Switzerland, July, 2009. (Lausanne, Switzerland, Ecole Polytechnique Federale de Lausanne), 850–1053.

Kurland, S. D. (2019). Energy use for GWh-scale lithium-ion battery production. *Environ. Res. Commun.* 2(1), 12001. doi:10.1088/2515-7620/ab5e1e

Levi, M. D., and Aurbach, D. (2005). A comparison between intercalation of Li and Mg ions into the model Chevrel phase compound (MxMo6S8): impedance spectroscopic studies. *J. Power Sources.* 146 (1), 349–354. doi:10.1016/j.jpowsour.2005.03.014

Li, L., Bian, Y., Zhang, X., Guan, Y., Fan, E., Wu, F., and Chen, R. (2018). Process for recycling mixed-cathode materials from spent lithium-ion batteries and kinetics of leaching. *Waste Manag.* 71, 362–371. doi:10.1016/j.wasman.2017.10.028

Li, M., Zhang, X., Li, M., Chen, R., Wu, F., Khalil, A., et al. (2018). The recycling of spent lithium-ion batteries: a review of current processes and technologies. *Electrochem. Energ. Rev.* 1 (4), 461–482. doi:10.1007/s41918-018-0012-1

Li, M., Lu, J., Ji, X., Li, Y., Saho, Y., Chen, Z., et al. (2020). Design strategies for nonaqueous multivalent-ion and monovalent-ion battery anodes. *Nat Rev Mater.* 5 (4), 276–294. doi:10.1038/s41578-019-0166-4

Liu, B., Zhang, H., and Zhu, S. (2016). "An incremental V-model process for automotive development," in 23rd asia-pacific software engineering conference: APSEC 2016: proceedings, Hamilton, New Zealand, 6-9 December 2016, 225–232.

Liu, Q., Du, C. Y., Shen, B., and Zuo, P. (2016). Understanding undesirable anode lithium plating issues in lithium-ion batteries. *RSC Adv.* 6 (91), 88683–88700. doi:10.1039/C6RA19482F

Luntz, A. C., Voss, J., and Reuter, K. (2015). Interfacial challenges in solid-state Li ion batteries. *J. Phys. Chem. Lett.* 6 (22), 4599–4604. doi:10.1021/acs.jpclett.5b02352

Lv, W., Wang, Z., Cao, H., Sun, Y., Zhang, Y., and Sun, Z. (2018). A critical review and analysis on the recycling of spent lithium-ion batteries. *ACS Sustain. Chem. Eng.* 6 (2), 1504–1521. doi:10.1021/acssuschemeng.7b03811

Manthiram, A. (2020). A reflection on lithium-ion battery cathode chemistry. *Nat. Commun.* 11 (1), 1–9. doi:10.1038/s41467-020-15355-0

Mayyas, A., Steward, D., and Mann, M. (2019). The case for recycling: overview and challenges in the material supply chain for automotive li-ion batteries. *Sustainable Materials and Technologies.* 19, e00087. doi:10.1016/j.susmat.2018.e00087

McKinsey and Company (2018). Metal mining constraints on the electric mobility horizon. Available at: https://www.mckinsey.com/industries/oil-and-gas/our-insights/metal-mining-constraints-on-the-electric-mobility-horizon.

Melin, H. E. (2019). "State-of-the-art in reuse and recycling of lithium-ion batteries – a research review". Available at: http://www.energimyndigheten.se/globalassets/forskning–innovation/overgripande/state-of-the-art-in-reuse-and-recycling-of-lithium-ion-batteries-2019.pdf

Mossali, E., Picone, N., Gentilini, L., Rodrìguez, O., Pérez, J. M., and Colledani, M. (2020). Lithium-ion batteries towards circular economy: a literature review of opportunities and issues of recycling treatments. *J. Environ. Manag.* 264, 110500. doi:10.1016/j.jenvman.2020.110500

Nassar, N. T., Graedel, T. E., and Harper, E. M. (2015). By-product metals are technologically essential but have problematic supply. *Science advances.* 1 (3), e1400180. doi:10.1126/sciadv.1400180

Neubauer, J., and Pesaran, A. (2011). The ability of battery second use strategies to impact plug-in electric vehicle prices and serve utility energy storage applications. *J. Power Sources.* 196 (23), 10351–10358. doi:10.1016/j.jpowsour.2011.06.053

Nishi, Y. (2001). Lithium ion secondary batteries; past 10 years and the future. *J. Power Sources.* 100 (1), 101–106. doi:10.1016/S0378-7753(01)00887-4

Oeser, D. (2018). Andreas Ziegler, Ansgar Ackva, "Single cell analysis of lithium-ion e-bike batteries aged under various conditions. *J. Power Sources.* 397, 25–31. doi:10.1016/j.jpowsour.2018.06.101

Olivetti, E. A., Ceder, G., Gaustad, G. G., and Fu, X. (2017). Lithium-ion battery supply chain considerations: analysis of potential bottlenecks in critical metals. *Joule.* 1 (2), 229–243. doi:10.1016/j.joule.2017.08.019

Pistoia, G. *Lithium-ion batteries: Advances and applications.* Amsterdam: Elsevier, (2014).

Peled, E., and Menkin, S. (2017). "Review—SEI: past, present and future. *J. Electrochem. Soc.* 164 (7), A1703. doi:10.1149/2.1441707jes

Perkins, G. (2018). Techno-economic comparison of the levelised cost of electricity generation from solar PV and battery storage with solar PV and combustion of bio-crude using fast pyrolysis of biomass. *Energy Convers. Manag.* 171, 1573–1588. doi:10.1016/j.enconman.2018.06.090

Pillot, C. (2017). *The rechargeable battery market and main trends 2011-2020.* "Paris: International Battery Seminar and Exhibit.

Quinn, J. B., Waldmann, T., Richter, K., Kasper, M., and Wohlfahrt-Mehrens, M. (2018). Energy density of cylindrical Li-ion cells: a comparison of commercial 18650 to the 21700 cells. *J. Electrochem. Soc.* 165 (14), A3284. doi:10.1149/2.0281814jes

Schmuch, R., Wagner, R., Hörpel, G., Placke, T., and Winter, M. (2018). Performance and cost of materials for lithium-based rechargeable automotive batteries. *Nat Energy.* 3 (4), 267–278. doi:10.1038/s41560-018-0107-2

Shi, Y., Chen, G., and Chen, Z. (2018). Effective regeneration of LiCoO 2 from spent lithium-ion batteries: a direct approach towards high-performance active particles. *Green Chem.* 20 (4), 851–862. doi:10.1039/C7GC02831H

Shin, S. M., Kim, N. H., Sohn, J. S., Yang, D. H., and Kim, Y. H. (2005). Development of a metal recovery process from Li-ion battery wastes. *Hydrometallurgy.* 79 (3-4), 172–181. doi:10.1016/j.hydromet.2005.06.004

Simon, B., Ziemann, S., and Weil, M. (2015). "Potential metal requirement of active materials in lithium-ion battery cells of electric vehicles and its impact on reserves: focus on Europe," *Resources. Conserv. Recycl.* 104, 300–310. doi:10.1016/j.resconrec.2015.07.011

Skeete, J.-P., Wells, P., Dong, X., Heidrich, O., and Harper, G. (2020). Beyond the EVent horizon: battery waste, recycling, and sustainability in the United Kingdom electric vehicle transition. *Energy Res. Soc. Sci.* 69, 101581. doi:10.1016/j.erss.2020.101581

Sonoc, A., Jeswiet, J., and Soo, V. K. (2015). Opportunities to improve recycling of automotive lithium ion batteries. *Procedia CIRP.* 29, 752–757. doi:10.1016/j.procir.2015.02.039

Study on the review of the list of critical raw materials: final report. Luxembourg: Publications Office of the European Union, (2017).

Thielmann, A., Sauer, A., and Wietschel, M. (2015). *Gesamt-roadmap lithium-ionen-batterien 2030.* Karlsruhe: Fraunhofer-Institut für System- und Innovationsforschung ISI.

United Nations Development Programme Available at: http://hdr.undp.org/en/content/human-development-index-hdi

Vaalma, C., Buchholz, D., Weil, M., and Passerini, S. (2018). A cost and resource analysis of sodium-ion batteries. *Nat Rev Mater.* 3(4), 1–11. doi:10.1038/natrevmats.2018.13

Velázquez-Martínez, V., Santasalo-Aarnio, R., and Serna-Guerrero, R. (2019). A critical review of lithium-ion battery recycling processes from a circular economy perspective. *Batteries.* 5 (4), 68. doi:10.3390/batteries5040068

Vezzini, A. (2014). "Manufacturers, materials and recycling technologies," in*Lithium-ion batteries: Advances and applications.* Editor G. Pistoia (Amsterdam, Netherlands: Elsevier), 529–551.

Wang, M.-M., Zhang, C.-C., and Zhang, F.-S. (2017). Recycling of spent lithium-ion battery with polyvinyl chloride by mechanochemical process. *Waste Manag.* 67, 232–239. doi:10.1016/j.wasman.2017.05.013

Xiang, H., Zhang, K., Ji, G., Lee, J.B., Changjiand, Z., Chen, X., et al. (2011). Graphene/nanosized silicon composites for lithium battery anodes with improved cycling stability. *Carbon.* 49(5), 1787–1796. doi:10.1016/j.carbon.2011.01.002

Xu, G., Han, P., Dong, S., Liu, H., Cui, G., Zou, C., et al. (2017). Li4Ti5O12-based energy conversion and storage systems: status and prospects. *Coord. Chem. Rev.* 343, 139–184. doi:10.1016/j.ccr.2017.05.006

Yao, Y., Zhu, M., Zhao, Z., Tong, B., Fan, Y., and Hua, Z. (2018). Hydrometallurgical processes for recycling spent lithium-ion batteries: a critical review. *ACS Sustain. Chem. Eng.* 6(11), 13611–13627. doi:10.1021/acssuschemeng.8b03545

Zaghib, K., Simoneau, M., Armand, M., and Gauthier, M. (1999). Electrochemical study of Li4Ti5O12 as negative electrode for Li-ion polymer rechargeable batteries. *J. Power Sources.* 81-82, 300–305. doi:10.1016/S0378-7753(99)00209-8

Zheng, F., Kotobuki, M., Song, S., Lai, M. O., and Lu, L. (2018). Review on solid electrolytes for all-solid-state lithium-ion batteries. *J. Power Sources.* 389, 198–213. doi:10.1016/j.jpowsour.2018.04.022

Zheng, X., Zhu, Z., Lin, X., Zhang, Y., He, Y., Cao, H., and Sun, Z. (2018). A mini-review on metal recycling from spent lithium ion batteries. *Engineering.* 4(3), 361–370. doi:10.1016/j.eng.2018.05.018

Zubi, G., Dufo-López, R., Carvalho, M., and Pasaoglu, G. (2018). The lithium-ion battery: state of the art and future perspectives. *Renew. Sustain. Energy Rev.* 89, 292–308. doi:10.1016/j.rser.2018.03.002

Conflict of Interest: The authors declare that the research was conducted in the absence of any commercial or financial relationships that could be construed as a potential conflict of interest.

frontiers in Energy Research

ORIGINAL RESEARCH
published: 24 November 2020
doi: 10.3389/fenrg.2020.599009

Tetrapropylammonium Hydroxide as a Zinc Dendrite Growth Suppressor for Rechargeable Aqueous Battery

Indira Kurmanbayeva[1,2], Lunara Rakhymbay[1], Kuralay Korzhynbayeva[1,2], Akylbek Adi[1], Dauren Batyrbekuly[1], Almagul Mentbayeva[2,3] and Zhumabay Bakenov[1,2,3]*

[1]National Laboratory Astana, Nur-Sultan, Kazakhstan, [2]Institute of Batteries LLC, Nur-Sultan, Kazakhstan, [3]Nazarbayev University, Nur-Sultan, Kazakhstan

Zinc metal is widely used as an anode in various aqueous systems. However, zinc anode suffers from the dendrite formation on the surface upon cycling leading to a poor cyclability of a cell and its termination due to short circuit. In this work, the effect of tetrapropylammonium hydroxide (TPAH) was studied as an electrolyte additive for aqueous Zn//$ZnCl_2$ + LiCl//$LiFePO_4$ battery. TPAH additive prolongs the battery cycle life depending on its concentration (0.01–0.1 M). The better capacity retention over 350 cycles was observed for a symmetrical Zn//$ZnCl_2$ + LiCl//Zn cell with 0.05 M TPAH whereas without additives the cell worked for only 110 cycles. The mechanism of TPAH influence on capacity retention is proposed based on the results of SEM and XRD analysis of the Zn anode and FTIR and NMR studies of the electrolyte. The XRD patterns of the negative electrode of the cell with TPAH indicates that zinc was preferentially deposited in a highly oriented (002) direction, which is more resistant against dendrite formation. These differences in deposited structure of Zn dendrites were confirmed by SEM images as well. FTIR and NMR spectra showed that TPAH decomposes to propylamine (R_nN^+H) and propene during cycling. TPAH also has an effect on the size and uniform distribution of Zn growth sides.

Keywords: tetrapropylammonium hydroxide, zinc anode, zinc dendrites suppression, aqueous electrolyte, lithium-ion battery

OPEN ACCESS

Edited by:
Soorathep Kheawhom, Chulalongkorn University, Thailand

Reviewed by:
Cheng Zhong, Tianjin University, China
Ning Zhang, Hebei University, China

****Correspondence:***
Indira Kurmanbayeva
indira.kurmanbayeva@nu.edu.kz

Specialty section:
This article was submitted to Electrochemical Energy Conversion and Storage, a section of the journal Frontiers in Energy Research

Received: *26 August 2020*
Accepted: *27 October 2020*
Published: *24 November 2020*

Citation:
Kurmanbayeva I, Rakhymbay L, Korzhynbayeva K, Adi A, Batyrbekuly D, Mentbayeva A and Bakenov Z (2020) Tetrapropylammonium Hydroxide as a Zinc Dendrite Growth Suppressor for Rechargeable Aqueous Battery. Front. Energy Res. 8:599009. doi: 10.3389/fenrg.2020.599009

INTRODUCTION

Zinc metal is considered as a promising anode material for rechargeable battery due to its high theoretical capacity (820 mAh g^{-1}), abundance, safety, scalability, low cost, and environmental friendliness (Zhang et al., 2017; Fang et al., 2018; Wang et al., 2018a; Li et al., 2019a; Zhang et al., 2020). Zinc based anode materials are used in such systems as zinc-manganese (Beck and Rüetschi, 2000; Zhu et al., 2018), zinc-air (Wang et al., 2018b), nickel-zinc (Moser et al., 2013; Parker et al., 2017), zinc-vanadium based battery (Hu et al., 2017; Batyrbekuly et al., 2020), and so forth. According to the Pourbaix diagram (Konarov et al., 2018; Li et al., 2019a; Zeng et al., 2019; Shin et al., 2020) zinc is thermodynamically unstable in the aqueous environment. It dissolves into Zn^{2+} ions under acidic conditions (pH < 4), it is more stable at neutral pH, and its solubility increases in alkaline media. Commercial, mainly used as primary batteries, aqueous zinc batteries (Zn-air, Zn-MnO_2, etc.) have alkaline media (Yufit et al., 2019; Zhang et al., 2020), where $Zn(OH)_4^{-2}$ complexes formed due to the abundance of OH^- ions. These zincate ions precipitate in the form of ZnO, resulting in dendrite growth or passivation of the anode. Mildly acidic aqueous (or neutral)

electrolyte for lithium-ion batteries is being investigated relatively recently (Xu et al., 2012; Yan et al., 2012; Zhang et al., 2017; Li et al., 2019a). Xu et al. (2012) show that the replacement of alkaline electrolyte to mild acidic in the Zn-MnO_2 battery changed the chemistry. In mild acidic media, Zn^{2+} ions are reduced and deposited in Zn metallic form, leaving place for side reaction (corrosion). However, nonuniform growth of dendrites and corrosion during cycling still prevents the widespread use of the zinc anode. Numerous works have been investigated to suppress the Zn dendrite formation, such as the modification of the zinc electrode surface (Wang et al., 2019; Zhou et al., 2019) or adding an organic and inorganic additive into electrolyte (Lan et al., 2007; Bani Hashemi et al., 2017).

Hoang et al. designed a hydrogel electrolyte (based on 1 M Li_2SO_4 and 2 M $ZnSO_4$) with fumed silica and $PbSO_4$ for Zn/$LiMn_2O_4$ cell. This gel electrolyte acts as a corrosion inhibitor and dendrite suppressor (Hoang et al., 2017). Organic molecules are commonly used additives to the electrolyte to suppress the Zn dendrite formation. According to the literature, they coordinate or complex with zinc ions (Xu et al., 2015; Wang et al., 2018c). Mitha et al. improved the electrochemical performances of Zn/$LiMn_2O_4$ rechargeable aqueous battery by adding of polyethylene glycol (PEG200) in Li_2SO_4 and $ZnSO_4$ electrolyte by approximately 32% in comparison with control sample (Mitha et al., 2018; Mitha et al., 2019). Kan et al. (1998) compared the effect of adding $PbCl_2$, sodium lauryl sulfate, and Triton X-100 to the electrolyte (2 M NH_4Cl and 2.5 M $ZnCl_2$) for Zn/polyaniline secondary battery, where Triton X-100 showed the most promising results. Lan et al. (2007) described the study of several tetraalkylammonium hydroxides as Zn dendrite's inhibition additives to alkaline 0.45 M ZnO + 6.6 M KOH electrolyte. Authors claim that inhibition of dendrites is positively correlated with the size of alkyl group of alkyl ammonium hydroxides. The authors claim that inhibition of dendrites is positively correlated with the size of alkyl group of alkylammonium hydroxides. The polarity of tetraalkylammonium hydroxides should be not too strong or too weak to uniformly cover the Zn electrode surface. 0.01 M TPAH was found as the best and ecologically friendly Zn dendrite inhibitor (Lan et al., 2007). The mechanism of zinc dendrites in alkaline electrolyte underlying the suppression of dendrite growth is related to the ability of additives to be absorbed on the surface of the electrode (Lan et al., 2007; Garcia et al., 2017; Lu et al., 2018; Li et al., 2019b). Ammonium based additives in electrolytes slowed down diffusional mass transport, were adsorbed on the specific sites of the electrode, and blocked the rapid growth of Zn dendrites via steric hindrance. That is why it was interesting to investigate the tetrapropylammonium hydroxide (TPAH) as Zn dendrite inhibitor in lithium-ion Zn/$LiFePO_4$ battery with mild acid aqueous electrolyte (pH = 4), containing 4 M $ZnCl_2$ and 3 M LiCl. The mechanism of TPAH interaction with electrolyte and Zn anode during cycling is proposed based on the results of SEM and XRD analysis of the Zn anode and FTIR and NMR studies of the electrolyte.

MATERIAL AND METHODS

Materials

$LiFePO_4$ (MTI, Corp., China), Ketjen black (Ketjen Black International, Co., Japan), and polyvinylidene fluoride (PVDF, Kynar, HSV900), 1-methyl-2-pyrrolidinone (NMP, Sigma-Aldrich), carbon fiber paper (Alfa Aesar, Co.), Cu foil with 30 μm thickness (MTI Corporation, United States), Zn foil with 100 μm thickness (Goodfellow, United States), LiCl (Sigma-Aldrich), $ZnCl_2$ (Sigma-Aldrich), TPAH (Sigma-Aldrich), and AGM (Adsorptive Glass Mat, NSG Corporation) were used.

Materials Preparation and Battery Cell Assembling

The electrodes and reference electrolyte were prepared as described in our previous work (Yesibolati et al., 2015). Briefly, to prepare a positive electrode an appropriate amount of $LiFePO_4$, Ketjen black, and PVDF, dissolved in NMP (90:4:6 wt %), were mixed to get homogeneous slurry. The slurry was then casted on carbon fiber paper and vacuum-dried at 70°C for 2 h in a vacuum oven and punched disks with 6 mm diameter. As a reference and counter electrode Zn foil discs with 8 mm diameter were used. The reference electrolyte was prepared by dissolving 3 M LiCl and 4 M $ZnCl_2$ in deionized water. TPAH was then introduced into the electrolyte at different concentrations. The pH of the electrolyte was adjusted to 4 by LiOH and HCl.

To study Zn dendrite suppression ability and mechanism of TPAH, three types of cells were assembled in this work.

Swagelok-type Zn//$ZnCl_2$ + LiCl//$LiFePO_4$ half cells were assembled in accordance with our previous report (Yesibolati et al., 2015). The assembled cells were galvanostatically cycled on a NEWARE battery tester (Neware Co, Ltd., China) in the potential window of 1.0–1.4 V at a current density of 0.1 C (1 C = 170 mAh g^{-1}). Cyclic voltammetry (CV) was performed with a VMP3 potentiostat/galvanostat (BioLogic Science Instrument, Co., France) in the potential window of 1.0–1.4 V at a scan rate of 0.1 mV s^{-1}.

Swagelok-type Zn//$ZnCl_2$ + LiCl//Zn symmetric cells were assembled in a similar way to the above half cells. The LiFePO4 positive electrode was replaced by the Zn disk with 8 mm diameter. Every charge/discharge cycling was carried out in 30 min at a current density of 1 mA cm^{-2}.

Beaker cell-type Zn//$ZnCl_2$ + LiCl//Cu cell was assembled to further study the zinc dendrite suppression mechanism by organic additives (TPAH). A zinc foil was used as a reference and counter electrode, and a copper foil served as a current collector for plating/stripping of a known amount of zinc. Both electrodes were 15 mm in diameter and separated by AGM glass separator. The electrodes were half-immersed into an aqueous electrolyte of 3/4 M lithium/zinc chlorides with and without TPAH. The assembled beaker cells were galvanostatically cycled using a BioLogic battery tester. In the first discharge, 1 mAh (or approximately 1.2 mg) Zn was deposited onto Cu foil, and then it was stripped during the charging up to 0.8 V (Higashi et al., 2016).

All electrochemical characterizations were performed at a room temperature.

Characterization

The morphology of the Zn electrodes was observed by Field emission scanning electron microscopy (FE-SEM, JEOL, JSM-7500F). X-Ray diffractometer (Rigaku SmartLab) was applied to identify phases on the surface of anode after cycling. The cycled Zn electrodes were washed by distilled water to remove residual electrolyte. The electrolyte solutions were analyzed by Fourier Transform Infrared Spectroscopy (Nicolet iS10 FT-IR) and FT NMR spectrometer (JEOL, ECA-500).

RESULTS AND DISCUSSION

To check a possible impact of TPAH on the electrochemical performance of the aqueous Zn//$ZnCl_2$ + LiCl//$LiFePO_4$ battery system, the cyclic voltammetry was performed for the cells with and without TPAH electrolyte additives. **Figure 1** shows CV profiles of the Zn//$ZnCl_2$ + LiCl//$LiFePO_4$ cells without and with 0.1 M TPAH in the potential window of 1.0–1.4 V at 0.1 mV s^{-1} for initial first, third, and fifth cycles.

Both cells had a single redox pair corresponding to lithiation/delithiation of $LiFePO_4$ at 1.14/1.28 V, respectively (Yesibolati et al., 2015). The absence of additional peaks in the CV curves of the cell with the electrolyte additive (**Figure 1B**) indicated that TPAH additive has no negative effect on the electrochemical reactions in aqueous Zn//$ZnCl_2$ + LiCl//$LiFePO_4$ battery system.

The Zn plating/stripping behavior was studied using the Zn//$ZnCl_2$ + LiCl//Zn symmetric cell without additive and with TPAH at different concentrations (0.01, 0.02, 0.05, and 0.1 M). **Figure 2** a shows the voltage versus time profiles of the symmetric cells without and with 0.05 M TPAH electrolyte additive at a current density of 1 mA cm^{-2}. The cell without TPAH electrolyte additive had lower polarization (less than 0.1 V) in the initial 40 h. However, the cell polarization increased to 0.45 V at a later time and the cell short-circuited by 60 h. On the other hand, the cell with TPAH electrolyte additive had a larger polarization (0.3 V) from the initial hours due to an increased resistance of the Zn electrode with adsorbed TPAH molecules (Garcia et al., 2017; Lu et al., 2018). The use of 0.05 M TPAH additive prolonged the cyclability of symmetric cell up to 352 cycles (or 180 h). The cell with lower concentration of TPAH (0.01 M, 0.02 M) overperformed the cell without the additive (**Supplementary Figure S1**). However, a further increasing of the additive concentration (0.1 M) had no significant improvement on the symmetric cell cycle life (**Supplementary Figure S1**).

Figures 2B,C present the SEM images of the Zn electrodes in symmetric cells without and with TPAH additive, respectively. Randomly oriented Zn hexagonal disks with average size 1–3 μm can be seen on the surface of both electrodes. Zn dendrite has grown into flower-like agglomerate with a size of approximately 18–20 μm in width on the additive-free symmetric cell, which cycled 60 h (**Figure 2B**). Only hexagonal Zn disks (mostly horizontally oriented) are seen from the image of anode with 0.05 M TPAH addition (**Figure 2C**). The TPAH additive prevents such big Zn dendrite growth even though the cell cycled for about 180 h. Zn disks in **Figure 2C** just have become thicker.

In order to understand the positive effect of TPAH on Zn dendrite suppression, the large-scaled beaker cell-type Zn//$ZnCl_2$ + LiCl//Cu battery was designed and assembled (**Supplementary Figure S2**). Increasing of TPAH concentration two times (0.02 M) does not give twice improvement of the cell cyclability, the same situation for 0.05 M additive concentration. Increased concentrations will not be economically effective as with 0.01 M TPAH. Due to this, the 0.01 M concentration was chosen for further investigation. Using a copper foil as a current collector instead of a zinc foil allows for quantifying an amount of Zn deposited onto Cu foil and then calculating the Coulombic efficiency. In the first discharge, 1.2 mg Zn was deposited onto Cu foil, and then it was charged until 0.8 V during which the deposited zinc stripped from Cu foil (Higashi et al., 2016). **Figures 3A,B** show charge/discharge curves of the cells without and with 0.01 M TPAH electrolyte additive, respectively, at a current density of 20 mA cm^{-2}. The cell without TPAH additive demonstrated a stable zinc deposition/stripping performance up to 50 cycles with an overpotential of ~120 mV (**Figure 3A**). However, a sharp decrease of overpotential from ~120 to ~60 mV occurred after 50 cycles associated with a short circuit of the cell, whereas the presence of TPAH additive in the electrolyte improved cycle stability of the cell over 70 cycles due to its zinc dendrite suppression effect (**Figure 3B**) (**Supplementary Figure S5**).

Figure 3C shows Coulombic efficiency versus cycle number profiles of the beaker cells without and with TPAH additive. The beaker cell without TPAH additive had a constant Coulombic efficiency of 99% over 50 cycles, while the Coulombic efficiency of the cell with TPAH additive fluctuated in the initial cycles and then stabilized to 98.5% in the subsequent cycles. However, the cell without TPAH additive short-circuited after 50 cycles with an abrupt increase of the Coulombic efficiency, whereas the cell with TPAH additive demonstrated a stable cycle performance. The improved cycle stability of the cell further confirms a significant effect of TPAH additive on zinc dendrite suppression. To study the mechanism of TPAH additive for the dendrite suppression, the electrodes and electrolyte were analyzed by many characterization techniques before and after cycling.

Dendrite deposition behavior of both Zn electrodes after cycling was investigated by XRD. **Figure 4** demonstrates XRD patterns of the Zn electrodes before and after cycling with and without TPAH additive. The pattern obtained on both electrodes after cycling has no significant difference from pure Zn reference, suggesting reversible behavior of Zn deposition/dissolution. Significant lattice planes (002), (100), (101), and (102) are identical with a literature (Gomes and da Silva Pereira, 2006; Nayana and Venkatesha, 2011; Nayana and Venkatesha, 2015) and demonstrate the different directions of crystal growth. The highest intensity peak at 42° indicated Zn growth in mostly directed (101) orientation, which causes the formation of tips (Nayana and Venkatesha, 2015). However, the intensity of (002) peak of Zn anode with TPAH addition increases, indicating that zinc was preferentially deposited in a basal (parallel) oriented direction

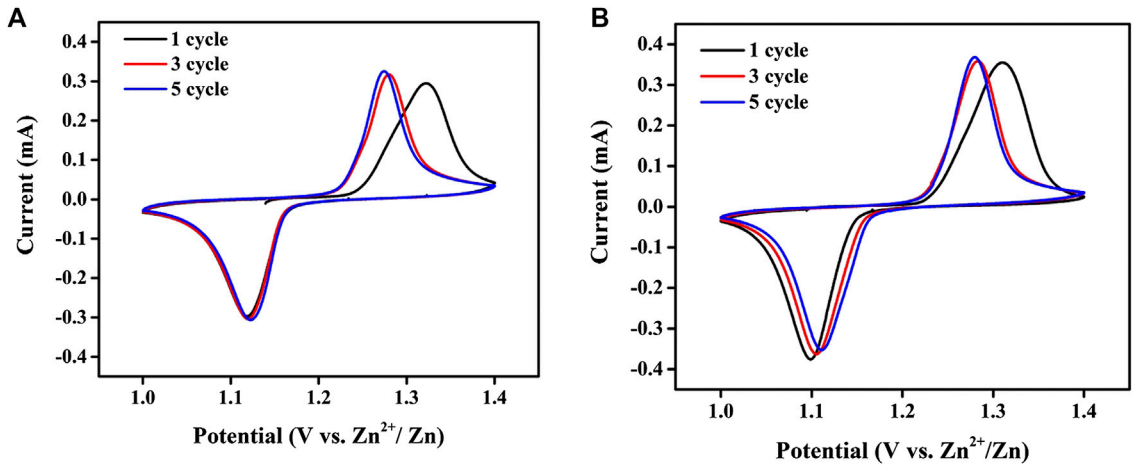

FIGURE 1 | CV profiles of Zn/$LiFePO_4$ cells **(A)** without and **(B)** with 0.1 M TPAH in the potential window of 1.0–1.4 V at 0.1 mV s^{-1}.

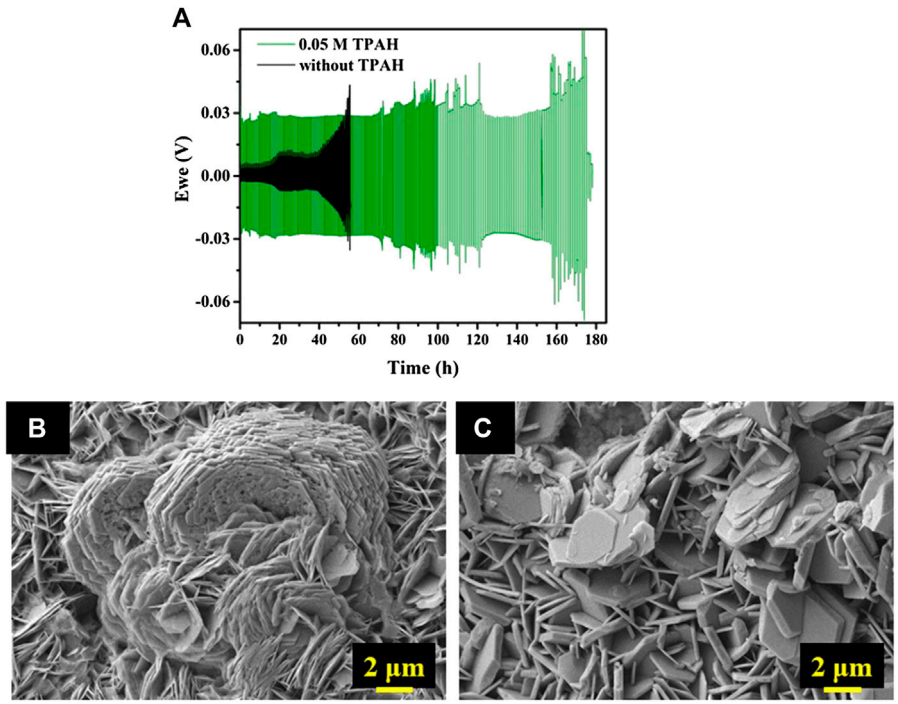

FIGURE 2 | (A) Voltage vs. time profiles of the Zn//$ZnCl_2$ + LiCl//Zn symmetric cells without and with 0.05 M TPAH electrolyte additive at a current density of 1 mA cm^{-2} and SEM images of Zn electrodes after cycling **(B)** without TPAH (cycled 60 h), **(C)** with TPAH (cycled 180 h).

to anode surface, which is more resistant against dendrite formation (Sun et al., 2018). Similar behavior of nitrogen-containing amine group of CTAB (cetyltrimethylammonium bromide) was investigated in zinc electrodeposition by Nayana (Nayana and Venkatesha, 2011). This may explain the good battery performance of battery with TPAH addition due to the more 002 oriented deposited zinc.

An additional phase in the XRD patterns was observed and identified as simonkolleite ($Zn_5(OH)_8Cl_2$ * H_2O) in both anodes after cycling (**Supplementary Figure S4**). This also was confirmed by EDS mapping of cycled Zn anodes with/without TPAH, which shows the presence of Zn, O, and Cl (**Supplementary Figure S3**). It can be noted that simonkolleite, which acts as a corrosion stabilizer, forms in

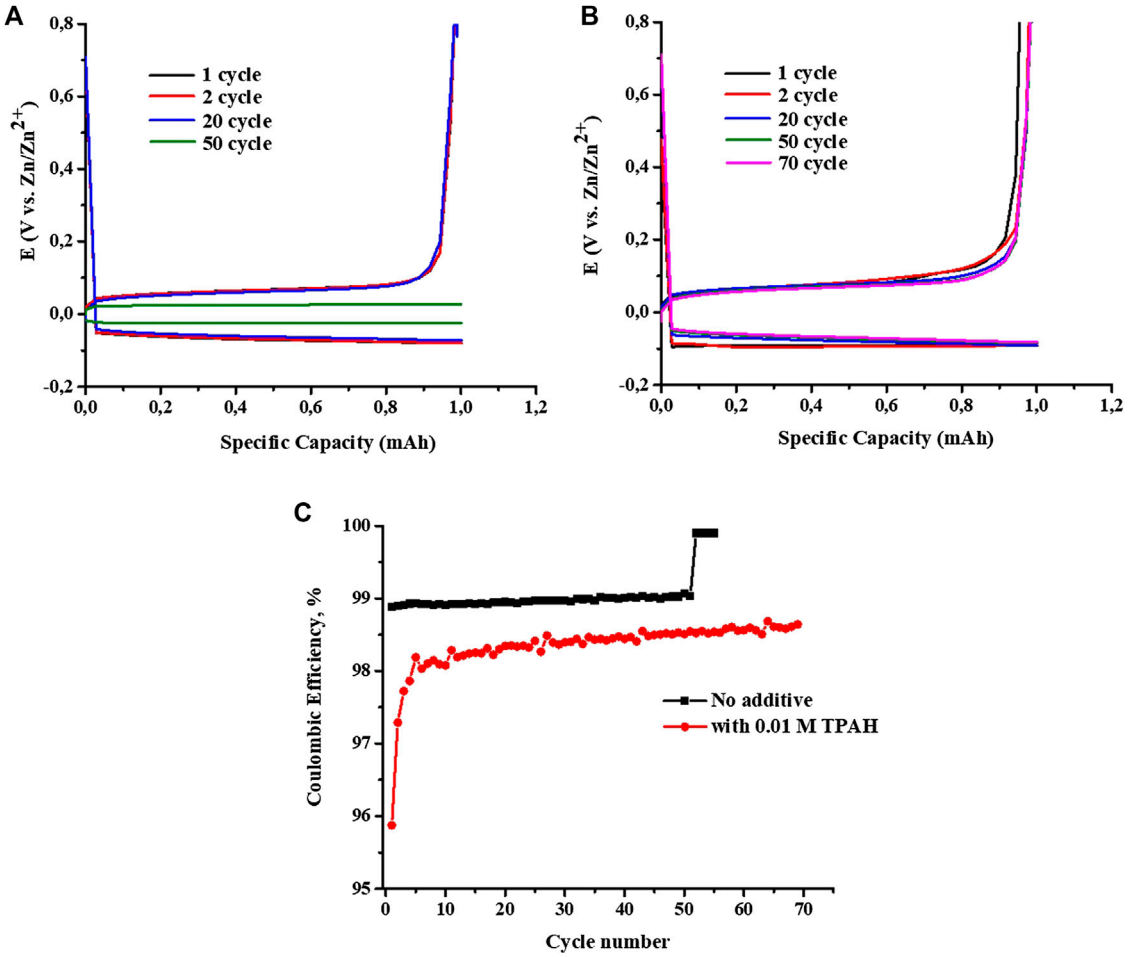

FIGURE 3 | Charge/discharge curves of Zn//$ZnCl_2$+LiCl//Cu beaker cell **(A)** without and **(B)** with 0.01 M TPAH electrolyte additive, and **(C)** the cyclability of cells with and without TPAH additive at 20 mA cm^{-2}.

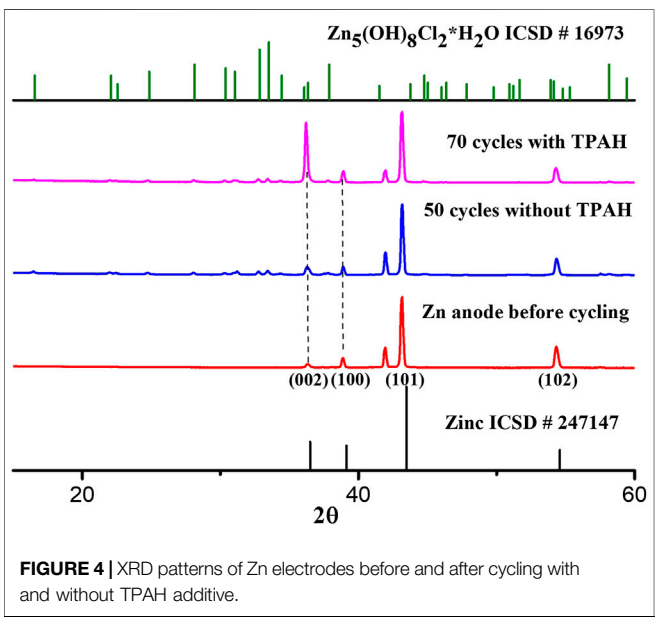

FIGURE 4 | XRD patterns of Zn electrodes before and after cycling with and without TPAH additive.

case of high Cl content and low pH value (Yoo et al., 2013; Cousy et al., 2017; Li et al., 2019c).

The comparison of Zn electrode surface morphology cycled in beaker cells with and without TPAH addition was done by SEM. It is clearly seen from SEM images that the Zn electrode surfaces of both beaker cells have dendrites, but the character of deposition is different (**Figures 5A,B**). It can be seen from images with small magnification that Zn anode of cell without TPAH has uneven growth of dendrites; they are almost located on the right side (**Figure 5A**). Due to the growth upon cycling and penetration of dendrites into AGM separator, it was not possible to detach. The fibers of the separator are seen in the picture, whereas the left corner of the image is clean from dendrites. The Zn dendrites are more uniformly distributed on the anode surface in case of battery with TPAH addition. The size of dendrites is smaller (**Figure 5B**) and, as a result, this cell worked longer for 20 cycles at 20°C in comparison with battery without TPAH. The larger magnification shows that dendrites of the anode without TPAH have a compact structure with closely packed Zn disks (**Figure 5C**), whereas TPAH addition makes these dendrites

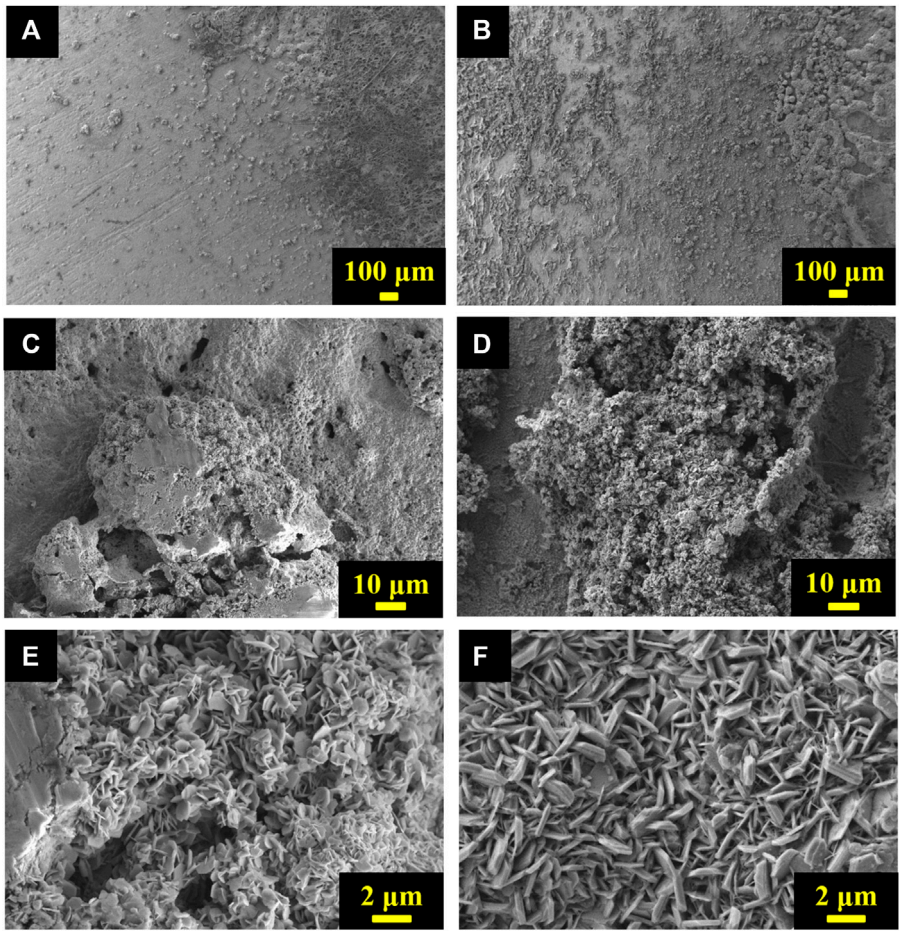

FIGURE 5 | SEM images of cycled Zn anodes **(A,C,E)** without TPAH and **(B,D,F)** with TPAH additive at different magnifications.

looser (**Figure 5D**). The high magnification images of Zn dendrites of both cells consist of the hexagonal disks (**Figures 5E,F**). The size of the disk is smaller in the left picture (about 1 µm in width), and they packed randomly and very close to each other like a sponge (**Figure 5C**). In the case of TPAH addition (**Figure 5F**), even distributed Zn disks have a size of 2–3 µm in width and they are much thicker than in **Figure 5C**.

Therefore, TPAH addition in electrolyte changed the distribution and structure of dendrites. With TPAH Zn dendrites grow on the surface of anode more uniformly. Dendrite aggregates on the surface of Zn anode of beaker cell with TPAH addition have almost the same size, even though they are cycled 70 times at 20°C. The beaker cell without TPAH short-circuited after 50 cycles due to the enlarged size of particular dendrites.

The electrolytes with TPAH before and after cycling were analyzed by FTIR and NMR. TPAH is a quaternary ammonium cation with four propyl substituents around the central nitrogen and hydroxyl group (**Figure 6A**). **Figure 6B** gives the FTIR spectra of the commercial TPAH, the electrolytes with TPAH before and after cycling. The peaks in the ranges of 1,630–1,650, 1,850–2,450, 3,200–3,500 cm^{-1} appear due to the water. The spectrum of commercial TPAH has its characteristic peaks due to propyl group (740–720, 1,390–1,375, 1,490–1,450, 3,000–2,850 cm^{-1}) and N-C vibrational mode (970–980 cm^{-1}) (**Figure 6B**, black line) (Spectroscopic Tools). When TPAH was added to $ZnCl_2$ and LiCl containing electrolyte, all corresponding to TPAH peaks disappear (**Figure 6B**, red line). We assume that aqueous electrolyte overloaded characteristic peaks, but new N-H vibration mode at 3,243 cm^{-1} (Zhai et al., 2006) is seen in solution of electrolyte before cycling. The ions in the solution interact with TPAH (**Supplementary Figure S4**) and break vibrational modes of N-C and propyl bonds. The cycled electrolyte shows several features. Shifted peaks appear at 1,050, 1,250 cm^{-1}, indicating the presence of amine groups in the electrolyte. In addition, the vibrational mode of $-CH = CH_2$ appears at 1,450 cm^{-1}, and the shoulder at 3,600 cm^{-1} which is ascribed to N-H vibration becoming more pronounced. These peaks confirm the aforementioned content of cycled electrolyte solution.

Figure 6 illustrates the 1H NMR spectrum of **(C)** 1 M TPAH commercial solution and **(D)** electrolyte with 0.01 M TPAH after cycling, respectively. The 1H NMR spectrum of initial TPAH is fully matched with published data (Tetrapropylammonium hydroxide - 1H NMR Chemical Shifts - SpectraBase). The 1H NMR spectrum of

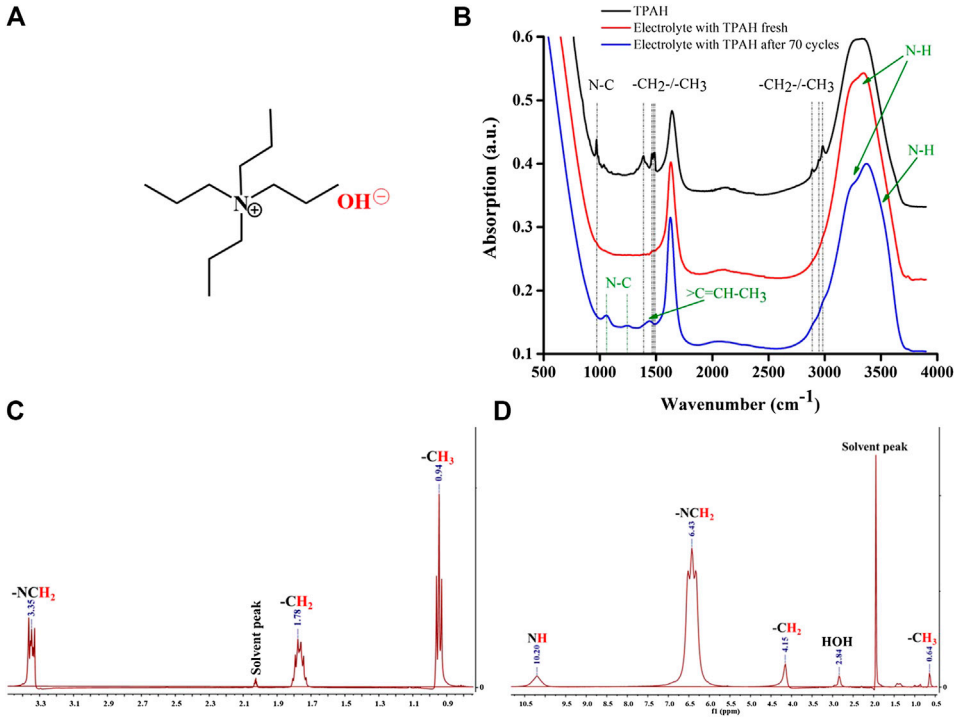

FIGURE 6 | (A) TPAH molecular structure, **(B)** FTIR absorption spectra of TPAH, **(C)** 1H NMR spectrum of 1 M TPAH commercial solution, and **(D)** 1H NMR spectrum of electrolyte with 0.01 M TPAH additive after cycling.

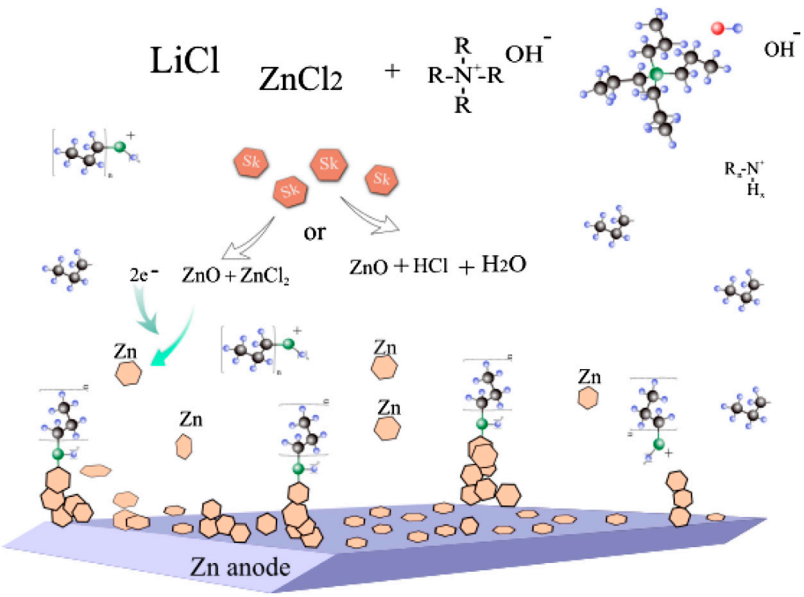

FIGURE 7 | A proposed mechanism of Zn dendrite suppression by TPAH electrolyte additive.

electrolyte after cycling revealed signals corresponding to methyl proton at 0.64 (m), methylene proton at 4.15 (br s), methylene proton attached to N atom at 6.43 (t), and amine group proton at 10.21 (br s). The structure of the propyl group attracted to N atom is assigned from the resonances at δH 0.64, 4.15, 6.43, and 10.21. From the NMR figures, we can observe the shifting of peaks that occurred due to the strong

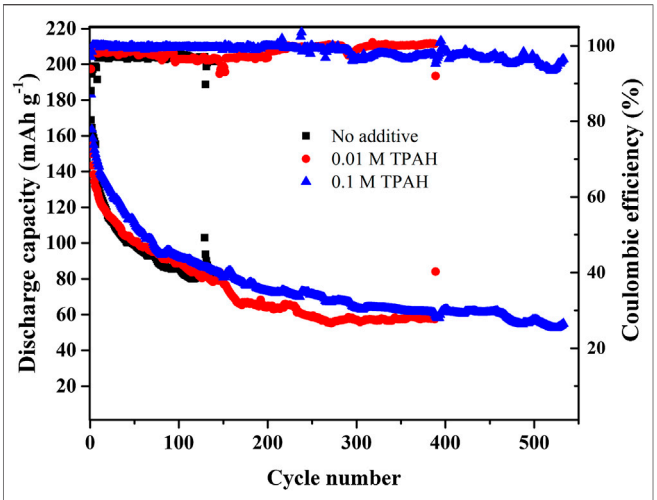

FIGURE 8 | The cyclability of Zn//$ZnCl_2$ + LiCl//$LiFePO_4$ batteries with and without TPAH additive in electrolyte at 0.5 C.

resonance effect of the amine group. All the presented data suggested (predicted) that TPAH in electrolyte after cycling was decomposed to R_n-NH and propene by comparison of spectra included in this study together with literature data (Spectroscopic Tools; Nishioka, 1974).

Based on all experimental results the following mechanism of the influence of TPAH addition to the electrolyte on battery cyclability is proposed (**Figure 7**). First, TPAH in electrolyte solution increased the yield of simonkolleite formation (**Supplementary Figure S4**). Simonkolleite is unstable and can decompose to ZnO and $ZnCl_2$ or to ZnO + HCl + H_2O (Zhang and Yanagisawa, 2007; Yoo et al., 2013; Moezzi et al., 2016). It is interesting to notice that simonkolleite disks appear with the combination of lower alkalinity, lower temperature, and higher NH_4^+ ions concentration and in existence of Cl^- anion (Li et al., 2011; Cousy et al., 2017). Second, when the battery starts to cycle at high C rate (20 C), Zn dendrites are formed on anode by applying a negative current. During the cycling TPAH decomposes to propylamine (R_nN^+H) and propene (Zhai et al., 2006; Prokopova et al., 2013). R_nN^+H adsorbs on the active site of Zn dendrite, preventing its further growth (Lan et al., 2007). Zinc in battery with TPAH addition deposited mostly in a basal (parallel) oriented direction to anode surface.

The cyclability and the Coulombic efficiency of the batteries without additive and with the smallest and highest concentration of TPAH as 0.01 and 0.1 M at 0.5 C are shown in **Figure 8**. The Coulombic efficiency of all systems is high (96–100%).

The specific discharge capacity of all batteries gradually decreases with each cycle. However, the cell without the additive is inferior in terms of the stability. Batteries with TPAH (0.01 and 0.1 M) performed better cyclability, which are over 380 and 570 cycles, rather than the system with bare electrolyte. Apparently, the addition of the TPAH can prevent zinc dendrite growth, consequently prolonging cycle life of Zn/$LiFePO_4$ system.

CONCLUSION

In summary, the effect of TPAH as an electrolyte additive on the inhibition of Zn dendrite growth in aqueous rechargeable Li-ion battery Zn/$LiFePO_4$ has been investigated. The TPAH additive inhibits the dendritic growth on the Zn anode surface, increasing the battery life cycle. The mechanism of this process is proposed based on the results of SEM and XRD analysis of the Zn anode and FTIR and NMR studies of the electrolyte solution. The XRD pattern of the negative electrode of battery with TPAH indicates that Zn from electrolyte solution was preferentially deposited in a highly oriented (002) direction, which is more resistant to dendrite formation. Zn dendrites are deposited on the surface of anode more uniformly. During the electrochemical cycling TPAH decomposes to propylamine (R_nN^+H) and propene. They adsorb on the tip of Zn nucleation site and cover the surface of the electrode, preventing further growth of dendrite.

DATA AVAILABILITY STATEMENT

The original contributions presented in the study are included in the article/**Supplementary Materials**; further inquiries can be directed to the corresponding author/s.

AUTHOR CONTRIBUTIONS

AM and ZB contributed to conception and design of the study, IK analyzed data and contributed to the final version of the manuscript, KK carried out the experiment and wrote the first draft of the manuscript, and AA, LR, and DB carried out the experiment. All authors contributed to manuscript revision, read, and approved the submitted version.

FUNDING

This work was supported by the research grant AP05136016 "Zinc Based Rechargeable Aqueous Battery: A Green, Safe and Economic Battery for Space Applications (ZRABS)" and targeted the program BR05236524 "Innovative Materials and Systems for Energy Conversion and Storage" from the Ministry of Education and Science of the Republic of Kazakhstan.

ACKNOWLEDGMENTS

The authors thank their colleagues Dr. B. Uzakbaiuly and Dr. I. Trussov who greatly assisted the research with analytical techniques.

SUPPLEMENTARY MATERIAL

The Supplementary Material for this article can be found online at: https://www.frontiersin.org/articles/10.3389/fenrg.2020.599009/full#supplementary-material

REFERENCES

Bani Hashemi, A., Kasiri, G., and La Mantia, F. (2017). The effect of polyethyleneimine as an electrolyte additive on zinc electrodeposition mechanism in aqueous zinc-ion batteries. *Electrochim. Acta.* 258, 703–708. doi:10.1016/j.electacta.2017.11.116

Batyrbekuly, D., Cajoly, S., Laïk, B., Pereira-Ramos, J., Emery, N., Bakenov, Z., et al. (2020). Mechanistic investigation of a hybrid Zn/V_2O_5 rechargeable battery with a binary Li^+/Zn^{2+} aqueous electrolyte. *ChemSusChem.* 13, 724–731. doi:10.1002/cssc.201903072

Beck, F., and Rüetschi, P. (2000). Rechargeable batteries with aqueous electrolytes. *Electrochim. Acta.* 45, 2467–2482. doi:10.1016/S0013-4686(00)00344-3

Cousy, S., Gorodylova, N., Svoboda, L., and Zelenka, J. (2017). Influence of synthesis conditions over simonkolleite/ZnO precipitation. *Chem. Pap.* 71, 2325–2334. doi:10.1007/s11696-017-0226-4

Fang, G., Zhou, J., Pan, A., and Liang, S. (2018). Recent advances in aqueous zinc-ion batteries. *ACS Energy Lett.* 3, 2480–2501. doi:10.1021/acsenergylett.8b01426

Garcia, G., Ventosa, E., and Schuhmann, W. (2017). Complete prevention of dendrite formation in Zn metal anodes by means of pulsed charging protocols. *ACS Appl. Mater. Interfaces.* 9, 18691–18698. doi:10.1021/acsami.7b01705

Gomes, A., and da Silva Pereira, M. I. (2006). Zn electrodeposition in the presence of surfactants. Part I. Voltammetric and structural studies. *Electrochim. Acta.* 52, 863–871. doi:10.1016/j.electacta.2006.06.025

Higashi, S., Lee, S. W., Lee, J. S., Takechi, K., and Cui, Y. (2016). Avoiding short circuits from zinc metal dendrites in anode by backside-plating configuration. *Nat. Commun.* 7, 1–6. doi:10.1038/ncomms11801

Hoang, T. K. A., Acton, M., Chen, H. T. H., Huang, Y., Doan, T. N. L., and Chen, P. (2017). Sustainable gel electrolyte containing Pb2+ as corrosion inhibitor and dendrite suppressor for the zinc anode in the rechargeable hybrid aqueous battery. *Mater. Today Energy.* 4, 34–40. doi:10.1016/j.mtener.2017.03.003

Hu, P., Yan, M., Zhu, T., Wang, X., Wei, X., Li, J., et al. (2017). Zn/V_2O_5 aqueous hybrid-ion battery with high voltage platform and long cycle life. *ACS Appl. Mater. Interfaces.* 9, 42717–42722. doi:10.1021/acsami.7b13110

Kan, J., Xue, H., and Mu, S. (1998). Effect of inhibitors on Zn-dendrite formation for zinc-polyaniline secondary battery. *J. Power Sources.* 74, 113–116. doi:10.1016/S0378-7753(98)00040-8

Konarov, A., Voronina, N., Jo, J. H., Bakenov, Z., Sun, Y. K., and Myung, S. T. (2018). Present and future perspective on electrode materials for rechargeable zinc-ion batteries. *ACS Energy Lett.* 3, 2620–2640. doi:10.1021/acsenergylett.8b01552

Lan, C. J., Lee, C. Y., and Chin, T. S. (2007). Tetra-alkyl ammonium hydroxides as inhibitors of Zn dendrite in Zn-based secondary batteries. *Electrochim. Acta.* 52, 5407–5416. doi:10.1016/j.electacta.2007.02.063

Li, H., Ma, L., Han, C., Wang, Z., Liu, Z., Tang, Z., et al. (2019a). Advanced rechargeable zinc-based batteries: recent progress and future perspectives. *Nanomater. Energy.* 62, 550–587. doi:10.1016/j.nanoen.2019.05.059

Li, M., He, Q., Li, Z., Li, Q., Zhang, Y., Meng, J., et al. (2019b). A novel dendrite-free Mn^{2+}/Zn^{2+} hybrid battery with 2.3 V voltage window and 11000-cycle lifespan. *Adv. Energy Mater.* 9, 1–10. doi:10.1002/aenm.201901469

Li, S., Chen, X., Wang, X., Xiong, Y., Yan, Y., Tan, Z., et al. (2019c). Simonkolleite coating on poly(amino acids) to improve osteogenesis and suppress osteoclast formation *in vitro*. *Polymers (Basel).* 11, 1505. doi:10.3390/polym11091505

Li, Y., Zou, Y., and Hou, Y. (2011). Synthesis and characterization of simonkolleite nanodisks and their conversion into ZnO nanostructures. *Cryst. Res. Technol.* 46, 305–308. doi:10.1002/crat.201000673

Lu, W., Xie, C., Zhang, H., and Li, X. (2018). Inhibition of zinc dendrite growth in zinc-based batteries. *ChemSusChem.* 11, 3996–4006. doi:10.1002/cssc.201801657

Mitha, A., Mi, H., Dong, W., Cho, I. S., Ly, J., Yoo, S., et al. (2019). Thixotropic gel electrolyte containing poly(ethylene glycol) with high zinc ion concentration for the secondary aqueous $Zn/LiMn_2O_4$ battery. *J. Electroanal. Chem.* 836, 1–6. doi:10.1016/j.jelechem.2019.01.014

Mitha, A., Yazdi, A. Z., Ahmed, M., and Chen, P. (2018). Surface adsorption of polyethylene glycol to suppress dendrite formation on zinc anodes in rechargeable aqueous batteries. *ChemElectroChem.* 5, 2409–2418. doi:10.1002/celc.201800572

Moezzi, A., Cortie, M., and McDonagh, A. (2016). Transformation of zinc hydroxide chloride monohydrate to crystalline zinc oxide. *Dalton Trans.* 45, 7385–7390. doi:10.1039/c5dt04864h

Moser, F., Fourgeot, F., Rouget, R., Crosnier, O., and Brousse, T. (2013). *In situ* X-ray diffraction investigation of zinc based electrode in Ni-Znsecondary batteries. *Electrochim. Acta.* 109, 110–116. doi:10.1016/j.electacta.2013.07.023

Nayana, K. O., and Venkatesha, T. V. (2011). Synergistic effects of additives on morphology, texture and discharge mechanism of zinc during electrodeposition. *J. Electroanal. Chem.* 663, 98–107. doi:10.1016/j.jelechem.2011.10.001

Nayana, K. O., and Venkatesha, T. V. (2015). Bright zinc electrodeposition and study of influence of synergistic interaction of additives on coating properties. *J. Ind. Eng. Chem.* 26, 107–115. doi:10.1016/j.jiec.2014.11.021

Nishioka, A. (1974). High resolution NMR. San Diego, CA: Academic Press. doi:10.1295/kobunshi.23.310

Parker, J. F., Chervin, C. N., Pala, I. R., Machler, M., Burz, M. F., Long, J. W., et al. (2017). Rechargeable nickel–3D zinc batteries: an energy-dense, safer alternative to lithium-ion. *Science.* 356, 415–418. doi:10.1126/science.aak9991

Prokopova, O., Bernauer, B., Frycova, M., Hrabanek, P., Zikanova, A., and Kocirik, M. (2013). Principal features of tetrapropylammonium hydroxide removal kinetics from silicalite-1 in quasi-isothermal heating regimes. *J. Phys. Chem. C.* 117, 1468–1476. doi:10.1021/jp3090364

Science and Fun. Spectroscopic tools. Available at: https://www.science-and-fun.de/tools/ (Accessed July 20, 2020).

Shin, J., Lee, J., Park, Y., and Choi, J. W. (2020). Aqueous zinc ion batteries: focus on zinc metal anodes. *Chem. Sci.* 11, 2028–2044. doi:10.1039/d0sc00022a

SpectraBase. Tetrapropylammonium hydroxide-1H NMR chemical Shifts. Available at: https://spectrabase.com/spectrum/KLXRcA3Yuni (Accessed July 20, 2020).

Sun, K. E. K., Hoang, T. K. A., Doan, T. N. L., Yu, Y., and Chen, P. (2018). Highly sustainable zinc anodes for a rechargeable hybrid aqueous battery. *Chem. A Eur. J.* 24, 1667–1673. doi:10.1002/chem.201704440

Wang, F., Borodin, O., Gao, T., Fan, X., Sun, W., Han, F., et al. (2018a). Highly reversible zinc metal anode for aqueous batteries. *Nat. Mater.* 17, 543–549. doi:10.1038/s41563-018-0063-z

Wang, K., Pei, P., Wang, Y., Liao, C., Wang, W., and Huang, S. (2018b). Advanced rechargeable zinc-air battery with parameter optimization. *Appl. Energy.* 225, 848–856. doi:10.1016/j.apenergy.2018.05.071

Wang, Y., Niu, Z., Zheng, Q., Zhang, C., Ye, J., Dai, G., et al. (2018c). Zn-based eutectic mixture as anolyte for hybrid redox flow batteries. *Sci. Rep.* 8, 8–15. doi:10.1038/s41598-018-24059-x

Wang, M., Emre, A., Tung, S., Gerber, A., Wang, D., Huang, Y., et al. (2019). Biomimetic solid-state Zn^{2+} electrolyte for corrugated structural batteries. *ACS Nano.* 13, 1107–1115. doi:10.1021/acsnano.8b05068

Xu, C., Li, B., Du, H., and Kang, F. (2012). Energetic zinc ion chemistry: the rechargeable zinc ion battery. *Angew. Chem. Int. Ed.* 51, 933–935. doi:10.1002/anie.201106307

Xu, M., Ivey, D. G., Qu, W., and Xie, Z. (2015). Study of the mechanism for electrodeposition of dendrite-free zinc in an alkaline electrolyte modified with 1-ethyl-3-methylimidazolium dicyanamide. *J. Power Sources.* 274, 1249–1253. doi:10.1016/j.jpowsour.2014.10.140

Yan, J., Wang, J., Liu, H., Bakenov, Z., Gosselink, D., and Chen, P. (2012). Rechargeable hybrid aqueous batteries. *J. Power Sources.* 216, 222–226. doi:10.1016/j.jpowsour.2012.05.063

Yesibolati, N., Umirov, N., Koishybay, A., Omarova, M., Kurmanbayeva, I., Zhang, Y., et al. (2015). High performance Zn/LiFePO4 aqueous rechargeable battery for large scale Applications. *Electrochim. Acta.* 152, 505–511. doi:10.1016/j.electacta.2014.11.168

Yoo, J. D., Volovitch, P., Abdel Aal, A., Allely, C., and Ogle, K. (2013). The effect of an artificially synthesized simonkolleite layer on the corrosion of electrogalvanized steel. *Corrosion Sci.* 70, 1–10. doi:10.1016/j.corsci.2012.10.024

Yufit, V., Tariq, F., Eastwood, D. S., Biton, M., Wu, B., Lee, P. D., et al. (2019). Operando visualization and multi-scale tomography studies of dendrite formation and dissolution in zinc batteries. *Joule.* 3, 485–502. doi:10.1016/j.joule.2018.11.002

Zeng, X., Hao, J., Wang, Z., Mao, J., and Guo, Z. (2019). Recent progress and perspectives on aqueous Zn-based rechargeable batteries with mild aqueous electrolytes. *Energy Storage Mater.* 20, 410–437. doi:10.1016/j.ensm.2019.04.022

Zhai, J. P., Tang, Z. K., Li, Z. M., Li, I. L., Jiang, F. Y., Sheng, P., et al. (2006). Carbonization mechanism of tetrapropylammonium-hydroxide in channels of $AlPO_4$-5 single crystals. *Chem. Mater.* 18, 1505–1511. doi:10.1021/cm0526821

Zhang, N., Chen, X., Yu, M., Niu, Z., Cheng, F., and Chen, J. (2020). Materials chemistry for rechargeable zinc-ion batteries. *Chem. Soc. Rev.* 49, 4203–4219. doi:10.1039/c9cs00349e

Zhang, N., Cheng, F., Liu, J., Wang, L., Long, X., Liu, X., et al. (2017). Rechargeable aqueous zinc-manganese dioxide batteries with high energy and power densities. *Nat. Commun.* 8, 405. doi:10.1038/s41467-017-00467-x

Zhang, W., and Yanagisawa, K. (2007). Hydrothermal synthesis of zinc hydroxide chloride sheets and their conversion to ZnO. *Chem. Mater.* 19, 2329–2334. doi:10.1021/cm0626841

Zhou, Z., Zhang, Y., Chen, P., Wu, Y., Yang, H., Ding, H., et al. (2019). Graphene oxide-modified zinc anode for rechargeable aqueous batteries. *Chem. Eng. Sci.* 194, 142–147. doi:10.1016/j.ces.2018.06.048

Zhu, H. W., Ge, J., Peng, Y. C., Zhao, H. Y., Shi, L. A., and Yu, S. H. (2018). Dip-coating processed sponge-based electrodes for stretchable Zn-MnO_2 batteries. *Nano Res.* 11, 1554–1562. doi:10.1007/s12274-017-1771-4

Conflict of Interest: Authors IK, KK, AM and ZB were employed by company Institute of Batteries LLP.

The remaining authors declare that the research was conducted in the absence of any commercial or financial relationships that could be construed as a potential conflict of interest.

frontiers in Energy Research

REVIEW
published: 21 December 2020
doi: 10.3389/fenrg.2020.605129

Sodium-Based Batteries: In Search of the Best Compromise Between Sustainability and Maximization of Electric Performance

Duygu Karabelli[1], Soumya Singh[1], Steffen Kiemel[1], Jan Koller[2], Aishuak Konarov[3], Frank Stubhan[4], Robert Miehe[1], Max Weeber[1], Zhumabay Bakenov[3] and Kai Peter Birke[1,5]*

[1] Fraunhofer Institute for Manufacturing Engineering and Automation IPA, Stuttgart, Germany, [2] Fraunhofer Institute for Manufacturing Engineering and Automation IPA, Bayreuth, Germany, [3] Department Chemical and Materials Engineering, School of Engineering and Digital Sciences, Nazarbayev University, Nur-Sultan, Kazakhstan; National Laboratory Astana, Nazarbayev University, Nur-Sultan, Kazakhstan, [4] ACI-Systems GmbH, Zimmern ob Rottweil, Germany, [5] Chair for Electrical Energy Storage Systems, Institute for Photovoltaics, University of Stuttgart, Stuttgart, Germany

Till 2020 the predominant key success factors of battery development have been overwhelmingly energy density, power density, lifetime, safety, and costs per kWh. That is why there is a high expectation on energy storage systems such as lithium-air (Li-O_2) and lithium-sulfur (Li-S) systems, especially for mobile applications. These systems have high theoretical specific energy densities compared to conventional Li-ion systems. If the challenges such as practical implementation, low energy efficiency, and cycle life are handled, these systems could provide an interesting energy source for EVs. However, various raw materials are increasingly under critical discussion. Though only 3 wt% of metallic lithium is present in a modern Li-ion cell, absolute high amounts of lithium demand will rise due to the fast-growing market for traction and stationary batteries. Moreover, many lithium sources are not available without compromising environmental aspects. Therefore, there is a growing focus on alternative technologies such as Na-ion and Zn-ion batteries. On a view of Na-ion batteries, especially the combination with carbons derived from food waste as negative electrodes may generate a promising overall cost structure, though energy densities are not as favorable as for Li-ion batteries. Within the scope of this work, the future potential of sodium-based batteries will be discussed in view of sustainability and abundance vs. maximization of electric performance. The major directions of cathode materials development are reviewed and the tendency towards designing high-performance systems is discussed. This paper provides an outlook on the potential of sodium-based batteries in the future battery market of mobile and stationary applications.

Keywords: sodium battery chemistries, X electric vehicle, stationary batteries, Na-ion batteries, post-Li-ion technologies, raw materials, battery cost

OPEN ACCESS

Edited by:
Yan-Bing He,
Tsinghua University, China

Reviewed by:
Yong Liu,
Henan University of Science and Technology, China
Danni Lei,
Sun Yat-sen University, China

****Correspondence:***
Duygu Karabelli
duygu.kaus@fraunhofer.ipa.de

Specialty section:
This article was submitted to Electrochemical Energy Conversion and Storage, a section of the journal Frontiers in Energy Research

Received: *11 September 2020*
Accepted: *16 November 2020*
Published: *21 December 2020*

Citation:
Karabelli D, Singh S, Kiemel S, Koller J, Konarov A, Stubhan F, Miehe R, Weeber M, Bakenov Z and Birke KP (2020) Sodium-Based Batteries: In Search of the Best Compromise Between Sustainability and Maximization of Electric Performance. Front. Energy Res. 8:605129. doi: 10.3389/fenrg.2020.605129

INTRODUCTION

Among secondary batteries, lithium-ion batteries (LIBs) play an important role in many areas of energy storage systems. Since their first commercialization by Sony in 1991, further research efforts have been devoted to the LIBs technology. However, the highest achievable energy density for LIBs in the near future (around 250–260 Wh kg^{-1}) is insufficient (Ding et al., 2019), thus limiting the range

of practical electric vehicles (EVs). As a fact, there is a high demand and interest for other energy storage technologies with higher energy densities. Lithium-air (Li-O_2) and lithium-sulfur (Li-S) systems have higher theoretical specific energy densities (3,600 and 2,600 Wh $kg^{-1,}$ respectively) compared with those for LIBs (Liu et al., 2018). Nevertheless, the cycle lifetime and safety concerns have to be overcome in order to have a mature technology. Moreover, one of the major concerns is that the markets will be facing depletion of lithium sources and, as a result, high production cost if recycling technology is not implemented on a large scale (Al-Thyabat et al., 2013; Ahmadi et al., 2017; Dolega, 2019; Ambrose and Kendall, 2020a; Ambrose and Kendall, 2020b).

Taking into account that it is already difficult to scale current LIBs for a different type of applications (e.g., grid-scale storage) mainly due to production and maintenance costs (Etacheri et al., 2011; Habib and Sou, 2018; Chen et al., 2020; Cole and Frazier, 2019), the cutting-edge innovations in battery energy storage systems (BESS) is indispensable in order to achieve high-performance, cost-efficient and environmentally friendly batteries. Novel beyond lithium-ion chemistries (e.g., sodium, potassium, magnesium and zinc) have been developed in order to address the present limitations of conventional LIBs (Ellis and Nazar, 2012; Yabuuchi et al., 2014; Barker, 2017; Hwang et al., 2017; Delmas, 2018; You and Manthiram, 2018; Li et al., 2019; MacLaughlin, 2019; Ming et al., 2019). Among many anode candidates, Sodium (Na) based anodes have attracted tremendous attention, thanks to mainly high Na abundance (the fourth abundant metallic element), low supply cost (Na_2CO_3, \$150 ton^{-1}; Li_2CO_3, \$5,000 ton^{-1}), as well as its safety (Zhao et al., 2017). However, LIBs technology is a mature technology, and there are currently no equivalent alternatives to LIBs. Since lithium is very light and has a high theoretical specific capacity (3,860 mAh g^{-1}) (Liu et al., 2018), it is very challenging to compensate for it, for high capacity and low-cost battery production. Indeed, the studies show that the overall cost of Na-ion Batteries (SIBs) is still higher than that of LIBs (in terms of \$ kWh^{-1}), even though Na itself is a cheaper anode material.

The crucial question is: What is the cost-effectiveness of Li recycling in the future? The prospect of producing large modules will increase the cost of LIBs with uncertainties in the supply of lithium. At present, one-third of the lithium produced worldwide is already being used by the LIBs industry. Last but not least, the availability of other LIBs main raw materials, particularly cobalt, are facing market instabilities due to political and environmental requirements. If it is possible to close the loop for LIBs and to establish a circular economy, in this case, the manufacturers will not be looking for alternatives. In case of sodium, there will be no pressure for "low-cost recycling" since Na can easily be obtained by evaporation of seawater (11,000 mg L^{-1} in seawater) where the lithium content in seawater is much lower than that of Na (0.18 mg L^{-1}) (Adelhelm et al., 2015). From this perspective, sodium-based batteries are well suited to mass production and the manufacture of large modules.

High-temperature Sodium/sulfur has already been commercialized for decades with liquid sodium at 300°C (Oshima et al., 2004). Its specific capacity is indeed lower than the one of actual LIBs since this battery system needs a solid housing and thermal insulation. Moreover, the presence of liquid Na obstructs its application in EVs. That type of batteries can be considered most likely for low-cost stationary energy storage systems.

The concept of rechargeable sodium-air (Na-O_2) systems has also been reported (Zhao et al., 2014; Landa-Medrano et al., 2016). The Na-O_2 cell indeed shows some promising advantages over the Li/O_2 because the discharge reaction product NaO_2 presents higher energy efficiency and reversibility (Zhao et al., 2014). Nevertheless, it is still in the initial stage of development and faces significant challenges such as higher cycle numbers, minimization of side reaction products. As it is like in Na-S, this type of battery is also very unlikely to be used in EVs.

Apart from Na-S and Na-O_2 technologies, SIBs can be considered as more realistic alternative energy storage technology to today's LIBs (Ellis and Nazar, 2012; Ponrouch et al., 2015; Hwang et al., 2017; Bin et al., 2018). The most common cathodes for SIBs are sodium oxides ($NaMO_2$, M = V, Fe, Mn, Cu, Co., and Ni), sodium phosphates ($Na_7V_3(P_2O_7)_4$, $NaFePO_4$, transition metal oxides (V_2O_5) and Prussian blue (PB, $Na_2M[Fe(CN)_6]$) (Ellis and Nazar, 2012; Delmas, 2018). A British company Faradion has recently announced that its high energy Na-MO_2 cells will be used in commercial EVs in India and declared that they estimate 30% of cost reduction at the cell level (Barker, 2017). Previously, the company had conducted several prototype demonstrations, including e-bikes and golf trolleys, but the project in Australia poses a more significant engineering challenge for today's SIBs technology. Apart from Faradion, a start-up company Tiamat (France) and HiNa Battery Technology (China), and other key innovators, have built SIB prototypes for low-speed EVs, start&stop 12 V batteries, e-bikes, and e-scooters.

Two different types of electrolytes can be introduced for SIBs: i) aqueous and ii) organic (Ellis and Nazar, 2012; Delmas, 2018). The aqueous medium can be favorable due to:

- Low risk of explosion or flammability of the battery during heating;
- No strict control of humidity during assembly, which reduces the cost of the battery;
- High ionic conductivity

However, a narrow potential window remains a major obstacle, and very few materials can operate in an aqueous environment (Vignarooban et al., 2016; Bin et al., 2018).

At present, most sodium-ion batteries contain an organic electrolyte. These electrolytes generally consist of a sodium salt dissolved in one or more organic solvents. The most commonly used organic solvents are carbonates such as pro; pylene carbonate (PC), ethylene carbonate (EC), dimethyl carbonate (DMC), fluoro-ethylene carbonate (FEC) or vinylene carbonate (VC) (Ponrouch et al., 2015; Vignarooban et al., 2016; Zhao et al., 2017).

This paper discusses beyond Li-ion chemistry with a focus on organic electrolyte-based SIBs. This technology is being analyzed

in terms of performance and cost and is then compared to today's LIBs technology in order to make a prediction in which use case scenarios, the SIBs potentially will outperform existing LIBs.

The methodology is based on literature research, followed by analysis of material/cost and effect of Na batteries on circular economy. This study is presented by authors with an interdisciplinary background (Material science, electrochemistry, raw material refinement, and recycling).

SODIUM-ION BATTERIES WITH ORGANIC ELECTROLYTE

State-of-the-Art

Development of renewable and environmentally responsible organic electrolyte based SIBs has gained remarkably increased attention in the past 6 years (Adelhelm et al., 2015; Barker, 2017; Bauer et al., 2018). To arrive at implications regarding the performance and cost of SIBs and to address the critical questions from the introduction, the first step of this study reviews the existing literature about organic electrolyte-based SIBs. These type of electrolytes are prepared by dissolving one of ionic sodium salts ($NaClO_4$, $NaPF_6$ and NaTFSI) in a non-aqueous solvents such as EC, PC, DMC, DEC, DME, like in Li-ion batteries (Vignarooban et al., 2016). It has been reported that an ionic conductivity of an electrolyte prepared with 1 M $NaClO_4$ in EC:DME (50:50 wt%) reached to 12.5 ms cm^{-1} which is almost the same value as the electrolyte prepared with 1 M $LiPF_6$ in EC: DMC (50:50 wt%) (Vignarooban et al., 2016).

The large atomic radius of Na (0.97 Å for Na^+ and 0.68 Å for Li^+), causes sluggish sodium diffusion kinetics and large volume expansion, which are both critical parameters for revolutionary power density performance that can meet the real needs of power grids and large-scale EESs (Chen et al., 2019). Therefore, it is important to explore novel cathode materials for SIBs with improved Na kinetics (Chen et al., 2020). The energy density of the Na-ion batteries is directly related to the cathode material's performance. Similar to LIBs, sodium cathodes are divided into three main groups: layered, olivine (NASICON), and spinel. Among them, layered oxides (Guo et al., 2014; Liu et al., 2015; Ortiz-Vitoriano et al., 2017; Konarov et al., 2018; Deng et al., 2018; Li et al., 2019) and NASICON structure phosphates showed promising performance (Chen et al., 2019). More recently, Prussian blue analogs [PBAs, Na2M[Fe(CN)6], M = Fe, Co, Mn, Ni, Cu, etc.] have been extensively studied due to their large gaps in lattice space structure, which can provide abundant sites and transport channels for reversible de-intercalation of sodium-ion (Luo et al., 2017; Wang et al., 2018; You et al., 2014).

Layered oxide compounds that are of interest as cathode materials for SIBs have a common formula Na_xMO_2, where M denotes one or several transition metals (Ti, V, Cr, Mn, Fe, Co, or Ni). 2D layered structure sodium transition metal oxides are widely studied due to their enhanced electrochemical performance compared with other compounds. These materials are classified as an O3 and P2 type structure which letter O and P represents the location of sodium ion in the crystal structure (P-prismatic site, O-octahedral site) (**Figure 1**). The numbers represent the transition metal layer in the repeating unit cell in the structure (Delmas, 2018). O3 and P2-types are the most-common structural polymorphs of layered oxides.The P2-type structure has better ionic conductivity and delivers higher discharge capacity than the O3-type structure (Qi et al., 2017). Moreover, P2-type material is less hygroscopic than O3-type.

Among P2-type materials, manganese-based ($Na_{2/3}MnO_2$) cathode has been attracted much attention due to the low price of manganese, and it delivers high discharge capacity (>150 mAh g^{-1}) compared to other studied cathodes (Zhu et al., 2018). However, the use of manganese causes structural distortions as the Mn^{3+} ions are dominant in the structure. This is associated with Jahn-Teller distortion, which consists of Mn^{3+} elongation or compression in the *z*-axis. The anisotropic changes in the lattice parameters during cycling lead to rapid capacity fading (Liu et al., 2015). One of the ways to overcome this problem is to dilute the concentration of Mn^{3+} ions in the crystal structure and decrease the anisotropic change by substituting it with other electrochemically active or non-active metal cations (Guo et al., 2017; El Moctar et al., 2018; Kim et al., 2018; Irisarri et al., 2018).

In this matter, Clément et al. (2016) studied the effect of Mg doping on the P2-type $Na_{2/3}MnO_2$ compound by varying the amount of dopant: $Na_{2/3}Mn_{1-y}Mg_yO_2$ (y = 0.0, 0.05, 0.1). Partial substitution of Mn^{3+} by Mg led to a smoother potential profile and enhanced the electrochemical performance of the composite. Successful doping by Mg suppressed the Jahn-Teller distortion, which reduced the number of Mn^{3+} by Mg in P2-$Na_{2/3}MnO_2$. Among the compositions, the 5% Mg-doped compound delivered the highest capacity and better electrochemical properties compared to the one with 10% Mg doping.

Kang et al. (2015) studied copper-substituted P2-type $Na_{0.67}Cu_xMn_{1-x}O_2$ (x = 0, 0.14, 0.25, 0.33) compound to improve the electrochemical performance of P2-type $Na_{0.7}MnO_2$. When the amount of Cu increased in the composite, the discharge capacity decreased. However, the reaction potential increased due to the redox reaction of Cu^{2+}/Cu^{3+}. In the case of x = 0.25, both Mn and Cu were responsible for delivering the capacity. By substitution of part of Mn^{3+} by Cu led to significant improvement in the rate performance and stability of the material.

Lu and Dahn (2001) reported nickel substituted P2-type $Na_{2/3}[Mn_{2/3}Ni_{1/3}]O_2$ composite, where all the Mn^{3+} was replaced with Ni^{2+} due to the similarity of ionic sizes. Composite showed a high operating potential with Ni^{2+}/Ni^{4+} redox pair and delivered a relatively high discharge capacity. Besides, the compound illustrated high operating potential (~3.5 V) and stability in aqueous solution. Even after 1 year in water, the structure did not change much. The excellent properties of the P2-type $Na_{2/3}[Mn_{2/3}Ni_{1/3}]O_2$ compound make it attractive for further commercialization. However, the compound suffered from rapid capacity fading; this fading does not relate to the Jahn-Teller distortion due to the absence of Mn^{3+}. The phase change during cycling from the P2 to O2 was responsible for the capacity fade because of the large volume change (~23%) during phase transition. There have been many approaches to suppress this issue by partially substituting the Ni with other metals [Mg Zheng

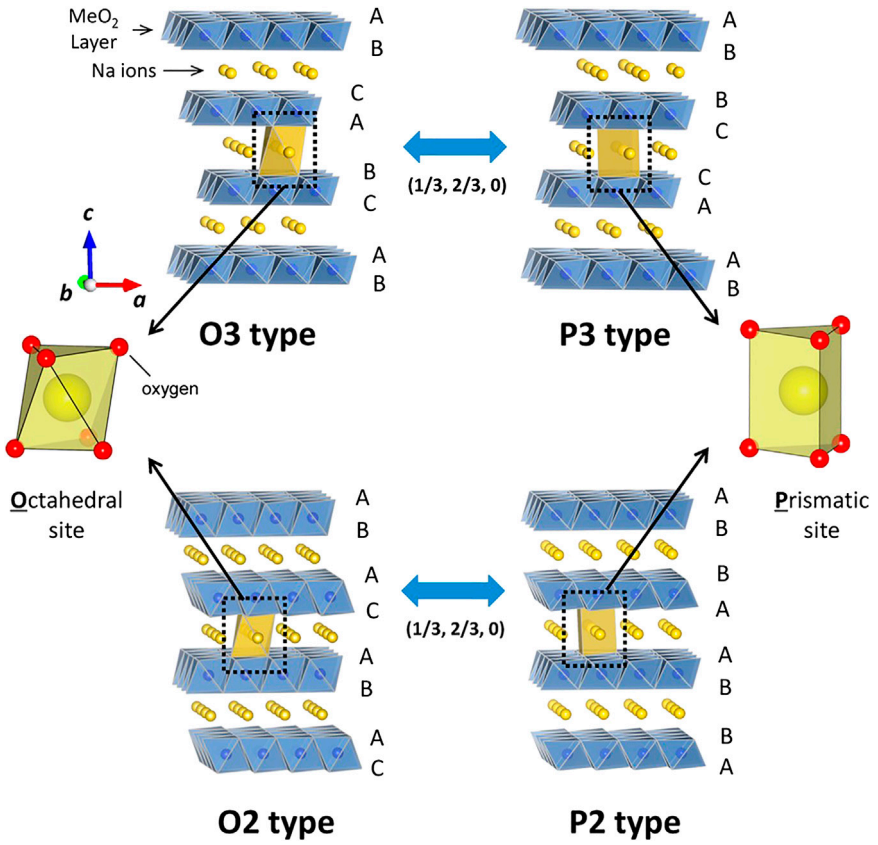

FIGURE 1 | Classification of Na–Me–O layered materials with sheets of edge-sharing MeO6 octahedra and phase transition processes induced by sodium extraction. Reprinted with permission from [ref. Yabuuchi et al. (2014)]. Copyright (2014) American Chemical Society.

et al. (2017), Cu Zheng et al. (2017), Zn Xu et al. (2014), Al Hasa et al. (2017), and Li Xu et al. (2014)].

Konarov et al. studied Konarov et al. (2018) the variation of Ni content in P2-type $Na_{2/3}Mn_{1-x}Ni_xO_2$ (x = 0, 0.1, 0.2) in order to find the optimal performance, which is to suppress the Jahn–Teller distortion and phase change from P2 to O2. Among studied compounds, $Na_{2/3}[Mn_{0.8}Ni_{0.2}]O_2$ exhibited the optimal electrochemical properties. The compound delivered high capacity at high current densities (10C = 90 mAh g^{-1}) compared with the previously reported. Although a P2–O2 bi-phasic reaction occurred during the cycling, the volume change was only approximately 10%, which is smaller than that for P2-type $Na_{2/3}[Mn_{2/3}Ni_{1/3}]O_2$.

Ortiz-Vitoriano et al. (2017) provided a proof-of-concept for full cells utilizing layered sodium manganese oxides (Liu et al., 2015). The material $Na_{0.78}Li_{0.18}Ni_{0.25}Mn_{0.583}O_w$ demonstrated moderate to good electrochemical performances, a high discharge capacity of 240 mAh g^{-1} in the voltage range of 1.5–4.5 V, thus the total energy density of the material level reaches 675 Wh kg^{-1}. When cycled between 1.5 and 4.2 V, the discharge capacity was maintained at around 190 mAh g^{-1} after 30 cycles.

Yabuuchi et al. (2014) increased the concentration of electrochemically inactive Mg in P2-$Na_{2/3}MnO_2$ to 28%, substituting almost all the Mn^{3+} ions and obtaining $Na_{2/3}[Mn_{0.72}Mg_{0.28}]O_2$ compound where the manganese oxidation state was close to 4+. Interestingly, electrochemically inactive material delivered about 150 mAh g^{-1} of capacity in the initial charge and over 200 mAh g^{-1} of capacity in the following cycles. An anomalously large reversible capacity is expected to originate from the oxygen redox and activation of Mn^{3+} in the following cycles, like in Li-rich cathodes. Lately, Bruce's group studied the same material ($Na_{2/3}[Mn_{0.72}Mg_{0.28}]O_2$) and confirmed the reversible oxygen redox over cycles via state-of-art tools (Maitra et al., 2018). Unlike in Li-rich material, the activation of oxygen redox does not require alkali ions to be in the transition metal layer. Because of that, the oxygen loss was suppressed by Mg^{2+}, which bond with oxygen, as in the case of Li-rich materials, when the Li-ion is removed from the transition metal layer, and it causes the non-bonded oxygen, which leads to oxygen evolution (Maitra et al., 2018).

Recently, Konarov et al. (2019) studied the effect of Mn substitution via Zn in P2-$Na_{2/3}Mn_{1-x}Zn_xO_2$ (x = 0, 0.1, 0.2, 0.3). As the Zn content is increased, the capacity generated from the oxygen redox is increased. Among the different compositions, the P2-$Na_{2/3}Mn_{0.7}Zn_{0.3}O_2$ compound illustrated excellent electrochemical performance. The existence of Zn ion in the transition metal layer stabilized the crystal structure and

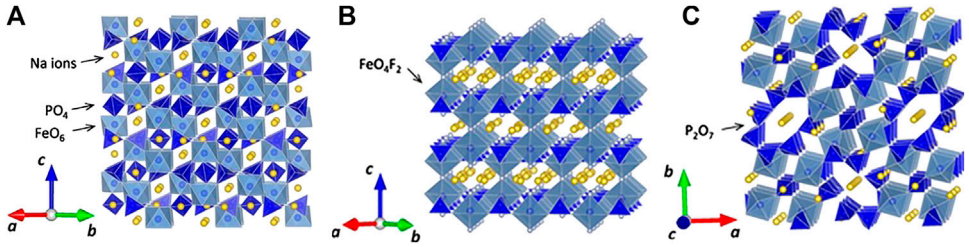

FIGURE 2 | Crystal structures for vanadium-based polyanionic compounds: **(A)** Na3V2(PO4)3 (NASICON-type), **(B)** Na3V2(PO4)2F3, and **(C)** Na7V4(P2O7)4PO4. Reprinted with permission from [ref. Yabuuchi et al. (2014)]. Copyright (2014) American Chemical Society.

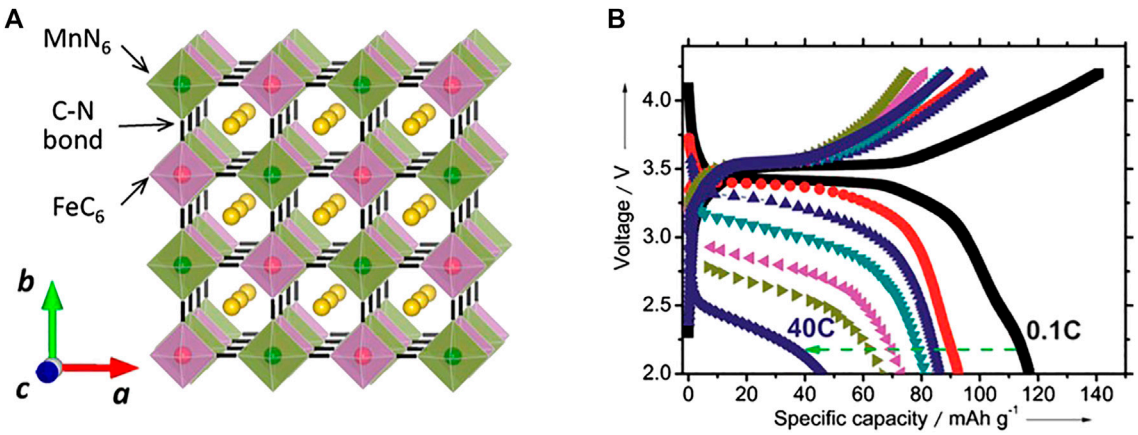

FIGURE 3 | (A) Crystal structure of NaxMnFe(CN)6, and **(B)** Electrode performance of NaxMnFe(CN)6 in Na cells. Reprinted with permission from ref. Yabuuchi et al. (2014)]. Copyright (2014) American Chemical Society.

triggered the oxygen redox. As a result, a discharge capacity of 190 mAh g^{-1} was delivered, and 80% of it remained after 200 cycles. However, the operating potential of such a system is comparatively low. To address this issue, the Ni was introduced to the crystal structure by substituting half of the Zn in structure (P2-$Na_{2/3}Mn_{0.7}Zn_{0.15}Ni_{0.15}O_2$). The addition of the Ni resulted in an increase in the operating potential to 3.5 V (Konarov et al., 2020).

Among NASICON type of cathodes which shown in **Figure 2**, $Na_3V_2(PO_4)_3$ and its derivatives exhibited excellent electrochemical performance (Guo et al., 2017). Even though the delivered capacity is smaller than the layered oxides, the operating potential makes it most promising. However, the price and toxicity of the vanadium limit its further steps to the market. Prussian blue (PB) and its analogs (PBAs) are a large family of transition-metal hexacyanoferrates with open framework structure, abundant redox-active sites, and strong structural stability. Particularly, due to their large ionic channels and interstices in the lattice, PBs are one of the few host materials that can accommodate larger alkali cations, such as Na^+ and K^+ ions, for facile and reversible insertion reactions (**Figure 3**). Benefiting from this structural feature, PB compounds have been intensively investigated as a new alternative and low-cost Na-insertion cathode during the past 5 years, although there is still room for improvement (Zhang, 2019). The intrinsic performance of PBAs electrodes is strongly affected by the presence of crystal imperfections, such as vacancies and water molecules. An increase in vacancies raises the coordinated water content, which reduces redox-active sites. Hence, these challenges, such as low discharge capacity, poor cyclic stability, and low Coulombic efficiency, need to be addressed before the commercialization of PBAs electrodes (Wang et al., 2018).

Various studies (You et al., 2014; Hwang et al., 2019; Chen et al., 2020) have performed a consolidated study of the electrochemical performance of different cathode materials. Considerable comparision can be made between the charge-discharge profiles for these materials, in order to draw conclusions about the cathode behavior.

The types of cathodes studied in this section are categorized and summarized according to their performance parameters in **Table 1**.

Considering negative electrodes, various type of materials such as carbon-based materials, titanates, alloys, and metal oxides/sulfides can be used in SIB (Yu et al., 2020). Among them carbon based materials offer the best cost and performance correlation. Ji *et* al. (Hou et al., 2017), categorized carbonaceous materials as an anode under four groups: i) graphite, ii) hard carbon, iii) heteroatom doped carbon and iv) biomass derived carbon

TABLE 1 | Performance characteristics of cathode materials for organic sodium-ion batteries.

Cathode type	Structure	Category	Cathode material	Potential (V)	Discharge capacity (mAh g^{-1})	Energy density (kWh g^{-1})	References
Transition metal oxides	Cubic close-packed arrangement with 1D-, 2D- or 3D-type tunnels	P2-layered	$Na_{2/3}Mn_{1-y}Mg_yO_2$	1.5–4.0	140	—	Clément et al. (2016)
		P2-layered	$Na_{2/3}[Mn_{2/3}Ni_{1/3}]O_2$	2.9–4.0	161	—	Lu and Dahn (2001)
		O2-layered	$Na_{2/3}[Mn_{0.8}Ni_{0.2}]O_2$	2.0–4.3	162	—	Konarov et al. (2018)
		O3-layered	$Na_{0.78}Li_{0.18}Ni_{0.25}Mn_{0.583}O_w$	1.5–4.5	240	675	Liu et al. (2015)
		P2-layered	$Na_{2/3}[Mn_{0.72}Mg_{0.28}]O_2$	1.5–4.4	~180	—	Yabuuchi et al. (2014)
		P2-layered	$Na_{2/3}Mn_{0.7}Zn_{0.3}O_2$	1.5–4.6	190	—	Konarov et al. (2019)
		P2-layered	$Na_{2/3}M_{n0.8}Fe_{0.1}Ti_{0.1}O_2$	2.0–4.0	144.16	399.32	Han et al. (2016)
Transition metal fluorides	Weberite-type	Sodium metal fluorides	Na_2FeTiF_7	3.26	190	GED 620	Euchner et al. (2019)
Polyanionic compounds	Olivine structure with rhombohedral R-3 symmetry	Phosphates and NASICON type	$NaFePO_4$	3	150	450	Hasa et al. (2017)
			$Na_3V_2(PO_4)_3$	3.3	117	394	Guo et al. (2017)
			$Na_3V_2(PO_4)_2O_2F$	3.8	128	486	Guo et al. (2017)
		Fluorophosphates	NASICON-type $Na_3V_2(PO_4)_2F_3$	1.6–4.6	111	—	Song et al. (2014)
		Sulfates	$Na_2Fe_2(SO_4)_3$@C@GO	3.8	107.9	400	Chen et al. (2018)
Prussian blue analogs	Face-centered cubic geometry and open-framework lattice	Binder free cathode - Fe-HCF NSs@GRs	Sodium iron hexacyanoferrate (Fe-HCF)	2.0–4.2	110	—	Luo et al. (2017)
		High-quality PB nanocrystals	$Na_{0.61}Fe[Fe(CN)_6]_{0.94}$	4.0–2.7	170	—	You et al. (2014)
		Ferrocyanide	$Na_{1.92}Mn[Fe(CN)_6]_{0.98}$	3.34	105.7	—	Peng et al. (2019)
		Poly (hexaazatrinaphthalene)	PHATN	1.0–3.5	Reversible capacity of 220	440	Mao et al. (2019)
		$C_6R_4O_2$ molecules (R = F, Cl, Br)	Quinone-derivative, $C_6Cl_4O_2$	~2.72 V vs. Na/Na+	161	420	Kim et al. (2015)

materials. A conventional graphite anode performs poorly in SIBs. Due to the thermodynamical instability of the sodiated graphite, the formation of these compounds is predicted to be stable only at lower potentials. Since graphite delivers small capacity, hard carbon (HC) is considered as promising material due to a high potential and wider interlayer spacing, which led to a high reversible capacity and excellent cyclability (Nayak et al., 2018). However, there are still several challenges related to the hard carbon (El Moctar et al., 2018). One of them is the rate performance; it shows poor rate capability due to the long diffusion distance. Another one is the low potential plateau, which is close to the sodium plating that threatens battery safety especially at a high rate. Nevertheless some recent (Yu et al., 2020; Ma et al., 2019) studies showed that, it is possible to enhance electrochemical properties of these type of materials by surface modification techniques. Wang et al. showed that sulfur, nitrogen co-doped carbon nanofiber (SNCNF) results with the specific capacity of 247.4 mA h g^{-1} (with 98.2% retention at 0.5 A g^{-1}) over 600 cycles (Yu et al., 2020). Although heteroatom doping of the carbonaceous materials are able to improve sodium intercalation, some other challenges remain open. Li *et* al. reported that heteroatom doping usually brings a lower internal Coulombic efficiency compared to the original hard carbon which effects the ratio of total cost to discharge energy per cycle life (Chen et al., 2019). As the economic competitiveness is really important for SIBs, novel designs of SIB anodes need to address both performance and cost requirements.

Cost Analysis

The costs of a BESS play a major role, especially for electric cars, where the cost of a battery pack close to 40–50 percent of the cost of the vehicle (Curry, 2017). Production costs depend on many factors. e.g., material costs, production equipment, and if it is required, additional technologies (sensors, cooling system, and safety measurements).

Costs of Na based batteries are believed to be lower than for Li batteries in the near future. This is not only because the Na the fourth most abundant element on earth but also as Na salts are more stable, and their preparation is easier than that of Li salts (Zhao et al., 2017). Na-ion batteries utilize the same manufacturing process that LIBs, and to date, there are commercially available sodium-ion batteries. Due to using highly abundant sodium, cobalt-free active materials, inexpensive electrolytes, and on-hand available anode materials, make SIBs very attractive for battery manufacturers in terms of cost savings. Additional cost reduction can be obtained by using an aluminum current collector instead of high-cost copper because an alloying reaction between Na and Al does not exist (Nayak et al., 2018).

For realistic cost predictions, calculations must be done for a certain battery cell with defined kWh. As sodium has a higher molecular weight (M_w) and a larger size than that of lithium (Yabuuchi et al., 2014), the theoretical energy density may decrease, and the cost at the cell level can increase. Another "cost-influencer" in SIBs is the choice of anode. As it was mentioned in the previous section, a conventional LIB anode material graphite is not suitable for SIB due to intercalation problems and a lack of stable Na-C compounds. As a result hard carbon can be considered as a performance effective alternative anode material for SIBs (El Moctar et al., 2018). Hard carbon is relatively more expensive than a conventional graphite anode and the challenge associated with the high price can be solved by preparing the hard carbon from environmentally friendly and renewable bio-waste materials. Numerous studies have been performed by researchers around the world to solve the issues as mentioned above of hard carbon, in order to make it more practical (Kim et al., 2018; Irisarri et al., 2018).

Up to date, commercial HC prices kg^{-1} are not available. But it has been reported that higher price comes from the high-cost precursors (Kim et al., 2018). There are many studies that focus on low-cost/high yield synthesis of HC via cheaper precursors (e.g., cellulose, corn stalks, phenolic resin) in order to optimize the cost and performance of SIBs (Irisarri et al., 2018). Buchholz et al. used \$15 kg^{-1} as a price of HC; however, it can be lowered up to \$8 $kg^{-1,}$ considering the efforts are being done to enhance the properties of the hard carbon (Vaalma et al., 2018).

Argonne National Lab's BatPaC model is another commonly applied battery cost model, with specifications for many common cathode chemistries, including SIBs technology. Recently, Buchholz et al. presented a detailed cost analysis for SIBs by using this model (Vaalma et al., 2018). Apart from material costs, they have taken into account many other factors such as battery pack design (including overhead), hardware, target power and energy in order to calculate the cost at system level.

As we mentioned previously, the use of cobalt-free cathode material reduces the cost already very significantly. Current LIBs technology tends to use either cobalt-free cathodes ($LiMn_2O_4$, $LiFePO_4$) and/or Ni-rich cathodes (NMC 532, NMC 622, NMC 811). That's why future trends for SIBs technology must be considered with a similar type of cathode. If we make a direct comparison between LIBs and SIBs with their -MnO_2 cathodes, it is seen that at the cell level LIBs offer 13% cheaper cost, even positive active material and negative current collector (copper) for LIBs is more expensive than that of SIBs. At system level (11.5 kWh battery), this price gap decreases up to 11%.

Detailed material costs for layered oxide cathode based LIBs and SIBs and a calculated total system cost (\$ kWh^{-1}) taken from BatPaC model are given in **Figure 4** and **Table 2**.

Another beneficial study was conducted by Peters et al. (2017). By using the same BatPaC model, they have compared layered oxide ($Na_{1.1}Ni_{0.3}Mn_{0.5}Mg_{0.05}Ti_{0.05}O_2$) SIBs cells with two different LIBs cell chemistries: lithium-nickel-manganese-cobalt-oxide cathodes ($Li_{1.05}Ni_{0.33}Mn_{0.33}Co_{0.33}O_2$; NMC111) and lithium-iron-phosphate cathodes ($LiFePO_4$; LFP). According to their calculations, cost/kW^{-1} h is \$263 for SIBs, \$270 for LFP, and \$198 for NMC111. It is very obvious that SIBs cannot compete with NMC based LIBs. Additionally, one should strongly consider that future designs tend to increase Ni content in the cathode (NMC622, NMC811). As cobalt is a costly raw material, decreasing Co will automatically reduce the cost of the battery while increasing the energy density thanks to high Ni content. Table 3 summarizes the literature values in terms of battery chemistries and their cost.

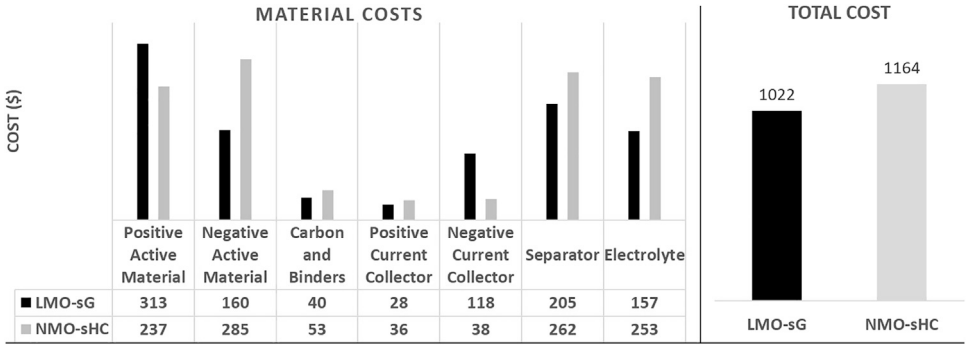

FIGURE 4 | Material costs of layered oxide cathode based lithium-ion batteries and SIBs. Data are redrawn from Vaalma et al. (2018).

TABLE 2 | Total system cost ($ kWh^{-1}) of layered oxide cathode based LIBs and SIBs for 11 kWh systems (Vaalma et al., 2018).

	Unit	LMO-sG	NMO-sHC
Materials			
Cathode material price	$	10.0	7.6
Cathode material spec. capacity	mAh g^{-1}	100.0	160.0
Cathode material density	g cm^{-3}	4.2	4.2
Positive current collector	Metal	Aluminum	Aluminum
Anode material price	$	15.0	15.0
Anode material spec. capacity	mAh g^{-1}	360.0	300.0
Anode material density	g cm^{-3}	2.2	1.5
Negative current collector	Metal	Copper	Aluminum
OCV at 50% SOC	V	4.0	2.5
Battery system values			
Target power	kW	7.0	7.0
Approximately, target power for 30-s pulse	kW	5.6	5.6
Energy	kWh	11.5	11.5
Modules per battery	—	2.0	2.0
Total number of cells per battery	—	72.0	72.0
Mass	Kg	89.5	111.6
Volume	L	51.3	73.9
Specific energy density	Wh kg^{-1}	128.5	103.1
Volumetric energy density	Wh L^{-1}	224.1	155.7
Price per energy	$ kWh^{-1}	259,2	286,9

The best cost/performance relation is given for advanced SIBs, which is designed based on future development predictions. Yet the price per kWh is still much higher than LIBs.

Apart from research studies, the market analysis also agrees that SIBs do not provide cost advantage compared to LIBs (Frost and Sullivan, 2019a; Frost and Sullivan, 2019b). It has been reported that SIBs may offer better cost if only Li price increases sharply. As it will be discussed in *Summary and Outlook*, an increase in Li prices depends on reserve depletion, and this will not occur in the near time frame, not probably before 2028.

EFFECT OF NA-BATTERIES ON CIRCULAR ECONOMY

Availability of Raw Materials

Battery Grade Li vs. Battery Grade Na

In recent years, many lithium mining projects have been expanded or set up newly, driven by the huge demand of LIBs as it is forecasted for the coming years, mainly based on the expected growth of electromobility (Graedel et al., 2015; Nassar et al., 2015; Roskill, 2019). This led to an increase in the lithium mining capacity by a factor of more than two in the years from 2015 (ca. 269,000 t lithium carbonate, Li_2CO_3, equivalent (LCE) to 2018 (ca. 649,000 t LCE. While the utilization rate in 2018 only reached about 60%, the lithium mining capacities are expected to increase further, again by a factor of more than two until 2024, reaching ca. 1,500,000 t LCE per year (**Table 4**).

Even if the total lithium demand for first use is forecasted to more than triple in the period from 2018 to 2023, reaching 699,000 t LCE per year, the lithium mining capacity can easily

TABLE 3 | Comparison of different type of SIBs and LIBs in terms of their energy densities and costs (Peters et al., 2017; Vaalma et al., 2018).

Battery	Cathode	Anode	Electrolyte	Energy density (Wh kg^{-1})	Cost ($ kWh^{-1})
SIB1-1	$Na_{1.1}Ni_{0.3}Mn_{0.5}Mg_{0.05}Ti_{0.05}O_2$	HC on Al foil	$NaPF_6$ in ethylene carbonate/dimethyl carbonate	138.8	263
SIB-2	β-$NaMnO_2$	HC on Al foil	$NaPF_6$ in ethylene carbonate/ethyl methyl carbonate	103.1	259.2
SIB-3	Advanced Na-ion cathode[a]	Phosphorus HC composite on Al foil	$NaPF_6$ in ethylene carbonate/ethyl methyl carbonate	152	248.5
LIB-1	$Li_{1.05}Ni_{0.33}Mn_{0.33}Co_{0.33}O_2$	Graphite on Cu foil	$LiPF_6$ in ethylene carbonate/dimethyl carbonate	208	198
LIB-2	$LiFePO_4$	Graphite on Cu foil	$LiPF_6$ in ethylene carbonate/dimethyl carbonate	143.1	270
LIB-3	$LiMn_2O_4$	Graphite on Cu foil	$LiPF_6$ in ethylene carbonate/ethyl methyl carbonate	128.5	286.9

[a]$Na_{0.76}Mn_{0.5}Ni_{0.3}Fe_{0.1}Mg_{0.1}O_2$, $Na_{0.6}Ni_{0.22}Al_{0.11}Mn_{0.66}O_2$, *etc.*

TABLE 4 | Lithium mining and production capacities for selected years (Roskill, 2019).

Mine capacity	Cap. 2015	Prod. 2015	Cap. 2018	Prod. 2018	Utilization 2018	Cap. 2024	Cap. 2028
	t LCE	t LCE	t LCE	t LCE	%	t LCE	t LCE
Total	269.000	186.000	645.000	398.000	61	1,498.000	1,543.000
Thereof brine cap	130.000	—	222.000	145.000	66	493.000	537.000
Thereof mineral cap	139.000	—	423.000	253.000	59	1,005.000	1,006.000

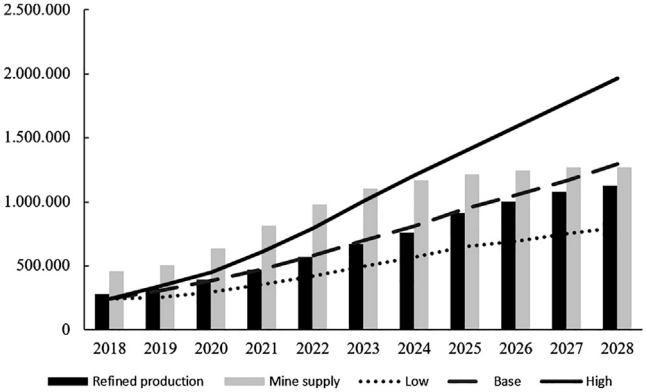

FIGURE 5 | Lithium market balance 2018–2028: base, low, high case demand (LCE t). Data are redrawn from Ref. Roskill (2019).

cover the forecasted demand, probably until 2025, according to our expectations (**Figure 5**). This led to a decrease in the price of Li_2CO_3 and lithium hydroxide monohydrate (LiOH) in the past 2 years, which slows down the expansion of lithium mining capacities. However, most of the projects are not canceled, but are put on hold, so that they can be reactivated if the market demand makes it feasible. Looking further into the future, until 2028, a growing shortage of refined lithium is expected due to further strong growth of the lithium demand, despite the fact that there is no shortage of lithium in general. There areworldwide lithium reserves in the amount of 17 million tons of elemental lithium (Fortier et al., 2018), which is equivalent to about 90 million tons LCE. However, there are some challenges and risks to be tackled: i) The current lithium market is dominated by an oligopoly of the five biggest lithium producers, ii) The lithium supply chain is strongly influenced by Chinese companies, iii) The quality of battery-grade lithium is challenging for lithium producers, especially as the producers must increase the portion of battery-grade lithium from about 40% in 2018 to about than 90% in 2028 (Roskill, 2019). Reaching this target under the condition of cost-competitiveness will be challenging.

To conclude, there will be most likely enough lithium to satisfy the market demand for LIBs. However, if the few accessible lithium reserves come under the control of one or a few actors (today more than 70% of lithium raw material production is under Chinese influence or control), or if the current oligopoly is even more concentrated, and under consideration of the technical challenge to produce battery-grade lithium raw materials, LIBs producers in some countries might experience serious difficulties in getting enough lithium raw materials for a competitive price. The establishment of cost-effective recycling technologies as a part of a LIBs circular economy, may critically influence this market not only from the point of cost and material availability but also homogeneous access to the resources (Graedel et al., 2011; U. G. Survey, 2015).

Sodium carbonate or soda ash (Na_2CO_3) is refined from trisodium hydrogendicarbonate dehydrate (trona, $Na_2CO_3.NaHCO_3.2H_2O$) (Dai and Chung, 1996). Trona is found in a tremendous amount in seawater (Hwang et al., 2017) and contains over 90% of a mixture of sodium carbonate and bicarbonate ($NaHCO_3$) (Dai and Chung, 1996). The world-leading largest known resources for trona are in Wyoming with 47 billion tons of identified soda ash resources and. It is estimated that worldwide, trona beds contain about 75 billion metric tons of ore, and about 1.8 tons of trona yields 1 ton of Na_2CO_3 (USGS National Minerals Information Center, 2020).

As trona is highly soluble in water "monohydrate process" is mainly used to collect Na_2CO_3. Solvay announces their position as a "world leader" in soda ash with their 500 kt production capacity. Apart from trona, they also produce synthetic Na_2CO_3 by an industrial process which is named as "Solvay ammonia process" (Solvay). However, this process is not advantageous or favorable due to its relatively high production costs and higher environmental impacts (more carbon dioxide release during production) (USGS National Minerals Information Center, 2020).

Cathode Materials

The material use of currently dominant cell chemistries for Lithium-ion batteries (LIB) is assessed as critical, concerning its supply risk (SR). Cobalt-free battery technologies beyond LIBs, e.g., Li-S or SIBs bear the potential of easing the supply situation for future technologies. The supply risk of resources is predominantly assessed by the methodology introduced by Graedel et al. (2012) and summarized by Benjamin Achzet (2013). Various predefined indicators are analyzed, representing the risk arising from future supply reduction, demand increase market concentration as well as political conditions in resource mining countries. Recent work by Helbig et al. (2018), Wentker et al. (2019) apply the methodology of supply risk evaluation to different battery technologies. Initially, the materials of various cell chemistries are assessed on an element level. Thereupon, the results are aggregated on a battery level on the basis of mass [Helbig et al. used various other aggregation methods (Helbig et al., 2018)]. Hence, the overall supply risk of the assessed cell chemistries equals the weighted average of the supply risk of the contained materials. While Helbig et al. focus on Li-Ion

TABLE 5 | Supply risk and supply/demand situation of various battery materials.

Battery Type		LCO	LEP	LMO	NMC	NCA	NNMO	NFPF	NTP	NVP	SR Helbig et al. (2018)	SR Wentker et al. (2019)	Reserves [kt]	Production Rate [kt]	Static Reach [years]
Only LIB	Co	x			x	x					54	60.4	7	148	47
	Li	x	x		x	x					54	58.6	17	95	179
LIB and SIB	Fe		x					x			49	47.2	81,000,000	1,470,000	55
	Mn			x	x		x				52	52.4	810	18.9	43
	Ni				x	x	x				50	55.6	89	2.4	37
	P		x					x	x	x	53	52.9			
Only SIB	Na						x	x	x	x		27.3			
	Ti								x		43	37.8	820	7.46	110
	V									x		53.4	22	71.2	309

batteries, Wentker et al. include various Na-ion batteries in their evaluation (Helbig et al., 2018; Wentker et al., 2019). Nevertheless, some materials are used in either cathode technology, which is why the results of Helbig et al. are also discussed in this article. Furthermore, it is examined if both articles draw similar conclusions concerning such materials and cell chemistries that are assessed by both.

The results on an element level are summarized in **Table 5**: Both studies use a scale from 0 to 100 supply risk points, where a score of 100 equals "the highest possible supply risk" for the assessed material. As can be observed, the supply risk scores of the respective materials are in a similar range. Small derivations occur due to different applied weightings (each determined in an analytical hierarchy process) of the indicators and the baseline year of the data used.

Helbig et al. compared different technologies among each other but abstained from making general statements about the criticality of supply. In contrast, Wentker et al. defined a "supply risk threshold" at 50 points. Bypassing this value, the assessed materials and technologies are estimated to be critical concerning their supply situation. According to this classification, cobalt, lithium, manganese, nickel, phosphorus, and vanadium are rated as critical (Helbig et al., 2018). With the exception of manganese (which is marginally beneath the supply risk criticality-threshold defined by the EU) and nickel, this corresponds to the findings of the EU study about critical raw materials (Sun et al., 2019). Graedel et al. also evaluate manganese and nickel as rather not critical concerning the respective supply risk (Graedel et al., 2012). However, it needs to be stated that the demand for nickel will increase significantly due to rising demands for EVs and the simultaneous wider application of nickel-rich cathodes. This and the resource consumption of other future technologies and applications, like for example, solar thermal power plants, wind turbines, superalloys, and others bear the potential of increasing the supply risk of nickel significantly within the next years. Helbig et al. rate phosphorus and manganese with higher criticality scores than nickel, while this is not the case in the evaluation of Wentker et al. From the assessed materials, cobalt and lithium obtain the highest supply risk scores in both researches. In contrast, sodium is scored with the lowest supply risk by far, followed by titanium, which is applied in some versions of SIBs. Sodium is abundant in the earth's crust due to its occurrence as various salts in different minerals and brines.

Table 5 also lists the static reach of the considered materials in order to give an impression about the current supply and demand situation. Neither increases in supply due to recycling and exploration/economical extraction of new reserves, nor future increases in demand are taken into account by the static reach indicator. According to this simplified approach, nickel has the lowest reach in material availability, followed by manganese and cobalt. In contrast to lithium's high supply risk score, which mainly depends on its inability concerning recyclability and substitutability as well as company and country concentration of mine production, the static reach of lithium supply is very uncritical (Sun et al., 2019). This is in consensus with the findings discussed in *Battery Grade Li vs. Battery Grade Na*.

Table 6 lists the aggregated results for the supply risk of the individual cell chemistries. From the Li-Ion Battery technologies, Helbig et al., as well as Wentker et al. score the LFP cathode with the lowest supply risk (although Helbig et al. distinguish between LFP with graphite- and with lithium-titanate anodes) (Helbig et al., 2018; Wentker et al., 2019). Homogenous results can also be observed concerning the evaluation of NMC and NCA. Assessed as two of the more critical cell chemistries, both receive similar supply risk scores. The only significant difference between the two articles concerns the LCO cell chemistry. Wentker et al. evaluate it as the most critical while Helbig et al. instead classify the supply risk of LCO in the midst of the assessed cell chemistries. It is noticeable that all Na-Ion Battery technologies are evaluated with lower supply risk scores than Li-Ion Battery technologies. None of the considered cell chemistries containing sodium surpasses the defined criticality threshold of 50 supply risk points. The fact that NNMO and NVP are rated as more critical than NFPF and NTP are due to the supply risks of the contained nickel and vanadium. Furthermore, manganese increases the supply risk of NNMO significantly. The use of phosphorus has a considerable impact on the supply risk of NFPF, NTP, and NVP. The change of cell chemistry often is accompanied with variations in material composition of various other components of battery systems. The impact of varying materials for anodes is shown by Helbig et al. for LFP.

TABLE 6 | Supply risk of various battery technologies/cell chemistries.

Battery technology	Cathode	SR Helbig et al. (2018)	SR Wentker et al. (2019)
LIB	LCO	47	60.2
	LFP-C	49	49.9
	LFP-LTO	45	—
	LMO	48	52.8
	NMC	50	56.4
	NCA	49	56.4
SIB	NNMO	—	46.3
	NFPF	—	41.6
	NTP	—	43.3
	NVP	—	46.4

Wentker et al. also assess the environmental impact score of the considered cell chemistries. The environmental impact score (EI) is measured by taking various criteria for the dimensions "damage to the ecosystem" and "damage to human health" into account. According to Wentker et al., the EI of Na-Ion Technology is significantly lower than for currently predominant cell chemistries (NCA, NMC). This is partly due to the use of lithium and cobalt, but more significantly due to the environmental impact of nickel production (especially in nickel-rich cathode NMC as well as NCA). The impact of nickel in NNMO is compensated by the very low environmental impact of the remaining cathode materials (manganese and sodium).

In summary, NIB technologies are more favorable compared to LIB technologies concerning the supply risk of their contained materials, mainly due to cobalt- and lithium-free cathodes in Na-Ion batteries. However, nickel, which is also used in NNMO has a considerable impact on the supply risk of battery technologies. This is why the supply risk of Li-Ion batteries with high nickel content (e.g., NMC811) does not significantly differ from NMC111, although minimizing the amount of contained cobalt. Considering material aspects, the advantage of Na-Ion over Li-Ion batteries is even more obvious by taking the environmental impacts (EI) of material supply into account.

Recycling Forecast for Lithium

Recycling of used LIBs is a key element to keep materials in a closed-loop system, which reduces the demand for primary raw materials in production and potential supply risk of critical raw materials. Extension of LIB lifetime in second life applications, like decentralized energy storage is desirable. However, even these battery systems must ultimately be recycled at the end of their life in order to establish a circular economy.

Since the concentration of lithium in used LIBs (ca. 5–7 wt%) is higher than in natural resources, LIBs can be considered as a large reserve of lithium (Shin et al., 2005; Yao et al., 2018; Liu et al., 2019). Nevertheless, the main research focus in the field of recycling LIBs lies especially in the recovery of cobalt due to economic reasons (Liu et al., 2019). From both an ecological and socio-economic point of view, the recovery of lithium plays an important role, even if, as described above, the reserves will not run out until 2030. On the one hand, the extraction of lithium is associated with high water consumption and the resulting ecological effects. On the other hand, Europe, in particular, is dependent on the supply of lithium from a few countries worldwide.

In general, there are two different recycling methods for the recovery of lithium from LIBs: pyrometallurgical and hydrometallurgical methods, as shown in **Figure 6** (Mossali et al., 2020). Other forms such as repair and regeneration of cathode materials using solid-phase sintering are not considered in this work. In the following, the advantages and disadvantages of both recycling methods and their process steps are described briefly. The recovery of lithium by the two recycling methods is of particular interest in this work.

As shown in **Figure 2**, the used LIBs are discharged prior to the actual recycling to prevent short-circuiting and self-ignition of the battery systems (Hanisch et al., 2015; Li et al., 2018b; Mossali et al., 2020). This is usually done using salt-saturated solutions with the drawback that lithium incorporated in the electrolyte is lost in this process step (Chen et al., 2019; Han et al., 2016).

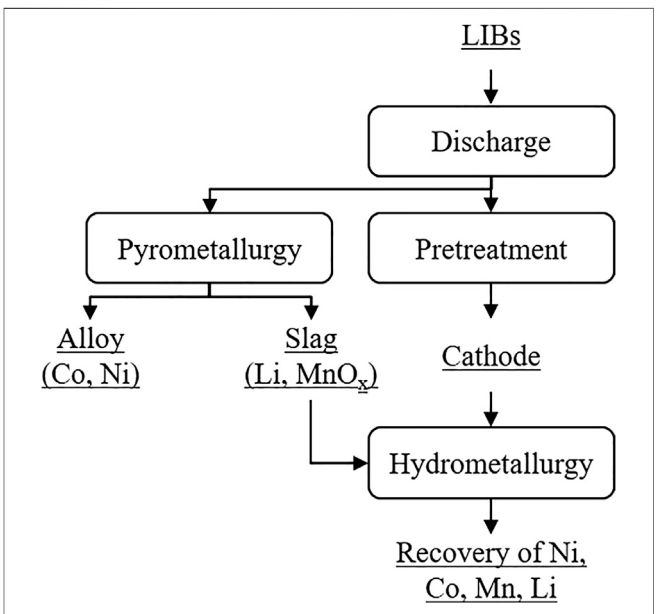

FIGURE 6 | Processes for the recycling of lithium-ion batteries (Mossali et al., 2020).

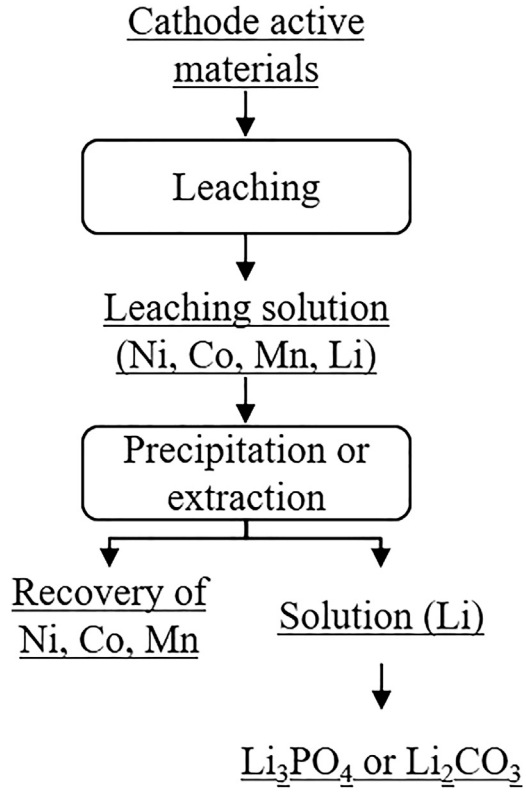

FIGURE 7 | Recovery of active cathode materials from lithium-ion batteries (Liu et al., 2019).

Without further treatment, the discharged LIBs can be used as input for pyrometallurgical recycling.

Pyrometallurgical recycling is the most mature battery recycling technology and used to extract target metals by high temperatures, which leads to physical and chemical transformations. The simple operation, which is also easy to scale up, and the ability to recycle different battery chemistries simultaneously are one of the main advantages of this recycling method (Baltac and Slater, 2019; Fan et al., 2020). In pyrometallurgical recycling, the LIBs are fed to a high-temperature shaft furnace together with a slag forming agent (Gaines, 2014; Harper et al., 2019). Redox reactions are activated to smelt and purify valuable metals (Lv et al., 2018; Zheng et al., 2018; Velázquez-Martínez et al., 2019). The output of the pyrometallurgical process is a metallic alloy fraction containing, e.g., Ni and Co, slag, and gases (Harper et al., 2019). To avoid the release of potentially toxic by-products, gas clean-up steps are necessary (Gaines, 2014). The resulting furnace slag consists of ashes and burnt components, primarily containing aluminum, lithium, and other materials (Shin et al., 2005; Yao et al., 2018; Liu et al., 2019). The recovery of lithium from the slag is possible using further treatment in the form of hydrometallurgical recycling (see **Figure 6**). However, this is not economically viable and, therefore, usually not performed (Gaines, 2018; Mossali et al., 2020). Instead, the slag can be reused, e.g., as a cement additive (Gaines, 2018).

Despite disadvantages of the pyrometallurgical process, like high capital costs, production of toxic gases, high-energy consumption, and a limited number of reclaimed materials, pyrometallurgical recycling remains a frequently used, economical process for the extraction of high-value transition metals such as cobalt and nickel (Joulié et al., 2014; Gaines, 2014; Chen et al., 2015; Harper et al., 2019; Mossali et al., 2020).

Hydrometallurgical recycling of active cathode materials consists of leaching, precipitation and/or solvent extraction, as shown in **Figure 4** (Liu et al., 2019). The main operating parameters of this recycling method are temperature, acid and reducing agent concentration and species, reaction time, and solid/liquid ratio (Li et al., 2018a; Harper et al., 2019; Mossali et al., 2020). In contrast to pyrometallurgical recycling, the LIBs receive pre-treatment depending on, e.g., cell chemistry and target materials, before they are hydrometallurgically recycled in order to increase recycling efficiency (Baltac Slater, 2019; Mossali et al., 2020). The pre-treatment includes different processes such asmechanical separation, thermal processes, dissolution processes, and mechanochemical methods(Lv et al., 2018; Zheng et al., 2018; Mossali et al., 2020). After the pre-treatment, the leaching, i.e., the dissolution of the target materials by leaching reagents, takes place. Mainly the leaching reagents include inorganic acids, organic acids, and alkaline solutions (Liu et al., 2019). The output is a leaching solution containing metals like Ni, Co, Mn, and Li. Trough precipitation and/or solvent extraction, these metals can be separated from the solution. For economic reasons, research has mainly focused on the separation of Ni, Co, and Mn from the leaching solution, the recovery of lithium in contrast, is of lesser importance. As shown in **Figure 7**, the recovery of lithium in the form of Li_3PO_4 or Li_2CO_3 is usually one of the last process. (Liu et al., 2019). Since the loss of lithium is inevitable and accumulated during the separation of Ni, Co, and Mn from the leaching solution, the recycling efficiency of lithium depends on the previous process steps.

In general, the main advantages of hydrometallurgical processes compared with pyrometallurgical processes are higher recovery efficiency of valuable metals, especially regarding lithium, lower energy consumption, less production of toxic gases, and lower capital costs (Lv et al., 2018; Fan et al., 2020; Mossali et al., 2020). The main drawbacks of using hydrometallurgical processes for LIBs recycling are high dependency on pre-treatments and used technologies, emissions associated with the used chemicals, and difficulty to process different battery chemistries at once (Baltac and Slater, 2019; Mossali et al., 2020). This is because each recycling sequence has to be optimized for certain battery chemistry to ensure a high recovery of materials and favorable economics (Baltac and Slater, 2019). Hydrometallurgical recycling allows a recovery rate of around 95% regarding Ni and Co as salts, while Cu can be recovered up to 100% and Li by around 90%. To achieve these high rates, the leaching processes are usually tailored for specific battery chemistries, and extensive pre-treatment processes are necessary. Using hydrometallurgical recycling after the pyrometallurgy process a cost-intensive recovery of about 50–60% of Li is possible (Fan et al., 2020; Frost and Sullivan, 2020). In the future, hydrometallurgical recycling processes require an efficient and more rapid removal of impurities to increase the

purity of the recovered materials (Fan et al., 2020; Frost and Sullivan, 2020). Furthermore, new combinations of pyrometallurgical recycling at lower temperatures and acid/alkaline free hydrometallurgical recycling, such as vacuum carbothermal reduction and sulfation roasting, seem promising and require future research and industrial implementation (Liu et al., 2019).

Research of Liu et al. shows that recovery of lithium on an industrial scale has so far played only a minor role. Currently, only two out of fourteen analyzed recycling processes for LIBs from different companies recover lithium (Liu et al., 2019). From an economic point of view, the recovery of lithium is currently not viable. Instead, the focus is on the recovery of the more expensive metals: cobalt, nickel (Swain, 2017).

Little information was found about recycling strategies for SIBs. This is due to the non-existence of relevant amounts of EoL-Na-Ion batteries. However, one part of the agenda of the ongoing NAIMA project is to develop a "sustainable and cost-efficient recycling process for SIBs" (European Comission, 2019). Furthermore, the Association of European Automotive and Industrial Battery Manufacturers describes sodium-nickel chloride batteries as "fully recyclable within existing industries for the production of stainless steel and road paving" (Association of European Automotive and Industrial Battery Manufacturers). Although only on a laboratory scale, Liu et al. recently developed a design-for-recycling sodium-ion batteries. The recycling of this battery resulted in a recycling efficiency of more than 98% concerning its solid components (Liu et al., 1965). The phase of product design is also highlighted by Hirsh et al. As manufacturers for SIBs are at the beginning of upscaling their production, they are expected to be more flexible in incorporating methods of sustainable product design than established LIBs manufacturers. Also, traceability concerning material composition is seen as an important aspect for the future recycling of SIBs. The need for information transfer throughout the whole supply chain is intensified due to the expected main application of SIBs as stationary storage batteries and the associated lifespan (Hirsh et al., 2020).

SUMMARY AND OUTLOOK

Although SIB technology and its manufacturing is already at the commercialization level, so far it has found little commercial application possibilities. SIBs use the same manufacturing process as LIBs, which is a great advantage for manufacturers. Cost-driven advantages of SIBs are sustainable and cheap cathode materials ($NaCO_3$, cobalt-free active materials) as well as the use of aluminum current collectors for both negative and positive electrodes. However, as explained in the previous chapters, these advantages are not enough to reduce battery cost. Additionally, the specific energy density of today's SIBs is also not higher than LIBs.

An innovative cell design strategy for these batteries is indispensable to balance both high energy density and the decrease in total battery cost. According to market reports SIBs technology can reach to more competitive level after 2025, especially for large-scale energy storage systems.

After 2025 the required battery capacity for EV market is 1,559 GWh (Automotive Competence Center & Forschungsgesellschaft Kraftwahrwesen mbH Aachen, 2018). As a result a growing shortage of refined lithium is expected after 2028 due to further strong growth of the lithium demand. This demand will mainly consist of battery grade lithium for which the proportion is expected to increase from 40% in 2018 to about 90% in 2028. Reaching this target under the condition of cost-competitiveness will be challenging. This implies that the use of SIBs in parallel to LIBs for stationary and short lifetime electromobility applications (E-bikes, e-scooters) will definitely decrease the pressure on lithium supply chain.

Moreover, today's lithium recycling technology is highly costly, and battery manufacturing costs must include recycling costs. So far, there are no such cost studies concerning recycling. Last but not least, it is known that an EV with LIBs technology generates more CO_2 emissions during production than a vehicle with a combustion engine, due to the highly energy-consuming production of LIBs and their raw materials such as battery-grade lithium. As battery-grade sodium can be extracted from seawater and produced relatively easier than lithium, these batteries can be assumed more environmentally friendly.

There is no doubt that the competition between LIBs and SIBs will continue. However, the major advancement toward SIBs will be achieved by introducing cost-efficient new materials and new cell concepts.

AUTHOR CONTRIBUTIONS

The authors confirm contribution to the paper as follows: study conception and design: DK, KB, and ZB; data collection, analysis and interpretation of results, and draft manuscript preparation: DK, SS, SK, JK, AK, FS, RM, MW, ZB, and KB. All authors reviewed the results and approved the final version of the manuscript.

ACKNOWLEDGMENTS

This research was conducted within the scope of the project "DigiBattPro 4.0 BW". The authors gratefully acknowledge the financial support of the Ministry of Economic Affairs, Labor and Housing Baden-Württemberg.

REFERENCES

Adelhelm, P., Hartmann, P., Bender, C. L., Busche, M., Eufinger, C., and Janek, J. (2015). From lithium to sodium: cell chemistry of room temperature sodium-air and sodium-sulfur batteries. *Beilstein J. Nanotechnol.* 6, 1016–1055. doi:10.3762/bjnano.6.105

Ahmadi, L., Young, S. B., Fowler, M., Fraser, R. A., and Achachlouei, M. A. (2017). A cascaded life cycle: reuse of electric vehicle lithium-ion battery packs in energy storage systems. *Int. J. Life Cycle Assess.* 22 (1), 111–124. doi:10.1007/s11367-015-0959-7

Al-Thyabat, S., Nakamura, T., Shibata, E., and Iizuka, A. (2013). Adaptation of minerals processing operations for lithium-ion (LiBs) and nickel metal hydride (NiMH) batteries recycling: critical review. *Miner. Eng.* 45, 4–17. doi:10.1016/j.mineng.2012.12.005

Ambrose, H., and Kendall, A. (2020a). Understanding the future of lithium: Part 1, resource model. *J. Ind. Ecol.* 24 (1), 80–89. doi:10.1111/jiec.12949

Ambrose, H., and Kendall, A. (2020b). Understanding the future of lithium: Part 2, temporally and spatially resolved life-cycle assessment modeling. *J. Ind. Ecol.* 24 (1), 90–100. doi:10.1111/jiec.12942

Association of European Automotive and Industrial Battery Manufacturers. Sodium based battery technologies. Available at: https://www.eurobat.org/batteries-contribution/battery-technologies/sodium-based (Accessed August, 2019).

Automotive Competence Center & Forschungsgesellschaft Kraftwahrwesen mbH Aachen (2018). *E-mobility index 2018*. Roland Berger.

Baltac, S., and Slater, S. (2019). Batteries on wheels: the role of battery electric cars in the EU power system and beyond. Element Energy.

Barker, J. (2017). "Progress in the commercialization of faradion's Na-ion battery technology," 4th international conference on sodium batteries, Tokyo, Japan, November 28–30, 2017.

Bauer, A., Song, J., Vail, S., Pan, W., Barker, J., and Lu, Y. (2018). The scale-up and commercialization of nonaqueous Na-ion battery technologies. *Adv. Energy Mater.* 8 (17), 1702869. doi:10.1002/aenm.201702869

Benjamin Achzet, C. H. (2013). "How to evaluate raw material supply risks—an overview. *Resour. Pol.* 38 (4), 435–447. doi:10.1016/j.resourpol.2013.06.003

Bin, D., Wang, F., Tamirat, A. G., Suo, L., Wang, Y., Wang, C., et al. (2018). Progress in aqueous rechargeable sodium-ion batteries. *Adv. Energy Mater.* 8 (17), 1703008. doi:10.1002/aenm.201703008

Chen, M., Cortie, D., Hu, Z., Jin, H., Wang, S., Gu, Q., et al. (2018). A novel graphene oxide wrapped Na 2 Fe 2 (SO 4) 3/C cathode composite for long life and high energy density sodium-ion batteries. *Adv. Energy Mater.* 8 (27), 1800944. doi:10.1002/aenm.201800944

Chen, M., Hua, W., Xiao, J., Cortie, D., Chen, W., Wang, E., Hu, Z., et al. (2019). NASICON-type air-stable and all-climate cathode for sodium-ion batteries with low cost and high-power density. *Nat. Commun.* 10 (1), 1–11. doi:10.1038/s41467-019-09170-5

Chen, M., Zhang, Y., Xing, G., and Tang, Y. (2020). Building high power density of sodium-ion batteries: importance of multidimensional diffusion pathways in cathode materials. *Front. Chem.* 8, 152. doi:10.3389/fchem.2020.00152

Chen, T., Jin, Y., Lv, H., Yang, A., Liu, M., Chen, B., et al. (2020). Applications of lithium-ion batteries in grid-scale energy storage systems. *Trans. Tianjin Univ.* 26 (3), 208–217. doi:10.1007/s12209-020-00236-w

Chen, X., Chen, Y., Zhou, T., Liu, D., Hu, H., and Fan, S. (2015). Hydrometallurgical recovery of metal values from sulfuric acid leaching liquor of spent lithium-ion batteries. *Waste Manag.* 38, 349–356. doi:10.1016/j.wasman.2014.12.023

Chen, X., Zheng, Y., Liu, W., Zhang, C., Li, S., and Li, J., (2019). "High-performance sodium-ion batteries with a hard carbon anode: transition from the half-cell to full-cell perspective. *Nanoscale* 11 (46), 22196–22205. doi:10.1039/C9NR07545C

Clément, R. J., Billaud, F., Armstrong, A. R., Singh, G., Rojo, T., Brucebd, P. G., et al. (2016). Structurally stable Mg-doped P2-Na2/3Mn1−yMgyO2 sodium-ion battery cathodes with high rate performance: insights from electrochemical, NMR and diffraction studies. *Energy Environ. Sci.* 9 (10), 3240–3251. doi:10.1039/C6EE01750A

Cole, W. J., and Frazier, A. (2019). *Cost projections for utility-scale battery storage*. Golden, CO: NREL.

Curry, C. (2017). *Lithium-ion battery costs & market*. Bloomberg- New Energy Finance.

Dai, Q., and Chung, K. H. (1996). Trona mineral grade sodium carbonate as A process aid for the hot water process. *J. Can. Petrol. Technol.* 35 (1). doi:10.2118/96-01-08

Delmas, C. (2018). Sodium and sodium-ion batteries: 50 years of research. *Adv. Energy Mater.* 8 (17), 1703137. doi:10.1002/aenm.201703137

Deng, J., Luo, W. B., Lu, X., Yao, Q., Wang, Z., Liu, H. K., et al. (2018). High energy density sodium-ion battery with industrially feasible and air-stable O3-type layered oxide cathode. *Adv. Energy Material.* 8 (5), 1701610. doi:10.1002/aenm.201701610

Ding, Y., Cano, Z. P., Yu, A., Lu, J., and Chen, Z. (2019). Automotive Li-ion batteries: current status and future perspectives. *Electrochem. Energ. Rev.* 2 (1), 1–28. doi:10.1007/s41918-018-0022-z

Dolega, P. (2019). *Gigafactories für Lithium-Ionen-Zellen, Rohstoffbedarfe für die globale Elektromobilität bis 2050*. Darmstadt: Öko-Institut e-V.

El Moctar, I., Ni, Q., Bai, Y., Wu, F., and Wu, C. (2018). Hard carbon anode materials for sodium-ion batteries. *Funct. Mater. Lett.* 11 (6), 1830003. doi:10.1142/S1793604718300037

Ellis, B. L., and Nazar, L. F. (2012). Sodium and sodium-ion energy storage batteries. *Curr. Opin. Solid State Mater. Sci.* 16 (4), 168–177. doi:10.1016/j.cossms.2012.04.002

Etacheri, V., Marom, R., Elazari, R., Salitra, G., and Aurbach, D. (2011). Challenges in the development of advanced Li-ion batteries: a review. *Energy Environ. Sci.* 4 (9), 3243. doi:10.1039/c1ee01598b

Euchner, H., Clemens, O., and Reddy, M. A. (2019). Unlocking the potential of weberite-type metal fluorides in electrochemical energy storage. *Npj Comput Mater* 5 (1), 1–10. doi:10.1038/s41524-019-0166-3

European Comission (2019). Na-ion materials as essential components to manufacture robust battery cells for non.automotive applications: NAIMA Project- H2020. Available at: https://cordis.europa.eu/project/id/875629 (Accessed August, 2019).

Fan, E., Li, L., Wang, Z., Lin, J., Huang, Y., Yao, Y., et al. (2020). Sustainable recycling technology for Li-ion batteries and beyond: challenges and future prospects. *Chem. Rev.* 120 (14), 7020–7063. doi:10.1021/acs.chemrev.9b00535

Fortier, S. M., Hammarstrom, J. H., Ryker, S. J., Day, W. C., and Seal, R. R. (2018). *U.S. Geological Survey, 806 "Mining Engineering2019-USGS Critical Minerals Review. U.S. Department of Commerce.*

Frost and Sullivan (2019a). *Disruptive battery storage technologies: novel battery technologies beyond lithium-ion chemistry are expected to disrupt the battery market in the next decade*. Santa Clara: Frost&Sullivan.

Frost and Sullivan (2019b). *Global Li-ion batteries market, forecast to 2025*. Santa Clara: Frost&Sullivan.

Frost and Sullivan (2020). *Managing end-of-life Li-ion batteries: battery recycling technologies: innovative technologies for the recovery and reuse of valuable metals from end-of-life lithium-ion batteries*. D952-TV.

Gaines, L. (2014). The future of automotive lithium-ion battery recycling: charting a sustainable course. *Sustainable Material. Technolo.* 1–2, 2–7. doi:10.1016/j.susmat.2014.10.001

Gaines, L. (2018). Lithium-ion battery recycling processes: research towards a sustainable course. *Sustainable Material. Technol.* 17, e00068. doi:10.1016/j.susmat.2018.e00068

Graedel, T. E., Allwood, J., Birat, J.-P., Reck, B. K., Sibley, S. F., Sonnemann, G., et al. (2011). *UNEP (2011) Recycling rates of metals – a status report, A report of the working group on the global metal flows to the international resource panel.*

Graedel, T. E., Barr, R., Chandler, C., Chase, T., Choi, J., Christoffersen, L., et al. (2012). Methodology of metal criticality determination. *Environ. Sci. Technol.* 46 (2), 1063–1070. doi:10.1021/es203534z

Graedel, T. E., Harper, E. M., Nassar, N. T., and Reck, B. K. (2015). On the materials basis of modern society. *Proc. Natl. Acad. Sci. U.S.A.* 112 (20), 6295–6300. doi:10.1073/pnas.1312752110

Guo, J.-Z., Wang, P. F., Wu, X. L., Zhang, X. H., Yan, Q., Chen, H., et al. (2017). High-energy/power and low-temperature cathode for sodium-ion batteries: in situ XRD study and superior full-cell performance. *Adv. Material. (Deerfield Beach, Fla.)* 29, 33. doi:10.1002/adma.201701968

Guo, S., Yu, H., Jian, Z., Liu, P., Zhu, Y., Guo, X., et al. (2014). A high-capacity, low-cost layered sodium manganese oxide material as cathode for sodium-ion batteries. *ChemSusChem* 7 (8), 2115–2119. doi:10.1002/cssc.201402138

Habib, A., and Sou, C. (2018). Analytical review on the trends and present situation of large-scale sustainable energy storage technology. *Eur. J. Sustainable Dev. Res.* 2 (3). doi:10.20897/ejosdr/86200

Han, M. H., Gonzalo, E., Sharma, N., López del Amo, J. M., Armand, M., Avdeev, M., et al. (2016). High-performance P2-phase Na 2/3 Mn 0.8 Fe 0.1 Ti 0.1 O 2 cathode material for ambient-temperature sodium-ion batteries. *Chem. Mater.* 28 (1), 106–116. doi:10.1021/acs.chemmater.5b03276

Hanisch, C., Loellhoeffel, T., Diekmann, J., Markley, K. J., Haselrieder, W., and Kwade, A. (2015). Recycling of lithium-ion batteries: a novel method to separate coating and foil of electrodes. *J. Clean. Prod.* 108, 301–311. doi:10.1016/j.jclepro.2015.08.026

Harper, G., Sommerville, R., Kendrick, E., Driscoll, L., Slater, P., Stolkin, R., et al. (2019). Recycling lithium-ion batteries from electric vehicles. *Nature* 575 (7781), 75–86. doi:10.1038/s41586-019-1682-5

Hasa, I., Passerini, S., and Hassoun, J. (2017). Toward high energy density cathode materials for sodium-ion batteries: investigating the beneficial effect of

aluminum doping on the P2-type structure. *J. Mater. Chem.* 5 (9), 4467–4477. doi:10.1039/C6TA08667E

Helbig, C., Bradshaw, A. M., Wietschel, L., Thorenz, A., and Tuma, A. (2018). Supply risks associated with lithium-ion battery materials. *J. Clean. Prod.* 172, 274–286. doi:10.1016/j.jclepro.2017.10.122

Hirsh, H. S., Li, Y., Tan, D. H. S., Zhang, M., Zhao, E., and Meng, Y. S. (2020). Sodium-Ion batteries paving the way for grid energy storage. *Adv. Energy Material.* 10, 32. doi:10.1002/AENM.22001274

Hou, H., Qiu, X., Wei, W., Zhang, Y., and Ji, X. (2017). Carbon anode materials for advanced sodium-ion batteries. *Adv. Energy Mater.* 7 (24), 1602898. doi:10.1002/aenm.201602898

Hwang, J.-Y., Myung, S.-T., and Sun, Y.-K. (2017). Sodium-ion batteries: present and future. *Chem. Soc. Rev.* 46 (12), 3529–3614. doi:10.1039/C6CS00776G

Hwang, J.-Y., Kim, J., Yu, T.-Y., and Sun, Y.-K. (2019). "A new P2-type layered oxide cathode with extremely high energy density for sodium-ion batteries. *Adv. Energy Mater.* 9 (15), 1803346. doi:10.1002/aenm.201803346

Irisarri, E., Tennison, S., Ghimbeu, C., Gorka, J., Vix, C., Ponrouch, A., et al. (2018). Optimization of large scale produced hard carbon performance in Na-ion batteries: effect of precursor, temperature and processing conditions. *J. Electrochem. Soc.* 165 (16), A4058–A4066. doi:10.1149/2.1171816jes

Joulié, M., Laucournet, R., and Billy, E. (2014). Hydrometallurgical process for the recovery of high value metals from spent lithium nickel cobalt aluminum oxide based lithium-ion batteries. *J. Power Sources* 247, 551–555. doi:10.1016/j.jpowsour.2013.08.128

Kang, W., Zhang, Z., Lee, P. K., Ng, T. W., Li, W., Tang, Y., et al. (2015). Copper substituted P2-type Na0.67CuxMn1−xO2: a stable high-power sodium-ion battery cathode. *J. Mater. Chem.* 3 (45), 22846–22852. doi:10.1039/C5TA06371J

Kim, H., Eon Kwon, J., Lee, B., Hong, J., Lee, M., Young Park, S., et al. (2015). High energy organic cathode for sodium rechargeable batteries. *Chem. Mater.* 27 (21), 7258–7264. doi:10.1021/acs.chemmater.5b02569

Kim, Y., Kim, J.-K., Vaalma, C., Bae, G. H., Kim, G.-T., Passerini, S., and Kim, Y. (2018). Optimized hard carbon derived from starch for rechargeable seawater batteries. *Carbon* 129, 564–571. doi:10.1016/j.carbon.2017.12.059

Konarov, A., Choi, J. U., Bakenov, Z., and Myung, S.-T. (2018). Revisit of layered sodium manganese oxides: achievement of high energy by Ni incorporation. *J. Mater. Chem.* 6 (18), 8558–8567. doi:10.1039/C8TA02067A

Konarov, A., Jae Kim, H., Jo, J. H., Voronina, N., Lee, Y., Bakenov, Z., et al. (2020). High-Voltage oxygen-redox-based cathode for rechargeable sodium-ion batteries. *Adv. Energy Mater.* 10 (24), 2001111. doi:10.1002/aenm.202001111

Konarov, A., Jo, J. H., Choi, J. U., Bakenov, Z., Yashiro, H., Kim, J., and Myung, S.-T. (2019). Exceptionally highly stable cycling performance and facile oxygen-redox of manganese-based cathode materials for rechargeable sodium batteries. *Nanomater. Energy* 59, 197–206. doi:10.1016/j.nanoen.2019.02.042

Landa-Medrano, I., Li, C., Ortiz-Vitoriano, N., Ruiz de Larramendi, I., Carrasco, J., and Rojo, T. (2016). Sodium-oxygen battery: steps toward reality. *J. Phys. Chem. Lett.* 7 (7), 1161–1166. doi:10.1021/acs.jpclett.5b02845

Li, L., Biana, Y., Zhanga, X., Guanc, Y., Fana, E., Wu, F., et al. (2018a). Process for recycling mixed-cathode materials from spent lithium-ion batteries and kinetics of leaching. *Waste Manag.* 71, 362–371. doi:10.1016/j.wasman.2017.10.028

Li, L., Li, L., Zhang, X., Li, M., Chen, R., Wu, F., et al. (2018b). The recycling of spent lithium-ion batteries: a review of current processes and technologies. *Electrochem. Energ. Rev.* 1 (4), 461–482. doi:10.1007/s41918-018-0012-1

Li, L., Lu, Y., Zhang, Q., Zhao, S., Hu, Z., and Chou, S.-L. (2019). Recent progress on layered cathode materials for nonaqueous rechargeable magnesium batteries. *Small* e1902767. doi:10.1002/smll.201902767

Liu, B., Zhang, J.-G., and Xu, W. (2018). Advancing lithium metal batteries. *Joule* 2 (5), 833–845. doi:10.1016/j.joule.2018.03.008

Liu, C., Lin, J., Cao, H., Zhang, Y., and Sun, Z. (2019). Recycling of spent lithium-ion batteries in view of lithium recovery: a critical review. *J. Clean. Prod.* 228, 801–813. doi:10.1016/j.jclepro.2019.04.304

Liu, H., Xu, J., Ma, C., and Meng, Y. S. (2015). A new O3-type layered oxide cathode with high energy/power density for rechargeable Na batteries. *Chem. Commun.* 51 (22), 4693–4696. doi:10.1039/c4cc09760b

Liu, T., Zhang, Y., Chen, C., Lin, Z., Zhang, S., and Lu, J. (1965). Sustainability-inspired cell design for a fully recyclable sodium ion battery. *Nat. Commun.* 10, 1. doi:10.1038/s41467-019-09933-0

Liu, Y., He, P., and Zhou, H. (2018). Rechargeable solid-state Li-air and Li-S batteries: materials, construction, and challenges. *Adv. Energy Mater.* 8 (4), 1701602. doi:10.1002/aenm.201701602

Lu, Z., and Dahn, J. R. (2001). I*n situ* X-ray diffraction study of P 2 Na2/3 [Ni1/3Mn2/3] O 2. *J. Electrochem. Soc.* 148, 11. doi:10.1149/1.1407247.A1225

Luo, J., Sun, S., Peng, J., Liu, B., Huang, Y., Wang, K., et al. (2017). Graphene-roll-wrapped prussian blue nanospheres as a high-performance binder-free cathode for sodium-ion batteries. *ACS Appl. Mater. Interfaces* 9 (30), 25317–25322. doi:10.1021/acsami.7b06334

Lv, W., Wang, Z., Cao, H., Sun, Y., Zhang, Y., and Sun, Z. (2018). A critical review and analysis on the recycling of spent lithium-ion batteries. *ACS Sustain. Chem. Eng.* 6 (2), 1504–1521. doi:10.1021/acssuschemeng.7b03811

Ma, X., Xiong, X., Zou, P., Liu, W., Wang, F., Liang, X., et al. (2019). "General and scalable fabrication of core–shell metal sulfides@C anchored on 3D N-doped foam toward flexible sodium ion batteries. *Small* 15–45. doi:10.1002/smll.201903259

MacLaughlin, C. M. (2019). Status and outlook for magnesium battery technologies: a conversation with stan whittingham and sarbajit banerjee. *ACS Energy Lett.* 4 (2), 572–575. doi:10.1021/acsenergylett.9b00214

Maitra, U., House, R. A., Somerville, J. W., Tapia-Ruiz, N., Lozano, J. G., Guerrini, N., et al. (2018). Oxygen redox chemistry without excess alkali-metal ions in Na2/3Mg0.28Mn0.72O2. *Nat. Chem.* 10 (3), 288–295. doi:10.1038/nchem.2923

Mao, M., Luo, C., Pollard, T. P., Hou, S., Gao, T., Fan, X., Cui, C., et al. (2019). A pyrazine-based polymer for fast-charge batteries. *Angew. Chem.* 58 (49), 17820–17826. doi:10.1002/anie.201910916

Ming, J., Guo, J., Xia, C., Wang, W., and Alshareef, H. N. (2019). Zinc-ion batteries: materials, mechanisms, and applications. *Mater. Sci. Eng. R. Rep.* 135, 58–84. doi:10.1016/j.mser.2018.10.002

Mossali, E., Picone, N., Gentilini, L., Rodriguez, O., Pérez, J. M., and Colledani, M. (2020). Lithium-ion batteries towards circular economy: a literature review of opportunities and issues of recycling treatments. *J. Environ. Manag.* 264, 110500. doi:10.1016/j.jenvman.2020.110500

Nassar, N. T., Graedel, T. E., and Harper, E. M. (2015). By-product metals are technologically essential but have problematic supply. *Sci. Adv.* 1 (3), e1400180. doi:10.1126/sciadv.1400180

Nayak, P. K., Yang, L., Brehm, W., and Adelhelm, P. (2018). From lithium-ion to sodium-ion batteries: advantages, challenges, and surprises. *Angew. Chem.* 57 (1), 102–120. doi:10.1002/anie.201703772

Ortiz-Vitoriano, N., Drewett, N. E., Gonzalo, E., and Rojo, T. (2017). High performance manganese-based layered oxide cathodes: overcoming the challenges of sodium ion batteries. *Energy Environ. Sci.* 10 (5), 1051–1074. doi:10.1039/C7EE00566K

Oshima, T., Kajita, M., and Okuno, A. (2004). "Development of sodium-sulfur batteries. *Int. J. Appl. Ceram. Technol.* 1 (3), 269–276. doi:10.1111/j.1744-7402.2004.tb00179.x

Peng, F., Yu, L., Yuan, S., Liao, X. Z., Wen, J., Tan, G., et al. (2019). Enhanced electrochemical performance of sodium manganese ferrocyanide by Na3(VOPO4)2F coating for sodium-ion batteries. *ACS Appl. Mater. Interfaces* 11 (41), 37685–37692. doi:10.1021/acsami.9b12041

Peters, J. F., Baumann, M., Zimmermann, B., Braun, J., and Weil, M. (2017). The environmental impact of Li-Ion batteries and the role of key parameters – a review. *Renew. Sustain. Energy Rev.* 67, 491–506. doi:10.1016/j.rser.2016.08.039

Ponrouch, A., Monti, D., Boschin, A., Steen, B., Johansson, P., and Palacín, M. R. (2015). Non-aqueous electrolytes for sodium-ion batteries. *J. Mater. Chem.* 3 (1), 22–42. doi:10.1039/C4TA04428B

Qi, X., Liu, L., Song, N., Gao, F., Yang, G., Lu, Y., et al. (2017). Design and comparative study of O3/P2 hybrid structures for room temperature sodium-ion batteries. *ACS Appl. Mater. Interfaces* 9 (46), 40215–40223. doi:10.1021/acsami.7b11282

Roskill (2019). *Lithium: outlook to 2028*. 16th Edn. Roskill.

Shin, S. M., Kim, N. H., Sohn, J. S., Yang, D. H., and Kim, Y. H. (2005). Development of a metal recovery process from Li-ion battery wastes. *Hydrometallurgy* 79 (3–4), 172–181. doi:10.1016/j.hydromet.2005.06.004

Song, W., Jia, X., Wu, Z., Yanga, Y., Zhoua, Z., Lia, F., et al. (2014). Exploration of ion migration mechanism and diffusion capability for Na3V2(PO4)2F3 cathode utilized in rechargeable sodium-ion batteries. *J. Power Sources* 256, 258–263. doi:10.1016/j.jpowsour.2014.01.025

Solvay. Available at: https://www.solvay.com/en/brands/soda-solvay.

Sun, X., Hao, H., Hartmann, P., Liu, Z., and Zhao, F. (2019). Supply risks of lithium-ion battery materials: an entire supply chain estimation. *Material. Today Energy* 14, 100347. doi:10.1016/j.mtener.2019.100347

Swain, B. (2017). Recovery and recycling of lithium: a review. *Separ. Purif. Technol.* 172, 388–403. doi:10.1016/j.seppur.2016.08.031

U. G. Survey (2015). "Mineral commodity summaries 2015," *Mineral commodity summaries*. Reston, VA: U.S. Geological Survey. doi:10.3133/70140094

USGS National Minerals Information Center (2020). *Mineral commodity summaries 2020*. . Reston, VA: U.S. Geological Survey.

Vaalma, C., Buchholz, D., Weil, M., and Passerini, S. (2018). A cost and resource analysis of sodium-ion batteries. *Nat Rev Mater* 3 (4), 1–11. doi:10.1038/natrevmats.2018.13

Velázquez-Martínez, V., Santasalo-Aarnio, R., and Serna-Guerrero, R. (2019). A critical review of lithium-ion battery recycling processes from a circular economy perspective. *Batteries* 5 (4), 68. doi:10.3390/batteries5040068

Vignarooban, K., Kushagra, R., Elango, A., Badami, P., Mellander, B. E., Xu, X., et al. (2016). Current trends and future challenges of electrolytes for sodium-ion batteries. *Int. J. Hydrogen Energy* 41 (4), 2829–2846. doi:10.1016/j.ijhydene.2015.12.090

Wang, B., Han, Y., Wang, X., Bahlawane, N., Pan, H., Yan, M., et al. (2018). Prussian blue analogs for rechargeable batteries. *iScience* 3, 110–133. doi:10.1016/j.isci.2018.04.008

Wentker, M., Greenwood, M., Chofor Asaba, M., and Lekera, J. (2019). A raw material criticality and environmental impact assessment of state-of-the-art and post-lithium-ion cathode technologies. *J. Energy Storage* 26, 101022. doi:10.1016/j.est.2019.101022

Xu, J., Lee, D. H., Clément, R. J., Yu, X., Leskes, M., Pell, A. J., et al. (2014). Identifying the critical role of Li substitution in P2–Na x [Li y Ni z Mn 1– y – z] O 2 (0 < x y z < 1) intercalation cathode materials for high-energy Na-ion batteries. *Chem. Mater.* 26 (2), 1260–1269. doi:10.1021/cm403855t

Yabuuchi, N., Hara, R., Kubota, K., Paulsen, J., Kumakura, S., and Komaba, S. (2014). A new electrode material for rechargeable sodium batteries: P2-type Na 2/3 [Mg 0.28 Mn 0.72]O 2 with anomalously high reversible capacity. *J. Mater. Chem.* 2 (40), 16851–16855. doi:10.1039/C4TA04351K

Yabuuchi, N., Kubota, K., Dahbi, M., and Komaba, S. (2014). Research development on sodium-ion batteries. *Chem. Rev.* 114 (23), 11636–11682. doi:10.1021/cr500192f

Yao, Y., Zhu, M., Zhao, Z., Tong, B., Fan, Y., and Hua, Z. (2018). Hydrometallurgical processes for recycling spent lithium-ion batteries: a critical review. *ACS Sustain. Chem. Eng.* 6 (11), 13611–13627. doi:10.1021/acssuschemeng.8b03545

You, Y., and Manthiram, A. (2018). Progress in high-voltage cathode materials for rechargeable sodium-ion batteries. *Adv. Energy Material.* 8. 2. doi:10.1002/aenm.201701785

You, Y., Wu, X.-L., Yin, Y.-X., and Guo, Y.-G. (2014). High-quality Prussian blue crystals as superior cathode materials for room-temperature sodium-ion batteries. *Energy Environ. Sci.* 7 (5), 1643–1647. doi:10.1039/C3EE44004D

Yu, M., Yin, Z., Yan, G., Wang, Z., Guo, H., Li, G., et al. (2020). Synergy of interlayer expansion and capacitive contribution promoting sodium ion storage in S, N-Doped mesoporous carbon nanofiber. *J. Power Sources* 449, 227514. doi:10.1016/j.jpowsour.2019.227514

Zhang, H. (2019). *Polyanionic cathode materials for sodium-ion batteries. Karlsruhe: Karlsruhe Institute of Technology*.

Zhao, N., Li, C., and Guo, X. (2014). Long-life Na–O 2 batteries with high energy efficiency enabled by electrochemically splitting NaO 2 at a low overpotential. *Phys. Chem. Chem. Phys.* 16 (29), 15646–15652. doi:10.1039/C4CP01961J

Zhao, Q., Lu, Y., and Chen, J. (2017). Advanced organic electrode materials for rechargeable sodium-ion batteries. *Adv. Energy Mater.* 7 (8), 1601792. doi:10.1002/aenm.201601792

Zheng, L., Li, J., and Obrovac, M. N. (2017). "Crystal structures and electrochemical performance of air-stable Na 2/3 Ni 1/3– x Cu x Mn 2/3 O 2 in sodium cells. *Chem. Mater.* 29 (4), 1623–1631. doi:10.1021/acs.chemmater.6b04769

Zheng, X., Zhu, Z., Lin, X., Zhang, Y., He, Y., Cao, H., et al. (2018). A mini-review on metal recycling from spent lithium ion batteries. *Engineering* 4 (3), 361–370. doi:10.1016/j.eng.2018.05.018

Zhu, X., Lin, T., Manning, E., Zhang, Y., Yu, M., Zuo, B., et al. (2018). Recent advances on Fe- and Mn-based cathode materials for lithium and sodium ion batteries. *J. Nano Res.* 20 (6). doi:10.1007/s11051-018-4235-1

Conflict of Interest: The authors declare that the research was conducted in the absence of any commercial or financial relationships that could be construed as a potential conflict of interest.

frontiers in Energy Research

ORIGINAL RESEARCH
published: 29 January 2021
doi: 10.3389/fenrg.2020.615677

$Na_{0.44}MnO_2$/Polyimide Aqueous Na-ion Batteries for Large Energy Storage Applications

*Satyanarayana Maddukuri, Amey Nimkar, Munseok S. Chae, Tirupathi Rao Penki, Shalom Luski and Doron Aurbach **

Department of Chemistry and BINA (BIU Center for Nano-Technology and Advanced Materials), Bar-Ilan University, Ramat-Gan, Israel

Aqueous salt batteries with high concentrations of salt or water in salt aqueous systems have received considerable attention with focus on improving working voltage range and energy density. Here, the effect of $NaClO_4$ salt concentration on the electrochemical performance and stability of tunnel-type $Na_{0.44}MnO_2$ (NMO) cathodes and organic polyimide (PI) derivative anodes was studied. High capacity retention and 100% coulombic efficiency were shown for NMO/PI full cell in saturated $NaClO_4$ electrolyte. A high, stable capacity of 115 mAh/g was achieved for the PI anode material, and the full cell showed a stable capacity of 41 mAh/g at 2C rate for 430 cycles (calculated for the weight of NMO cathode). Even at a fast 5C rate, a discharge capacity of 33 mAh/g was maintained for 2,400 prolonged cycles with nearly 100% efficiency. The full cell device can achieve an average voltage of 1 V with energy density of 24 Wh/kg. This study highlights concentrated sodium perchlorate as a promising electrolyte solution for stabilization of electrodes and enhancement of electrochemical performance in aqueous media.

Keywords: aqueous Na-ion batteries, water in salt electrolytes, intercalation materials, aqueous batteries, polyimide anodes

OPEN ACCESS

Edited by:
Zhumabay Bakenov, Nazarbayev University, Kazakhstan

Reviewed by:
Almagul Mentbayeva, Nazarbayev University, Kazakhstan
Yuesheng Wang, Hydro-Québec's Research Institute, IREQ, Canada
Fudong Han, Rensselaer Polytechnic Institute, United States

****Correspondence:***
Doron Aurbach
Doron.Aurbach@biu.ac.il

Specialty section:
This article was submitted to Electrochemical Energy Conversion and Storage, a section of the journal Frontiers in Energy Research

Received: *09 October 2020*
Accepted: *15 December 2020*
Published: *29 January 2021*

Citation:
Maddukuri S, Nimkar A, Chae MS, Penki TR, Luski S and Aurbach D (2021) $Na_{0.44}MnO_2$/Polyimide Aqueous Na-ion Batteries for Large Energy Storage Applications. Front. Energy Res. 8:615677. doi: 10.3389/fenrg.2020.615677

INTRODUCTION

Electrochemical devices for large energy storage are in high demand and the technologies based on batteries as well as capacitors are explored. Commercial batteries are working on high energy and low power density with low rate capability, while capacitors combine low energy and high power density with high rate capability (Barbieri et al., 2005; Armand and Tarascon, 2008; Poonam et al., 2019). Due to the increased use of nonaqueous Li ion batteries in mobile electronics and electric vehicles, capacity-based systems have emerged, offering low-cost devices with pure adsorption and desorption of ions at the electrode surface, a nonfaradaic mechanism that delivers a low energy density of 10 Wh/kg (Simon and Gogotsi, 2008). In organic and ionic liquid-based electrolyte solution, capacitors allow operation of devices even at high voltage around 3 V with increased energy density (Brandt et al., 2013; Brandt and Balducci, 2014; Yu and Chen, 2019). Large energy storage requires safe, cheap, and environmentally friendly materials. Lead acid batteries are used in commercial devices with good energy density of 40 Wh/kg; however, the failure of lead acid battery related with low discharge efficiency, usage of toxic lead, highly corrosive nature of acidic electrolyte which leads to search for alternative technologies (Yolshina et al., 2015; Yang et al., 2017b; Sadeghi and Javaran, 2019). Devices based on aqueous electrolytes have proved to be safer in spite of low energy production compared to nonaqueous systems.

In order to achieve a low-cost device with high capacity, rate capability, and efficiency, one needs to consider components such as current collectors, electrolytes, and electrode materials. Sodium-based electrolytes are cheaper than lithium-based electrolytes, owing to the abundant nature of sodium vs. lithium salts in the earth's crust. In general, chemically modified or coated metal grid/sheets are used as current collectors for studying aqueous batteries. For example, aluminum, stainless steel, and nickel foil current collectors are handicapped by their highly corrosive nature in aqueous systems (Li and Church, 2016; Li, 2017). Gheytani et al. explored a chromate conversion–coated Al collector for aqueous Li ion batteries (Gheytani et al., 2016). Carbon-coated stainless steel mesh was investigated for corrosion resistance in aqueous media (Wen et al., 2017). In order to avoid the high toxicity of chromium, to reduce coating thickness, and to maintain electrodes' uniformity during prolonged cycling, it is important to develop flexible, corrosion-resistive, and conductive composite foils as current collectors and cases. Recent studies presented some attractive energy storage devices for power supply including low-cost, nontoxic, lightweight, flexible, and wearable batteries' components (Li et al., 2014a; Yang et al., 2017a). Graphene and CNT fibers were explored for Li ion batteries and capacitor applications (Li et al., 2012; Kim et al., 2013). Such composites should contain conductive polymeric matrices that can exhibit high mechanical strength and flexibility. Tang et al. showed electrically conductive and mechanically stable current collectors made by self-assembly of CNT and RGO/polystyrene composites (Tang et al., 2014). Full cells studies of aqueous Li ion battery systems using polyimide (PI)/LMO couples showed a stable capacity at a high current rate of 20C with capacity retention of 95% after 500 cycles using stretchable carbon filler/polymer composites as current collectors (Song et al., 2018). Evanko et al. also demonstrated carbon black/polyethylene composite as corrosion-resistant collectors for stationary Zn/Br_2 aqueous batteries. These current collectors demonstrated a high overpotential for hydrogen evolution, compared to stainless steel (SS), Ti, Ni, and a high overpotential for O_2 evolution compared to SS and Ni in neutral, acidic, and basic electrolyte solutions (Evanko et al., 2018). Other types of conductive vinyl films (z-flo® 2267P) were explored for aqueous and nonaqueous supercapacitors, using aqueous KOH solutions and solutions containing tetraethylammonium tetrafluoroborate in propylene carbonate, with working voltage ranges of 0–1 and 0–2.7 V, respectively (Stoller et al., 2008; Kang et al., 2019). We also analyzed such conductive vinyl films (abbreviated as PW, which means polymeric web) as current collectors and case materials in aqueous and nonaqueous solutions.

Taking into account the abundance of elements and cost-effectiveness, we explored manganese oxides as attractive cathode materials in batteries for large energy storage applications. $Mn_3O_4/NaTi_2(PO_4)_3$ cells and symmetric devices comprising Mn_3O_4 electrodes were investigated, using aqueous Na_2SO_4 electrolyte solutions (Cao et al., 2018). Cells comprising λ-MnO_2 cathodes and capacitive activated carbon anodes with 1 M Na_2SO_4 solutions could be charged up to 2.2 V and deliver a specific energy density of 19.5 Wh/kg (Shin et al., 2020). A study of cells comprising $K_xMnO_2.xH_2O$ cathodes using Li^+, Na^+, and K^+ salts solutions exhibited high capacity, efficiency, and prolonged cycle life due to contributions of both redox and nonfaradaic adsorption/desorption interactions (Shao et al., 2013). The performance of MnO_2 was explored in different nitrate-based electrolyte solutions including $Zn(NO_3)_2$, $Mg(NO_3)_2$, $Ba(NO_3)_2$, and $Ca(NO_3)_2$ (Xu et al., 2009a). Xu et al. reported insertion and de-insertion of Zn^{2+} ions in MnO_2 electrodes using 0.1 M $Zn(NO_3)_2$ electrolyte solutions (Xu et al., 2009b). Tunnel-type $Na_{0.44}MnO_2$ (NMO) material was found to be conducive for sodium aqueous and nonaqueous batteries in terms of stability and rate capability, due to its unique structure that allows fast solid-state diffusion of relatively large Na ions. NMO material can deliver a specific capacity of around 45 mAh/g with existence of fast Na ion diffusion coefficient (within the range of $10^{-}11–10^{-12}$) (Whitacre et al., 2010). In nonaqueous media, the diffusion coefficient was lower, in the range of 10^{-14}–10^{-16} cm^2 s^{-1} (Bin et al., 2018).

In order to benefit from NMO as a cathode material for large energy storage applications, it is important to couple it with anode materials that are highly stable at the necessary low potential regions, demonstrating fast rate capability in aqueous media. NASICON-type $NaTi_2(PO_4)_3$ anode in aqueous systems has the advantage of high capacity over fully capacitive carbon materials but is handicapped by poor cycling performance as a result of low electronic conductivity, dissolution of Ti ions, and voltage limitation of aqueous electrolytes (Li et al., 2014b). Other anodes for aqueous devices were recently explored that take advantage of the low cost, easy production, and possible multi-electron transfer of organic molecules and polymers within the limits of water decomposition. Chemical modification of carbon materials with functionalized groups allowed for the delivery of high energy density for prolonged cycles. AC and Kynol cloth with electrochemically active anthraquinone and catechol showed enhanced capacitance, attributed to the redox phenomena of the attached moieties with association/dissociation of ions during discharge/charge (Pognon et al., 2011; Pognon et al., 2012; Weissmann et al., 2012; Comte et al., 2015). Anthraquinone-functionalized kynol showed association and dissociation of protons in aqueous H_2SO_4 with enolization of carbonyl groups, exhibiting a 2.5-fold increase in capacity of the modified carbon material (65 vs. 25 mAh/g); however, commercial application needs to address detachment of redox-active groups (Malka et al., 2019).

Robust organic polymer materials with stable structure are extensively studied for both aqueous and nonaqueous systems. The issue of dissolution of small organic molecules in electrolyte solutions is mitigated by using polymeric materials, thus improving the life cycle of the batteries. These polymeric electrode materials are economically viable and environmentally benign. Such polymeric functional compounds offer improved aqueous battery devices (Haüpler et al., 2016; Bhosale et al., 2018; Hernández et al., 2018). Polyimides (PIs) in aqueous Li-ion batteries demonstrated a stable capacity performance with 95% capacity retention for 1,000 cycles at 2C rate (Chen et al., 2015). PI anode material

explored by Chen et al. for Mg-aqueous ion battery using Prussian blue cathode and Mg^{2+} containing electrolyte solution showed excellent cycling performance, delivering an energy density of 40 Wh/kg. (Chen et al., 2017).

Here, a Na ion aqueous battery device for large energy storage applications is presented using tunnel-type $Na_{0.44}MnO_2$ (NMO) cathode and organic PI anode materials. The stability and performance of NMO is demonstrated as intercalation/de-intercalation cathode in different concentrations of $NaClO_4$ electrolyte solution using flexible polymeric web (PW) substrate as a current collector. We studied the polyimide derivative as anode and demonstrated the high capacity retention performance in saturated $NaClO_4$ electrolyte solution. We propose in our study that the full cells comprising NMO and PI as electrodes with an aqueous electrolyte solution can demonstrate high performance as a fast energy conversion device for load leveling and large energy storage applications.

MATERIALS AND METHODS

Material Synthesis and Electrodes Preparation

1,4,5,8-naphthalenetetracarboxylic dianhydride (NTCDA)-derived PI polymer was prepared according to the procedure reported in the literature (Song et al., 2010; Chen et al., 2014; Dong et al., 2016). Equimolar quantities of NTCDA (Apollo Scientific) and ethylene diamine (Alfa Aesar Ltd.) were added to 1-methyl-2-pyrrolidone and the reaction mixture was refluxed for 6 h by stirring. Solid residue was filtered, washed several times with ethanol, and dried in air at 120°C for 12 h. The product was heated at 300°C under nitrogen atmosphere for 8 h to complete the imidization and remove residual solvent. The purity of NMO (NEI Co. Ltd.) was determined by powder X-ray diffraction (XRD) analysis. Conductive vinyl film (Polymeric web) was used as current collector and case (purchased from Transcontinental Ltd.).

Electrode materials were dried overnight at 100°C in air, prior to electrode preparation. The weight percentage of active material, conductive agent, and binder in the cathode and anode was 75:15:10 and 60:30:10, respectively. Acetylene black and graphene (XG-Sciences) in 50:50 ratio were jointly used as a conductive agent for improving PI conductivity. The AC-based counter electrode (CE) consisted of 80:10:10 AC: acetylene black: PTFE binder (60% PTFE dispersed in water, Sigma Aldrich). The electrode composite was ball-milled at 200 rpm for 2 h using isopropanol as a solvent with the electrode material to balls weight ratio of 1:20 (7 mm dia, zirconia oxide balls were used). The obtained composite was then pressed in order to make flexible thin electrodes using a rolling machine. We reached the required size and then dried overnight at 80°C. The thickness range of the electrodes was 300–400 μm for both NMO and PI, an area of 15*15 mm for full cells study. The thickness range of electrodes was 100 and 700–800 μm for NMO or PI and activated carbon electrodes, respectively, for three electrodes cells characterization. The electrodes are cut into 15*15 mm for full cells analysis. The sizes of the electrodes were in the range of 10*10 mm for three electrodes cells analyses with excess in counter electrode. The electrodes were loaded on the PW matrices using an adhesive Graphene conductive ink (obtained from XG-sciences, in order to have a better contact) and then dried at 70°C overnight. The cells including cathode, anode, and NKK separator between them were pressed and closed by nonconductive adhesive tape (obtained from 3M™ Adhesive 300LSE) after adding a few drops of electrolyte solution. The weight of the working electrode (WE) in three-electrode cell measurements was 7.5–8.5 mg for both PI and NMO. The specific surface area was around 27 and 9 mg/cm^2 for the cathode and anode materials, respectively, used in full cells analysis.

Physical and Electrochemical Characterization

The WE and CE were dried overnight at 100°C and subjected to electrochemical analysis. Electrochemical measurements were carried out in homemade pouch-type cells for 3-electrode measurements and cells for 2-electrode measurements. A polymeric web was used as case and current collector for making pouch-type cells with NKK paper as a separator and Ag/Ag_2SO_4 as RE. Homemade aqueous electrolyte solutions were prepared with 1, 8 m and saturated $NaClO_4$. We believe that the choice of this electrolyte is good because the potential window of its aqueous solutions is wide, the safety features of its aqueous solutions are appropriate for battery applications, and it is a good choice in terms of cost-effectiveness. The electrolyte solutions were purged under N_2 atmosphere for 2 h before use for cells preparation, in order to remove dissolved oxygen. Galvanostatic charge–discharge characterization, CV, and self-discharge measurements were performed with a Bio-Logic computerized instrument. Powder XRD measurements were performed with a Bruker AXS D8 Advance diffractometer and the obtained patterns were refined using GSAS Rietveld refinement software (Toby, 2001). Morphology images were obtained by high-resolution scanning electron microscopy (HRSEM) using a JEOL-JEM-2011 (200 kV) Oxford instrument. Inductively coupled plasma-optical emission spectroscopy (ICP-OES) analysis of manganese dissolution in separators and electrolytes was carried out using a Spectro Arcos ICP-OES MultiView FHX22. The synthesized PI was characterized by Fourier-transform infrared spectroscopy (FTIR, Thermo Scientific SMART iTX).

RESULTS AND DISCUSSION

The Current Collector Stability in $NaClO_4$ Electrolyte Solutions

The photographic images of the polymeric web substrates used as current collectors (**Figure 1A,B**) show that they can be bent or twisted for device flexibility. HRSEM images of PW (**Figure 1C,D**) and CVs with different $NaClO_4$ electrolyte concentrations and Ag/Ag_2SO_4 as Pseudo reference (RE) show that the PW substrates are highly stable in the potential range of

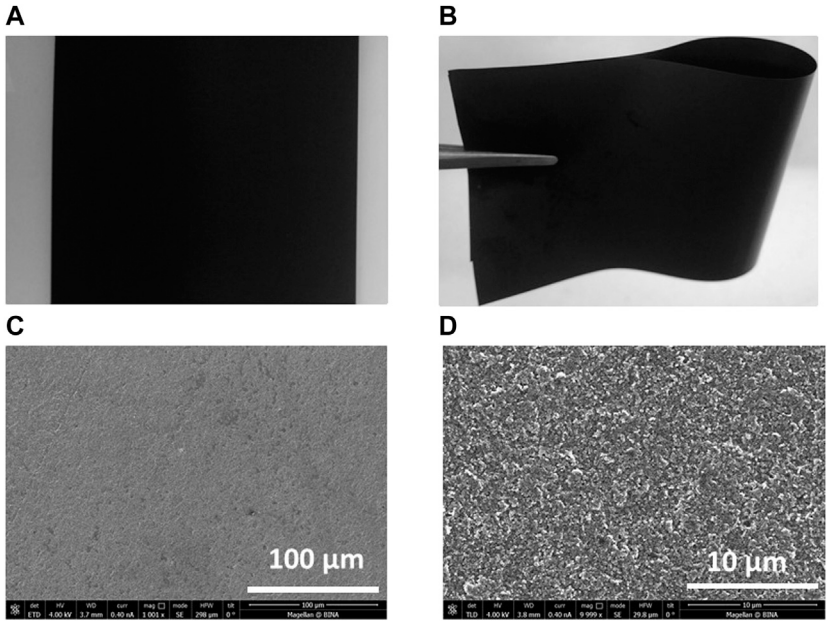

FIGURE 1 | Photographic images of the polymeric web **(A)** flat and **(B)** bent polymeric web and HRSEM images at ranges of **(C)** 100 µm at 1 k magnification and **(D)** 10 µm at 10 k magnification.

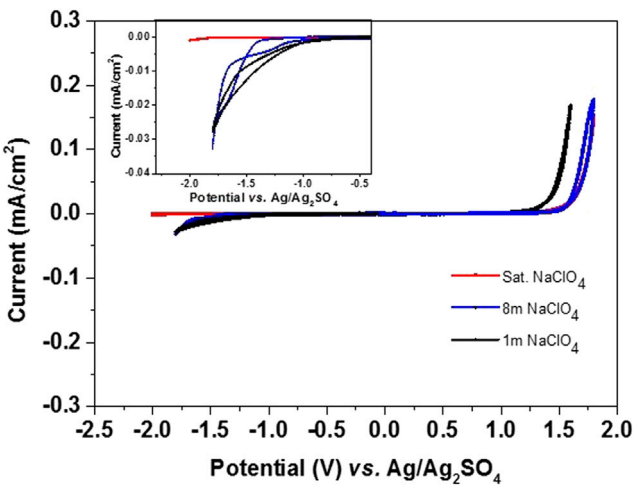

FIGURE 2 | CVs of the polymeric web substrate (case and current collector) at 1 mV/s scan rate with Ag/Ag_2SO_4 RE and 1 m (pink), 8 m (blue), and saturated (red) $NaClO_4$ electrolyte solution. The inset in the figure shows the enlarged area of the negative potential range.

−2.0 and 1.5 V vs. Ag/Ag_2SO_4 without observing any hydrogen and oxygen evolution during polarization in this potential rage in saturated NaClO4 electrolyte medium (**Figure 2**). The results indicate that the full cell charging voltage can be extended to 3.5 V using this electrolyte solution. The stability was also analyzed at electrolyte concentrations of 1 and 8 m $NaClO_4$, as shown in **Figure 2**. The stability of the less concentrated solutions is limited to −1.1 V and 1.2 vs. Ag/Ag_2SO_4 at the negative and positive edges, respectively (due to hydrogen and oxygen evolution reactions). One would think that Na_2SO_4, $NaNO_3$ NaCl, or CH_3COONa are preferable than $NaClO_4$ due to their lower cost (Lee et al., 2019). However, based on previous studies (Kim et al., 2014; Wang et al., 2015), it is possible to conclude that from an electrochemical point of view $NaClO_4$ is the best choice (as we mentioned above). As analyzed by Lee *et al.*, the highly concentrated sodium perchlorate electrolyte solution showed extended voltage ranges without decomposition relating to H_2 and O_2 evolution, due to the low concentration of the free water molecules in solution, as identified by Raman spectroscopic analysis (Lee et al., 2019). Taking into account their high stability, we used these flexible substrates in our aqueous battery studies for both electrode material characterization and devices fabrication.

Study of NMO Electrodes in $NaClO_4$ Electrolyte Solutions

The obtained Powder XRD patterns of NMO samples were refined by Rietveld analysis using GSAS, in order to verify the formation of an orthorhombic phase with the space group *Pbam*. As presented in **Figure 3A**, the measured patterns' peaks were well matched (in red color) with the calculated peaks (in green color) and the fitting parameter values were R_p = 0.017, R_{wp} = 0.028, R_{exp} = 0.011, $R(F^2)$ = 0.13086, χ^2 = 5.905, as shown in **Figure 3A**. The refined lattice parameter values are a = 9.0815(3) Å, b= 26.455(1) Å, and c = 2.8244(1) Å, in agreement with report literature (Sauvage et al., 2007; Pang et al., 2014). HRSEM images

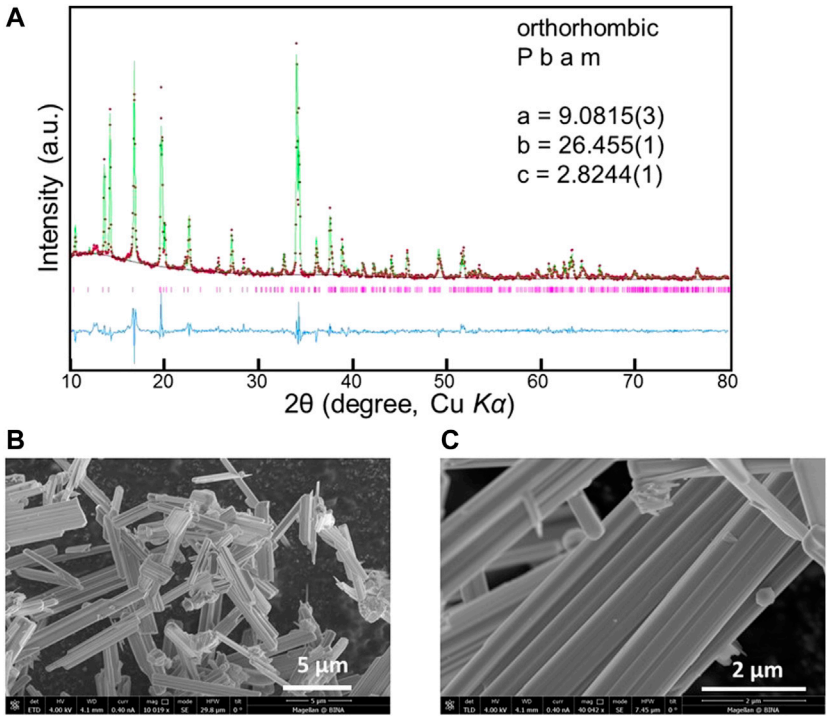

FIGURE 3 | (A) Powder XRD Rietveld refinement profile for $Na_{0.44}MnO_2$ (red points: experimental data. green line: calculated data. blue line: difference. pink bars: Bragg positions). **(B)** HRSEM images at magnification of ×10k at 5 μm range and **(C)** ×40k at 2 μm range.

of NMO are presented in **Figure 3B,C**, showing needle-shape particles. These particles are distributed with different lengths from 1 to 5 μm and are arranged in an agglomerated fashion.

In order to evaluate the electrochemical stability, the NMO electrodes were tested in 3-electrodes cells using activated carbon (AC) counter electrodes in enough excess of active mass, and Ag/Ag_2SO_4 as RE. The effect of $NaClO_4$ electrolyte concentration was studied by voltammetry using electrolyte solutions with 8m and saturated $NaClO_4$ as shown in **Figure 4** and **Figure 5**, respectively. The applied potential window was 0–0.8 V vs. Ag/Ag_2SO_4 for 20 cycles at a scan rate of 0.1 mV/s (**Figure 4A,B** and **Figure 5A,B**). The anodic and cathodic profiles show three redox peaks at potentials of 0.17/0.09, 0.40/0.32, and 0.62/0.55 V vs. Ag/Ag_2SO_4 using 8m $NaClO_4$ electrolyte, which correlate well with the reported literature (Tekin et al., 2017; Lim et al., 2018). The initial anodic capacity is 50 mAh/g with extraction of nearly 0.18 Na ions from the NMO lattice. At the end of 20 cycles, the observed discharge capacity was 35.7 mAh/g with 80% retention and a coulombic efficiency was 98%. **Figure 4C** demonstrates the CV curves at 0.5 mV/sec scan rate after scanning at 0.1 mV/s (see in **Figure 4A**). At this rate, a stable discharge capacity of 29 mAh/g was observed with an efficiency of 99% up to 50 cycles as shown in **Figure 4**. **Figure 5** shows a similar voltammetric profile with saturated $NaClO_4$ solution and redox couples at potentials of 0.21/0.12, 0.45/0.34, and 0.68/0.58 V vs. Ag/Ag_2SO_4. A stable discharge capacity of 45 mAh/g was observed after 20 cycles at slow scan rates, with a coulombic efficiency of 99.5%. Scanning was continued at 0.5 mV/s up to 50 cycles, resulting in a stable discharge capacity of 38 mAh/g. High discharge capacity and very good capacity retention were observed with the saturated electrolyte solution. These are attributed to the favorable electrodes and their interfacial stability, better charge transfer kinetics, very low content of oxygen contamination in the concentrated electrolyte solution. The advantage of concentrated solutions related to low level of dissolved oxygen was confirmed (Luo et al., 2010; Li et al., 2017).

Focusing on the high capacity and stability of NMO with concentrated electrolyte solutions, cathodes samples were stored with 8 m and saturated $NaClO_4$ solutions at 60° C for one week, then filtered and heated for drying at 100°C overnight before XRD analysis. The XRD patterns of the aged samples clearly matches with that of the parent material, showing very minor impurity peaks of Mn_2O_3 and $NaClO_4$ (as marked in **Figure 6**). The inset in the figure shows that the peak positions are nearly the same, without change in 2θ positions, and clear separation of the (0 10 0) and (3 5 0) peaks for both samples, indicating no observable loss of sodium ions from the lattice. The treatment of NMO in distilled water for one week leads to displacement of Na^+ ions with protons, resulting in a merge of the (0 10 0) and (3 5 0) peaks with lattice shrinkage of the unit cell (Dall'Asta et al., 2017).

In order to assess the contribution of Mn dissolution to capacity loss, cells were dismantled, and ICP analysis was conducted for Mn ions that present in the separators and the electrolyte solutions. The saturated electrolyte solution from cycled cells showed very minor Mn dissolution of 0.0298 μg/ml while the 8 m $NaClO_4$ electrolyte solution displays much higher Mn dissolution of about 0.306 μg/ml. These results

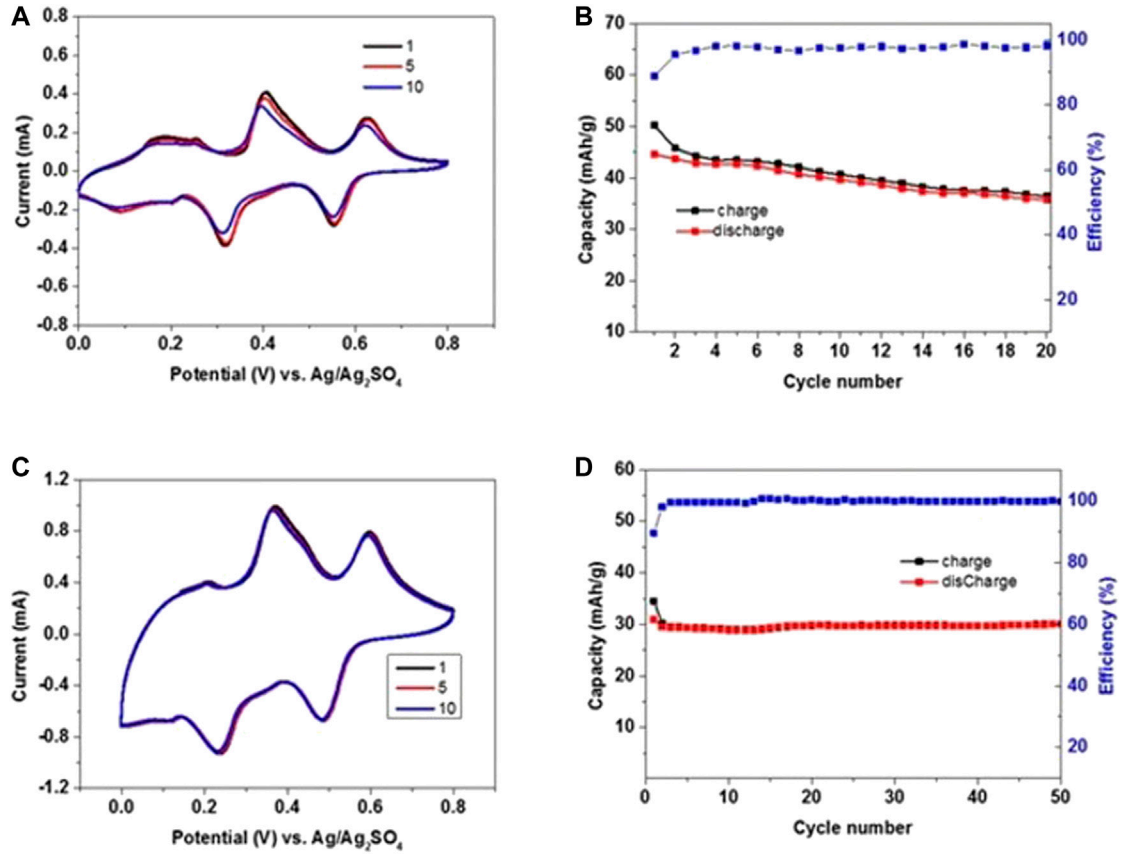

FIGURE 4 | CVs of $Na_{0.44}MnO_2$ WE and AC-rich CE in three-electrode cell configuration (electrodes were pressed onto a polymeric web current collector) in 8 m $NaClO_4$ electrolyte solution and Ag/Ag_2SO_4 RE **(A)** measured at a scan rate of 0.1 mV/s up to 20 cycles in the voltage window of 0–0.8 V vs. Ag/Ag_2SO_4 **(B)** Corresponding charge and discharge values in mAh/g during anodic and cathodic scan, respectively. **(C)** The scan rate is increased to 0.5 mV/s after 20 cycles within the same voltage range. **(D)** Charge and discharge values up to 50 cycles at 0.5 mV/s.

show that the use of highly concentrated solutions increases the stability of such types of transition metal oxide electrodes and mitigates detrimental phenomena such as dissolution of transition metal cations.

The Study of Polyimide as an Anode Material in $NaClO_4$ Electrolyte Solutions

The synthesized solid PI polymer was characterized by FTIR to confirm the structure (**Figure 7**), showing the expected bands for vibrations of imide C-N and naphthalene unit at 1349 and 1581 cm^{-1}, respectively; bands for imide vibration (C=O) at 768 cm^{-1} were found along with asymmetric and symmetric stretching at 1700 and 1660 cm^{-1}, respectively. The characterization data are in good agreement with the literature (Song et al., 2010; Chen et al., 2014; Dong et al., 2016).

The electrochemical performance of PI electrodes was also tested in electrolyte solutions of saturated $NaClO_4$, as shown in **Figure 7**. CV measurements were done at a scan rate of 0.1 mV/sec for the initial 20 cycles in the voltage window of 0 to −1.0 V vs. Ag/Ag_2SO_4; redox peaks related to reversible enolization of carbonyl groups in the PI moieties within this low voltage range are shown with no observation of hydrogen evolution. A high capacity of 160 mAh/g is observed in the initial cathodic scan, which is due to association of nearly two Na^+ ions at the carbonyl groups of PI (as shown in **Scheme 1**). After the first cycle, the discharge capacity is somewhat lower at 152 mAh/g. The retention of capacity is 91.3% with a coulombic efficiency of 99% at the end of 20 cycles at 0.1 mV/s. The better conjugation of this PI derivative results in high electronic conductivity as concluded based on DFT calculation (Andrzejak et al., 2000).

As was clearly studied for different PI derivatives like PMDA and NTCDA for lithium ion batteries by Song *et al.*, highly stable electrochemical performance was observed for the NTCDA derivative in nonaqueous media for Li ion batteries with reversible capacity of 173 mAh/g at C/5 rate (Song et al., 2010).

After completion of 20 cycles at 0.1 mV/sec, the scan rate was changed to 0.5 mV/sec. The obtained discharge capacity was 123 mAh/g and shows a stable reversible capacity of 115 mAh/g up to 50 cycles within the potential range of 0 to −1 V vs. Ag/Ag_2SO_4. The cycling efficiency reached was around 100%, as shown in **Figure 8A,B**. We attribute the stable capacity of PI at a fast scan rate with 100% coulombic efficiency not only to intrinsic properties of

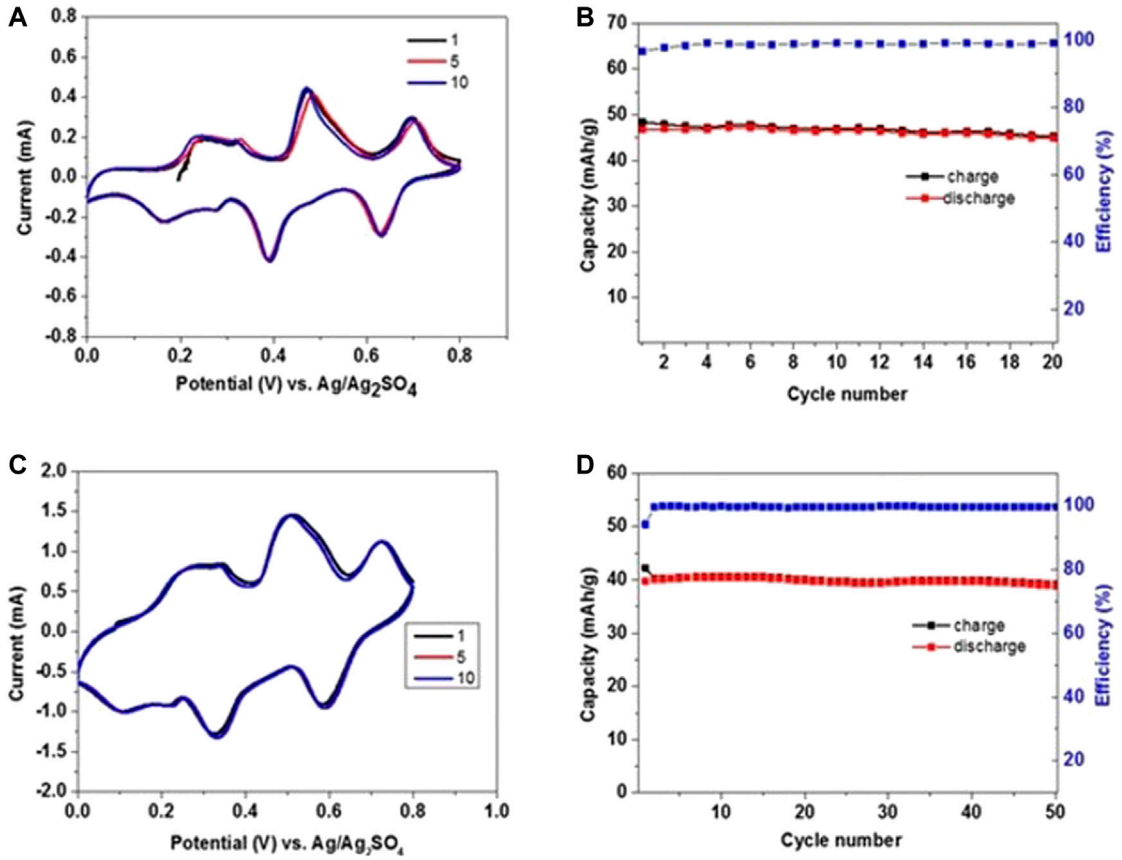

FIGURE 5 | CVs of NMO electrodes in saturated $NaClO_4$ electrolyte solution. The counter electrode comprised activated carbon and the reference electrode was Ag/Ag_2SO_4 **(A)** A scan rate of 0.1 mV/s for 20 cycles in the voltage window of 0–0.8 V vs. Ag/Ag_2SO_4 and **(B)** corresponding charge and discharge values during repeated anodic and cathodic cycling. **(C)** The scan rate is changed to 0.5 mV/s after 20 cycles within the same voltage range. **(D)** Charge and discharge values up to 50 cycles at 0.5 mV/s.

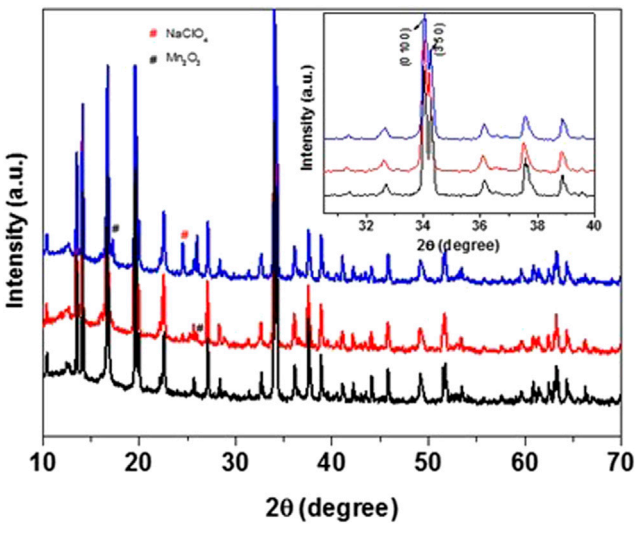

FIGURE 6 | Powder XRD patterns of NMO samples: untreated (black) and heat-treated (60°C for one week) in 8 m (red) and saturated (blue) $NaClO_4$ electrolyte solutions.

the active mass but also to the unique structure of the composite electrodes we used, which involved graphene as a conductive agent and the favorable use of saturated electrolyte solution. The effect of conductive additives like graphite and graphene or CNTs for enhancement of performance is well-known for nonaqueous and aqueous systems (Huang et al., 2018; Khamsanga et al., 2019). Potassium-organic batteries with pure PI and composites of acetylene black/PI and graphite/PI showed very poor capacity retention with the conductive additive acetylene black and 83% retention of capacity after 500 cycles for graphite/PI composite (Hu et al., 2019). Likewise, the graphene additive in our study contributed to the stable PI behavior during anodic and cathodic scan with low polarization.

Analysis of Full Cells Comprising $Na_{0.44}MnO_2$ Cathodes, PI Anodes, and Saturate Aqueous $NaClO_4$ Solution

The electrochemical performance of full cells containing cathodes comprising NMO and anodes comprising PI the active masses (respectively) in saturated aqueous $NaClO_4$

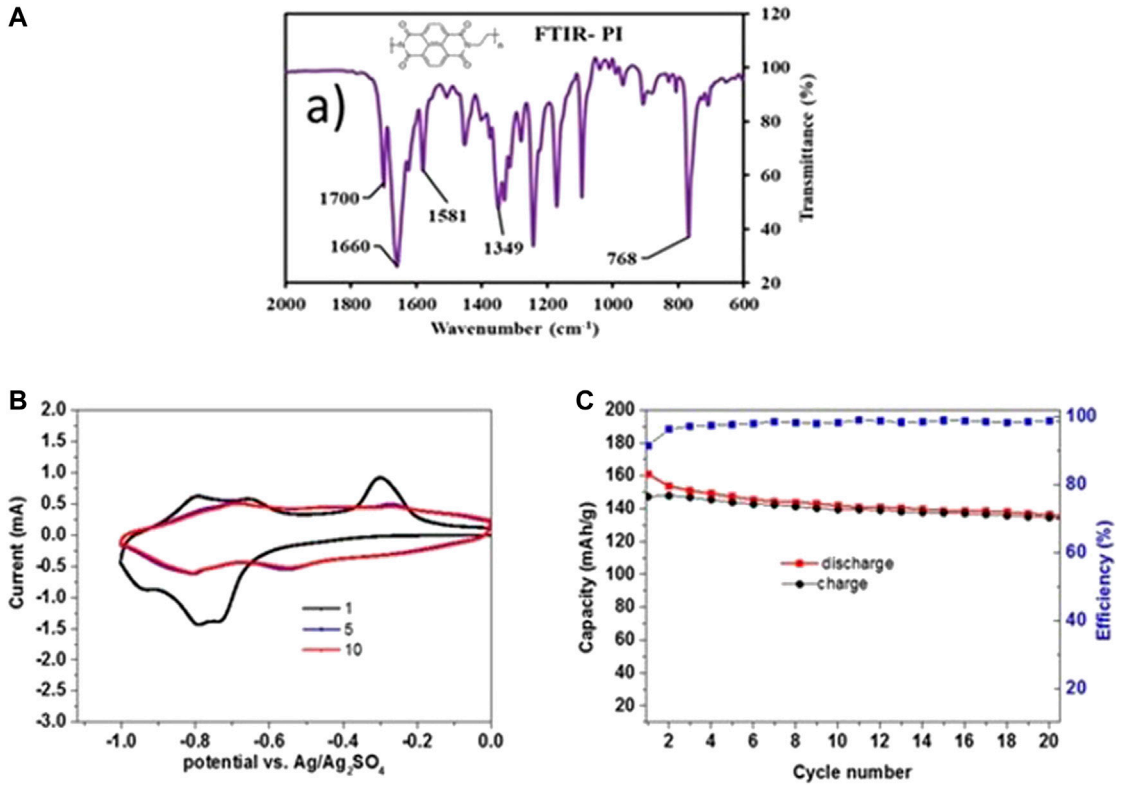

FIGURE 7 | (A) A FTIR spectrum of synthesized PI polymer (the insert shows the PI structure). **(B)** CVs were measured in saturated $NaClO_4$ electrolyte solutions with electrodes comprising PI as the active mass (the working electrodes, WE) and counter electrodes (CE) comprising NMO in excess, in three-electrodes cells at a scan rate of 0.1 mV/s in the voltage window of 0 to −1.0 V vs. Ag/Ag_2SO_4 (reference electrode) **(C)** Charge and discharge capacity values and cycling efficiency (as marked).

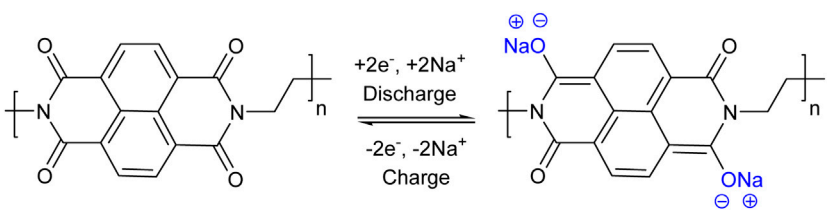

Scheme 1 | Redox reactions of PI anode in saturated $NaClO_4$ aqueous electrolyte solution.

electrolyte solution was characterized. The operation described schematically in **Figure 9** includes reversible Na ion de-insertion from NMO and its oxidation upon charging. In this stage, the PI is being coherently reduced in parallel and interacts with Na ions. In the spontaneous discharge process, sodium ions are inserted into the NMO cathode through a reduction process (through the external electricity flow of the battery) and the Na ions are desorbed from the PI (the PI is oxidized). This is a classical "rocking chair" mechanism, somewhat similar to that which works in Li ion batteries. The active sodium ions are initially included in the cathode. The charge step moves the ions from the cathode to the anode while the discharge processes return them back to the NMO cathode. With such a mechanism, the electrolyte solution's role is only to serve as thin ions conveyer between the electrodes. Hence, a minimal amount of electrolyte solution is needed for appropriate cell's operation, which helps to optimize the cells' parameters (specific capacity and energy density). Based on the characterization of the electrodes in half cells (voltammetric measurements, **Figure 5** and **Figure 8**), the balanced weight ratio between the cathode and the anode was around 3.0.

In order to confirm the validity of the cells' balance, galvanostatic experiments of three-electrodes' cells were carried out at 2C rate for up to 15 cycles, in which both electrodes could be measured in parallel. Stable performance

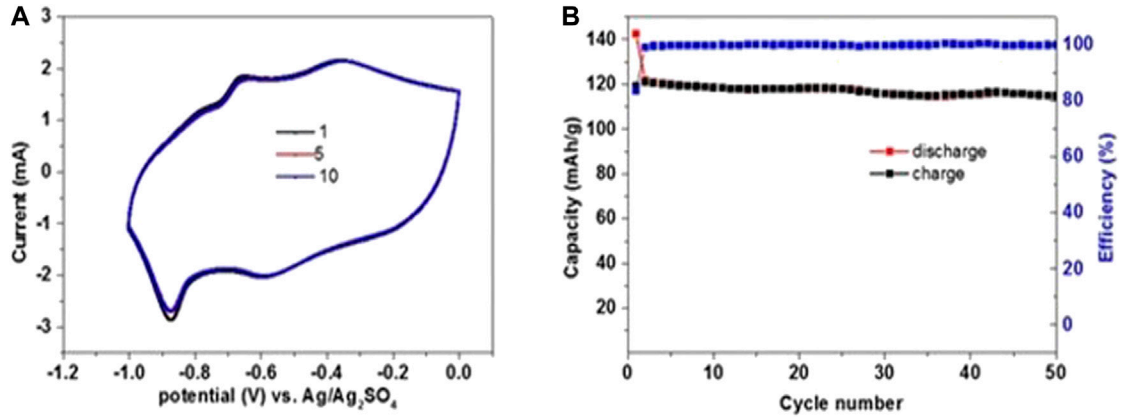

FIGURE 8 | (A) CVs of PI electrodes in 3 electrodes' cells, using counter electrodes containing excess of NMO and Ag/Ag_2SO_4 reference electrodes in saturated $NaClO_4$ electrolyte solution, scanning at 0.1 mV/s for 20 cycles (presented in Figure 7B) and then scanned at 0.5 mV/s in the voltage window of 0 to −1.0 V. **(B)** Charge (black) and discharge (red) capacities during anodic and cathodic scans at 0.5 mV/s up to 50 cycles, respectively, and cycling efficiency (blue).

was noticed for both NMO and PI electrodes (as can be seen in the supporting information, SI, **Supplementary Figure S1**). **Figure 10A** shows the rate capability for NMO/PI full cells operating galvanostatically in the voltage range of 0–1.7 V at a current rate of C/2, 1C, 2C, 5C, and 10C, up to six cycles at each rate. The corresponding stable discharge capacity values are 43, 41, 40, 36, and 28 mAh/g, respectively. The capacity is well retained upon cycling at 1C rate, as shown in **Figure 10A**. The charge–discharge profiles at different current rates are shown in **Figure 10B**. A stable capacity of 28 mAh/g (a reasonable value for such systems) is observed even at 10C rate, indicating the fast kinetics of both $Na_{0.44}MnO_2$ and PI electrodes in saturated aqueous $NaClO_4$ solution. As reported by Bu *et al.*, faster ionic and charge transfer kinetics was demonstrated in water-in-salt (WIS)-based electrolytes (17 m $NaClO_4$) for carbon-based supercapacitors (Bu et al., 2019). The voltage profiles of the cells show three inflections (degenerated plateaus) during charge/discharge reflecting properly the de-intercalation and intercalation processes of Na ions with the NMO as apparent from the CVs in **Figure 4** and **Figure 5**. The stability of these cells was further analyzed by subjecting them to prolonged cycling at different rates of C/2, 2C, and 5C, as presented in **Figure 11** and **Figure 12**. Average discharge capacities of 43.5, 41, and 35 mAh/g after 100, 430, and 2400 cycles, respectively, exhibit a reasonable stability. The efficiency was 96 and 98.8% at current rates of C/2 and 2C, respectively. The retention of capacity was 99.9% after 430 cycles at 2C rate (**Figure 11B**).

The charge and discharge voltage profiles per cycle nearly overlap during cycling at a fast 5C rate during prolonged cycling, as shown in **Figure 12B** for different cycles. These voltage profiles indicated no ohmic resistance during Na ion insertion and de-insertion in both electrodes. The discharge capacity was around 34 mAh/g with retention of 89.8% after 2,400 prolonged cycles with a coulombic efficiency of nearly 100% (see **Figure 12C**). The average voltage of 1.0 V was achieved for full cells with energy density around 24 Wh/kg, calculated based on the active materials weight of both PI and NMO electrodes. The prolonged cycling stability of 100%, indicating no water decomposition, may suggest the formation of metastable situation at the electrodes surfaces, thanks to the high concentration of the electrolyte solutions. The metastability leads to high overvoltage for releasing hydrogen and oxygen at the electrodes. A study of cells comprising $Na_{0.66}[Mn_{0.66}Ti_{0.34}]O_2$ cathode and $NaTi_2(PO_4)_3$ anode examined the advantage of WIS electrolyte, over conventional salt-in-water (SIW) solution using 1 M Na_2SO_4 solution. A high efficiency of 99.2% with better cycling stability and capacity retention was achieved with WIS, compared to

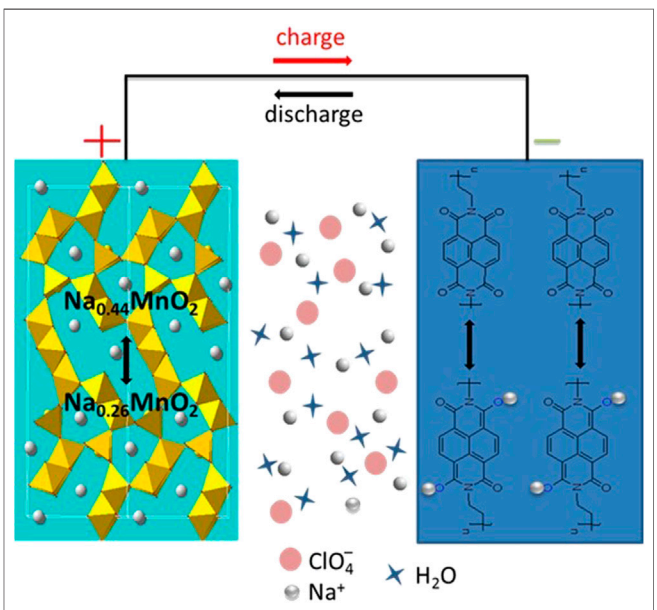

FIGURE 9 | A description of aqueous Na-ion battery with tunnel-type $Na_{0.44}MnO_2$ cathode and PI anode.

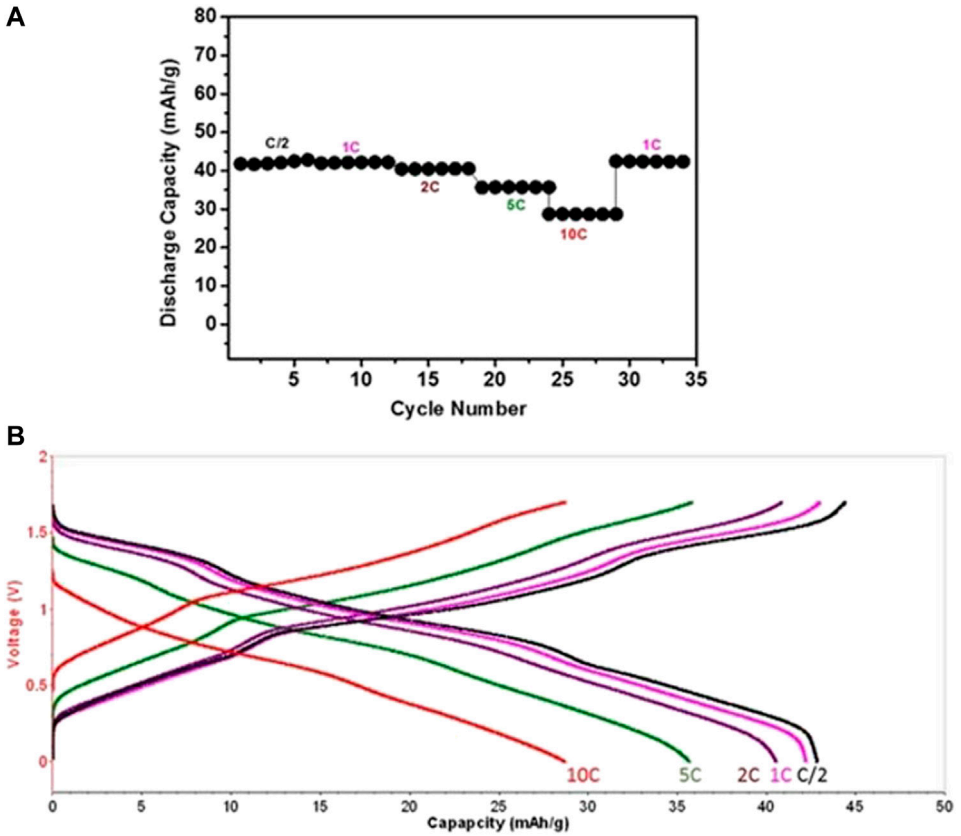

FIGURE 10 | (A) Representative plot of capacity vs. cycle number of balanced NMO-PI/saturated aqueous $NaClO_4$ electrolyte solution full cells operating galvanostatically between 0 and 1.7 V at C/2, 1C, 2C, 5C, and 10C (six cycles at each rate). **(B)** Corresponding sixth cycle charge–discharge voltage profiles of these full cells at different rates. 1C meaning a current density adjusted for full charge and discharge process within 1 h.

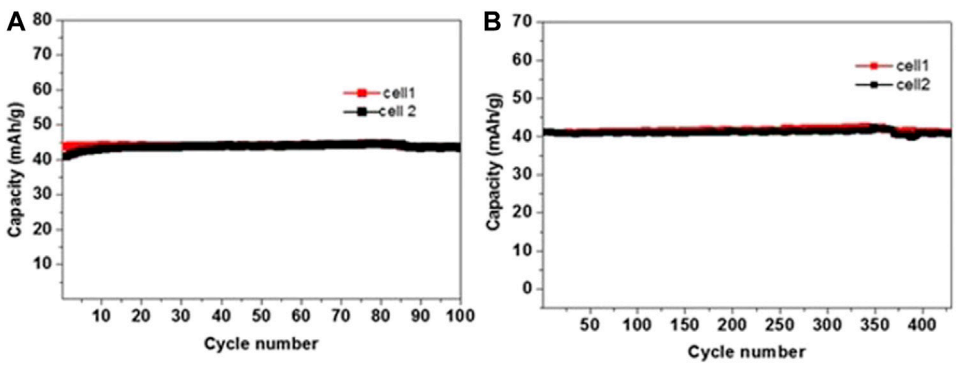

FIGURE 11 | Representative plots of discharge capacity for NMO-PI/saturated $NaClO_4$ solution full cells in long-term galvanostatic experiments, operating in the 0–1.7 V range at **(A)** C/2 and **(B)** 2C rate. The reproducibility is demonstrated by showing results from 2 cells in parallel experiments.

parallel experiments with 1 m Na_2SO_4 (SIW) solutions (Suo et al., 2017).

The effect of using saturated electrolyte solutions on the capacity losses and voltage fading of the cells described herein due to possible side reaction and material degradation processes was investigated by self-discharge analysis. Charged cells were held in solutions during several days and their OCV was measured, as presented in **Figure 13**. Initially, the cells were subjected to 10 cycles at 1C rate within the voltage window of 0–1.7 V, then charged at 1.7 V, and the voltage change was monitored. After four days, the cells were discharged to 0 V before undergoing five additional cycles. As shown in **Figure 13B**, the discharge capacity loss was 10.8% after four days

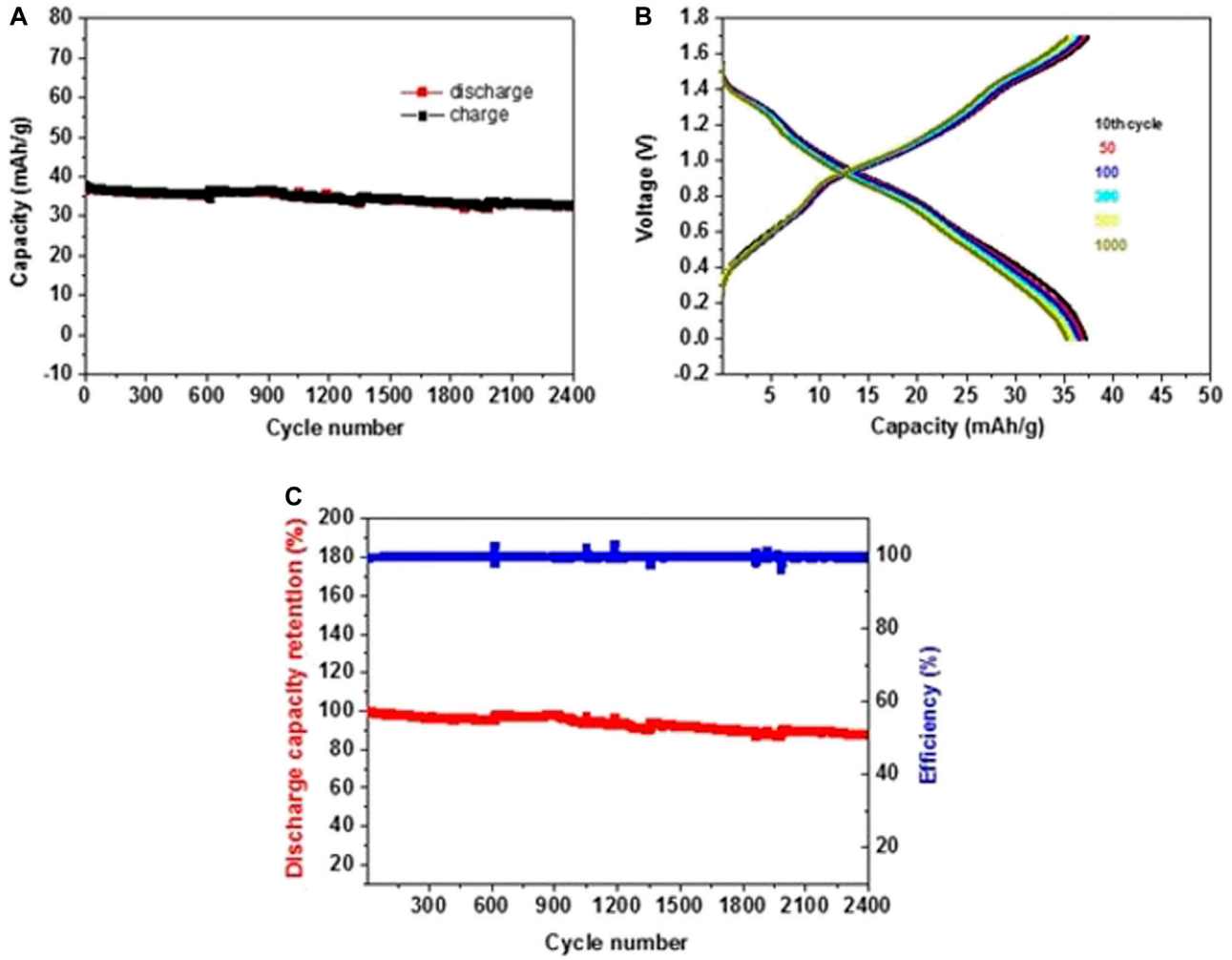

FIGURE 12 | (A) Galvanostatic charge–discharge capacity vs. cycle number at 5 C rate for NMO-PI/saturated $NaClO_4$ solution full cells operating in the range 0–1.7 V. **(B)** Charge–discharge profiles for different cycles. **(C)** Discharge capacity retention (red) and cycling efficiency (blue) vs. cycle number.

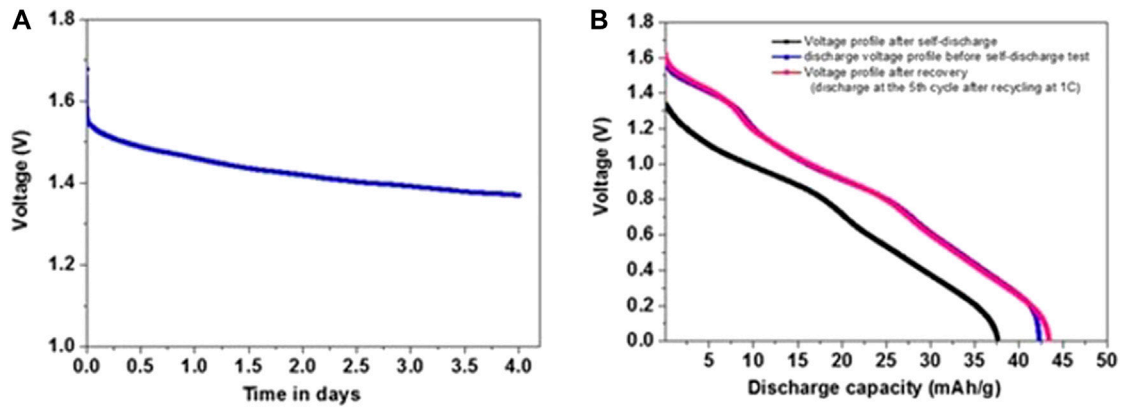

FIGURE 13 | (A) OCV changes of charged NMO/PI full cells held at 1.7 V after being cycled at 1C rate 10 times. **(B)** Representative discharge voltage-capacity profiles of these cells before the self-discharge experiment (in blue) and after being held at the charged state during 4 days in order to measure their self-discharge (black). The voltage profile in pink belongs to a typical discharge process (fifth cycle) of these cells upon their recycling after the end of the self-discharge experiment (storing the charged cells at OCV during 4 days).

at a charged state. The capacity could be fully recovered upon cycling after the self-discharge testing, as reflected in **Figure 13B**. These results indicate that the observed self-discharge is not related to any degradation of the electrodes. It can relate to current leaks in the cells. This phenomenon is still being explored.

CONCLUSION

In summary, $Na_{0.44}MnO_2$/polyimide (NMO/PI) aqueous Na ion batteries with high capacity retention for large energy storage applications were presented. The electrochemical performance of the tunnel-type NMO cathodes was studied in three-electrode cells. Low Mn ions dissolution from these cathodes was observed when saturated $NaClO_4$ electrolyte solution was used. A deliverable capacity of 38 mAh/g and a coulombic efficiency of 100% could be achieved for these NMO cathodes in the saturated solution, compared to the performance in 8 m $NaClO_4$ solution, a deliverable capacity of 29 mAh/g. The PI derivative showed excellent stability in the low potential range and a reversible capacity of 115 mAh/g could be obtained in the saturated electrolyte solutions.

Full cells with NMO cathodes and PI derivative anodes, with appropriate mass balance that takes into account the specific capacities ratio of the electrodes, were composed and tested. The NMO/PI full cells can operate at a voltage span of 1.7 V, delivering capacities of 43, 41, 35, and 28 mAh/g-cathode at C/2, 2C, 5C, and 10C, respectively. The fast rate capability of these full cells may result from better ionic and charge transfer kinetics that can be reached in the saturated $NaClO_4$ solutions. During 2,400 cycles at 5C rates, these cells demonstrated a capacity of 33 mAh/g-cathode with fully reversible charge and discharge voltage profiles, and a negligible ohmic drop. These cycling results indicate no dissolution of cations from the cathodes or any degradation of both electrodes during cycling. The low ohmic resistance means a very low hysteresis between the charge and discharge processes. The important consequence of that is excellent energy efficiency per cycle, which makes these systems really suitable for large energy storage. In prolonged cycling experiments, the capacity retention of these cells was nearly 90% with a coulombic efficiency of 100% after 2,400 cycles.

The high stability of the electrode materials without degradation and their interactions in saturated electrolyte media were further confirmed by maintaining cells at their charged state, namely, 1.7 V during several days. While showing 10% discharge capacity loss, upon resuming their cycling, a full capacity recovery and retention was demonstrated.

These cells comprise environmentally friendly and low-cost manganese oxides and organic-based materials, containing most abundant elements. Hence, we have demonstrated highly stable aqueous Na-ion battery technology, the rate capability and energy efficiency of which are excellent, which in turn makes it very suitable for large energy storage applications. Using highly concentrated electrolyte solutions for these systems helped to reach this high performance.

DATA AVAILABILITY STATEMENT

The original contributions presented in the study are included in the article/**Supplementary Material**, further inquiries can be directed to the corresponding author.

AUTHOR CONTRIBUTIONS

SM, AN, SL, and DA conceived the idea, designed experiments, and analyzed data. AN synthesized organic polyimide for anode material. SM analyzed data and wrote the manuscript. All authors contributed to the discussion.

FUNDING

A partial support for this work was obtained from the Israeli Ministry of Energy, from the Israeli Prime-Minister office, and the Israeli Committee for High Education (CHE) in the framework of the INREP project.

SUPPLEMENTARY MATERIAL

The Supplementary Material for this article can be found online at: https://www.frontiersin.org/articles/10.3389/fenrg.2020.615677/full#supplementary-material.

REFERENCES

Andrzejak, M., Mazur, G., and Petelenz, P. (2000). Quantum chemical results as input for solid state calculations: charge transfer states in molecular crystals. *J. Mol. Struct.* 527, 91–102. doi:10.1016/S0166-1280(00)00481-4

Armand, M., and Tarascon, J.-M. (2008). Building better batteries. *Nature* 451, 652–657. doi:10.1038/451652a

Barbieri, O., Hahn, M., Herzog, A., and Kötz, R. (2005). Capacitance limits of high surface area activated carbons for double layer capacitors. *Carbon N. Y.* 43, 1303–1310. doi:10.1016/j.carbon.2005.01.001

Bhosale, M. E., Chae, S., Kim, J. M., and Choi, J. Y. (2018). Organic small molecules and polymers as an electrode material for rechargeable lithium ion batteries. *J. Mater. Chem. A.* 6, 19885–19911. doi:10.1039/c8ta04906h

Bin, D., Wang, F., Tamirat, A. G., Suo, L., Wang, Y., Wang, C., et al. (2018). Progress in aqueous rechargeable sodium-ion batteries. *Adv. Energy Mater.* 8, 1–31. doi:10.1002/aenm.201703008

Brandt, A., and Balducci, A. (2014). Theoretical and practical energy limitations of organic and ionic liquid-based electrolytes for high voltage electrochemical double layer capacitors. *J. Power Sources* 250, 343–351. doi:10.1016/j.jpowsour.2013.10.147

Brandt, A., Pires, J., Anouti, M., and Balducci, A. (2013). An investigation about the cycling stability of supercapacitors containing protic ionic liquids as electrolyte components. *Electrochim. Acta.* 108, 226–231. doi:10.1016/j.electacta.2013.06.118

Bu, X., Su, L., Dou, Q., Lei, S., and Yan, X. (2019). A low-cost "water-in-salt" electrolyte for a 2.3 V high-rate carbon-based supercapacitor. *J. Mater. Chem. A.* 7, 7541–7547. doi:10.1039/c9ta00154a

Cao, X., Wang, L., Chen, J., and Zheng, J. (2018). A low-cost Mg2+/Na+ hybrid aqueous battery. J. Mater. Chem. A6, . 15762–15770. doi:10.1039/c8ta04930k

Chen, L., Bao, J. L., Dong, X., Truhlar, D. G., Wang, Y., Wang, C., et al. (2017). Aqueous Mg-ion battery based on polyimide anode and Prussian blue cathode. *ACS Energy Lett.* 2, 1115–1121. doi:10.1021/acsenergylett.7b00040

Chen, L., Li, W., Guo, Z., Wang, Y., Wang, C., Che, Y., et al. (2015). Aqueous lithium-ion batteries using O_2 self-elimination polyimides electrodes. *J. Electrochem. Soc.* 162, A1972–A1977. doi:10.1149/2.0101510jes

Chen, L., Li, W., Wang, Y., Wang, C., and Xia, Y. (2014). Polyimide as anode electrode material for rechargeable sodium batteries. *RSC Adv.* 4, 25369–25373. doi:10.1039/c4ra03473b

Comte, A. L., Chhin, D., Gagnon, A., Retoux, R., Brousse, T., and Belanger, D. (2015). Spontaneous grafting of 9,10-phenanthrenequinone on porous carbon as an active electrode material in an electrochemical capacitor in an alkaline electrolyte. *J. Mater. Chem. A.* 3, 6146–6156. doi:10.1039/c4ta05536e

Dall'Asta, V., Buchholz, D., Chagas, L. G., Dou, X., Ferrara, C., Quartarone, E., et al. (2017). Aqueous processing of $Na_{0.44}MnO_2$ cathode material for the development of greener Na-ion batteries. *ACS Appl. Mater. Interfaces.* 9, 34891–34899. doi:10.1021/acsami.7b09464

Dong, X., Chen, L., Liu, J., Haller, S., Wang, Y., and Xia, Y. (2016). Environmentally-friendly aqueous Li (or Na)-ion battery with fast electrode kinetics and super-long life. *Sci. Adv.* 2, 1–9. doi:10.1126/sciadv.1501038

Evanko, B., Yoo, S. J., Lipton, J., Chun, S. E., Moskovits, M., Ji, X., et al. (2018). Stackable bipolar pouch cells with corrosion-resistant current collectors enable high-power aqueous electrochemical energy storage. *Energy Environ. Sci.* 11, 2865–2875. doi:10.1039/c8ee00546j

Gheytani, S., Liang, Y., Jing, Y., Xu, J. Q., and Yao, Y. (2016). Materials chemistry A. *J. Mater. Chem. A.* 4, 395–399. doi:10.1039/c5ta07366a

Haüpler, B., Rössel, C., Schwenke, A. M., Winsberg, J., Schmidt, D., Wild, A., et al. (2016). Aqueous zinc-organic polymer battery with a high rate performance and long lifetime. *NPG Asia Mater.* 8, e283. doi:10.1038/am.2016.82

Hernández, G., Casado, N., Zamarayeva, A. M., Duey, J. K., Armand, M., Arias, A. C., et al. (2018). Perylene polyimide-polyether anodes for aqueous all-organic polymer batteries. *ACS Appl. Energy Mater.* 1, 7199–7205. doi:10.1021/acsaem.8b01663

Hu, Y., Ding, H., Bai, Y., Liu, Z., Chen, S., Wu, Y., et al. (2019). Rational design of a polyimide cathode for a stable and high-rate potassium-ion battery. *ACS Appl. Mater. Interfaces* 11, 42078–42085. doi:10.1021/acsami.9b13118

Huang, Y., Liu, J., Huang, Q., Zheng, Z., Hiralal, P., Zheng, F., et al. (2018). Flexible high energy density zinc-ion batteries enabled by binder-free MnO_2/reduced graphene oxide electrode. *npj Flex. Electron.* 21, 1–6. doi:10.1038/s41528-018-0034-0

Kang, J., Lim, T., Jeong, M. H., and Suk, J. W. (2019). Graphene papers with tailored pore structures fabricated from crumpled graphene spheres. *Nanomaterials* 9, 815. doi:10.3390/nano9060815

Khamsanga, S., Pornprasertsuk, R., Yonezawa, T., Mohamad, A. A., and Kheawhom, S. (2019). δ-MnO2 nanoflower/graphite cathode for rechargeable aqueous zinc ion batteries. *Sci. Rep.* 9, 8441. doi:10.1038/s41598-019-44915-8

Kim, D., Shin, G., Kang, Y. J., Kim, W., and Ha, J. S. (2013). Fabrication of a stretchable solid-state micro-supercapacitor array. *ACS Nano* 7, 7975–7982. doi:10.1021/nn403068d

Kim, H., Hong, J., Park, K. Y., Kim, H., Kim, S. W., and Kang, K. (2014). Aqueous rechargeable Li and Na ion batteries. *Chem. Rev.* 114, 11788–11827. doi:10.1021/cr500232y

Lee, M. H., Kim, S. J., Chang, D., Kim, J., Moon, S., Oh, K., et al. (2019). Toward a low-cost high-voltage sodium aqueous rechargeable battery. *Mater. Today.* 29, 26–36. doi:10.1016/j.mattod.2019.02.004

Li, L., Wu, Z., Yuan, S., and Zhang, X. B. (2014a). Advances and challenges for flexible energy storage and conversion devices and systems. *Energy Environ. Sci.* 7, 2101–2122. doi:10.1039/c4ee00318g

Li, X., Zhu, X., Liang, J., Hou, Z., Wang, Y., Lin, N., et al. (2014b). Graphene-supported $NaTi_2(PO_4)_3$ as a high rate anode material for aqueous sodium ion batteries. *J. Electrochem. Soc.* 161, A1181–A1187. doi:10.1149/2.0081409jes

Li, N., Chen, Z., Ren, W., Li, F., and Cheng, H. M. (2012). Flexible graphene-based lithium ion batteries with ultrafast charge and discharge rates. *PNAS.* 109, 17360–17365. doi:10.1073/pnas.1210072109

Li, S. (2017). Electrochemical stability of aluminum current collector in aqueous rechargeable lithium-ion battery electrolytes. *J. Appl. Electrochem.* 47, 839–853. doi:10.1007/s10800-017-1081-2

Li, S. Y., and Church, B. C. (2016). Effect of aqueous-based cathode slurry pH and immersion time on corrosion of aluminum current collector in lithium-ion batteries. *Mater. Corros.* 67, 978–987. doi:10.1002/maco.201608843

Li, W., Zhang, F., Xiang, X., and Zhang, X. (2017). High-efficiency Na-storage performance of a nickel-based ferricyanide cathode in high-concentration electrolytes for aqueous sodium-ion batteries. *ChemElectroChem* 4, 2870–2876. doi:10.1002/celc.201700776

Lim, H., Jung, J. H., Park, Y. M., Lee, H. N., and Kim, H. J. (2018). High-performance aqueous rechargeable sulfate- and sodium-ion battery based on polypyrrole-MWCNT core-shell nanowires and $Na_{0.44}MnO_2$ nanorods. *Appl. Surf. Sci.* 446, 131–138. doi:10.1016/j.apsusc.2018.02.021

Luo, J., Cui, W., He, P., and Xia, Y. (2010). Raising the cycling stability of aqueous lithium-ion batteries by eliminating oxygen in the electrolyte. *Nat. Chem.* 2, 760–765. doi:10.1038/nchem.763

Malka, D., Giladi, S., Hanna, O., Weitman, M., Cohen, R., Elias, Y., et al. (2019). Catechol-modified carbon cloth as hybrid electrode for energy storage devices. *J. Electrochem. Soc.* 166, A1147–A1153. doi:10.1149/2.0911906jes

Pang, G., Nie, P., Yuan, C., Shen, L., Zhang, X., Zhu, J., et al. (2014). Enhanced performance of aqueous sodium-ion batteries using electrodes based on the $NaTi_2(PO_4)_3$/MWNTs-$Na_{0.44}MnO_2$ system. *Energy Technol.* 2, 705–712. doi:10.1002/ente.201402045

Pognon, G., Brousse, T., and Bélanger, D. (2011). Effect of molecular grafting on the pore size distribution and the double layer capacitance of activated carbon for electrochemical double layer capacitors. *Carbon* 49, 1340–13488. doi:10.1016/j.carbon.2010.11.055

Pognon, G., Cougnon, C., Mayilukila, D., and Bélanger, D. (2012). Catechol-modified activated carbon prepared by the diazonium chemistry for application as active electrode material in electrochemical capacitor. *ACS Appl. Mater. Interfaces.* 4, 3788–3796. doi:10.1021/am301284n

Poonam, S., Sharma, K., Arora, A., and Tripathi, S. K. (2019). Review of supercapacitors: materials and devices. *J. Energy Storage.* 21, 801–825. doi:10.1016/j.est.2019.01.010

Sadeghi, S., and Javaran, E. J. (2019). Comparison of combining redox flow and lead-acid batteries with On-grid and stand-alone photovoltaic systems. *Environ. Prog. Sustain. Energy* 38, 1–10. doi:10.1002/ep.13182

Sauvage, F., Laffont, L., Tarascon, J. M., and Baudrin, E. (2007). Study of the insertion/deinsertion mechanism of sodium into $Na_{0.44}MnO_2$. *Inorg. Chem.* 46, 3289–3294. doi:10.1021/ic0700250

Shao, J., Li, X., Qu, Q., and Wu, Y. (2013). Study on different power and cycling performance of crystalline $K_xMnO_2{\cdot}nH_2O$ as cathode material for supercapacitors in Li_2SO_4, Na_2SO_4, and K_2SO_4 aqueous electrolytes. *J. Power Sources* 223, 56–61. doi:10.1016/j.jpowsour.2012.09.046

Shin, J., Seo, J. K., Yaylian, R., Huang, A., and Meng, Y. S. (2020). A review on mechanistic understanding of MnO_2 in aqueous electrolyte for electrical energy storage systems. *Int. Mater. Rev.* 65, 356–387. doi:10.1080/09506608.2019.1653520

Simon, P., and Gogotsi, Y. (2008). Materials for electrochemical capacitors. *Nat. Mater.* 7, 845–854. doi:10.1038/nmat2297

Song, W. J., Park, J., Kim, D. H., Bae, S., Kwak, M. J., Shin, M., et al. (2018). Jabuticaba-inspired hybrid carbon filler/polymer electrode for use in highly stretchable aqueous Li-ion batteries. *Adv. Energy Mater.* 8, 1–10. doi:10.1002/aenm.201702478

Song, Z., Zhan, H., and Zhou, Y. (2010). Polyimides: Promising energy-storage materials. *Angew. Chem. Int. Ed.* 49, 8444–8448. doi:10.1002/anie.201002439

Stoller, M. D., Park, S., Yanwu, Z., An, J., and Ruoff, R. S. (2008). Graphene-Based ultracapacitors. *Nano Lett.* 8, 3498–3502. doi:10.1021/nl802558y

Suo, L., Borodin, O., Wang, Y., Rong, X., Sun, W., Fan, X., et al. (2017). "Water-in-salt " electrolyte makes aqueous sodium-ion battery safe, green, and long-lasting. *Adv. Energy Mater.* 7, 1701189. doi:10.1002/aenm.201701189

Tang, C., Long, G., Hu, X., Wong, K.-W., Lau, W.-M., Fan, M., et al. (2014). Conductive polymer nanocomposites with hierarchical multi-scale structures via self-assembly of carbon-nanotubes on graphene on polymer-microspheres. *Nanoscale*, 6, 7877–7888. doi:10.1039/C3NR06056J

Tekin, B., Sevinc, S., Morcrette, M., and Demir-cakan, R. (2017). A new sodium-based aqueous rechargeable battery System: the special case of $Na_{0.44}MnO_2$/dissolved sodium polysulfide. *Energy technol.* 5, 2182–2188. doi:10.1002/ente.201700245

Toby, B. H. (2001). EXPGUI, a graphical user interface for GSAS. *Journal of Applied Crystallography* 2001 (34), 210. doi:10.1107/S0021889801002242

Wang, Y., Mu, L., Liu, J., Yang, Z., Yu, X., Gu, L., et al. (2015). A novel high capacity positive electrode material with tunnel-type structure for aqueous sodium-ion batteries. *Adv. Energy Mater.* 5, 1–8. doi:10.1002/aenm.201501005

Weissmann, M., Crosnier, O., Brousse, T., and Bélanger, D. (2012). Electrochemical study of anthraquinone groups, grafted by the diazonium chemistry, in different aqueous media-relevance for the development of aqueous hybrid electrochemical capacitor. *Electrochim. Acta.* 82, 250–256. doi:10.1016/j.electacta.2012.05.130

Wen, Y. H., Shao, L., Zhao, P. C., Wang, B. Y., Cao, G. P., and Yang, Y. S. (2017). Carbon coated stainless steel mesh as a low-cost and corrosion-resistant current collector for aqueous rechargeable batteries. *J. Mater. Chem. A.* 5, 15752–15758. doi:10.1039/c7ta03500d

Whitacre, J. F., Tevar, A., and Sharma, S. (2010). $Na_4Mn_9O_{18}$ as a positive electrode material for an aqueous electrolyte sodium-ion energy storage device. *Electrochem. commun.* 12, 463–466. doi:10.1016/j.elecom.2010.01.020

Xu, C., Du, H., Li, B., Kang, F., and Zeng, Y. (2009a). Asymmetric activated carbon-manganese dioxide capacitors in mild aqueous electrolytes containing alkaline-earth cations. *J. Electrochem. Soc.* 156, A435–A441. doi:10.1149/1.3106112

Xu, C., Du, H., Li, B., Kang, F., and Zeng, Y. (2009b). Reversible insertion properties of zinc ion into manganese dioxide and its application for energy storage. *Electrochem. Solid-State Lett.* 12, A61–A65. doi:10.1149/1.3065967

Yang, C., Ji, X., Fan, X., Gao, T., Suo, L., Wang, F., et al. (2017a). Flexible aqueous Li-ion battery with high energy and power densities. *Adv. Mater.* 29, 1–8. doi:10.1002/adma.201701972

Yang, J., Hu, C., Wang, H., Yang, K., Liu, J. B., and Yan, H. (2017b). Review on the research of failure modes and mechanism for lead–acid batteries. *Int. J. Energy Res.* 41, 336–352. doi:10.1002/er.3613

Yolshina, L. A., Yolshina, V. A., Yolshin, A. N., and Plaksin, S. V. (2015). Novel lead-graphene and lead-graphite metallic composite materials for possible applications as positive electrode grid in lead-acid battery. *J. Power Sources* 278, 87–97. doi:10.1016/j.jpowsour.2014.12.036

Yu, L., and Chen, G. Z. (2019). Ionic liquid-based electrolytes for supercapacitor and supercapattery. *Front. Chem.* 7, 1–15. doi:10.3389/fchem.2019.00272

Conflict of Interest: The authors declare that the research was conducted in the absence of any commercial or financial relationships that could be construed as a potential conflict of interest.

frontiers in Energy Research

REVIEW
published: 12 February 2021
doi: 10.3389/fenrg.2020.602918

Divalent Nonaqueous Metal-Air Batteries

Yi-Ting Lu[1,2], *Alex R. Neale*[1], *Chi-Chang Hu*[2] *and Laurence J. Hardwick*[1]*

[1]*Department of Chemistry, Stephenson Institute for Renewable Energy, University of Liverpool, Liverpool, United Kingtom,*
[2]*Department of Chemical Engineering, National Tsing Hua University, Hsin-Chu, Taiwan*

In the field of secondary batteries, the growing diversity of possible applications for energy storage has led to the investigation of numerous alternative systems to the state-of-the-art lithium-ion battery. Metal-air batteries are one such technology, due to promising specific energies that could reach beyond the theoretical maximum of lithium-ion. Much focus over the past decade has been on lithium and sodium-air, and, only in recent years, efforts have been stepped up in the study of divalent metal-air batteries. Within this article, the opportunities, progress, and challenges in nonaqueous rechargeable magnesium and calcium-air batteries will be examined and critically reviewed. In particular, attention will be focused on the electrolyte development for reversible metal deposition and the positive electrode chemistries (frequently referred to as the "air cathode"). Synergies between two cell chemistries will be described, along with the present impediments required to be overcome. Scientific advances in understanding fundamental cell (electro)chemistry and electrolyte development are crucial to surmount these barriers in order to edge these technologies toward practical application.

Keywords: metal-air batteries, divalent cations, magnesium batteries, calcium batteries, metal electroplating, oxygen electrochemistry

OPEN ACCESS

Edited by:
Jian Liu,
University of British Columbia Okanagan, Canada

Reviewed by:
Liqiang Mai,
Wuhan University of Technology, China
Vincenzo Baglio,
National Research Council (CNR), Italy

***Correspondence:**
Laurence J. Hardwick
hardwick@liverpool.ac.uk

Specialty section:
This article was submitted to Electrochemical Energy Conversion and Storage, a section of the journal Frontiers in Energy Research

Received: *04 September 2020*
Accepted: *20 November 2020*
Published: *12 February 2021*

Citation:
Lu Y-T, Neale AR, Hu C-C and Hardwick LJ (2021) Divalent Nonaqueous Metal-Air Batteries. Front. Energy Res. 8:602918. doi: 10.3389/fenrg.2020.602918

INTRODUCTION

Energy storage technologies are under extensive investigation because they could contribute towards resolving a major challenge encountered by modern society, that is, the increasing demand for energy. Batteries can be used to achieve this goal by storing energy from intermittent renewable energy sources (such as solar and wind) and releasing the energy at the point of use when required. Lithium-ion batteries are the most advanced technology, which can store and deliver energy through thousands of cycles or even more (Li et al., 2020b; Ng et al., 2020). However, though enormous progress has been made improving specific energy (Wh kg^{-1}) and reducing costs of Li-ion over the past decade, the specific energy of this cell chemistry is nearing its theoretical limit. Therefore, alternative battery chemistries such as metal-air batteries are becoming attractive for their much higher theoretical specific energies than those of Li-ion, as shown in **Table 1**. Much attention has been focused on the Li-air cell since Abraham et al. reintroduced the concept (Abraham and Jiang, 1996), and Bruce's group demonstrated that lithium peroxide (Li_2O_2) could be oxidized from the cathode (Ogasawara et al., 2006). Since then, Li and its analogs such as Na and K have been studied to make metal-air batteries (Hartmann et al., 2013; Ren and Wu, 2013; Luo et al., 2019b; Gilmore and Sundaresan, 2019; Li et al., 2020a; Ha et al., 2020; Han et al., 2020; Hu et al., 2020). Until now, many issues remain unsolved for these metal-air batteries. For example, Li, Na, and K anodes are plagued with poor reversibility because of their high reactivity with the electrolyte and the severe dendrite formation, which may trigger short circuits within the cell and even lead to serious fires or explosions

TABLE 1 | Theoretical specific energies and cell voltages for various nonaqueous metal-air batteries and conventional Li-ion batteries.

Cell chemistry	Cell voltage (V)	Theoretical specific energy (Wh kg^{-1})
Li-ion: $Ni_{0.8}Mn_{0.1}Co_{0.1}O_2 + LiC_6 \rightarrow LiNi_{0.8}Mn_{0.1}Co_{0.1}O_2 + C_6$	3.9	617
Li-O_2	2.96 (Li_2O_2)	3,456 (Li_2O_2)
Na-O_2	2.33 (Na_2O_2)	1,602 (Na_2O_2)
	2.27 (NaO_2)	1,105 (NaO_2)
K-O_2	2.20 (K_2O_2)	1,070 (K_2O_2)
	2.48 (KO_2)	935 (KO_2)
Mg-O_2	2.95 (MgO)	3,921 (MgO)
	2.94 (MgO_2)	2,801 (MgO_2)
Ca-O_2	3.13 (CaO)	2,989 (CaO)
	3.38 (CaO_2)	2,515 (CaO_2)
Zn-O_2	1.65 (ZnO)	1,086 (ZnO)

Chemical formula of primary discharge product shown in brackets.

TABLE 2 | Theoretical capacities (gravimetric and volumetric), redox potentials under standard aqueous conditions, and abundance of various metal anodes. Abundance values are taken from reference (Haynes, 2014).

Metal anode	Redox potential (V vs. SHE)	Gravimetric capacity (mAh g^{-1})	Volumetric capacity (mAh cm^{-3})	Abundance in earth's crust (ppm by mass)
Li	−3.04	3,860	2,062	20
Na	−2.71	1,166	1,129	23,600
K	−2.90	685	591	20,900
Mg	−2.37	2,205	3,832	23,300
Ca	−2.87	1,337	2,073	41,500
Zn	−0.80	820	5,851	70

(Yu et al., 2017; Hardwick and De León, 2018; Xiao et al., 2018). Some strategies may improve the cyclability of these alkali metals; for instance, Liu and coworkers performed a cell-level analysis to provide suggestions that integrate the best material properties with optimal cell design parameters. Following these design tips, a lithium-metal cell having specific energy beyond 500 Wh kg^{-1} can be achieved with good cycling (Liu et al., 2019). Jiao's group demonstrated stable Na cycling with an average Coulombic efficiency of 97% over 400 cycles by adding sodium hexafluoroarsenate ($Na[AsF_6]$) as an additive in organic carbonate-based electrolytes (Wang et al., 2019b). Xu's group fabricated a SnO_2-coated porous carbon nanofiber as the host for K metal anodes, wherein SnO_2 facilitates uniform K nucleation and deposition to suppress the dendritic growth of K (Zhao et al., 2020). Such design of a K host enabled dendrite-free K deposition/stripping with ultralong cycling for over 1700 h.

More recently, divalent metal anodes (Mg, Ca) have received increased attention due to their natural abundance, low cost, high theoretical capacity, low redox potential (see **Table 2**), and anticipated improved safety. Note that literature about the electrochemistry of Be, Sr, and Ba is rarely seen (Leisegang et al., 2019); to the best of our knowledge, demonstration of metal-air cells using these metals has not so far been reported. Beyond the Group 2 elements, Cu has a comparably high reduction potential (Cu^{2+}/Cu, 0.34 vs. SHE), and the resultant cell voltage is not comparable to those common anodes Li, Na, and K and therefore would be an impractical battery chemistry. Zn is mainly applied in aqueous rechargeable Zn-air battery chemistries because of its high theoretical specific energy and safety (Lu et al., 2017; Fu et al., 2019). Conversely, research into the nonaqueous Zn-air battery is still quite limited (Gelman et al., 2019; Chen et al., 2020). Some works have studied the Zn deposition in nonaqueous electrolytes (Liu et al., 2016); however, nonaqueous Zn-ion batteries, rather than nonaqueous Zn-air, are the primary subjects of these recent investigations (Han et al., 2016; Zhang et al., 2019). Therefore, this work focuses primarily on the electrochemistry of metallic Mg and Ca and their use in metal-air batteries. Furthermore, both Mg and Ca are thought to have lower propensity toward dendrite formation during battery cycling, possibly resulting from their lower self-diffusion barrier for adatoms during the plating process (Jäckle et al., 2018; Ponrouch et al., 2019; Biria et al., 2020). In addition, divalent metal-air batteries have superior theoretical specific energies compared to Na-air and K-air and can be comparable to Li-air, as summarized in **Table 1**. Additionally, the natural abundance of Mg and Ca greatly outweighs that of Li (**Table 2**), indicating that lower costs per unit energy stored could be more readily achieved for Mg and Ca (for assumed similarly performing practical systems). Despite these advantages, realizing divalent metal-air batteries using earth-abundant anodes still remains rather challenging with respect to all aspects of the cell configuration, the anode,

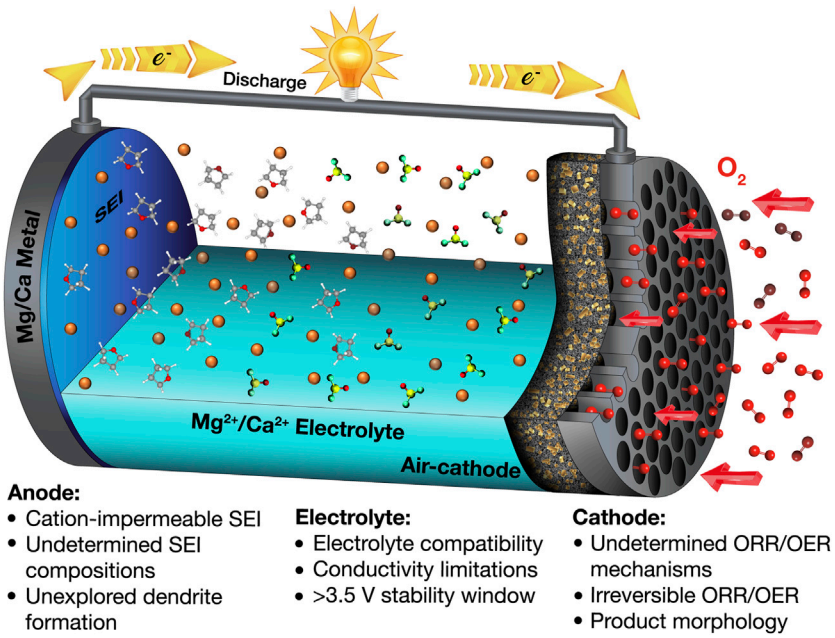

FIGURE 1 | Schematic of a discharging Mg/Ca-O_2 cell and the challenges for nonaqueous alkaline-earth metal-air batteries.

cathode, and electrolyte, as summarized in **Figure 1**. By comparison to monovalent Li^+/Na^+-based electrolytes, the higher charge density of divalent Mg^{2+}/Ca^{2+} cations yields increased interaction strength with counter-anion and surrounding environment and, thus, can inhibit solubilities, ionic transport/conductivity, and electrochemical rate capability in conventional solvent media. In terms of the anode, the solid electrolyte interphase (SEI) formed spontaneously on Mg and Ca metals is mostly impermeable to the cation in many conventional electrolyte materials, unlike the SEI on Li, Na, and K metal anodes, hampering the deposition/dissolution processes (Muldoon et al., 2014; Yao et al., 2019). Regarding the air cathode, the discharge products (MO and/or MO_2, where M = Mg, Ca) generated in the oxygen reduction reaction (ORR) are usually electrochemically very stable and electrically insulating and therefore cannot be decomposed without significant applied overpotentials via the oxygen evolution reaction (OER) upon charging (Shiga et al., 2013; Reinsberg et al., 2016b; Smith et al., 2016; Li et al., 2017; Shiga et al., 2017). For the electrolyte, the most important issue is its mutual compatibility with both electrode interfaces (Hardwick and De León, 2018). Therefore, an electrolyte with a wide electrochemical window (i.e., good stability against electrochemical oxidation and reduction) is highly desirable. However, at present, an electrolyte that allows high-efficiency electrochemical reactions on both the anode (negative electrode) and cathode (positive electrode) is yet to be developed. One strategy would be using Mg^{2+}/Ca^{2+} permeable membranes to separate the anolyte and catholyte compartments, as can be seen in other metal-air systems (Leng et al., 2015; Liang and Hayashi, 2015; Hwang et al., 2016), although extra cost, technical challenges, and rate capability of the cell need to be considered. On the other hand, issues concerning CO_2/moisture crossover will require consideration when practical cells are fabricated.

This review will critically discuss advances in the electrolyte development for the electrochemistry at both the anode and cathode for Mg/Ca-O_2 batteries. Starting from the development of electrolytes for reversible divalent metal deposition, various established solution systems are reviewed. Although most of these electrolyte formulations are originally designed for reversible Mg/Ca deposition or rechargeable Mg/Ca-ion batteries, some can be possible candidates to accommodate suitable oxygen electrochemistry on the cathode after modification. On the other hand, the investigations concerning the cathode electrochemistry of divalent cations that have been reported in various electrolytes are also explored. Insights into the potential ORR/OER mechanisms can be gleaned by applying various electrochemical/material characterizations. A further aspect of divalent metal-air batteries that may become critical, similar to challenges within Li-air cells, is the use of redox mediators that may address the challenge of irreversible ORR/OER. Hence, by employing an efficient redox mediator that provides an alternate lower energy pathway toward oxidation of discharge products, a rechargeable metal-air battery could be achieved with high round-trip efficiency and avoid likely decomposition reactions commonly observed at large overpotentials. Divalent metal-air battery research is still in its infancy, and most of the recent works only target the processes at one electrode interface. Therefore, this review will discuss what has been reported previously for the anode and cathode, respectively, and aims to inspire possible future research directions for the full divalent metal-air cell (and/or battery).

ELECTROLYTE DEVELOPMENT FOR METAL ELECTRODEPOSITION

Electrolyte development for divalent cation-based metal-air batteries creates different challenges from the analogous monovalent alkali metals, primarily attributed to the nature of divalent cations. Owing to their high charge density (i.e., chemical hardness), divalent cations suffer from significantly stronger cation-anion (ion pairing) and cation-solvent interactions, resulting in lower cation mobility and higher energy penalty for desolvation during the process of electroplating (Tchitchekova et al., 2017). Much of the electrolyte development for Mg- and Ca-based electrolytes has concerned the stable plating and stripping processes at the metal anodes. This work and the current state of the art are explored and discussed in the following sections. Furthermore, the realization of an electrolyte formulation with suitable properties for good performance at the anode, as well as at the air cathode, is likely to prove a serious challenge. Consideration is given to the applicability of these systems for use at the air cathodes, and recommendations made for systems deserve further investigations or considerable modifications before use.

Magnesium Metal

Grignard Reagents for Magnesium Deposition

Early research on Mg^{2+}-containing electrolytes was predominantly focused on the electrodeposition of Mg metal. The combination of simple Mg salts (magnesium bromide, ethoxide, methoxide, perchlorate, and thiocyanate) and commonly used solvents (acetonitrile, aniline, benzonitrile, bromoethane, dimethylaniline, ether, formamide, o-toluidine, and pyridine) did not result in any Mg electrodeposition. By contrast, the use of organomagnesium halides (so-called Grignard reagent, RMgX, R = alkyl or aryl group and X = halide like Cl or Br) in ethereal solutions enabled the electroplating of Mg (Overcash and Mathers, 1933). Connor and coworkers investigated the Mg electrodeposition in Grignard reagents, wherein the deposit obtained from Grignard reagent ethylmagnesium bromide (EtMgBr in diethyl ether, 2.5 M) contained 71% Mg (Connor et al., 1957). Although these deposits were white and metallic, they were not pure and very brittle and the reversibility of the Mg plating process was not explored in this article. On the other hand, it could be concluded that this Grignard reagent as a deposition bath is unsatisfactory because of the irreversible deposition, byproducts, and the short life of the Grignard solution. More recently, Liebenow reported the reversible deposition of Mg on Ag and Au substrates using EtMgBr in tetrahydrofuran (THF) (Liebenow, 1997). Conversely, at Ni and Cu substrates, great losses of electrochemically active Mg were observed, indicating the substrate-dependent reversibility of Mg plating in this class of electrolyte. Even though the reversible Mg plating was observed, the EtMgBr/THF electrolyte had low ionic conductivity and poor anodic stability, rendering it unsuitable in full-cell applications. Some studies have studied the direct use of Grignard reagents for Mg deposition (Haas and Gedanken, 2008; Guo et al., 2010; Zhao et al., 2011; Cheng et al., 2013; Chang et al., 2015). However, their limited anodic stability remains a major issue, which precludes practical applications.

Organomagnesium with Aluminum- or Boron-Based Lewis Acid for Magnesium Deposition

Apart from pure Grignard-type electrolytes (RMgX in ethereal solution), other organomagnesium-based systems have also been extensively studied, and, for instance, the combination of organomagnesium (MgR_2 or RMgX) as Lewis bases with aluminum- or boron-based Lewis acids (Liebenow et al., 2000; Muldoon et al., 2012; Carter et al., 2014; Zhu et al., 2014; Dongmo et al., 2020). Brenner found that the addition of boron-containing compounds (boranes, alkylboranes, and boron halides) to Grignard reagents improves the Mg deposition, although a small amount of B could be codeposited with Mg (Brenner, 1971; Brenner and Sligh, 1971). Later, Gregory and coworkers made a breakthrough and showed that the addition of aluminum halides, which are less expensive and less toxic than boron-type compounds, to the Grignard solutions resulted in high current efficiencies of deposition and gave good Mg deposits, with the purity higher than 99.9% (Gregory et al., 1990). In this work, the RMgCl-$AlCl_3$/THF (R = methyl, ethyl, and butyl) electrolytes were prepared at various ratios of RMgCl:$AlCl_3$, and all gave high Coulombic efficiencies (over 90%) and bright, crystalline deposits. This work also demonstrated a simple synthesis of magnesium organoborates for the first time. Based on these exciting improvements as a result of combining the Lewis acid and Lewis base, many efforts have been made to design new aluminum- and boron-based Mg electrolytes and a variety of well-performing systems have been invented. For example, Aurbach's group optimized the PhMgCl-$AlCl_3$/THF (Ph = phenyl group) electrolyte, which exhibited 100% reversibility combined with oxidative stability of approximately 3 V vs. Mg metal for the anodic scan (Mizrahi et al., 2008). Guo and coworkers reported the Mes_3B-$(PhMgCl)_2$/THF electrolyte (Mes = 3,5-dimethylphenyl), which showed greater anodic stability up to 3.5 V vs. Mg metal (**Figure 2A-i**), leading to almost 100% Coulombic efficiency for Mg deposition (Guo et al., 2012). Also, cyclic voltammograms (CVs) of Mes_3B-$(PhMgCl)_2$/THF electrolyte on various electrodes revealed that the anodic stability could reach up to 3 V (vs. Mg) at Pt, Ni, and Al electrodes, enabling a large operation window with such current collector materials (**Figure 2A-ii**).

Magnesium Halide-Based Electrolytes for Magnesium Deposition

Another emerging class of Mg electrolytes is the magnesium halide-based electrolyte (Doe et al., 2014; Canepa et al., 2015; Ha et al., 2016; See et al., 2017; Hegemann et al., 2019). Replacing the organomagnesium, organoborate- and organoaluminate-type electrolytes with inorganic magnesium halide can be more favorable for practical Mg rechargeable batteries since the nucleophilic organic ligands in the former materials can be too reactive and unstable. The use of magnesium halide can be dated back to 1957. Conner and coworkers found that 2.5 M $MgBr_2$/diethyl ether as the electrolyte yielded dark and brittle Mg deposits, with the purity being 60–70%, whereas a metallic Mg

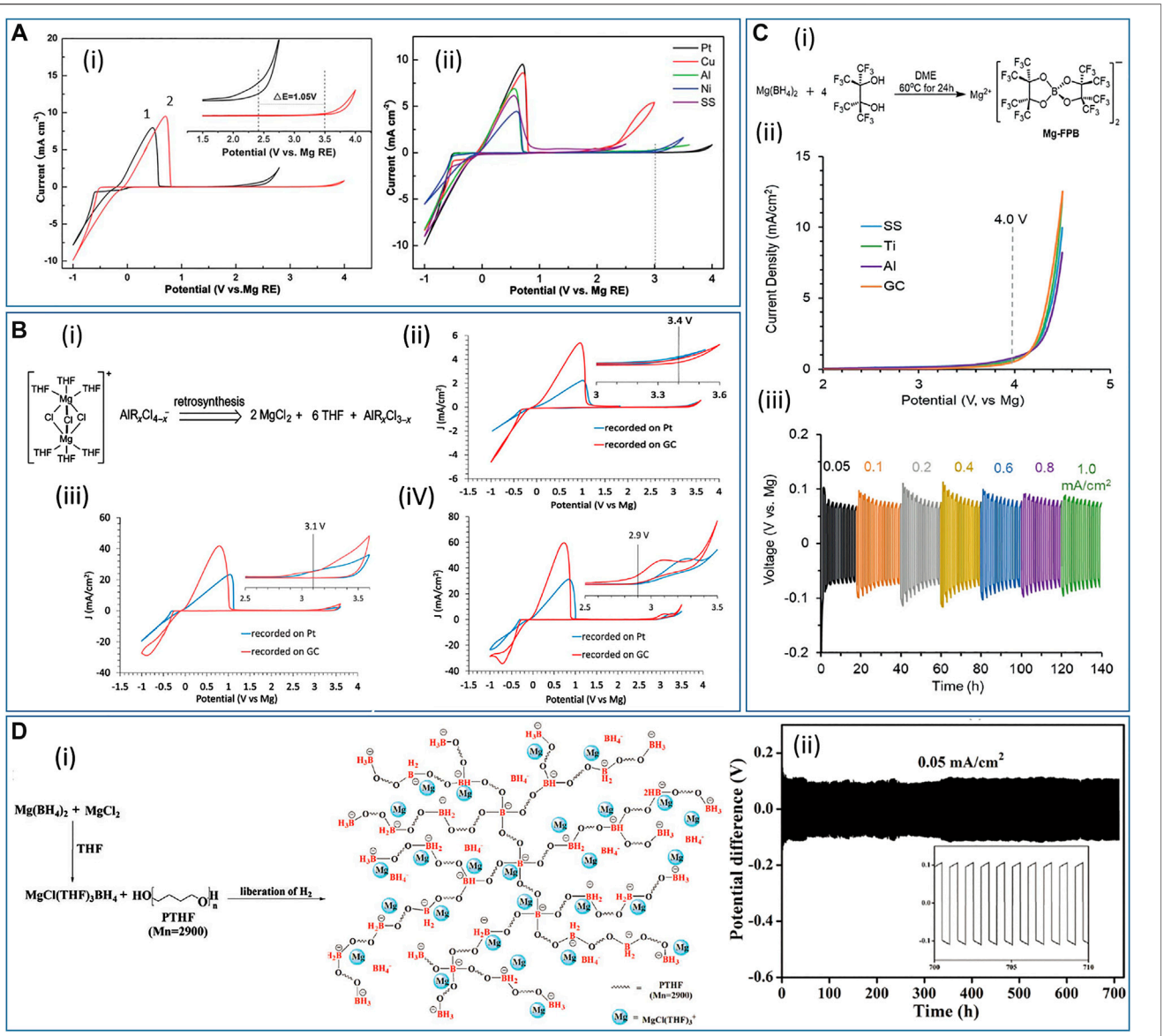

FIGURE 2 | (A-i) Cyclic voltammograms of Pt electrodes at 50 mV s^{-1} in **(1)** 0.4 M Mes_3B-PhMgCl and 2) 0.5 M Mes_3B-$(PhMgCl)_2$. Inset is an enlargement of the 1.5–4 V region. **(A-ii)** Cyclic voltammograms of Mes_3B-$(PhMgCl)_2$/THF on several working electrodes. Reproduced with permission from (Guo et al., 2012). **(B-i)** Retrosynthesis of electroactive $[(\mu\text{-}Cl)_3Mg_2(THF)_6]^+$ species. Cyclic voltammograms of **(B-ii)** $MgCl_2$-$AlCl_3$/THF, (B-iii) $MgCl_2$-$AlPh_3$/THF, and (B-iV) $MgCl_2$-$AlEtCl_2$/THF at 50 mV s^{-1} on GC and Pt. All insets show the enlargement of the oxidation region. Reproduced with permission from (Liu et al., 2014). **(C-i)** Synthesis of Mg-FPB. **(C-ii)** Linear sweep voltammograms of Mg-FPB at 50 mV s^{-1} on different working electrodes. **(C-iii)** Mg plating/stripping at current densities from 0.05 to 1 mA cm^{-2} in Mg/0.5 M Mg-FPB (in diglyme)/Mg symmetric cell. Reproduced with permission from (Luo et al., 2019a). **(D-i)** Synthetic route of PTB-GPE based on the reaction of Mg $[BH_4]_2$ with $MgCl_2$ and PTHF. **(D-ii)** Mg plating/stripping at 0.05 mA cm^{-2} over 700 h in Mg/PTB@GF-GPE/Mg symmetric cell. Reproduced with permission from (Du et al., 2019).

deposit with a purity of 90% was observed when a small amount of $Li[BH_4]$ was added to the $MgBr_2$/ether electrolyte (Connor et al., 1957). Another Mg electrolyte of $MgBr_2$/ether with the addition of $Li[AlH_4]$ also showed enhanced Mg deposition. In this solution, the Mg deposit coexisted with Al as an alloy, with Al making up 1–10% of the deposited layer. On the other hand, early attempts to apply $MgCl_2$ as the source of Mg were studied by Aurbach's group and the first use of $MgCl_2$-$AlCl_3$/THF electrolyte was proposed (Viestfrid et al., 2005). In this study, the resulting CV exhibited a Coulombic efficiency of 34% and a large cycling overpotential over 1 V. The same group claimed in a later work that enhancing the electrochemical performance of Mg deposition and dissolution could be achieved by an electrochemical conditioning process consisting of a repeated cyclic voltammetry treatment (Shterenberg et al., 2014). However, such a conditioning process is not reported in many other publications. The explanation is probably related to contaminants (e.g., water, oxygen, and reactive organic

molecules) that affect the electrochemistry, giving rise to poor Mg deposition behaviors (He et al., 2017). On the other hand, a dimer species $[(\mu\text{-Cl})_3Mg_2(THF)_6]^+$ has been identified as the active species in electrochemically active electrolytes derived from organomagnesium precursors with Lewis acids in THF (Pour et al., 2011; Guo et al., 2012). In 2014, based on a retrosynthesis rationale (**Figure 2B-i**), Liu's group designed a simple synthesis that produces the electrochemically active dimer $[(\mu\text{-Cl})_3Mg_2(THF)_6]^+$ in THF as electrolytes (Liu et al., 2014). In this work, $MgCl_2$ was used as the Mg source in combination with various aluminum-based Lewis acids ($AlCl_3$, $AlPh_3$, $AlEtCl_2$), and these three electrolytes revealed Coulombic efficiencies above 90%. The $MgCl_2$-$AlCl_3$ electrolyte showed improved oxidation stability (3.4 V vs. Mg, **Figure 2B-ii**) compared to $MgCl_2$-$AlPh_3$ (3.1 V, **Figure 2B-iii**) and $MgCl_2$-$AlEtCl_2$ (2.9 V, **Figure 2B-iV**). Nevertheless, $MgCl_2$-$AlCl_3$ had a low conductivity (0.26 mS cm^{-1}) and poor solubility (0.04 M), whereas $MgCl_2$-$AlPh_3$ and $MgCl_2$-$AlEtCl_2$ displayed better conductivities (2.96 and 6.99 mS cm^{-1}, respectively) and solubilities (0.43 and 0.67 M, respectively). Although each of the electrolyte formulations had some disadvantages, it is suggested that properties of the $MgCl_2$-AlR_xCl_{3-x} electrolytes, including anodic stability, conductivity, and solubility, can be modulated by the Lewis acid components.

Ionic Liquids for Magnesium Deposition

Mg deposition in ionic liquids (ILs) has also been under intense investigation due to their negligible vapor pressure, nonflammability, moderate ionic conductivity, good thermal stability, and electrochemical stability (Abdallah et al., 2012). For example, Morita's group reported an optimized cation structure of imidazolium-based ILs as "ionic solvents" to accommodate the Grignard reagent MeMgBr/THF complex (Kakibe et al., 2010). Introducing a methyl substituent group at the 2-position of the imidazolium ring cation can suppress the reaction of imidazolium cation with MeMgBr, stabilizing the electrolyte formulation. The authors demonstrated that utilizing an asymmetric structure of imidazolium cation, thereby lowering viscosity and increasing ionic conductivity, leads to the improved reversibility of Mg deposition. The optimal Coulombic efficiency in this work was 71%, and the electrochemical window had a range between −1 and 3.7 V (vs. Mg). Later, the same group studied binary IL electrolytes $[DEME][TFSI]_n[FSI]_{1-n}$ (DEME = N,N-diethyl-N-methyl-N-(2-methoxyethyl)ammonium, TFSI = bis{(trifluoromethyl)sulfonyl}imide, FSI = bis(fluorosulfonyl) imide) containing MeMgBr/THF (Kakibe et al., 2012). The authors described the use of binary IL with mixed anions inspired by the good rechargeability and electrochemical properties demonstrated in lithium-ion battery electrolytes. CVs of Mg electrodeposition exhibited that $[DEME][TFSI]_{0.5}[FSI]_{0.5}$ has the highest deposition charge and lowest overpotentials of plating/stripping compared to other binary IL formulations, which could be the preferable ionic structure of this IL composition for Mg deposition to proceed. A Coulombic efficiency above 90% could be achieved over 100 cycles in the galvanostatic Mg deposition/dissolution test. These works revealed that ILs have primarily been used to dissolve Mg salts as solvents, suggesting that ILs can potentially be applied to various electrolyte systems aside from Grignard reagents; for example, IL-based electrolytes containing $Mg[BH_4]_2$, $Mg[TFSI]_2$, or $Mg[ClO_4]_2$ salts can be seen in the literature (Narayanan et al., 2009; Watkins et al., 2016; Lee et al., 2018; Gao et al., 2019; Ma et al., 2019). Since the characteristic properties of ILs can be modified by controlling the ion structures, ILs with improved (electro)chemical properties could potentially be designed to facilitate high-performance Mg deposition/dissolution.

Solid-State Electrolytes for Magnesium Deposition

Besides liquid electrolytes, the use of solid-state electrolytes for Mg deposition has also been explored (Kumar and Munichandraiah, 1999; Pandey and Hashmi, 2009; Sarangika et al., 2017; Deivanayagam et al., 2019; Fan et al., 2020). Despite their low ionic conductivities, solid-state electrolytes are in general safer because they are leak-proof and nonflammable (Jaschin et al., 2020). For example, Higashi and coworkers invented an inorganic solid-state electrolyte of $Mg[BH_4][NH_2]$ (Higashi et al., 2014). $Mg[BH_4][NH_2]$ was derived from $Mg[BH_4]_2$ and possessed much higher ionic conductivity (10^{-3} and 10^{-6} mS cm^{-1} for $Mg[BH_4][NH_2]$ and $Mg[BH_4]_2$, respectively, at 150 °C). Although the Coulombic efficiency is not high (*ca.* 50%), negligible onset potential difference between plating and stripping processes indicates the reversibility could be acceptable at 150 °C, and the anodic stability is shown to be ca. 3 V (vs. Mg). In addition to acting as the electrolyte, the authors commented that such a thin solid electrolyte can be utilized as a coating layer for Mg metal, which separates the Mg metal from the conventional liquid electrolytes, therefore allowing for versatile applications. Polymer electrolytes, which may combine the high conductivity of liquid electrolytes and the above-mentioned advantages of solid electrolytes, can also be utilized as solid-state electrolytes for Mg plating (Kim et al., 2013). In 2003, Aurbach's group first reported a polymer electrolyte Mg $[AlCl_2EtBu]_2$/tetraglyme/PVdF tested in a rechargeable Mg-ion cell that had good cyclability in a wide temperature range between 0 and 80 °C (Chusid et al., 2003). This polymer electrolyte had good anodic stability up to 2.5 V (vs. Mg) and ionic conductivity of 3.7 mS cm^{-1} at 25 °C. In 2015, Shao and coworkers fabricated a nanocomposite electrolyte based on polyethylene oxide (PEO), MgO, and $Mg[BH_4]_2$ with a Coulombic efficiency of 98% at 100 °C, and the voltage gap between the onset potentials for stripping and plating was only 0.2 V (Shao et al., 2015). The PEO has electron lone pairs on its ether-type oxygen, which exhibits strong coordinating capability. Therefore, even though complete dissociation is proven unlikely, the dissociation of $Mg[BH_4]_2$ in PEO could be enhanced, leading to better deposition performance.

Other Design Concepts of Electrolytes for Magnesium Deposition

As the development of electrolytes proceeds, some state-of-the-art electrolytes have been reported with new design concepts. In 2019, Liu's group developed a chloride-free, electrochemically active, and anodically stable magnesium fluorinated pinacolatoborate electrolyte, $Mg[B(O_2C_2(CF_3)_4)_2]_2$ (abbreviated as Mg-FPB, **Figure 2C-i**) in diglyme, in order to replace

chloride-based electrolytes that are possibly corrosive at positive potentials (Luo et al., 2019a). The strong chelating effect of bidentate alkyloxide ligands can stabilize the B center and, therefore, the resultant anion can withstand larger positive polarization. The Mg-FPB/diglyme electrolyte delivered a Coulombic efficiency of 95% for the Mg plating/stripping processes, and the anodic stability was up to 4 V (vs. Mg) on stainless steel, Ti, Al, and glassy carbon (GC) electrodes (**Figure 2C-ii**). The weakly coordinating $B[O_2C_2(CF_3)_4]_2^-$ anion plays a pivotal role in providing a wide potential window, which is potentially suitable to high-voltage cathode materials. In addition, the weak cation-anion interaction gives higher solubility and good ionic conductivity in the electrolyte (0.5 M and 3.95 mS cm^{-1}). A symmetric Mg/0.5 M Mg-FPB (in diglyme)/Mg cell was assembled to evaluate the long-term electrochemical performance at various current densities (**Figure 2C-iii**), and the polarization under galvanostatic control was below 100 mV for all current densities measured. More surprisingly, nuclear magnetic resonance (NMR) results suggested negligible hydrolysis of the electrolyte two days after the addition of water (10,000 ppm). This observation implies that Mg-FPB/diglyme is a promising choice for practical metal-air batteries where moisture impurities from the external gas supply are possible and likely.

Another work presented by Wang and coworkers demonstrated reversible Mg deposition in the dual-salt electrolyte 0.4 M $Mg[TFSI]_2$/0.1 M $Mg[BH_4]_2$/diglyme (Wang et al., 2019a). The addition of a relatively small amount of Mg $[BH_4]_2$ prevents the decomposition of $[TFSI]^-$, rendering the electrodeposition reversible. This article proposed that although Mg can be deposited from the conventional electrolyte without $Mg[BH_4]_2$, the deposited Mg reacts rapidly with the $[TFSI]^-$ anion in the $[Mg[TFSI](diglyme)_2]^+$ cluster present in the bulk electrolyte. In contrast, introducing Mg $[BH_4]_2$ neutralizes the solvation shell of the $[Mg[TFSI](diglyme)_2]^+$ cluster, turning it into $[Mg[BH_4][TFSI](diglyme)]$, since $[BH_4]^-$ is a rather strong coordinating ligand. This neutralized cation cluster somehow inhibits the decomposition of $[TFSI]^-$ in the solvation shell. With this advantageous dual-salt formulation, a Coulombic efficiency of 99% was achieved, and X-ray photoelectron spectroscopy (XPS) results displayed that most of the Mg deposits were Mg metal instead of Mg^{2+}. Besides, no B, N, F, or S signals were found on the deposited Mg. As for solid-state electrolytes, Du and coworkers developed a crosslinked polytetrahydrofuran-borate-based gel polymer electrolyte (**Figure 2D-i**) with the addition of $MgCl_2$ inside a glass fiber membrane (PTB@GF-GPE), which allowed not only reversible Mg plating/stripping for 700 h at 0.05 mA cm^{-2} (**Figure 2D-ii**), but also a wide operation temperature range between −20 and 60 °C (Du et al., 2019). Differing from other works using $Mg[BH_4]_2$/THF liquid electrolyte, this work attempted to design a crosslinked polymer matrix, which enables facile Mg^{2+} transfer, to act as a gel polymer electrolyte with improved mechanical strength and thermal stability. To achieve this goal, polytetrahydrofuran (PTHF, average molecular weight = 2,900) and $Mg[BH_4]_2$ were dissolved in THF, and a reaction between $[BH_4]^-$ and the hydroxyl functional groups occurred *in situ* on a glass fiber membrane. After the crosslinking, the anion $[BH_4]^-$ reacted with the PTHF polymer, generating a PTHF-borate-based gel polymer electrolyte, PTB@GF-GPE. In such structure, the anion can be incorporated into the large, immobilized polymer matrix, resulting in a high transference number of 0.73 for Mg^{2+} cations at the room temperature.

Summary of Electrolyte Development and Outlook for Magnesium Deposition

For rechargeable Mg-air batteries, irreversible Mg plating/stripping should be overcome first. Also, the oxidative stability of electrolytes should be high enough to be compatible with the electrochemistry of oxygen and reaction intermediates generated at the positive electrode interface. To be more specific, the electrolyte must, at least, keep stable at *ca.* 3 V (vs. Mg), considering the theoretical cell voltage of Mg-O_2 cell (refer to **Table 1**). In practicality, significant overpotentials for the recharging (oxidative decomposition) of any MgO/MgO_2 discharge products are likely. Consequently, anodic stability limits exceeding *ca.* 3.5 V would likely be required. A variety of electrolyte systems have been investigated to achieve these goals, and progress has been summarized in **Figure 3**, along with comparative information for Ca-based systems discussed in the next subsection. Many sorts of Grignard reagents are sufficiently electroactive; nevertheless, their instability caused by the nucleophilic nature restricts their practical application. Lewis acids as additives could be an effective solution to the instability of Grignard reagents, as demonstrated by the aluminum- or boron-based Lewis acids. Meanwhile, a retrosynthesis strategy suggests that it is possible to use Mg halides as Mg sources for the Mg electrodeposition with high reversibility. Substituting Mg halides for any possible organic species as the Mg source can be used to enhance the electrochemical stability of electrolyte. However, the relatively low conductivity and salt solubility of such systems still need to be resolved. Another concern is that the electrochemical oxidation stability of electrolytes containing chloride substantially depends on the current collector used (Liu et al., 2014). The incompatibility of chloride-containing electrolytes with certain current collectors (e.g., Al or stainless steel) could easily cause electrolyte degradation during cycling.

The appeal of ILs as candidate electrolyte solvents is related to the excellent safety, negligible volatility, and good ionic conductivity of many different cation and anion combinations. As the cation and anion structures both contribute to the properties of ILs, modification of ILs for better properties tailored toward electrochemical deposition can be achieved through structure optimization. Given that metal-air batteries require an electrolyte compatible with the cathode and the ORR intermediates and products (i.e., superoxide and peroxide), ILs could be a potential candidate owing to their typically good (electro)chemical stability. More investigations on IL blends (with another ionic liquid or another organic solvent) are also recommended, considering many synergistic effects on electrochemistry in such blends have been reported in the literature (Lair et al., 2010; Giridhar et al., 2012; Grande et al.,

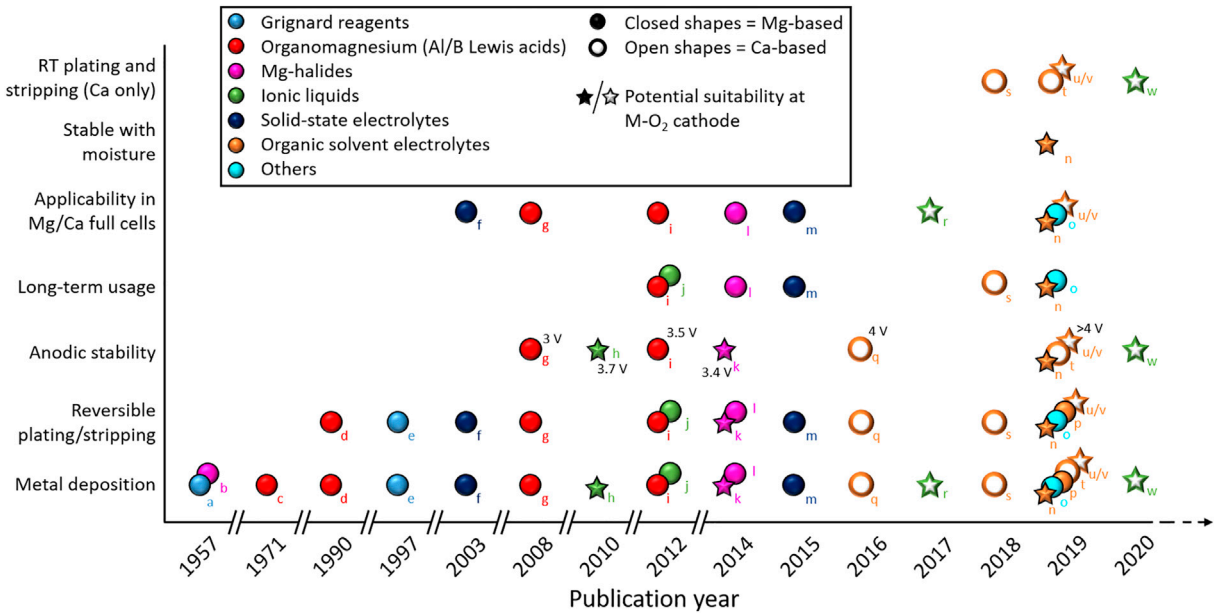

FIGURE 3 | Summary figure of the progress of electrolyte development, highlighting various technical achievements, for Mg (closed shapes) and Ca (open shapes) plating/stripping cycling. Electrolytes are grouped by color to show the type of materials used and the star symbols highlight particular formulations that possess properties making them promising candidates for future investigations in Mg/Ca-O_2 batteries. Labels a-w refer to literature cited in this section and are summarized in the supporting information (RT = room temperature).

2015; Neale et al., 2017). Solid-state electrolytes are also promising electrolyte systems for metal-air batteries, taking into account their mechanical strength, leak-free feature, and nonflammability. Gel polymer electrolytes are, in particular, a famous subject to be applied in Li-air cells (Yi et al., 2015). In recent decades, an emerging class of materials called organic ionic plastic crystals (OIPCs) have been studied as solid-state electrolytes. Such plastic crystals have a definite three-dimensional lattice, but some fraction can be allowed to flow under stress due to the structural disorder stemming from rotational or reorientational motions of cations and/or anions (Pringle et al., 2010; Goossens et al., 2019). Some research about OIPCs applied in Li-battery applications can be found in the literature (MacFarlane et al., 1999; Zhou and Matsumoto, 2007; Jin et al., 2014). Nonetheless, the direct use of OIPCs for efficient Mg stripping/plating is yet to be reported to the best of our knowledge. On the other hand, it will also be valuable to continue working on electrolytes with innovative design concepts. As discussed, Mg-FPB/diglyme shows good anodic stability and good reversibility, while the addition of $Mg[BH_4]_2$ can allow reversible Mg deposition in conventional electrolyte $Mg[TFSI]_2$/diglyme that is unstable with Mg metal. Also, glyme-based electrolytes have been used widely in metal-air battery applications (Aldous and Hardwick, 2016; Yu et al., 2017; Carbone et al., 2018). Considering new approaches that enable the utilization of conventional electrolytes in Mg deposition, some traditional electrolytes could be worthy of a reevaluation, suggesting another possible research direction.

Calcium Metal

Staniewicz reported the earliest work on Ca-metal based cells, based on a thionyl-chloride ($SOCl_2$) system, utilizing a tetrachloroaluminate calcium salt ($Ca[AlCl_4]_2$) in $SOCl_2$ (Staniewicz, 1980). The Ca-metal surface suffered serious corrosion under discharge and storage, generating $CaCl_2$ as a primary product and electroplating of Ca (onto a Ni substrate) could not be observed in this electrolyte system. Later, the important work of Aurbach et al. demonstrated the practical impossibility of achieving Ca electroplating in a series of more conventional nonaqueous electrolyte systems (Aurbach et al., 1991). Therein, reducing currents were ascribed to the reductive decomposition of the electrolyte solvent or salt and no evidence for electroplated Ca was observed. The authors attributed this to surface passivation and the lack of Ca^{2+} ion mobility in the surface films formed.

Organic Solvent Electrolytes for Calcium Deposition and the Importance of Borate-Based Salts

Ponrouch and coworkers demonstrated the first evidence for the electroplating of Ca metal four years ago (Ponrouch et al., 2016). By employing raised temperatures (75–100 °C), plating/stripping redox was achieved on stainless steel electrodes using a $Ca[BF_4]_2$ salt in a 1:1 mixture of propylene carbonate (PC) and ethylene carbonate (EC, see **Figure 4A**). The authors demonstrated some evidence that $Ca[ClO_4]_2$ salts also support plating and stripping but with poorer reversibility, whereas $Ca[TFSI]_2$ electrolytes showed no evidence of stripping electrochemistry. Deposited

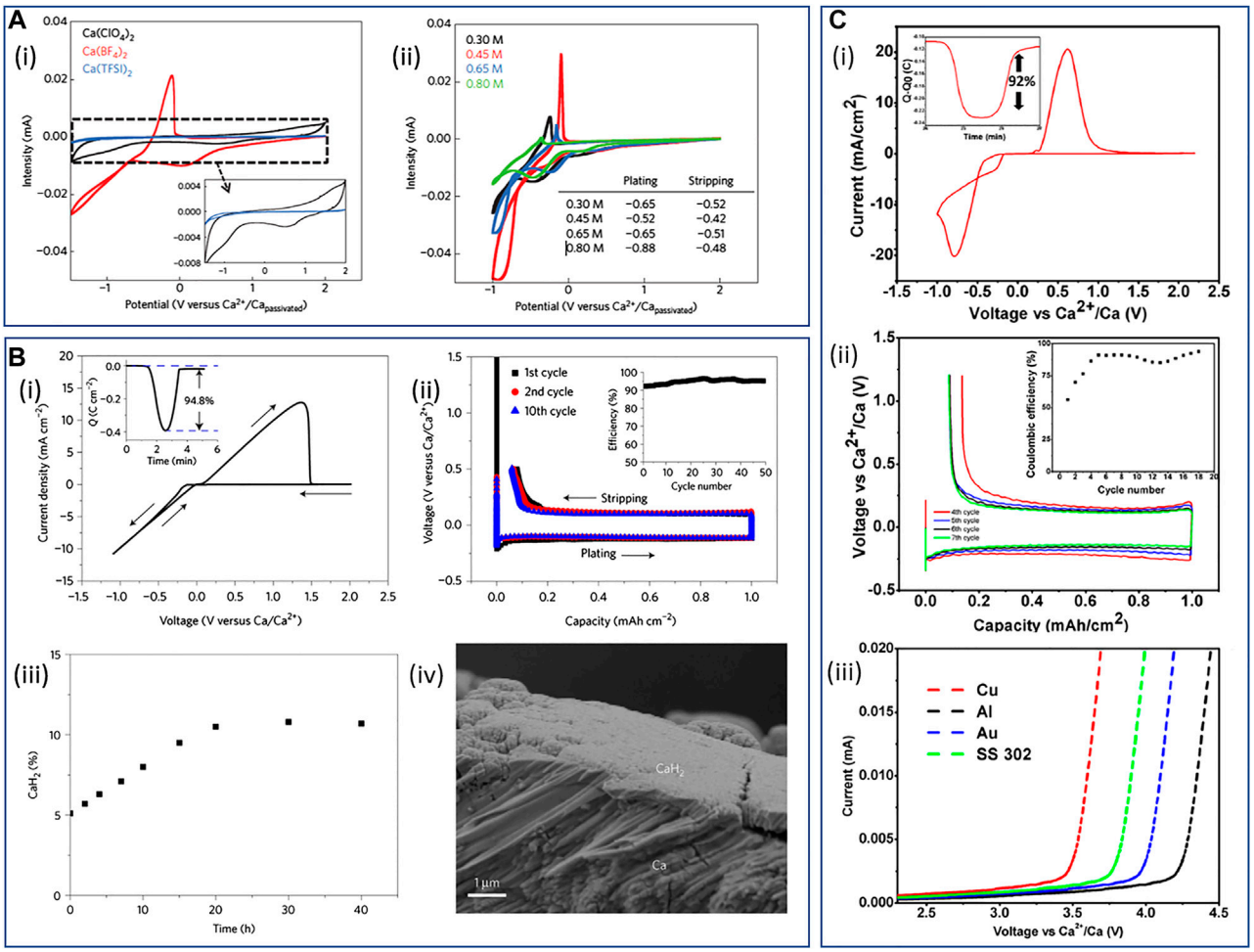

FIGURE 4 | (A) Cyclic voltammograms of EC:PC-based electrolytes (0.5 mV s^{-1} scan rate) at 100 °C with **(i)** a 0.3 M concentration of different Ca^{2+} salts and **(ii)** a range of $Ca[BF_4]_2$ concentrations from 0.3 to 0.8 M. Reproduced with permission from (Ponrouch et al., 2016). **(B)** Calcium plating/stripping in 1.5 M $Ca[BH_4]_2$/THF; **(i)** Cyclic voltammogram of calcium plating/stripping. The working, reference, and counter electrode are Au, Ca, and Pt, respectively. Scan rate 25 mV s^{-1}. Inset shows charge passed on plating/stripping from the CV. **(ii)** Galvanostatic calcium plating/stripping at a rate of 1 mA cm^{-2} (iR-corrected). The working, reference, and counter electrode are Au, Ca, and Ca, respectively. **(iii)** Accumulation of CaH_2 at open circuit after depositing 1 mAh cm^{-2} of calcium on the electrode, expressed as a mole percentage of the charge passed and **(iv)** the cross-sectional image of the electrode after 20 h rest at open circuit. Reproduced with permission from (Wang et al., 2018a). **(C)** Electrochemical measurements in $Ca[B(Ohfip)_4]_2$/DME electrolyte: **(i)** fourth CV cycle on an Au substrate with calcium as the reference and counter electrode (scan rate of 25 mV s^{-1}); **(ii)** galvanostatic plating/stripping of calcium on an Au electrode with Ca counter- and reference electrodes at 0.2 mA cm^{-2} to a capacity of 1 mAh cm^{-2}; **(iii)** linear sweep voltammograms recorded on various substrates at a scan rate of 0.05 mV s^{-1} with Ca as both the reference and counterelectrodes. Reproduced with permission from (Shyamsunder et al., 2019). Copyright 2019 American Chemical Society.

layers were shown to contain primarily phases of Ca and CaF_2, where the fraction of the latter decreased on continued cycling, attributed to initial SEI formation (of CaF_2 rich phases) in early stages of plating. Through the optimization of $Ca[BF_4]_2$ electrolyte conductivity, the authors were even able to demonstrate some stable electroplating/stripping cycling within symmetrical Ca/Ca cells at 100 °C. More recently, Biria and coworkers reported on the room temperature Ca plating/stripping in $Ca[BF_4]_2$ in PC/EC electrolytes by utilizing Cu as an inert substrate (Biria et al., 2019). Therein, the process appears to be of good Coulombic efficiency (>96%) but requires large overpotentials to support plating and stripping (>1 V vs. Ca^{2+}/Ca at 0.55 mA cm^{-2}). The resulting surface films contained no observable CaF_2 phase (by X-ray diffraction), which was attributed to reduced electrolyte reactivity at lower temperatures relative to the earlier work. In the absence of additional crystalline phases, components of the carbonate solvents and entrapped $[BF_4]^-$, observed by FTIR spectroscopy, composed the Ca^{2+} conducting layer.

The first demonstration of reversible plating and stripping of Ca at room temperature utilized the formulation of a 1.5 M Ca $[BH_4]_2$/THF electrolyte (Wang et al., 2018a). Following an

electrochemical reducing cleaning step, the borohydride electrolyte facilitated minimal overpotentials (0.1 V at 1 mA cm^{-2}) and resulted in Coulombic efficiencies of 93–95% of Ca plating/stripping at a gold substrate (**Figures 4B-i,ii**). CaH_2 films form spontaneously from contact between Ca metal and the $Ca[BH_4]_2$/THF electrolyte and throughout deposited films during plating, contributing in part to the suppression of continued electrolyte decomposition. The accumulation of CaH_2 was demonstrated to saturate at the surface at open-circuit potential (OCP) (**Figures 4B-iii,iv**), but the reasonably thick films also contributed to increased overpotentials of stripping and losses in Coulombic efficiency. Ta and coworkers demonstrated that the deposition of Ca in $Ca[BH_4]_2$/THF electrolytes at inert Au and Pt substrates likely involves an initial slow chemical step in a chemical-electrochemical deposition mechanism (Ta et al., 2019). Unlike the above work of Wang et al., wherein spontaneous reaction between deposited Ca metal and THF in the electrolyte led to CaH_2 formation, the preceding chemical step at inert Au/Pt surfaces was ascribed to a hydride abstraction from the $[BH_4]^-$ anions (not THF) and was found to be substrate-dependent. By simulation of voltammetry at Au and Pt microelectrodes, the rate constant of the chemical step at Au was estimated as ca. 10 times smaller than that for Pt, contributing to smooth/uniform or island-like deposits at Au and Pt, respectively. This is attributed to the slower rate of the chemical step allowing time for lateral diffusion and well-distributed hydride on the Au surface, whereas less lateral diffusion can occur during the more rapid accumulation of the adsorbed hydride on Pt.

While favorable Ca plating/stripping is achieved on the Au surface, demonstrating the requirement for a stable SEI-type phase that supports Ca^{2+} mobility, the anodic stability of a Ca $[BH_4]_2$/THF electrolyte is only ca. 3 V vs. Ca^{2+}/Ca (Wang et al., 2018a). As such, due to the reducing nature of $[BH_4]^-$ anions, such a formulation is likely to be incompatible with a Ca-O_2 electrochemical system. In this context, Li et al. and Shyamsunder et al. both demonstrated good room temperature Ca plating/stripping using a $Ca[B(Ohfip)_4]_2$ (Ohfip = hexafluroisopropoxide) salt in dimethoxyethane (DME) (Li et al., 2019; Shyamsunder et al., 2019). Shyamsunder et al. demonstrated the electrolyte can facilitate a Coulombic efficiency of Ca plating/stripping up to 92% at Au (**Figure 4C-i**) but suffered from moderately higher overpotentials (0.3 V at 0.2 mA cm^{-2}, **Figure 4C-ii**) and short circuit failure owing to dendritic growth of Ca. Critically, both research groups reported good anodic stabilities for these electrolytes: 4.2 and 4.8 V vs. Ca^{2+}/Ca for stainless steel and Al, respectively, at 0.25 M (Li et al.); 3.8 and 4.1 V vs. Ca^{2+}/Ca for Au and Al, respectively, at 0.5 M (Shyamsunder et al., **Figure 4C-iii**). Both groups reported significant CaF_2 phases and, importantly, no evidence of CaH_2 in the SEI films on Ca deposits. However, upon prolonged cycling (Shyamsunder et al.), persistent growth of CaF_2 resulted in the surface passivation of the substrate electrodes. Furthermore, Shyamsunder et al. reported on the improved plating/stripping performance by doping the electrolyte with 0.1 M of tetrabutylammonium chloride ($[Bu_4N]Cl$), facilitating a conductivity enhancement that supported enhanced deposition and stripping rate capabilities, improving Coulombic efficiencies and improving the cycle lifetime of the cells. This effect was demonstrated by Ta et al. in their mechanistic study of Ca plating/stripping in $Ca[BH_4]_2$/THF electrolytes (Ta et al., 2019). In addition to improving electrolyte conductivity, the authors highlighted similar plating/stripping enhancements by chloride additive that have been seen in Mg systems; however, the underlying explanation for improved plating/stripping and cell performances is yet to be fully explored. While this electrolyte formulation is limited with respect to growing surface passivation and solvent volatility, the application of a novel salt toward supporting Ca deposition/stripping with good oxidative stability represents an important step for the use of Ca metal anodes in high-voltage systems. The reduction in susceptibility of electrolyte components to continued reductive decomposition and the introduction of additives to understand and control SEI formation should be key strategies toward developing Ca anode viability.

Ionic Liquids for Ca Deposition

The utilization of ILs as alternative nonaqueous electrolyte solvents to support Ca plating/stripping has also been explored in recent years. Shiga et al. explored the fabrication of a full Ca-O_2 cell with an ether functionalized quaternary ammonium-based IL, [DEME][TFSI] with 0.1 M $Ca[TFSI]_2$ (Shiga et al., 2017). Therein, while the full cell showed some evidence of reversibility with the use of a 2,2,6,6-tetramethylpiperidine-1-oxyl- (TEMPO) functionalized cathode and combined with parasitic decomposition reactions on charging (discussed in the following sections), the IL-based electrolyte did present evidence of Ca plating/stripping at a Pt substrate at 60 °C with faster scan rates. Under slower scan rates, where freshly deposited Ca can react with the electrolyte to a greater extent, stripping was reduced even further or not observed at all. However, even at higher scan rates (100–200 mV s^{-1}), the Coulombic efficiency of the plating/stripping process was less than 10% and required very high overpotentials (ca. 2 V vs. Ca^{2+}/Ca).

Subsequently, Biria et al. reported the room temperature plating/stripping of Ca in an ionic liquid electrolyte using 1-ethyl-3-methylimidazolium trifluoromethanesulfonate with 1 M $Ca[BF_4]_2$ salt (Biria et al., 2020). Plating and stripping overpotentials of the Ca at a Cu substrate under galvanostatic control were initially substantial (ca. ±4 V vs. Ca^{2+}/Ca) but stabilized with successive cycling to 1 V vs. Ca^{2+}/Ca, attributed to SEI formation by the authors. Therein, persistent quantities of CaF_2 and CaS are identified before and after stripping steps. Additionally, Coulombic efficiencies of Ca plating/stripping in this formulation stabilized to approximately 56% after the initial three stabilization cycles. Owing to the attractive properties presented by the potential use of ILs as electrolyte solvents in metal-air batteries, these works represent noteworthy preliminary work in this area. Further development of IL-based electrolytes, in the context of Ca-O_2 cells, should concern the realization of low overpotential plating and stripping with considerable improvements to Coulombic efficiencies.

Summary of Electrolyte Development and Outlook for Calcium Deposition

Within the general context of electrolyte development for electrochemical cells based on the use of Ca-metal anodes, significant developments have been achieved in only the last 4–5 years. While previously considered as somewhat a practical impossibility, these recent developments revealed the feasibility of electrodeposition and dissolution with moderate overpotentials and good efficiencies. The timeline for various scientific achievements for Ca (and Mg) plating/stripping is summarized in **Figure 3**. Electrolytes based on borate-based anions have been demonstrated with the most success at calcium anodes, supporting the formation of Ca^{2+} conductive surface films on the metal. While high temperatures were critical in the initial demonstration of more conventional $[BF_4]^-$-based salts, achieving reversible Ca plating/stripping at room temperature was an important step in understanding the viability of Ca cells. Depending on the salt/solvent combinations selected, CaF_2 and CaH_2 have been found to be important SEI components arising from electrolyte reducing reactions at Ca anodes. However, continuous accumulation of CaF_2 appears to eventually build passivation of the interface; thus controlling the first stages of SEI formation with, for example, the introduction of reactive additives or pretreatment steps should be considered. Further understanding of critical SEI components in different electrolytes and their effects on deposition/dissolution efficiency, stability, and morphology will be an important next step to aid in the design of new strategies for improving the reliability of the Ca/electrolyte interface. Additionally, methods for the promotion of salt solubility and electrolytic conductivity are vital for future material development.

However, applying the context of Ca-O_2 battery chemistry (and the wider general context of utilizing high-voltage cathodes), limitations in oxidative stability of the electrolyte materials are important to consider. Due to the challenges in recharging various M-oxide deposits, cell voltages in excess of 3.5 V are expected (even with potential redox mediators). In addition, stability toward reactive intermediates and products (not currently fully understood for Ca) is essential for any candidate electrolyte. Consequently, electrolytes based on the $[BH_4]^-$ anion are highly unlikely to be suitable for use in Ca-O_2 cells as oxidative decomposition of the THF/$Ca[BH_4]_2$ occurs just below 3 V vs. Ca^{2+}/Ca. Likewise, the understood reactivity of organic carbonates toward superoxide radical intermediates negates any formulations based on these solvents for further application in Ca-O_2.

Of the materials studied and discussed for Ca plating/stripping in this work, the fluorinated alkyl borate salt $Ca[B(Ohfip)_4]_2$ and its use in glyme solvents could be an interesting candidate material for initial studies of the ORR/OER. A reasonably high oxidative stability (>3.5 V depending on the electrode material) combined with no directly obvious protons susceptible to attack by superoxide radical intermediates is encouraging. Furthermore, owing to the good anodic stability (4 V vs. Mg^{2+}/Mg) of the Mg-FPB/diglyme electrolyte, discussed in a previous section (Luo et al., 2019a), as well as the improved plating/stripping efficiency and reductive stability at Mg metal compared to the Mg $[B(Ohfip)_4]_2$ salt, the related Ca analog (i.e., Ca-FPB) should be considered for future investigations of both Ca plating/stripping and Ca-O_2 electrochemistry. However, for extended practical full-cell use, electrolyte volatility must be a considered factor. In this regard, low chain length glymes (like dimethoxyethane) are unlikely to be practically suitable. Conversely, while much effort is required to improve the reversibility of plating/stripping in the IL-based electrolytes discussed here, the nonvolatility of ILs addresses the critical aspect of electrolyte evaporation under conventional cell operation.

OXYGEN REDUCTION AND EVOLUTION REACTIONS IN NONAQUEOUS ELECTROLYTES

Understanding the fundamental electrochemistry and ORR/OER mechanisms is essential for the development of nonaqueous metal-air batteries (Johnson et al., 2014). The ORR in many nonaqueous electrolytes, in the absence of M^{n+} cations, can be quite reversible (or quasi reversible) via a one-electron transfer process (Sawyer et al., 1983; Aldous and Hardwick, 2014). When the alkali metal cation, including lithium, sodium, or potassium, is present, the oxygen reduction and evolution behaviors change significantly and the reversibility can decrease. This change can be ascribed to the surface passivation by the insoluble metal oxygen species formed by various reactions between the metal cation and superoxide radical anions (and various intermediary species) (De Giorgio et al., 2011; Khan and Zhao, 2014; Wang et al., 2018b; Sheng et al., 2018). However, the utilization of these monovalent alkali metal cations in rechargeable metal-air batteries is still promising with the assistance of appropriate electrolytes (Johnson et al., 2014), electrocatalysts (Yang et al., 2013), or additives like redox mediators (Kundu et al., 2015), which lead to improved ORR and OER performance. However, for divalent alkaline-earth cations, the reversibility of the ORR and OER can be significantly different and research is relatively limited to date. The ORR in Mg^{2+}/Ca^{2+}-containing electrolytes is scarcely reversible, as described in the introduction.

Magnesium

Oxygen Electrochemistry in Mg^{2+}-Containing Ionic Liquids

Investigations of the ORR and OER in ILs have been carried out in the past decade. AlNashef et al. first demonstrated that the superoxide ion can be stable in ILs without the presence of impurities (AlNashef et al., 2001). Among various ILs, $[Pyrr_{14}][TFSI]$ ($Pyrr_{14}$ = 1-butyl-1-methylpyrrolidinium) receives much attention as it exhibits relatively good stability with respect to the superoxide ion (enabling good reversibility of the ORR on the timescale of conventional cyclic voltammetry experiments) and has been studied in Li-O_2 applications (Katayama et al., 2005; Monaco et al., 2013; Das et al., 2015; Neale et al., 2016). Behm's group probed the oxygen reduction electrochemistry on Au and GC electrodes in 0.1 M $Mg[TFSI]_2$

in $[Pyrr_{14}][TFSI]$, employing a three-electrode cell with forced electrolyte convection (Law et al., 2016). They reported that the addition of Mg salt renders the ORR irreversible, with the ORR current decaying quickly in the first few cycles. However, the appearance of a small anodic peak was observed after some CV cycles. When CVs were recorded in an expanded potential window (where the negative potential limit was extended), a more pronounced anodic peak appeared already in the first cycle. When combined with a series of CV experiments in varied potential ranges, the anodic peak, which is thought of as the OER, is related to the reduction process in a more negative potential region. Therein, the ORR is coupled with the formation of a surface film of MgF_2 and other $[TFSI]^-$ decomposition products that were found to build passivation at the electrodes interface and impede reaction kinetics. In this work, the authors do not observe any MgO or MgO_2 ORR products by the postmortem XPS and they attributed this to a more favorable formation of MgF_2 generated from reaction with the electrolyte.

Behm's group later published another work about 0.1 M $Mg[TFSI]_2$ in $[Pyrr_{14}][TFSI]$ IL, where they studied the ORR and OER on a range of electrode materials, namely, Pt, Au, GC, Mn_2O_3, and MnO_2, in a rotating ring-disc electrode (RRDE) setup to gain more general insights (Bozorgchenani et al., 2018). However, in the Mg^{2+}-containing IL, none of these electrode materials exhibited any OER feature and the ring electrode (held at 1 V vs. Mg/MgO) did not capture any intermediates either. During the cycling, the cathodic current dropped quickly as a result of the passivation layer. On the other hand, it is noticeable that the electrode surface was not totally passivated after some cycles, indicated by the emergence of a small OER peak related to superoxide reoxidation. The XPS results revealed that MgO_2 composed a great portion of the passivation layer, which seems contradictory to the previous work where MgF_2 was the main component of the passivation layer (Law et al., 2016). However, although a number of additional tests were conducted, the authors were still not able to find parameters/conditions that resulted in the discrepancy between these two works.

In 2019, Behm's group reported a more comprehensive research work on the same IL, $[Pyrr_{14}][TFSI]$, where differential electrochemical mass spectrometry (DEMS) and *in situ* attenuated total reflectance-Fourier transform infrared (ATR-FTIR) measurements were simultaneously carried out in a thin-layer flow cell (Jusys et al., 2019). In the O_2-saturated $[Pyrr_{14}][TFSI]$, two well-defined mass transport-controlled reduction current plateaus can be observed during the ORR, and the DEMS result suggests superoxide and peroxide species are the products. By contrast, only a tiny OER peak can be seen, which is attributed to the removal of ORR products by the flowing electrolyte. On the other hand, comparing the ATR-FTIR results of N_2- and O_2-saturated $[Pyrr_{14}][TFSI]$, the –OH-stretching mode (from water impurities) is more intense in the O_2-enriched $[Pyrr_{14}][TFSI]$ on the negative scan. The authors suggest that it may result from the adsorbed (super)oxide anions formed during the ORR since water tends to adsorb preferably with adsorbed anions. Furthermore, two potential-dependent IR absorption bands, with one located between 1,000 and 1,100 cm^{-1} and the other at ca. 1,200 cm^{-1}, are both related to superoxide and/or peroxide. After carefully studying Mg^{2+}-free $[Pyrr_{14}][TFSI]$ with saturated N_2/O_2, the O_2-saturated $[Pyrr_{14}][TFSI]$ containing 0.1 M $Mg[TFSI]_2$ was examined under the same experimental conditions. The CV results are in agreement with previous results (see discussion above), where a serious passivation layer on the electrode is suggested. Again, DEMS results support that the main ORR product is MgO_2, consistent with the previous work using *ex situ* XPS (Bozorgchenani et al., 2018). In addition, *in situ* IR reveals an interaction of water with MgO_x or MgF_2 formation (the latter observed in reference (Law et al., 2016)). This article, in many aspects, is in agreement with the previous two articles about the ORR in Mg^{2+}-containing $[Pyrr_{14}][TFSI]$. Besides, utilization of *in situ* IR spectroscopy is demonstrated to be beneficial to study the interplay between IL ions and the ORR intermediates.

Oxygen Electrochemistry in Mg^{2+}-Containing Organic Electrolytes

Dimethyl sulfoxide (DMSO) is commonly selected as a suitable solvent for O_2 electrochemistry due to its appreciable ability to stabilize reactive intermediates of ORR (Trahan et al., 2012), but it should be noted that the solvent, as well as the anions and electrode substrates, may be expected to influence the ORR/OER electrochemistry, including the onset potential, reaction mechanism, and product distribution. Baltruschat's group carried out a detailed investigation in order to elucidate the underlying mechanism of ORR in 0.4 M $Mg[ClO_4]_2$/DMSO (Reinsberg et al., 2016a). CVs and corresponding mass spectrometric CV (MSCV) were recorded with the DEMS technique for a few cycles without obvious deactivation of the electrode. However, no oxygen evolution is visible during the positive sweep, indicating the irreversibility of ORR (**Figure 5A-i**). The authors inferred this phenomenon could be explained by the decomposition of ORR products or intermediates by unknown chemical reactions. It is worth noticing that the ORR onset potential is close to the O_2^- formation rather than MgO_2 formation (see **Figure 5A-i**). In this work, however, MgO_2 or other peroxide species (instead of MgO) was suggested to be the main ORR product during the cathodic polarization of CV on GC, Au, and Pt, whereas the partial formation of MgO was found on Ru and Rh, according to the DEMS results (**Figure 5A-ii**). Combining the DEMS results and some kinetics investigation, the authors proposed an ORR mechanism (**Figure 5A-iii**) where O_2^- forms at the initial step, followed by the hypothesized MgO_2^+ formation. Then, MgO_2 forms via the second reduction, in competition with other chemical reactions. Herein, the authors suggested that it is improbable for the cations to have a strong impact on the noncharged O_2 molecule as the onset of the ORR appears to be unaffected. In contrast, the cation does have a strong impact on the second reduction step, considering the ORR product distribution in electrolytes containing $[Bu_4N]^+$ or Li^+, wherein peroxide cannot form in the former case but can be found in the latter. Therefore, the existence of a hypothetical superoxide-cation complex (MgO_2^+) intermediate can rationalize why the type of cation has an impact on the reduction potential of the second electron transfer (corresponding to peroxide formation) instead of the

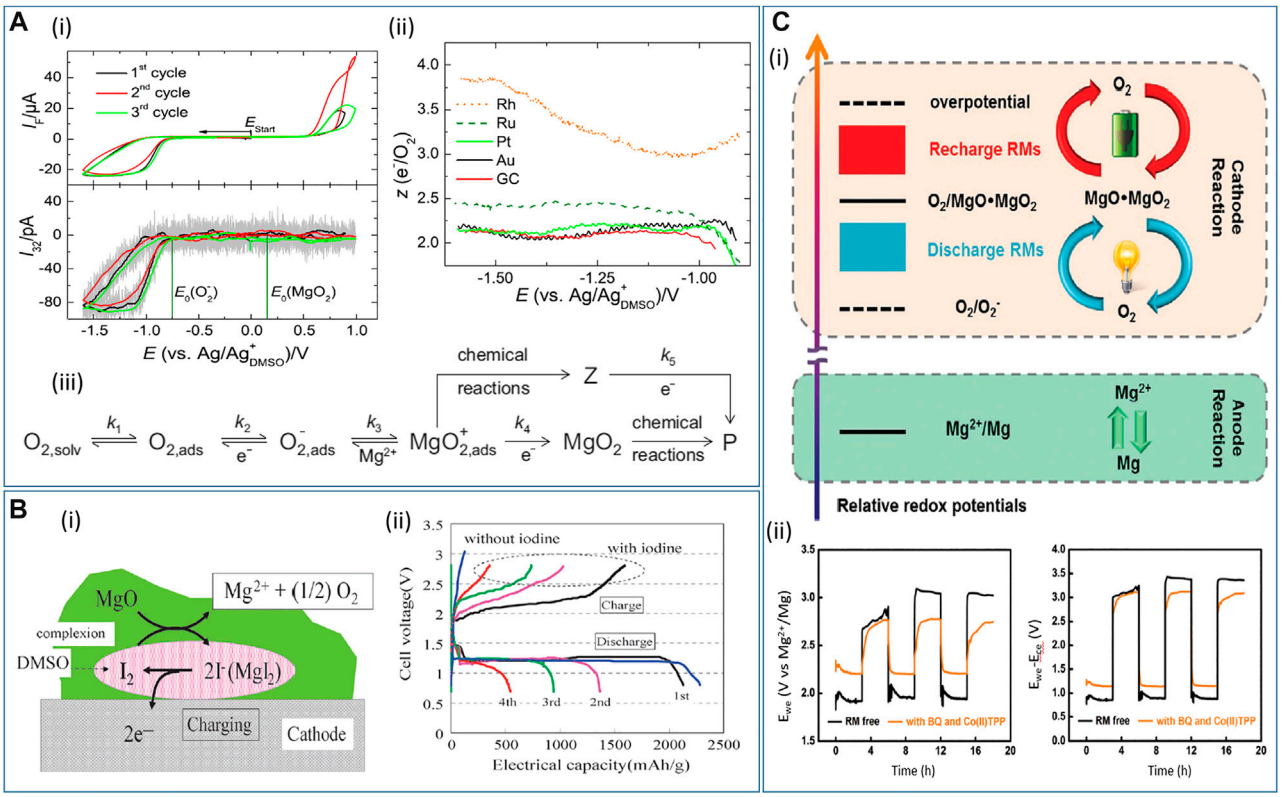

FIGURE 5 | (A-i) Subsequent CVs at 10 mV s^{-1} and corresponding mass spectrometric CVs for O_2 in 0.4 M $Mg[ClO_4]_2$/DMSO saturated with a mixture of Ar and O_2 (80 : 20) on Pt. **(A-ii)** Number of electrons z transferred per oxygen molecule on different electrode materials in 0.4 M $Mg[ClO_4]_2$/DMSO with 20% O_2 saturation. **(A-iii)** Proposed ORR mechanism on Pt in Mg^{2+}-containing DMSO electrolyte with k_i being the rate constant of step *i*, P being the unknown final products, and Z being an intermediate. Reproduced with permission from (Reinsberg et al., 2016a). **(B-i)** Proposed reaction mechanism of the charging process for Mg-O_2 cell using I_2 as the redox mediator. **(B-ii)** Discharge-charge curves of Mg-O_2 cell with I_2 at 60 °C. Reproduced with permission from (Shiga et al., 2013). **(C-i)** Operation principles of systems with dual redox mediators. **(C-ii)** Galvanostatic cycling of Mg-O_2 cell using 1,4-benzoquinone and 5,10,15,20-tetraphenyl-21H,23H-porphine cobalt(II) as dual redox mediators. The left panel shows the voltage profile measured against the Mg reference electrode in a three-electrode configuration, whereas the right panel shows the voltage profile against the counter electrode in a two-electrode configuration. Reproduced with permission from (Dong et al., 2016).

ORR onset potential (corresponding to superoxide formation). Later, Baltruschat's group published another work concerning the influence of divalent cations on the ORR (Reinsberg et al., 2018). The ORR and OER in 0.4 M $M[ClO_4]_2$ (M = Mg, Ca, Sr, Ba) electrolytes were investigated on Au, Pt, and GC electrodes. Different from its analogs (Ca^{2+}, Sr^{2+}, Ba^{2+}), peroxide forms in Mg^{2+}-containing DMSO on three different electrode materials according to the DEMS results. Conversely, the other divalent cations show some superoxide formation to various degrees on Pt and GC. Further elucidation of the difference in product distribution will be delivered in the section on Ca-O_2 electrochemistry. These two articles from the same group reported that the ORR/OER is scarcely reversible in the $Mg[ClO_4]_2$/DMSO electrolyte.

In 2015, Vardar et al. reported their study on the ORR discharge products in Mg-O_2 cell using PhMgCl-Al[OPh]$_3$/THF electrolyte (Vardar et al., 2015), since this electrolyte not only allows reversible plating/stripping at room temperature but has high oxidation stability above 4 V vs. Mg^{2+}/Mg. The measured OCP (ca. 2 V) and operating cell voltage (ca. 1.5 V) suggest free superoxide (O_2^-) forms in the first electrochemical step, followed by a chemical step where MgO_2 forms and an O_2 molecule is liberated. Then, MgO_2 undergoes disproportionation into MgO. The whole process is described in the following equations:

$$O_2 + e^- \leftrightarrow O_2^- \left(2.04\ \text{V vs}\ Mg^{2+}/Mg\right) \quad (1)$$

$$Mg^{2+} + 2O_2^- \leftrightarrow MgO_2 + O_2 \quad (2)$$

$$2MgO_2 \leftrightarrow 2MgO + O_2 \quad (3)$$

Thus, an ECC (electrochemical-chemical-chemical) mechanism is hypothesized. If MgO or MgO_2 is generated directly via electrochemical reactions (i.e., four-/two-electron transfer processes), the recorded OCP and operating cell potential must be larger and thus closer to the theoretical voltages of MgO_x (2.91 V for MgO_2 and 2.95 V for MgO, see **Table 1**). The postmortem characterization of discharged air electrodes by Auger electron spectroscopy (AES) showed that the discharge product was a mixture of MgO and MgO_2, with the volume percentage being 70% and 30%, respectively. After the air electrode was recharged, Raman and AES both revealed the preferential decomposition for MgO_2 but rather limited

decomposition for MgO. All these works suggest that MgO_2/MgO are not directly generated via electrochemical reactions but via multistep processes involving initial O_2^- formation.

Redox Mediators for Rechargeable Mg-O_2 Full Cells

In contrast to the ongoing research of the fundamental ORR/OER electrochemistry, redox mediators (RMs) can be incorporated into the electrolytes to construct practical rechargeable Mg-O_2 batteries because of the resulting stable and efficient battery cycling. The redox mediator is a molecule dissolved in a solution that is oxidized into RM^+ (or other oxidized forms) upon recharging, which in turn oxidizes the ORR products M_xO_y, with itself being reduced back to RM. RMs have been widely demonstrated in metal-air battery research at the Li-O_2 and Na-O_2 cathode (Chen et al., 2013; Yin et al., 2015). Shiga and coworkers first demonstrated a rechargeable Mg-O_2 cell at an elevated temperature (60 °C), using iodide (I^-) as the RM (Shiga et al., 2013). In this work, the proposed catalysis mechanism suggests that I^- is oxidized to I_3^- upon charge and then I_3^- decomposes the discharge product MgO (**Figure 5B-i**). Although obvious capacity fading was manifested over merely four cycles (**Figure 5B-ii**), the rechargeability of the Mg-O_2 cell proved to be possible. Herein, it is worth noting that the authors only investigated the decomposition of MgO rather than other possible reaction intermediates (superoxide and peroxide species). Although MgO is the final discharge product and is the most thermodynamically favorable compound, many recent studies also suggested (su)peroxide species as possible products during the ORR, as discussed above. Therefore, the interaction between $Mg(O_2)_2$ or MgO_2 and RMs and the resultant electrochemical response is also of great importance.

Another research article explored the simultaneous use of two RMs in a Mg-O_2 cell (working principles shown in **Figure 5C-i**), one for discharge and the other for recharge (Dong et al., 2016). More specifically, the discharge redox mediator (1,4-benzoquinone, BQ) promotes the formation of MgO_2 or MgO and limits the superoxide formation, which thereby alleviates the ORR overpotentials. Additionally, the presence of BQ as a discharge RM can produce small-sized, uniform MgO_2/MgO particles on the cathode, which could be able to increase the available capacity of Mg-O_2 cells. On the other hand, the recharge RM (5,10,15,20-tetraphenyl-21H,23H-porphine cobalt(II), Co(II)TPP) facilitates the decomposition of discharge products, confirmed by SEM and XPS. Overall, the charge-discharge gap is decreased by 0.6 V (0.3 V for each process, see the left panel in **Figure 5C-ii**), saving much energy wasted for sluggish kinetics of both oxygen electrochemistries. Note that, in a two-electrode configuration (the right panel in **Figure 5C-ii**), some overpotentials can be caused by the passivation of Mg counter electrode, which results in an underestimated round-trip efficiency. Furthermore, the long-term stability of any RMs at the anode interface requires significant consideration when investigating their application. However, this research gives the proof-of-concept demonstration that two different RMs can be applied at once to enhance the full-cell performance.

Calcium

Oxygen Electrochemistry in Ca^{2+}-Containing Electrolytes

The earliest report of a system based on electrochemical reactions of Ca and O_2 detailed the use of a molten salt electrolyte (29 mol% CaO, 71 mol% $CaCl_2$ with ZrO) at 850 °C, a CaSi alloy anode, and a perovskite positive electrode (Pujare, 1988). Fabricated cells were cycled at 850–900 °C presenting cell voltages in the range of ca. 1–2 V; while no characterization of products is reported, the authors describe the full-cell electrochemistry as in the following equation:

$$2CaSi + 1/2O_2 \leftrightarrow CaO\,(\text{in}\,CaCl_2) + CaSi_2 \quad (4)$$

More recently, while remaining relatively unexplored compared to analogous Mg-O_2 systems, several works focusing on the effect of Ca^{2+} on the ORR/OER and the investigation into nonaqueous Ca-O_2 full cells have been reported. Baltruschat's group conducted the first detailed investigations of the nature of electrochemical oxygen reduction within liquid nonaqueous Ca^{2+}-containing electrolytes, namely, $Ca[ClO_4]_2$ salts in DMSO (Reinsberg et al., 2016b). In this work, a combined series of CV, DEMS, and RRDE experiments are described at different electrode substrates to assess the ORR/OER. While the formation of CaO_2 (calcium peroxide) is favored at Au, with no evidence of any reversibility, $Ca(O_2)_2$ (calcium superoxide) is the dominant product of ORR at GC and Pt (as well as Rh and Ru). Interestingly, the two-electron (per mole O_2) reduction at Au, attributed to peroxide formation, is not coupled with passivation and deactivation of the surface (i.e., no large hysteresis after the potential sweep is reversed), unlike Li^+/DMSO systems. However, the reasons for the preferential formation of CaO_2 at Au is yet to be explored. For the Pt and GC electrodes, DEMS measurements combined with a secondary detection electrode held at oxidative potentials, and the analogous RRDE configuration experiments, confirmed the reoxidation of dissolved superoxide species to be approaching 90% of O_2 species reduced during the ORR at the reducing Pt/GC electrodes (**Figure 6A**). The secondary working electrode, an Au-sputtered Teflon membrane held close to the mass-spectrometer, reduced the total quantity of O_2 consumed during cyclic voltammetry (**Figure 6A-iii**), indicating significant regeneration of molecular O_2 from the oxidation of dissolved species. In combination with a degree of reoxidation of precipitated species at high voltages, these results indicate high Coulombic efficiency and good chemical reversibility of the ORR at Pt/GC. However, the significant overpotentials required for oxidation of the dissolved superoxide indicates that this is not free O_2^- (or loosely interacting) in solution, but rather the authors describe likely formation of contact ion pairs in solution with the dissolved Ca^{2+}.

In a subsequent study by Baltruschat's research group, the effect of different alkaline-earth cations on the ORR/OER in DMSO-type electrolytes was demonstrated, as discussed initially in the context of Mg^{2+} electrolytes in the previous section

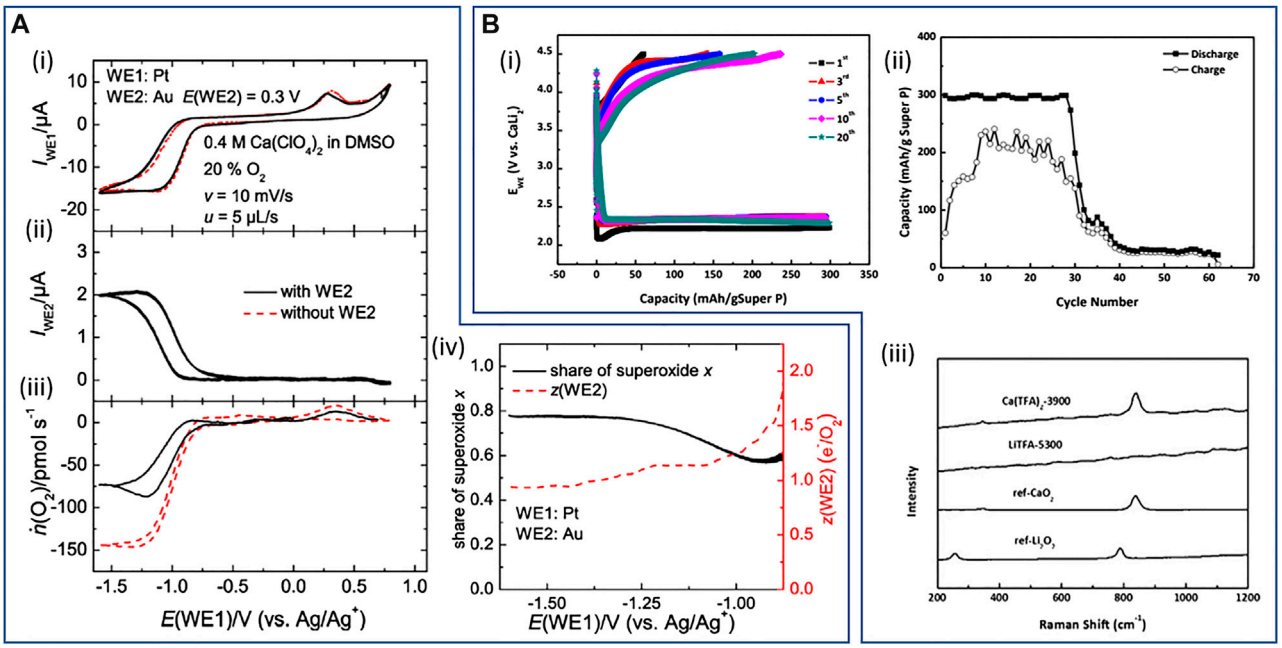

FIGURE 6 | (A) Identification of the soluble products via DEMS using 0.4 M $Ca[ClO_4]_2$/DMSO saturated with a mixture of 80% Ar and 20% O: **(i)** cyclic voltammograms at the Pt-working electrode (WE) with (black) and without (red) the use of an Au-sputtered Teflon membrane (E(WE2) = 0.3 V) in the detection compartment. **(ii)** Faradaic currents at the sputtered Teflon membrane. **(iii)** Corresponding flow of oxygen $\dot{n}(O_2)$. **(iv)** Resulting electron numbers at the second working electrode (black) and share of superoxide x (red) calculated. **(A)** Reproduced with permission from (Reinsberg et al., 2016b). Copyright 2016 American Chemical Society. **(B)** Intermetallic $CaLi_2$-O_2 batteries: **(i)** voltage profile of galvanostatic cycling and **(ii)** capacity retention of $CaLi_2$-O_2 cell using 0.1 M $Ca[OTf]_2$/TEGDME at a current density of 50 mA g^{-1}_{SuperP} and a capacity of 300 mAh g^{-1}_{SuperP}. **(iii)** Raman spectra of the fully discharged cathodes without PVDF of $CaLi_2$-O_2 cells where label the salt used and the number indicate the discharge capacity (mAh g^{-1}_{SuperP}). Discharged $Ca[OTf]_2$ (or $Ca[TFA]_2$) cell shows a clear band at 840 cm^{-1} in agreement with the reference spectra of CaO_2. **(B)** Reproduced with permission from (Kim et al., 2020).

(Reinsberg et al., 2018). As per the previous investigation, peroxide remains the dominant product at Au electrodes in DMSO electrolytes containing Ca^{2+} as well as Mg^{2+}, Sr^{2+}, and Ba^{2+} (where $[ClO_4]^-$ was used as the salt counter-anion in all electrochemical measurements). However, while the onset of O_2 reduction at Pt and GC remained consistent, the products of ORR were found to be highly dependent on the divalent cation. Therein, the tendency for peroxide formation over superoxide (as per the number of electrons per mole of O_2 consumed) increases from Ca^{2+}<Sr^{2+}<Ba^{2+}≈Mg^{2+}, such that superoxide dominates in Ca^{2+}-containing systems and exclusively peroxide forms in the presence of Mg^{2+}. The prevalence of superoxide or peroxide formation in these DMSO-based electrolytes is attributed, in part, to the type of interactions between superoxide generated in the first electron transfer and the cation at the electrode interface. The authors suggest that strongly polarizing cations with a large acceptor number (AN) may, by the withdrawal of electron density, polarize the superoxide radical anion and facilitate the second electron transfer. However, since there are no AN data available for Ca^{2+} (or Sr^{2+}), these trends were only compared for Mg^{2+}/Ba^{2+} with Li^+ and Na^+ cations and it remains to be seen if this parameter would also describe the very different behavior of the Ca^{2+} electrolyte.

Ca-O_2 Full Cells

The construction of Ca-O_2 full cells relies on the ability to stabilize and control both challenging interfaces for Ca-metal plating/stripping and the ORR/OER. Formulation of electrolytes suitable for both environments remains a challenge for all of the metal-O_2 battery chemistries; however, given the previous discussions of recent developments in these fields, such examples pertaining to Ca are still limited. The first such example made use of an IL-based electrolyte coupled with a RM-functionalized cathode framework and a Ca-metal chip anode, all held at 60 °C (Shiga et al., 2017). The electrolyte was a [DEME][TFSI] IL with 0.1 M $Ca[TFSI]_2$ and the redox mediator was TEMPO grafted to a polymer backbone. Herein, the reaction on discharge under an O_2 atmosphere was attributed to the formation of CaO at the cathode with greater than 1,500 mAh g^{-1} capacity at ca. 1.8 V on the first discharge. Upon charging, gas evolution analysis (by gas chromatography–mass spectrometry, GC-MS) demonstrated that oxidation of discharge products formed under O_2 was possible in the presence of the TEMPO-group RM. However, the charge/discharge efficiency fell in the range of 60–80%, and the observed significant capacity fade was attributed primarily to anode stability/reversibility issues. While the IL-based electrolyte somewhat facilitates plating/stripping, as discussed in the earlier section, large overpotentials (ca. 2 V) and

poor efficiencies (<10%) at the Ca-metal interface reduced cell voltages and led to rapid cell failure. Significant volumes of H_2 gas were also evolved during charging of the cell, likely originating from important routes to the decomposition of the electrolyte that would impact cell operation.

In a recent attempt to alleviate issues pertaining to the reactivity and conductivity of Ca interfaces, while enabling the use of more conventional electrolyte systems for the benefit of cathode processes, the use of an intermetallic $CaLi_2$ alloy electrode has been employed in full Ca/Li-O_2 cells (Kim et al., 2020). In conjunction with a simple carbon black (Super P)-based cathode, the $CaLi_2$ alloy anode supports full-cell cycling under O_2 with a tetraethylene glycol dimethyl ether (TEGDME)/trifluoromethanesulfone ($[OTf]^-$) electrolyte with 1 M Li[OTf] or 0.1 M $Ca[OTf]_2$. While the majority of testing relates to the use of the Li-salt electrolytes, wherein the $CaLi_2$ alloy anode supports cycling performances comparable to Li-metal, $CaLi_2$-O_2 cells employing Ca-electrolytes were able to cycle for more than 20 discharge/charge cycles (**Figure 6B-i,ii**). Reversible cycling was, therein, attributed to the formation of CaO_2 at the cathode confirmed by Raman spectroscopy (**Figure 6B-iii**) and XRD and XPS analysis. Notably, cycling was reported under comparatively low current density and capacity regimes due to the poor conductivity of this Ca-based electrolyte formulation. The full $CaLi_2$-O_2 cell employing $Ca[OTf]_2$ did, however, support a large single discharge capacity up to 5,300 mAh g^{-1} (based on mass of carbon cathode with a 2 V (vs. $CaLi_2$) cut-off limit). For both single salt electrolyte systems, the authors present evidence of the other cation at the cathode after cycling in various reaction products, demonstrating dissolution of both Ca and Li from the alloy anode occurs. While this factor may complicate prolonged cycling of full cells, the application of dual electrolytes containing Ca^{2+} and Li^+ warrants further investigations. Critically, this work highlights how the $CaLi_2$ alloy anode enables the possibility of employing commercially available electrolyte components to facilitate both the Ca plating/stripping steps and the ORR/OER in the same cell. Dedicated optimization of the electrolyte components to increase Ca^{2+} solubility (beyond 0.1 M) and ionic conductivity could further expand the performance and cyclability of such $CaLi_2$-O_2 systems.

Summary of Oxygen Electrochemistry in Mg^{2+}/Ca^{2+}-Containing Electrolytes and Future Outlook

The electrochemistry of the ORR and OER in aprotic electrolytes containing $Mg^{2+}$and Ca^{2+} divalent metal cations remains in the early stages of investigation. So far, Baltruschat's group has conducted a series of important fundamental investigations on the effects of divalent metal ions (mainly Mg/Ca and one including Sr/Ba) on the O_2 electrochemistry in DMSO. Therein, reaction mechanisms and product formation were shown to be dependent on substrate and cation species within the DMSO. Additionally, analogous to Li- and Na-based M-O_2 chemistry, the chosen solvent is also expected to affect these processes via solvation effects on the metal cations and the reaction intermediates at the electrode interface. Such mechanistic investigations still need to be expanded in more electrolyte systems to explore any general applicability and, subsequently, to inform the design of new materials/substrates toward minimizing passivation and promoting reversibility of the reactions. Furthermore, ILs have been demonstrated as promising candidates to accommodate the oxygen electrochemistry for Mg/Ca; however, in addition to solubility and transport limitations, such investigations suggest that the incorporation of RMs or effective electrocatalysts into the air electrode would be required to overcome passivation of the interface.

The nature of the discharge process and the final product at the cathode interface is critical for determining cell capacity and rechargeability in M-O_2 cells. For Li/Na/K-O_2 chemistries, the monovalent cation superoxides (MO_2, M = Li^+, Na^+, K^+) play a pivotal role in determining, to different degrees, the discharge performance (ORR). For example, the solvation of LiO_2 reaction intermediate has been found to affect how the final product Li_2O_2 can precipitate on the air cathode (Johnson et al., 2014); NaO_2 can make up a significant part of the discharge products (Ortiz-Vitoriano et al., 2015); KO_2 is the sole discharge product (Yu et al., 2017). In contrast, the dependence of the ORR on the superoxide (as product or reaction intermediate) has not been demonstrated in the comparative divalent Mg/Ca systems, and the formation of the peroxide and oxide species are primary products. The only exception is $Ca(O_2)_2$, which has been reported to form as the primary product on various working electrodes (aside from Au). However, this is only observed in the DMSO-based electrolyte, and the explanation is not yet fully understood. In order to obtain more information about the effect of electrolytes on the ORR/OER, the desired product distribution, and to ascertain critical stability information, operando spectroscopic investigations of the air-cathode interface in more electrolyte systems (DMSO, acetonitrile, ether, glyme, etc.) should be the focus of future research. Nevertheless, progress is highly dependent on the development of suitable Mg and Ca salts that have an appreciable solubility in these solvents to provide sufficient ionic conductivity.

On the other hand, the oxygen reduction is still rather irreversible in Mg/Ca systems compared with the Li/Na/K analogs, probably due to both the thermodynamically less favorable decomposition of ORR products and the more sluggish OER kinetics. To be more specific, MgO_2/MgO and CaO_2/CaO, main discharge products in Mg/Ca systems, are thermodynamically much more stable than LiO_2/Li_2O_2, NaO_2/Na_2O_2, and KO_2 (ΔG° = −230/−570.8 kJ mol^{-1} for LiO_2/Li_2O_2, ΔG° = −218.8/−449.7 kJ mol^{-1} for NaO_2/Na_2O_2, ΔG° = −239.4 kJ mol^{-1} for KO_2, ΔG° = −567.8/−568.9 kJ mol^{-1} for MgO_2/MgO, and ΔH° = −652* kJ mol^{-1} for CaO_2 and ΔG° = 603.5* kJ mol^{-1} for CaO; asterisk labeled value is for formation enthalpy since no ΔG° is available). Also, multiple-electron transfer (at least two electrons) during the OER can result in sluggish kinetics. Although rechargeable metal-air batteries in these systems can be realized using RMs, understanding the underlying mechanisms and how they are mediated by solvents, substrates, overpotentials, and discharge/charge rates is still essential to develop practically viable batteries. For instance, some studies suggested that the ORR in Mg^{2+}-

containing electrolytes proceeds via an inner-sphere route (Reinsberg et al., 2016a), while other articles observed an opposite behavior similar to the outer-sphere mechanism (Law et al., 2016). This difference in the observed ORR/OER mechanisms can cause confusion whether or not the electrocatalyst is needed, therefore impeding the design of proper air electrodes. On the other hand, having metal oxide as the final product in Mg-air or Ca-air batteries may not be ideal, although it delivers the largest discharge capacity and energy density. Considering the reversibility of the discharge product, the metal peroxide could be more desirable for rechargeable metal-air batteries (Smith et al., 2016). It has been well accepted that the properties of discharge products (composition, morphology, etc.), as well as their interaction with the electrolyte, can strongly influence the cell capacity and cycle life (Vardar et al., 2015). Therefore, designing the air cathode and electrolyte, which allows the targeted formation of desired ORR products, will be a future direction for investigations.

CONCLUDING REMARKS

Plating and stripping at Mg anodes have been studied for many years, with much progress being made within the past 2 decades. However, many reported electrolyte classes are expected to be incompatible in M-O_2 systems and for alternative high-voltage chemistries. Conversely, much of the evidence of successful Ca plating/stripping has arrived only in the previous 5 years and has been realized without comparative organometallic- or halide-based chemistries that may be expected to yield stability and corrosion issues. In light of the discussed developments, suggestions and recommendations have been made to inspire possible applications of some potentially suitable electrolytes in M-O_2 full cells, wherein pairing good oxidative stabilities and conductivities with low overpotential and efficient plating/stripping is a critical target for candidate electrolytes. Further understanding of the components that make for a good SEI on Mg/Ca anodes should be prioritized to support design of improved materials. Recent works on the cathode (electro)chemistries have then been discussed to glean information from these mechanistic studies. Such fundamental investigations, in the very early stages compared to the ongoing discoveries in comparative Li/Na-O_2 chemistries, are important especially for the continued optimization and control of the discharge and charge processes and, subsequently, designing suitable air cathodes therein. However, while degrees of reversibility have been observed in both Mg and Ca systems, only redox mediators show the potential ability to facilitate efficient ORR/OER during battery cycling. Consequently, the parallel development of electroactive redox mediator additives may be vital to support rechargeability of the ORR/OER in a meaningful way and their effects on the anode processes should be considered. To date, research on Mg/Ca has been still quite limited in comparison with Li/Na/K, particularly for the air cathode. More electrolyte systems containing various salts/solvents are required to be probed, in order to obtain more generalized understandings of important processes in divalent metal-air batteries and deeper insights into their underlying chemical nature.

AUTHOR CONTRIBUTIONS

Y-TL: writing original draft and review, editing, and visualization. AN: writing original draft and review, editing, and visualization. C-CH: supervision, writing review, and editing. LH: funding acquisition, project administration, supervision, writing review, and editing.

ACKNOWLEDGMENTS

We gratefully acknowledge the funding from EPSRC (EP/R020744/1 and EP/R000441/1). Additionally, the authors would like to acknowledge Callum Shields for the artistic contribution to create **Figure 1**.

SUPPLEMENTARY MATERIAL

The Supplementary Material for this article can be found online at: https://www.frontiersin.org/articles/10.3389/fenrg.2020.602918/full#supplementary-material.

REFERENCES

Abdallah, T., Lemordant, D., and Claude-Montigny, B. (2012). Are room temperature ionic liquids able to improve the safety of supercapacitors organic electrolytes without degrading the performances?. *J. Power Sources* 201, 353–359. doi:10.1016/j.jpowsour.2011.10.115

Abraham, K., and Jiang, Z. (1996). A polymer electrolyte-based rechargeable lithium/oxygen battery. *J. Electrochem. Soc.* 143, 1–5. doi:10.1149/1.1836378

Aldous, I. M., and Hardwick, L. J. (2014). Influence of tetraalkylammonium cation chain length on gold and glassy carbon electrode interfaces for alkali metal-oxygen batteries. *J. Phys. Chem. Lett.* 5, 3924–3930. doi:10.1021/jz501850u

Aldous, I. M., and Hardwick, L. J. (2016). Solvent-mediated control of the electrochemical discharge products of non-aqueous sodium-oxygen electrochemistry. *Angew Chem. Int. Ed. Engl.* 55, 8254–8257. doi:10.1002/anie.201601615

Alnashef, I. M., Leonard, M. L., Kittle, M. C., Matthews, M. A., and Weidner, J. W. (2001). Electrochemical generation of superoxide in room-temperature ionic liquids. *ECS Solid State Lett.* 4, D16–D18. doi:10.1149/1.1406997

Aurbach, D., Skaletsky, R., and Gofer, Y. (1991). The electrochemical behavior of calcium electrodes in a few organic electrolytes. *J. Electrochem. Soc.* 138, 3536. doi:10.1149/1.2085455

Biria, S., Pathreeker, S., Li, H., and Hosein, I. D. (2019). Plating and stripping of calcium in an alkyl carbonate electrolyte at room temperature. *ACS Appl. Energy Mater.* 2, 7738–7743. doi:10.1021/acsaem.9b01670

Biria, S., Pathreeker, S., Genier, F. S., Li, H., and Hosein, I. D. (2020). Plating and stripping calcium at room temperature in an ionic-liquid electrolyte. *ACS Appl. Energy Mater.* 3, 2310–2314. doi:10.1021/acsaem.9b02529

Bozorgchenani, M., Fischer, P., Schnaidt, J., Diemant, T., Schwarz, R. M., Marinaro, M., et al. (2018). Electrocatalytic oxygen reduction and oxygen evolution in Mg-free and Mg–containing ionic liquid 1-butyl-1-methylpyrrolidinium bis (trifluoromethanesulfonyl) imide. *ChemElectroChem.* 5, 2600–2611. doi:10.1002/celc.201800508

Brenner, A., and Sligh, J. (1971). Electrodeposition of magnesium and beryllium from organic baths. *Trans. Inst. Met. Finish*. 49, 71–78. doi:10.1080/00202967.1971.11870170

Brenner, A. (1971). Note on the electrodeposition of magnesium from an organic solution of a magnesium-boron complex. *J. Electrochem. Soc.* 118, 99. doi:10.1149/1.2407964

Canepa, P., Jayaraman, S., Cheng, L., Rajput, N. N., Richards, W. D., Gautam, G. S., et al. (2015). Elucidating the structure of the magnesium aluminum chloride complex electrolyte for magnesium-ion batteries. *Energy Environ. Sci*. 8, 3718–3730. doi:10.1039/c5ee02340h

Carbone, L., Moro, P. T., Gobet, M., Munoz, S., Devany, M., Greenbaum, S. G., et al. (2018). Enhanced lithium oxygen battery using a glyme electrolyte and carbon nanotubes. *ACS Appl. Mater. Interfaces*. 10, 16367–16375. doi:10.1021/acsami.7b19544

Carter, T. J., Mohtadi, R., Arthur, T. S., Mizuno, F., Zhang, R., Shirai, S., et al. (2014). Boron clusters as highly stable magnesium-battery electrolytes. *Angew Chem. Int. Ed. Engl*. 53, 3173–3177. doi:10.1002/anie.201310317

Chang, Z., Yang, Y., Wang, X., Li, M., Fu, Z., Wu, Y., et al. (2015). Hybrid system for rechargeable magnesium battery with high energy density. *Sci. Rep*. 5, 11931–11938. doi:10.1038/srep11931

Chen, Y., Freunberger, S. A., Peng, Z., Fontaine, O., and Bruce, P. G. (2013). Charging a Li-O_2 battery using a redox mediator. *Nat. Chem*. 5, 489. doi:10.1038/nchem.1646

Chen, P., Zhang, K., Tang, D., Liu, W., Meng, F., Huang, Q., et al. (2020). Recent progress in electrolytes for Zn–air batteries. *Front. Chem*. 8. doi:10.3389/fchem.2020.00372

Cheng, G., Xu, Q., Zhang, M., Ding, F., Liu, X., and Jiao, L. (2013). Electrochemical reversibility of magnesium deposition-dissolution on aluminum substrates in Grignard reagent/THF solutions. *Chin. Sci. Bull.* 58, 3385–3389. doi:10.1007/s11434-013-6008-7

Chusid, O., Gofer, Y., Gizbar, H., Vestfrid, Y., Levi, E., Aurbach, D., et al. (2003). Solid-state rechargeable magnesium batteries. *Adv. Mater*. 15, 627–630. doi:10.1002/adma.200304415

Connor, J. H., Reid, W. E., Jr, and Wood, G. B. (1957). Electrodeposition of metals from organic solutions: V. Electrodeposition of magnesium and magnesium alloys. *J. Electrochem. Soc*. 104, 38. doi:10.1149/1.2428492

Das, S., Højberg, J., Knudsen, K. B., Younesi, R., Johansson, P., Norby, P., et al. (2015). Instability of ionic liquid-based electrolytes in Li–O_2 batteries. *J. Phys. Chem. C*. 119, 18084–18090. doi:10.1021/acs.jpcc.5b04950

De Giorgio, F., Soavi, F., and Mastragostino, M. (2011). Effect of lithium ions on oxygen reduction in ionic liquid-based electrolytes. *Electrochem. Commun*. 13, 1090–1093. doi:10.1016/j.elecom.2011.07.004

Deivanayagam, R., Cheng, M., Wang, M., Vasudevan, V., Foroozan, T., Medhekar, N. V., et al. (2019). Composite polymer electrolyte for highly cyclable room-temperature solid-state magnesium batteries. *ACS Appl. Energy Mater*. 2, 7980–7990. doi:10.1021/acsaem.9b01455

Doe, R. E., Han, R., Hwang, J., Gmitter, A. J., Shterenberg, I., Yoo, H. D., et al. (2014). Novel, electrolyte solutions comprising fully inorganic salts with high anodic stability for rechargeable magnesium batteries. *Chem. Commun*. 50, 243–245. doi:10.1039/C3CC47896C

Dong, Q., Yao, X., Luo, J., Zhang, X., Hwang, H., and Wang, D. (2016). Enabling rechargeable non-aqueous Mg-O. *Chem. Commun*. 52, 13753–13756. doi:10.1039/C6CC07818D

Dongmo, S., Zaubitzer, S., Schüler, P., Krieck, S., Jörissen, L., Wohlfahrt-Mehrens, M., et al. (2020). Stripping and plating a magnesium metal anode in bromide-based non-nucleophilic electrolytes. *ChemSusChem*. 13, 3530–3538. doi:10.1002/cssc.202000249

Du, A., Zhang, H., Zhang, Z., Zhao, J., Cui, Z., Zhao, Y., et al. (2019). A crosslinked polytetrahydrofuran-borate-based polymer electrolyte enabling wide-working-temperature-range rechargeable magnesium batteries. *Adv. Mater*. 31, 1805930. doi:10.1002/adma.201805930

Fan, H., Zhao, Y., Xiao, J., Zhang, J., Wang, M., and Zhang, Y. (2020). A non-nucleophilic gel polymer magnesium electrolyte compatible with sulfur cathode. *Nano Res*., 1–6. doi:10.1007/s12274-020-2923-5

Fu, J., Liang, R., Liu, G., Yu, A., Bai, Z., Yang, L., et al. (2019). Recent progress in electrically rechargeable zinc–air batteries. *Adv. Mater*. 31, 1805230. doi:10.1002/adma.201805230

Gao, X., Mariani, A., Jeong, S., Liu, X., Dou, X., Ding, M., et al. (2019). Prototype rechargeable magnesium batteries using ionic liquid electrolytes. *J. Power Sources*. 423, 52–59. doi:10.1016/j.jpowsour.2019.03.049

Gelman, D., Shvartsev, B., and Ein-Eli, Y. (2019). "Challenges and prospect of non–aqueous non-alkali (NANA) metal–air batteries," in *Electrochemical energy storage: next generation battery concepts*. Editor R.-A. Eichel (Cham, Switzerland: Springer International Publishing), 127–168.

Gilmore, P., and Sundaresan, V. B. (2019). A functionally graded cathode architecture for extending the cycle-life of potassium-oxygen batteries. *Batteries Supercaps*. 2, 678–687. doi:10.1002/batt.201900025

Giridhar, P., El Abedin, S. Z., and Endres, F. (2012). Electrodeposition of aluminium from 1-butyl-1-methylpyrrolidinium chloride/AlCl3 and mixtures with 1-ethyl-3-methylimidazolium chloride/AlCl3. *Electrochim. Acta*. 70, 210–214. doi:10.1016/j.electacta.2012.03.056

Goossens, K., Rakers, L., Heinrich, B., Ahumada, G., Ichikawa, T., Donnio, B., et al. (2019). Anisotropic, organic ionic plastic crystal mesophases from persubstituted imidazolium pentacyanocyclopentadienide salts. *Chem. Mater*. 31, 9593–9603. doi:10.1021/acs.chemmater.9b02338

Grande, L., Von Zamory, J., Koch, S. L., Kalhoff, J., Paillard, E., and Passerini, S. (2015). Homogeneous lithium electrodeposition with pyrrolidinium-based ionic liquid electrolytes. *ACS Appl. Mater. Interfaces*. 7, 5950–5958. doi:10.1021/acsami.5b00209

Gregory, T. D., Hoffman, R. J., and Winterton, R. C. (1990). Nonaqueous electrochemistry of magnesium: applications to energy storage. *J. Electrochem. Soc*. 137, 775. doi:10.1149/1.2086553

Guo, Y., Yang, J., Nuli, Y., and Wang, J. (2010). Study of electronic effect of Grignard reagents on their electrochemical behavior. *Electrochem. Commun*. 12, 1671–1673. doi:10.1016/j.elecom.2010.08.015

Guo, Y.-S., Zhang, F., Yang, J., Wang, F.-F., Nuli, Y., and Hirano, S.-I. (2012). Boron-based electrolyte solutions with wide electrochemical windows for rechargeable magnesium batteries. *Energy Environ. Sci*. 5, 9100–9106. doi:10.1039/C2EE22509C

Ha, J. H., Adams, B., Cho, J.-H., Duffort, V., Kim, J. H., Chung, K. Y., et al. (2016). A conditioning-free magnesium chloride complex electrolyte for rechargeable magnesium batteries. *J. Mater. Chem*. 4, 7160–7164. doi:10.1039/C6TA01684G

Ha, T. A., Pozo-Gonzalo, C., Nairn, K., Macfarlane, D. R., Forsyth, M., and Howlett, P. C. (2020). An investigation of commercial carbon air cathode structure in ionic liquid based sodium oxygen batteries. *Sci. Rep*. 10, 1–10. doi:10.1038/s41598-020-63473-y

Haas, I., and Gedanken, A. (2008). Synthesis of metallic magnesium nanoparticles by sonoelectrochemistry. *Chem. Commun*., 1795–1797. doi:10.1039/B717670H

Han, S.-D., Rajput, N. N., Qu, X., Pan, B., He, M., Ferrandon, M. S., et al. (2016). Origin of electrochemical, structural, and transport properties in nonaqueous zinc electrolytes. *ACS Appl. Mater. Interfaces*. 8, 3021–3031. doi:10.1021/acsami.5b10024

Han, S., Cai, C., Yang, F., Zhu, Y., Sun, Q., Zhu, Y. G., et al. (2020). Interrogation of the reaction mechanism in a Na–O2 battery using in situ transmission electron microscopy. *ACS Nano*. 14, 3669–3677. doi:10.1021/acsnano.0c00283

Hardwick, L. J., and De León, C. P. (2018). Rechargeable multi-valent metal-air batteries. *Johnson Matthey Technol. Rev*. 62, 134–149. doi:10.1595/205651318X696729

Hartmann, P., Bender, C. L., Vračar, M., Dürr, A. K., Garsuch, A., Janek, J., et al. (2013). A rechargeable room-temperature sodium superoxide (NaO_2) battery. *Nat. Mater*. 12, 228–232. doi:10.1038/NMAT3486

Haynes, W. M. (2014). *CRC handbook of chemistry and physics*. Boca Raton, FL: CRC Press.

He, S., Nielson, K. V., Luo, J., and Liu, T. L. (2017). Recent advances on MgCl2 based electrolytes for rechargeable Mg batteries. *Energy Stor. Mater*. 8, 184–188. doi:10.1016/j.ensm.2016.12.001

Hegemann, P., Hegemann, M., Zan, L., and Baltruschat, H. (2019). Stability of tetraglyme for reversible magnesium deposition from a magnesium aluminum chloride complex. *J. Electrochem. Soc*. 166, A245. doi:10.1149/2.0871902jes

Higashi, S., Miwa, K., Aoki, M., and Takechi, K. (2014). A novel inorganic solid state ion conductor for rechargeable Mg batteries. *Chem. Commun*. 50, 1320–1322. doi:10.1039/C3CC47097K

Hu, K., Qin, L., Zhang, S., Zheng, J., Sun, J., Ito, Y., et al. (2020). Building a reactive armor using S-doped graphene for protecting potassium metal anodes from oxygen crossover in K–O_2 batteries. *ACS Energy Lett*. doi:10.1021/acsenergylett.0c00715

Hwang, H. J., Chi, W. S., Kwon, O., Lee, J. G., Kim, J. H., and Shul, Y.-G. (2016). Selective ion transporting polymerized ionic liquid membrane separator for enhancing cycle stability and durability in secondary zinc–air battery systems. *ACS Appl. Mater. Interfaces*. 8, 26298–26308. doi:10.1021/acsami.6b07841

Jäckle, M., Helmbrecht, K., Smits, M., Stottmeister, D., and Groβ, A. (2018). Self-diffusion barriers: possible descriptors for dendrite growth in batteries? *Energy Environ. Sci.* 11, 3400–3407. doi:10.1039/C8EE01448E

Jaschin, P. W., Gao, Y., Li, Y., and Bo, S.-H. (2020). A materials perspective on magnesium-ion-based solid-state electrolytes. *J. Mater. Chem.* 8, 2875–2897. doi:10.1039/C9TA11729F

Jin, L., Howlett, P. C., Pringle, J. M., Janikowski, J., Armand, M., Macfarlane, D. R., et al. (2014). An organic ionic plastic crystal electrolyte for rate capability and stability of ambient temperature lithium batteries. *Energy Environ. Sci.* 7, 3352–3361. doi:10.1039/C4EE01085J

Johnson, L., Li, C., Liu, Z., Chen, Y., Freunberger, S. A., Ashok, P. C., et al. (2014). The role of LiO_2 solubility in O_2 reduction in aprotic solvents and its consequences for Li–O_2 batteries. *Nat. Chem.* 6, 1091. doi:10.1038/nchem.2101

Jusys, Z., Schnaidt, J., and Behm, R. J. (2019). O_2 reduction on a Au film electrode in an ionic liquid in the absence and presence of Mg^{2+} ions: product formation and adlayer dynamics. *J. Chem. Phys.* 150, 041724. doi:10.1063/1.5051982

Kakibe, T., Yoshimoto, N., Egashira, M., and Morita, M. (2010). Optimization of cation structure of imidazolium-based ionic liquids as ionic solvents for rechargeable magnesium batteries. *Electrochem. Commun.* 12, 1630–1633. doi:10.1016/j.elecom.2010.09.012

Kakibe, T., Hishii, J.-Y., Yoshimoto, N., Egashira, M., and Morita, M. (2012). Binary ionic liquid electrolytes containing organo-magnesium complex for rechargeable magnesium batteries. *J. Power Sources.* 203, 195–200. doi:10.1016/j.jpowsour.2011.10.127

Katayama, Y., Sekiguchi, K., Yamagata, M., and Miura, T. (2005). Electrochemical behavior of oxygen/superoxide ion couple in 1-butyl-1-methylpyrrolidinium bis (trifluoromethylsulfonyl) imide room-temperature molten salt. *J. Electrochem. Soc.* 152, E247–E250. doi:10.1149/1.1946530

Khan, A., and Zhao, C. (2014). Enhanced performance in mixture DMSO/ionic liquid electrolytes: toward rechargeable Li–O_2 batteries. *Electrochem. Commun.* 49, 1–4. doi:10.1016/j.elecom.2014.09.014

Kim, Y.-S., Cho, Y.-G., Odkhuu, D., Park, N., and Song, H.-K. (2013). A physical organogel electrolyte: characterized by *in situ* thermo-irreversible gelation and single-ion-predominent conduction. *Sci. Rep.* 3, 1–6. doi:10.1038/srep01917

Kim, M.-J., Kang, H.-J., Im, W. B., and Jun, Y.-S. (2020). Rechargeable intermetallic calcium–lithium–O_2 batteries. *ChemSusChem.* 13, 574–581. doi:10.1002/cssc.201902925

Kumar, G. G., and Munichandraiah, N. (1999). Reversibility of Mg/Mg2+ couple in a gel polymer electrolyte. *Electrochim. Acta.* 44, 2663–2666. doi:10.1016/S0013-4686(98)00388-0

Kundu, D., Black, R., Adams, B., and Nazar, L. F. (2015). A highly active low voltage redox mediator for enhanced rechargeability of lithium–oxygen batteries. *ACS Cent. Sci.* 1, 510–515. doi:10.1021/acscentsci.5b00267

Lair, V., Sirieix-Plenet, J., Gaillon, L., Rizzi, C., and Ringuedé, A. (2010). Mixtures of room temperature ionic liquid/ethanol solutions as electrolytic media for cerium oxide thin layer electrodeposition. *Electrochim. Acta.* 56, 784–789. doi:10.1016/j.electacta.2010.09.102

Law, Y. T., Schnaidt, J., Brimaud, S., and Behm, R. J. (2016). Oxygen reduction and evolution in an ionic liquid ([BMP][TFSA]) based electrolyte: a model study of the cathode reactions in Mg-air batteries. *J. Power Sources.* 333, 173–183. doi:10.1016/j.jpowsour.2016.09.025

Lee, B., Cho, J.-H., Seo, H. R., Na, S. B., Kim, J. H., Cho, B. W., et al. (2018). Strategic combination of Grignard reagents and allyl-functionalized ionic liquids as an advanced electrolyte for rechargeable magnesium batteries. *J. Mater. Chem.* 6, 3126–3133. doi:10.1039/C7TA09330F

Leisegang, T., Meutzner, F., Zschornak, M., Münchgesang, W., Schmid, R., Nestler, T., et al. (2019). The aluminum-ion battery: a sustainable and seminal concept?. *Front. Chem.* 7, 268. doi:10.3389/fchem.2019.00268

Leng, L., Zeng, X., Chen, P., Shu, T., Song, H., Fu, Z., et al. (2015). A novel stability-enhanced lithium-oxygen battery with cellulose-based composite polymer gel as the electrolyte. *Electrochim. Acta.* 176, 1108–1115. doi:10.1016/j.electacta.2015.07.111

Li, C. S., Sun, Y., Gebert, F., and Chou, S. L. (2017). Current progress on rechargeable magnesium–air battery. *Adv. Energy Mater.* 7, 1700869. doi:10.1002/aenm.201700869

Li, Z., Fuhr, O., Fichtner, M., and Zhao-Karger, Z. (2019). Towards stable and efficient electrolytes for room-temperature rechargeable calcium batteries. *Energy Environ. Sci.* 12, 3496–3501. doi:10.1039/C9EE01699F

Li, C., Wei, J.-S., Qiu, K., and Wang, Y.-G. (2020a). Li–air battery with a super-hydrophobic Li-protective layer. *ACS Appl. Mater. Interfaces.* doi:10.1021/acsami.0c05494

Li, X., Xing, Y., Xu, J., Deng, Q., and Shao, L.-H. (2020b). Uniform yolk–shell structured Si–C nanoparticles as a high performance anode material for the Li-ion battery. *Chem. Commun.* doi:10.1039/C9CC07997A

Liang, F., and Hayashi, K. (2015). A high-energy-density mixed-aprotic-aqueous sodium-air cell with a ceramic separator and a porous carbon electrode. *J. Electrochem. Soc.* 162, A1215. doi:10.1149/2.0421507jes

Liebenow, C., Yang, Z., and Lobitz, P. (2000). The electrodeposition of magnesium using solutions of organomagnesium halides, amidomagnesium halides and magnesium organoborates. *Electrochem. Commun.* 2, 641–645. doi:10.1016/S1388-2481(00)00094-1

Liebenow, C. (1997). Reversibility of electrochemical magnesium deposition from Grignard solutions. *J. Appl. Electrochem.* 27, 221–225. doi:10.1023/A:1018464210084

Liu, T., Shao, Y., Li, G., Gu, M., Hu, J., Xu, S., et al. (2014). A facile approach using $MgCl_2$ to formulate high performance Mg^{2+} electrolytes for rechargeable Mg batteries. *J. Mater. Chem.* 2, 3430–3438. doi:10.1039/C3TA14825D

Liu, Z., Cui, T., Pulletikurthi, G., Lahiri, A., Carstens, T., Olschewski, M., et al. (2016). Dendrite-free nanocrystalline zinc electrodeposition from an ionic liquid containing nickel triflate for rechargeable Zn-based batteries. *Angew. Chem. Int. Ed.* 55, 2889–2893. doi:10.1002/anie.201509364

Liu, J., Bao, Z., Cui, Y., Dufek, E. J., Goodenough, J. B., Khalifah, P., et al. (2019). Pathways for practical high-energy long-cycling lithium metal batteries. *Nat. Energy.* 4, 180–186. doi:10.1038/s41560-019-0338-x

Lu, Y.-T., Chien, Y.-J., Liu, C.-F., You, T.-H., and Hu, C.-C. (2017). Active site-engineered bifunctional electrocatalysts of ternary spinel oxides, $M_{0.1}Ni_{0.9}Co_2O_4$ (M: Mn, Fe, Cu, Zn) for the air electrode of rechargeable zinc–air batteries. *J. Mater. Chem.* 5, 21016–21026. doi:10.1039/C7TA06302D

Luo, J., Bi, Y., Zhang, L., Zhang, X., and Liu, T. L. (2019a). A stable, non-corrosive perfluorinated pinacolatoborate Mg electrolyte for rechargeable Mg batteries. *Angew. Chem. Int. Ed.* 58, 6967–6971. doi:10.1002/anie.201902009

Luo, Z., Li, Y., Liu, Z., Pan, L., Guan, W., Liu, P., et al. (2019b). Prolonging the cycle life of a lithium–air battery by alleviating electrolyte degradation with a ceramic–carbon composite cathode. *ChemSusChem.* 12, 4962–4967. doi:10.1002/cssc.201901629

Ma, Z., Forsyth, M., Macfarlane, D. R., and Kar, M. (2019). Ionic liquid/tetraglyme hybrid $Mg[TFSI]_2$ electrolytes for rechargeable Mg batteries. *Green Energy Environ.* 4, 146–153. doi:10.1016/j.gee.2018.10.003

Macfarlane, D. R., Huang, J., and Forsyth, M. (1999). Lithium-doped plastic crystal electrolytes exhibiting fast ion conduction for secondary batteries. *Nature.* 402, 792–794. doi:10.1038/45514

Mizrahi, O., Amir, N., Pollak, E., Chusid, O., Marks, V., Gottlieb, H., et al. (2008). Electrolyte solutions with a wide electrochemical window for rechargeable magnesium batteries. *J. Electrochem. Soc.* 155, A103–A109. doi:10.1149/1.2806175

Monaco, S., Soavi, F., and Mastragostino, M. (2013). Role of oxygen mass transport in rechargeable Li/O_2 batteries operating with ionic liquids. *J. Phys. Chem. Lett.* 4, 1379–1382. doi:10.1021/jz4006256

Muldoon, J., Bucur, C. B., Oliver, A. G., Sugimoto, T., Matsui, M., Kim, H. S., et al. (2012). Electrolyte roadblocks to a magnesium rechargeable battery. *Energy Environ. Sci.* 5, 5941–5950. doi:10.1039/C2EE03029B

Muldoon, J., Bucur, C. B., and Gregory, T. (2014). Quest for nonaqueous multivalent secondary batteries: magnesium and beyond. *Chem. Rev.* 114, 11683–11720. doi:10.1021/cr500049y

Narayanan, N. V., Raj, B. A., and Sampath, S. (2009). Magnesium ion conducting, room temperature molten electrolytes. *Electrochem. Commun.* 11, 2027–2031. doi:10.1016/j.elecom.2009.08.045

Neale, A. R., Li, P., Jacquemin, J., Goodrich, P., Ball, S. C., Compton, R. G., et al. (2016). Effect of cation structure on the oxygen solubility and diffusivity in a range of bis{(trifluoromethyl)sulfonyl}imide anion based ionic liquids for lithium–air battery electrolytes. *Phys. Chem. Chem. Phys.* 18, 11251–11262. doi:10.1039/C5CP07160G

Neale, A. R., Goodrich, P., Hughes, T.-L., Hardacre, C., Ball, S. C., and Jacquemin, J. (2017). Physical and electrochemical investigations into blended electrolytes containing a glyme solvent and two bis {(trifluoromethyl) sulfonyl} imide-based ionic liquids. *J. Electrochem. Soc.* 164, H5124. doi:10.1149/2.0141708jes

Ng, B., Peng, X., Faegh, E., and Mustain, W. E. (2020). Using nanoconfinement to inhibit the degradation pathways of conversion-metal oxide anodes for highly stable fast-charging Li-ion batteries. *J. Mater. Chem.* 8, 2712–2727. doi:10.1039/C9TA11708C

Ogasawara, T., Débart, A., Holzapfel, M., Novák, P., and Bruce, P. G. (2006). Rechargeable Li_2O_2 electrode for lithium batteries. *J. Am. Chem. Soc.* 128, 1390–1393. doi:10.1021/ja056811q

Ortiz-Vitoriano, N., Batcho, T. P., Kwabi, D. G., Han, B., Pour, N., Yao, K. P. C., et al. (2015). Rate-dependent nucleation and growth of NaO_2 in $Na–O_2$ batteries. *J. Phys. Chem. Lett.* 6, 2636–2643. doi:10.1021/acs.jpclett.5b00919

Overcash, D. M., and Mathers, F. (1933). The electrodeposition of magnesium. *Trans. Electrochem. Soc.* 64, 305. doi:10.1149/1.3504531

Pandey, G., and Hashmi, S. (2009). Experimental investigations of an ionic-liquid-based, magnesium ion conducting, polymer gel electrolyte. *J. Power Sources.* 187, 627–634. doi:10.1016/j.jpowsour.2008.10.112

Ponrouch, A., Frontera, C., Bardé, F., and Palacín, M. R. (2016). Towards a calcium-based rechargeable battery. *Nat. Mater.* 15, 169–172. doi:10.1038/nmat4462

Ponrouch, A., Bitenc, J., Dominko, R., Lindahl, N., Johansson, P., and Palacin, M. R. (2019). Multivalent rechargeable batteries. *Energy Stor. Mater.* doi:10.1016/j.ensm.2019.04.012

Pour, N., Gofer, Y., Major, D. T., and Aurbach, D. (2011). Structural analysis of electrolyte solutions for rechargeable Mg batteries by stereoscopic means and DFT calculations. *J. Am. Chem. Soc.* 133, 6270–6278. doi:10.1021/ja1098512

Pringle, J. M., Howlett, P. C., Macfarlane, D. R., and Forsyth, M. (2010). Organic ionic plastic crystals: recent advances. *J. Mater. Chem.* 20, 2056–2062. doi:10.1039/B920406G

Pujare, N. U. (1988). A calcium oxygen secondary battery. *J. Electrochem. Soc.* 135, 260. doi:10.1149/1.2095574

Reinsberg, P., Bondue, C., and Baltruschat, H. (2016a). Mechanistic investigation of the oxygen reduction in magnesium ion-containing dimethyl sulfoxide. *Electrochim. Acta.* 200, 214–221. doi:10.1016/j.electacta.2016.03.157

Reinsberg, P., Bondue, C. J., and Baltruschat, H. (2016b). Calcium–oxygen batteries as a promising alternative to sodium–oxygen batteries. *J. Phys. Chem. C.* 120, 22179–22185. doi:10.1021/acs.jpcc.6b06674

Reinsberg, P., Abd-El-Latif, A.-E.-a. A., and Baltruschat, H. (2018). Investigation of the complex influence of divalent cations on the oxygen reduction reaction in aprotic solvents. *Electrochim. Acta.* 273, 424–431. doi:10.1016/j.electacta.2018.03.123

Ren, X., and Wu, Y. (2013). A low-overpotential potassium–oxygen battery based on potassium superoxide. *J. Am. Chem. Soc.* 135, 2923–2926. doi:10.1021/ja312059q

Sarangika, H., Dissanayake, M., Senadeera, G., Rathnayake, R., and Pitawala, H. (2017). Polyethylene oxide and ionic liquid-based solid polymer electrolyte for rechargeable magnesium batteries. *Ionics.* 23, 2829–2835. doi:10.1007/s11581-016-1870-3

Sawyer, D. T., Calderwood, T. S., Yamaguchi, K., and Angelis, C. T. (1983). Synthesis and characterization of tetramethylammonium superoxide. *Inorg. Chem.* 22, 2577–2583. doi:10.1021/ic00160a022

See, K. A., Liu, Y.-M., Ha, Y., Barile, C. J., and Gewirth, A. A. (2017). Effect of concentration on the electrochemistry and speciation of the magnesium aluminum chloride complex electrolyte solution. *ACS Appl. Mater. Interfaces.* 9, 35729–35739. doi:10.1021/acsami.7b08088

Shao, Y., Rajput, N. N., Hu, J., Hu, M., Liu, T., Wei, Z., et al. (2015). Nanocomposite polymer electrolyte for rechargeable magnesium batteries. *Nanomater. Energy.* 12, 750–759. doi:10.1016/j.nanoen.2014.12.028

Sheng, C., Yu, F., Wu, Y., Peng, Z., and Chen, Y. (2018). Disproportionation of sodium superoxide in metal–air batteries. *Angew. Chem. Int. Ed.* 57, 9906–9910. doi:10.1002/anie.201804726

Shiga, T., Hase, Y., Kato, Y., Inoue, M., and Takechi, K. (2013). A rechargeable non-aqueous $Mg–O_2$ battery. *Chem. Commun.* 49, 9152–9154. doi:10.1039/C3CC43477J

Shiga, T., Kato, Y., and Hase, Y. (2017). Coupling of nitroxyl radical as an electrochemical charging catalyst and ionic liquid for calcium plating/stripping toward a rechargeable calcium–oxygen battery. *J. Mater. Chem.* 5, 13212–13219. doi:10.1039/C7TA03422A

Shterenberg, I., Salama, M., Gofer, Y., Levi, E., and Aurbach, D. (2014). The challenge of developing rechargeable magnesium batteries. *MRS Bull.* 39, 453–460. doi:10.1557/mrs.2014.61

Shyamsunder, A., Blanc, L. E., Assoud, A., and Nazar, L. F. (2019). Reversible calcium plating and stripping at room temperature using a borate salt. *ACS Energy Lett.* 4, 2271–2276. doi:10.1021/acsenergylett.9b01550

Smith, J. G., Naruse, J., Hiramatsu, H., and Siegel, D. J. (2016). Theoretical limiting potentials in Mg/O_2 batteries. *Chem. Mater.* 28, 1390–1401. doi:10.1021/acs.chemmater.5b04501

Staniewicz, R. J. (1980). A study of the calcium-thionyl chloride electrochemical system. *J. Electrochem. Soc.* 127, 782. doi:10.1149/1.2129758

Ta, K., Zhang, R., Shin, M., Rooney, R. T., Neumann, E. K., and Gewirth, A. A. (2019). Understanding Ca electrodeposition and speciation processes in nonaqueous electrolytes for next-generation Ca-ion batteries. *ACS Appl. Mater. Interfaces.* 11, 21536–21542. doi:10.1021/acsami.9b04926

Tchitchekova, D., Monti, D., Johansson, P., Bardé, F., Randon-Vitanova, A., Palacín, M., et al. (2017). On the reliability of half-cell tests for monovalent (Li^+, Na^+) and divalent (Mg^{2+}, Ca^{2+}) cation based batteries. *J. Electrochem. Soc.* 164, A1384–A1392. doi:10.1149/2.0411707jes

Trahan, M. J., Mukerjee, S., Plichta, E. J., Hendrickson, M. A., and Abraham, K. (2012). Studies of Li-air cells utilizing dimethyl sulfoxide-based electrolyte. *J. Electrochem. Soc.* 160, A259. doi:10.1149/2.048302jes

Vardar, G., Nelson, E. G., Smith, J. G., Naruse, J., Hiramatsu, H., Bartlett, B. M., et al. (2015). Identifying the discharge product and reaction pathway for a secondary Mg/O_2 battery. *Chem. Mater.* 27, 7564–7568. doi:10.1021/acs.chemmater.5b03608

Viestfrid, Y., Levi, M., Gofer, Y., and Aurbach, D. (2005). Microelectrode studies of reversible Mg deposition in THF solutions containing complexes of alkylaluminum chlorides and dialkylmagnesium. *J. Electroanal. Chem.* 576, 183–195. doi:10.1016/j.jelechem.2004.09.034

Wang, D., Gao, X., Chen, Y., Jin, L., Kuss, C., and Bruce, P. G. (2018a). Plating and stripping calcium in an organic electrolyte. *Nat. Mater.* 17, 16–20. doi:10.1038/nmat5036

Wang, W., Lai, N. C., Liang, Z., Wang, Y., and Lu, Y. C. (2018b). Superoxide stabilization and a universal KO_2 growth mechanism in potassium–oxygen batteries. *Angew. Chem. Int. Ed.* 57, 5042–5046. doi:10.1002/anie.201801344

Wang, H., Feng, X., Chen, Y., Liu, Y.-S., Han, K. S., Zhou, M., et al. (2019a). Reversible electrochemical interface of Mg metal and conventional electrolyte enabled by intermediate adsorption. *ACS Energy Lett.* 5, 200–206. doi:10.1021/acsenergylett.9b02211

Wang, S., Cai, W., Sun, Z., Huang, F., Jie, Y., Liu, Y., et al. (2019b). Stable cycling of Na metal anodes in a carbonate electrolyte. *Chem. Commun.* 55, 14375–14378. doi:10.1039/C9CC07419H

Watkins, T., Kumar, A., and Buttry, D. A. (2016). Designer ionic liquids for reversible electrochemical deposition/dissolution of magnesium. *J. Am. Chem. Soc.* 138, 641–650. doi:10.1021/jacs.5b11031

Xiao, N., Gourdin, G., and Wu, Y. (2018). Simultaneous stabilization of potassium metal and superoxide in $K–O_2$ batteries on the basis of electrolyte reactivity. *Angew. Chem. Int. Ed.* 57, 10864–10867. doi:10.1002/anie.201804115

Yang, W., Salim, J., Ma, C., Ma, Z., Sun, C., Li, J., et al. (2013). Flowerlike Co_3O_4 microspheres loaded with copper nanoparticle as an efficient bifunctional catalyst for lithium–air batteries. *Electrochem. Commun.* 28, 13–16. doi:10.1016/j.elecom.2012.12.007

Yao, Z., Hegde, V. I., Aspuru-Guzik, A., and Wolverton, C. (2019). Discovery of calcium-metal alloy anodes for reversible Ca-ion batteries. *Adv. Energy Mater.* 9, 1802994. doi:10.1002/aenm.201802994

Yi, J., Liu, X., Guo, S., Zhu, K., Xue, H., and Zhou, H. (2015). Novel stable gel polymer electrolyte: toward a high safety and long life Li–air battery. *ACS Appl. Mater. Interfaces.* 7, 23798–23804. doi:10.1021/acsami.5b08462

Yin, W.-W., Yue, J.-L., Cao, M.-H., Liu, W., Ding, J.-J., Ding, F., et al. (2015). Dual catalytic behavior of a soluble ferrocene as an electrocatalyst and in the electrochemistry for Na–air batteries. *J. Mater. Chem.* 3, 19027–19032. doi:10.1039/C5TA04647E

Yu, W., Lau, K. C., Lei, Y., Liu, R., Qin, L., Yang, W., et al. (2017). Dendrite-free potassium–oxygen battery based on a liquid alloy anode. *ACS Appl. Mater. Interfaces.* 9, 31871–31878. doi:10.1021/acsami.7b08962

Zhang, J., Zhou, Q., Tang, Y., Zhang, L., and Li, Y. (2019). Zinc–air batteries: are they ready for prime time?. *Chem. Sci.* 10, 8924–8929. doi:10.1039/c9sc04221k

Zhao, Q. S., Nuli, Y. N., Guo, Y. S., Yang, J., and Wang, J. L. (2011). Reversibility of electrochemical magnesium deposition from tetrahydrofuran solutions containing pyrrolidinyl magnesium halide. *Electrochim. Acta.* 56, 6530–6535. doi:10.1016/j.electacta.2011.04.114

Zhao, X., Chen, F., Liu, J., Cheng, M., Su, H., Liu, J., et al. (2020). Enhanced surface binding energy regulates uniform potassium deposition for stable potassium metal anodes. *J. Mater. Chem.* 8, 5671–5678. doi:10.1039/C9TA14226F

Zhou, Z.-B., and Matsumoto, H. (2007). Lithium-doped, organic ionic plastic crystal electrolytes exhibiting high ambient-temperature conductivities. *Electrochem. Commun.* 9, 1017–1022. doi:10.1016/j.elecom.2006.12.012

Zhu, J., Guo, Y., Yang, J., Nuli, Y., Zhang, F., Wang, J., et al. (2014). Halogen-free boron based electrolyte solution for rechargeable magnesium batteries. *J. Power Sources* 248, 690–694. doi:10.1016/j.jpowsour.2013.09.124

Conflict of Interest: The authors declare that the research was conducted in the absence of any commercial or financial relationships that could be construed as a potential conflict of interest.

Advantages of publishing in Frontiers

OPEN ACCESS
Articles are free to read for greatest visibility and readership

FAST PUBLICATION
Around 90 days from submission to decision

HIGH QUALITY PEER-REVIEW
Rigorous, collaborative, and constructive peer-review

TRANSPARENT PEER-REVIEW
Editors and reviewers acknowledged by name on published articles

Frontiers
Avenue du Tribunal-Fédéral 34
1005 Lausanne | Switzerland

Visit us: www.frontiersin.org
Contact us: frontiersin.org/about/contact

REPRODUCIBILITY OF RESEARCH
Support open data and methods to enhance research reproducibility

DIGITAL PUBLISHING
Articles designed for optimal readership across devices

FOLLOW US
@frontiersin

IMPACT METRICS
Advanced article metrics track visibility across digital media

EXTENSIVE PROMOTION
Marketing and promotion of impactful research

LOOP RESEARCH NETWORK
Our network increases your article's readership